



---

# Maximising information from weak lensing galaxy surveys

---

**Alessandro Maraio**

*Institute for Astronomy, University of Edinburgh*

Doctor of Philosophy  
March 2025

# Abstract

---

Weak lensing galaxy surveys are currently undergoing a dramatic revolution as the dawn of the Stage-IV surveys is upon us. The quality and quantity of data that we are to receive over the next decade dwarfs the data we have from existing observatories and will undoubtedly lead to many cosmological discoveries. Therefore, ensuring that our analysis methods are as accurate and precise as the raw data is of upmost importance, and the driving force behind this thesis and the work contained within.

Understanding the details behind a modern cosmic shear analysis requires us to start with the fundamentals of cosmology and go from there. Chapter 1 provides us with a gentle introduction to some of the driving ideas and results that have compounded to form our modern cosmological model. Starting with Einstein’s general relativity, Chapter 2 derives many key results which are required for any cosmological analysis. We then focus on the specifics of a cosmic shear analysis in Chapter 3, with a brief look into some of the motivations behind the Stage-IV surveys in Chapter 4.

Returning to the theme of the development of accurate and precise statistical methods for use in cosmic shear analyses, Chapter 5 investigates a new implementation of the Quadratic Maximum Likelihood (QML) estimator. Previous implementations of the QML estimator required the direct evaluation of dense, high-dimensional matrices of either spherical harmonics or Legendre polynomials. This severely limits the application of these methods to the increased precision of Stage-IV survey data. The evaluation of each entry in these matrices is a major bottleneck in computational speed, combined with the extreme limitations in the RAM usage from the high dimensionality of the matrices makes these existing implementations of QML unsuitable for the next generation of cosmic shear surveys. I led the development of a new, alternative implementation of the QML estimator which side-steps the need to compute and store these massive matrices though using the conjugate-gradient and finite-differences methods. These allow for dramatically reduced run-times and RAM usage of my new estimator when compared to previous implementations. Applying this estimator to Stage-IV cosmic shear data finds that we achieve a 20 % decrement in the error bars on the largest angular scales for the  $E$ -modes, and over an order of magnitude decrement in the  $B$ -modes. This highlights the usefulness of QML methods when applied to cosmic shear survey data.

An accurate measurement of the observational power spectrum is useless without robust modelling of all the systematic effects that contribute to the cosmic shear signal. Of particular importance is the impact of baryonic feedback physics that exists on small-scales within our Universe, which can dramatically affect the cosmic shear power spectrum on small angular scales. Mitigating the effects of baryonic feedback bias in cosmic shear surveys has been the discussion of many papers in the literature. Chapter 6 investigates the implementation of the ‘theoretical uncertainties’ approach applied to baryonic feedback in the matter power spectrum, the underlying quantity that cosmic shear probes. By bench-

marking several baryonic feedback models to an ensemble of hydrodynamical simulations, we can quantify the error on each model as a function of wavenumber and redshift. These errors then inform us on how to smoothly down-weight the contaminating modes in the power spectrum, allowing us to gain maximum information from our observables without being susceptible to bias from inadequate modelling of baryonic feedback physics. We find that using a simple, one-parameter model of baryonic feedback leads to an unacceptable level of bias when including angular scales down to  $\ell_{\text{MAX}} = 5000$ , the nominal target for a Stage-IV survey. The inclusion of the theoretical error covariance mitigates these biases, with the results preferring a multi-parameter model of baryonic feedback to further mitigate biases.

We then turn our attention to deriving new methods for determining sets of binary scale cuts for future cosmic shear surveys in Chapter 7. Binary cuts have been well-studied in the literature, where they have been used extensively in previous Stage-III cosmic shear surveys and thus form the default choice for Stage-IV surveys. We find that if we apply existing methods for deriving binary cuts to Stage-IV survey data, then the results from our new surveys will be no better than existing results in the literature. Using this as motivation, we present three alternative methods for how the derivation of binary scale cuts might work for a Stage-IV survey. These aim to keep the maximum amount of information possible from the data, without incurring significant biases in the final results.

We present a summary of work completed in this thesis along with conclusions and some thoughts for the future in Chapter 8.

# Universal abstract

---

While astronomy may be considered one of the oldest natural sciences, it is remarkable that we could only begin to describe the large-scale properties of our Universe a little over a hundred years ago. Since then, the study of our Universe, cosmology, has evolved from us making primitive observations that distant galaxies were moving away from us, to making unimaginably precise measurements throughout our Universe’s evolution and across the entire spectrum of light. These observations have led to extraordinary discoveries about the properties of our Universe: that 25 % of it is in a type of matter that we’ve never observed on Earth, and 70 % of it acts in a way that no type of matter does on Earth, it has a negative gravitational attraction, and if we try to calculate its value, we get a value that is just fantastically away from what we measure!

What is even more perplexing is that the 5 % of our Universe that we are familiar with in our everyday lives — the ordinary ‘baryonic’ material that we, the Earth and planets, our Sun and distant stars are made from — is often too challenging to analyse or understand the physics of on cosmological scales. This motivates us to use our advanced telescopes to look out into our night’s sky and make observations that allow us to constrain the properties of our Universe and the physical laws that govern it.

One of the most powerful probes of our Universe comes from the effect of weak gravitational lensing, which is akin to how a magnifying glass can magnify and distort the image of objects behind it. However, instead of having a magnifying glass in space, we use the distribution of matter within our Universe to produce a similar effect. Sorry, there’s no *2001*-style space magnifying monoliths!

This lensing by the large-scale structure of our Universe induces slight changes in the apparent images of distant galaxies, which we can then try to measure with our telescopes. Since each individual galaxy’s distortion is only very slight, we rely on large-scale statistical analyses of galaxy images to derive insights into the physics of our Universe from them. The first such statistical technique that this thesis investigates is that of *power spectrum estimation*. This involves quantifying how important each scale is in distorting the images of galaxies. We are used to breaking down a signal into its components, for example a bass guitar produces very low frequency (boom) sounds whereas a high-hat cymbal can produce high frequency (tiss) sounds. We do much the same, but instead of sound frequencies, we break our signals down into large and small angular scales on the sky. Think of this very much like looking at a Dalmatian and counting the number of small and large spots that it has.

The technique that allows us to go from maps of galaxy images on the sky to a power spectrum is called a power spectrum estimator, with this thesis presenting a new implementation of the Quadratic Maximum Likelihood (QML) estimator. This aims to maximise the probability (or likelihood) of the values of the amplitude of the large- and small-scale distortions given a map of galaxy shapes. Our new implementation circumvents the need



to compute and store very many numbers in the computer’s memory, and so we can analyse far higher quality maps with improved performance than previous method allowed for.

Using the new implementation of our estimator, we found that we could decrease the error bars (how certain we are of different measurements) with respect to the nominal analysis choice by around 20 % on the largest angular scales for the ‘ $E$ -modes’, which carry the cosmological signal, and with a decrease of about a factor of 10 for the ‘ $B$ -modes’, which are tests of Einstein’s general relativity. These decrements represents a dramatic decrease in the error bars, and thus by using our new estimator we can be much more certain of our power spectrum estimate, and so more certain in any results using it — such as investigating the properties of our Universe.

As mentioned previously, the ordinary matter in our Universe that we are made from produce some remarkable physical processes within the Universe. We are already familiar with our Sun, which provides us with essential sunlight and warmth that’s essential to life on Earth. As our Sun ages, it will gradually run out of hydrogen to fuse, and so expand to form a red giant. After that, it will shrink down, forming a white dwarf star. We only have one star in our Solar System, but, like Tatooine, stars can form in pairs — a binary star system. If one of these stars becomes a white dwarf, and then eats material from the other star, the white dwarf can undergo a brilliant explosion, a supernova, which are bright enough to outshine entire galaxies. This puts a huge amount of energy into the galaxy, decimating any objects that are trying to form under gravity.

We have also observed that in the centre of many galaxies exist the presence of super-massive black holes, which can have masses from a million to billions of times the mass of our Sun. These truly massive objects pull in huge amounts of matter from their galaxy and emit vast quantities of radiation from the infalling matter back into their galaxies. This extreme amount of radiation further disrupts the gravitational attraction of matter within galaxies.

The physical processes that describe the properties of supernovae and supermassive black holes (dubbed baryonic feedback) are extremely complicated, and so we cannot write down simple formulae for their properties with pen-and-paper. Thus, we aim to capture their properties by running hydrodynamical simulations (hydro-sims), which aim to implement ‘the Universe in a computer’. However, it has been found that different collaborations who produce their own hydro-sims come up with very different results for the properties of these objects within their simulations! Thus, when we use models of baryonic feedback in our cosmological analyses of observational data, we need to ensure that our models can recreate all predictions from every hydro-sim. Otherwise, if we use an inadequate model on our observational data, we could be susceptible to bias in our results and come up with the wrong conclusions from it.

Thus, the process of comparing our analytic models of baryonic feedback to hydro-dynamical simulations results in the creation of the theoretical error covariance, which quantifies how badly our models fit the data as a function of scale and evolution in our Universe. This theoretical error covariance can then be included in our cosmological analyses, which, this thesis shows, can successfully mitigate biases associated from baryonic feedback. We find that we naturally down-weight angular scales that are contaminated with baryonic feedback, without having to impose hard cuts on our data-vectors as previous analyses have found. This comes at the cost of moderately increased error bars on our parameters. However, as ensuring that our final results remain unbiased is the most important criterion for any cosmological analysis, this is an acceptable trade-off compromise for correct results.

We then go on to develop new methods of constructing hard cuts in the data, again to alleviate the impact of baryonic feedback on our data-vectors, but in a way that is

much more easily extendable to include other sources of errors and uncertainties in our modelling. We extend existing methods that previous collaborations have used, finding that our new methods allow for much more information to be kept from our observations in a way that still leaves the final results unbiased.

We have now entered an era in which the quality of observations that we are getting from the next generation of telescopes is just amazing. It is hoped that the vast increase in the precision on the data, along with more accurate and precise statistical methods which this thesis has developed, will allow us to further uncover the fundamental physical properties of much of our Universe which has thus far eluded us.

*And they were a good friend*

—Obi Wan Kenobi

# Acknowledgements

---

First and foremost, I would like to thank my amazing supervisors, Alex and Andy, for their unwavering guidance, support, and infinite knowledge throughout the whole of my PhD. Especially since, while I may have tried to channel my inner Kimi Räikkönen of “*Leave me alone, I know what I’m doing*” — I am, in fact, not Kimi Räikkönen and I did *not* know what I was doing most of the time! This thesis, and the work contained within, would be nowhere near the quality that it is (or at least, I hope it is) without both of your help, patience, and many, many comment boxes! A sincere *thank you* to you both. I would also like to thank other members of the IfA, in particular Joe Zuntz, Catherine Heymans, and Britton Smith for their help, humour, and support in research, becoming a PhD student, and undergraduate teaching.

Secondly, I would like to thank all my amazing friends that I got to share the highs and lows of a PhD, and MPhys before that, with them:

To Ewan, thanks for putting up with this idiot for three years as your flatmate and friend. It’s fair to say that we were put in the deep end, but it was always fun to share our hours-long rants about Cuillin and what a ‘ $\chi^2$  bathtub’ is together!

Poppy: *Thank you.* Thank you for your unlimited infectious excitement and enthusiasm that always provided me with fresh motivation whenever we met up or Discorded. Thank you for our endless *Minecraft* nights where you were the Steve (or Shrek) to my Alex, spending over three hundred hours across one hundred evenings since 2020 with me. I look forward to reading your thesis, soon-to-be Dr Joshi, and for continuing our very many *Minecraft* nights together!

To Zoë: Thank you for introducing me to *Stardew Valley* and our many farming evenings spent together! Thank you also for a very comfy sofa in Geneva and for getting me into CERN (even if it was just for lunch!). I very much look forward to ABBA *Voyage* together, hopefully both as doctors!

Andrew & Annie: I would probably not be doing a PhD had I not signed up to a random ‘Doctor Who society’ one fateful Wednesday morning fresher’s fair. I most definitely caught the doctoral bug from you two, so I’m blaming you for being upgraded from The Master to The Doctor. I look forward to more Eurovision parties, fort building, and `<Stephan> dinner </Stephan>` parties together.

Hannah & Tom: *What can I say except thank you* for so many fun afternoons spent messing about by Kate’s hole. I never laugh as hard as I do when we’re together and Fordy takes all of our pieces in Ludo, we flail around in SPEED!, get blown up in MarioKart, mess around in the Mii creator, or Tom puts a black hole right by spawn. While Beales may be long gone, the spirit of the spirit of CMO will live on with all of us.

To Stephen: My life would absolutely have been different if not for our friendship dating back to our Broadwater years: no *Age of Empires II*, no *Star Wars: Battlefront II*, no Bon Jovi, no Doctor Who, and no 3am Monopoly! Thank you also to the rest of the

Dice (RIP) crew for many happy board game evenings together. *We're not old, just older.*

Matt: Thanks for being a great and close friend since Year 8, sorry I ignored you the first months at Durrington — but I hope I've redeemed myself somewhat in the last fourteen years! I may still be slightly salty about not signing up to the 'Nerd Academy' with Debbie and missing out on a free graphical calculator :p

Sam, I also probably wouldn't have embarked on a PhD had it not been for my wonderful experience as an MPhys student — of which I have you to thank for a large portion of that. I couldn't have asked for anyone better to spend many evenings in the MPhys Lab deeply troubled over that laser with, and I still crack up at our implementation of `FedjaFunc` and `FedjaFit`. Thankfully, I have not need to resort to putting pieces of BluTack on my monitor to measure graphs, and I've checked that this document is not called anything related to the Fabry-Pérot etalon! The question of "*Whom's't thou mind if I were to subscript with an eegrick and a YOT?*" still remains unanswered to this day.

I would also like to give a big cheers to all my old and new Sussex friends for accepting this interloper and for sharing very many Falmer Friday post-grad pints together. And to my countless old Q-Soc and DocSoc friends; thanks for very many evenings spent together, which always ended in a trip to Falmer Bar! After all, *who says you can't go home?*

The absolute highlight of my PhD experience has been the travel to amazing places for conferences and summer schools. I would like to thank everyone I met, interacted, karaoked, or shared a pint or meal with during my travels for making these events such welcoming and unforgettable to me. In particular, the memories made in Oslo, Les Houches, Copenhagen, Innsbruck, and Rome with my *Euclid* SWG-BOAT buddies (Natalie, Jonathan, Lucy, Josh, Casey, and Conor) will stay with me for a very, *very* long time.

It goes without saying that I would not be completing a PhD without inspiration and support from very many teachers and lecturers at school, college, and university. In particular, I would like to thank Ms Trignano, Mrs Baker, Mr Fairbairn, Miss Holt, Miss Schuler, Bernie Flint, Debbie Collier, Nicole Cozens, David Seery, and Kathy Romer.

Thank you to my paw-some companions Billy, Bonnie, Benny, Ralph, and Misty for very many fluffy cuddles spent together throughout the years. 🐾

Finally, I would also like to thank all developers of free and open-source software (FOSS) for making their codes, documentation, and examples publicly available allowing such incredible science to be done by the entire community. Some of the FOSS software which have been essential to my MPhys and PhD include, but not limited to: NumPy [3], SciPy [4], Pandas [5], Matplotlib [6], Seaborn [7], CAMB [8–10], GetDist [11], CCL [12], Flask [13], Glass [14], HEALPix [15], healpy [16], NaMaster [17], Eigen [18], Linux 🐧, Ubuntu, Python, and C++; with particular thanks to Joe Zuntz for his amazing CosmoSIS framework [19]. A large part of my second and third projects embodied the spirit of Gene Kranz of *Apollo 13*: *'I don't care what anything was DESIGNED to do, I care what it CAN do'*, and CosmoSIS certainly did not let me down — just like *Aquarius* didn't.



—Alex

Gauss House, Sussex  
15<sup>th</sup> November 2024

# Table of contents

---

<b>Abstract</b>	<b>i</b>
<b>Universal abstract</b>	<b>iii</b>
<b>Acknowledgements</b>	<b>vi</b>
<b>1 Introduction</b>	<b>1</b>
<b>2 Modern cosmology</b>	<b>5</b>
2.1 Cosmology from general relativity . . . . .	5
2.1.1 Ricci curvature . . . . .	6
2.1.2 The space-time metric . . . . .	6
2.1.3 The Friedmann equations . . . . .	8
2.1.4 Solutions to the Friedmann equations . . . . .	9
2.1.5 Cosmological redshift . . . . .	13
2.1.6 The generalised Hubble parameter . . . . .	15
2.1.7 Cosmological distances . . . . .	15
2.2 Inflation & the early universe . . . . .	17
2.2.1 The hot Big Bang model . . . . .	17
2.2.2 The Big Bang break down . . . . .	18
2.2.3 Inflate our problems away . . . . .	19
2.2.4 The physics of inflation . . . . .	21
2.2.5 The primordial perturbations . . . . .	23
2.3 Evolution of structure across cosmic time . . . . .	26
2.3.1 Linear density evolution . . . . .	26
2.3.2 Matter perturbations during radiation domination . . . . .	26
2.3.3 Matter perturbations during matter domination . . . . .	27
2.3.4 Matter perturbations during $\Lambda$ domination . . . . .	27
2.3.5 The Fourier underworld . . . . .	27
2.3.6 The photonic and baryonic perturbations . . . . .	29
2.4 The matter power spectrum . . . . .	30
2.4.1 Sigma-8 . . . . .	31
2.4.2 Evolution of the matter power spectrum . . . . .	32
2.4.3 Non-linear evolution . . . . .	33
2.5 The halo model . . . . .	34
2.6 Baryon feedback in the matter power spectrum . . . . .	34
2.6.1 Supermassive black holes and active galactic nuclei . . . . .	35
2.6.2 Supernovae . . . . .	37

2.6.3	Modelling baryon feedback . . . . .	37
2.7	Probes of the large-scale structure . . . . .	38
2.7.1	Supernovae and the distance-redshift relation . . . . .	39
2.7.2	The cosmic microwave background . . . . .	41
2.7.3	Baryonic acoustic oscillations . . . . .	45
2.7.4	Why use different probes? . . . . .	46
<b>3</b>	<b>Gravitational lensing analysis</b>	<b>48</b>
3.1	Gravitational lensing from a point-mass . . . . .	48
3.1.1	Lagrangians . . . . .	48
3.1.2	The Eddington expedition . . . . .	50
3.2	Weak gravitational lensing . . . . .	51
3.2.1	Propagation of light through the Universe . . . . .	53
3.2.2	The amplification matrix . . . . .	54
3.2.3	Physical interpretation of shear and convergence . . . . .	55
3.2.4	Overdensity projections . . . . .	56
3.2.5	Measuring shear . . . . .	58
3.3	Estimating source galaxy redshift . . . . .	59
3.4	Estimators of weak lensing . . . . .	60
3.4.1	Lensing power spectrum . . . . .	60
3.4.2	Real-space correlation functions & COSEBIs . . . . .	64
3.5	Parameter estimation . . . . .	66
3.5.1	Likelihoods . . . . .	67
3.5.2	Likelihood of $C_\ell$ values . . . . .	68
3.5.3	Priors . . . . .	70
3.5.4	Markov chain Monte Carlo . . . . .	70
3.5.5	Fisher matrix formalism . . . . .	71
3.6	$C_\ell$ Covariance matrix . . . . .	72
3.6.1	Gaussian covariance . . . . .	72
3.6.2	Super-sample and non-Gaussian covariances . . . . .	73
3.7	Information gain at high redshift . . . . .	73
3.7.1	Including cross-correlations . . . . .	74
3.8	Baryonic feedback in the angular power spectrum . . . . .	77
<b>4</b>	<b>Concordance cosmology in 2024</b>	<b>79</b>
4.1	Current tensions in cosmology . . . . .	79
4.1.1	The $H_0$ tension . . . . .	79
4.1.2	The $S_8$ tension . . . . .	82
4.2	The Next Generation <sup>TM</sup> . . . . .	84
<b>5</b>	<b>Testing quadratic maximum likelihood estimators for forthcoming Stage-IV weak lensing surveys</b>	<b>87</b>
5.1	Introduction . . . . .	88
5.2	Power spectrum estimators . . . . .	91
5.2.1	The quadratic maximum likelihood estimator . . . . .	91
5.2.2	Inverting the pixel covariance matrix . . . . .	93
5.2.3	Forming the Fisher matrix . . . . .	95
5.2.4	Review of the Pseudo- $C_\ell$ estimator . . . . .	96
5.3	Methodology . . . . .	98
5.3.1	Theory power spectrum . . . . .	98
5.3.2	Survey geometry . . . . .	99

5.3.3	Pseudo- $C_\ell$ implementation . . . . .	102
5.4	Results . . . . .	102
5.4.1	Benchmark against existing estimators . . . . .	102
5.4.2	Accuracy of numerical Fisher matrix . . . . .	104
5.4.3	Comparing $C_\ell$ variances of QML to Pseudo- $C_\ell$ . . . . .	106
5.4.4	Cosmological parameter inference . . . . .	110
5.4.5	Non-Gaussian maps . . . . .	112
5.5	Conclusions . . . . .	114
5.A	Demonstration of unbiased estimators . . . . .	116
5.B	Ratio of numeric to analytic Fisher . . . . .	119
5.C	Sensitivity to apodisation . . . . .	120
<b>6</b>	<b>Mitigating baryon feedback bias in cosmic shear through a theoretical error covariance in the matter power spectrum</b>	<b>124</b>
6.1	Introduction . . . . .	125
6.2	Modelling baryonic feedback in the matter power spectrum . . . . .	126
6.2.1	Theoretical error formalism . . . . .	130
6.3	Methodology . . . . .	131
6.3.1	Modelling forthcoming cosmic shear surveys . . . . .	131
6.3.2	Constructing our $k$ -space theoretical covariance . . . . .	132
6.3.3	Propagating covariances to $\ell$ -space . . . . .	133
6.3.4	Numerical evaluation of the matter power spectrum with baryon feedback	133
6.3.5	Chosen hydrodynamical simulations . . . . .	134
6.3.6	Fitting HMCode to hydrodynamical simulations . . . . .	134
6.3.7	Fitting the $C_\ell$ values . . . . .	135
6.4	Results . . . . .	136
6.4.1	Results of fitting HMCode to hydro-sims . . . . .	136
6.4.2	Constructing the envelope . . . . .	137
6.4.3	Constructing the $\ell$ -space theoretical uncertainty covariance matrix . . .	139
6.4.4	Parameter constraints and biases . . . . .	139
6.5	Discussion and conclusions . . . . .	153
6.A	Dependency of the covariance on the coupling parameters . . . . .	154
<b>7</b>	<b>Mitigating baryon feedback bias in cosmic shear through development of new techniques to optimise binary cuts</b>	<b>157</b>
7.1	Introduction & motivation . . . . .	157
7.2	The Dark Energy Survey's scale cuts approach . . . . .	158
7.3	Detailed look at the per-bin $\chi^2$ . . . . .	160
7.4	Insufficiencies of the DES-Y3 approach in the Stage-III era . . . . .	162
7.5	Insufficiencies of the DES-Y3 approach in the Stage-IV era . . . . .	163
7.5.1	Stage-IV cosmic shear surveys . . . . .	165
7.5.2	Extending the DES-Y3 approach to power spectra . . . . .	166
7.5.3	Scale cuts . . . . .	167
7.5.4	Illustration of data-loss from aggressive scale-cuts . . . . .	168
7.5.5	Verifying the scale cuts . . . . .	168
7.5.6	Comparing to a $k$ -space cut . . . . .	171
7.6	Extending the $\chi^2$ method . . . . .	171
7.6.1	Fitting baryonic feedback models to hydro-sims . . . . .	171
7.6.2	Results for our modified $\chi^2$ method . . . . .	174
7.7	Scale cuts in parameter-space . . . . .	176
7.7.1	The Fisher matrix and figures of merit & bias . . . . .	177

7.7.2	Using the figure of bias for scale cuts . . . . .	178
7.8	Scale cuts using the figure of bias statistic . . . . .	179
7.8.1	One-dimensional optimisations . . . . .	179
7.8.2	Comparison between 1D $\chi^2$ and FoB scale cuts . . . . .	179
7.8.3	Six-dimensional optimisation . . . . .	181
7.9	Discussion and conclusions . . . . .	183
7.9.1	Outlook . . . . .	184
<b>8</b>	<b>Conclusions</b>	<b>186</b>
8.1	Our place in the Universe . . . . .	186
8.2	Summary of work and results . . . . .	187
8.3	Future work . . . . .	188
8.4	Outlook to the future . . . . .	189
	<b>Appendices</b>	<b>192</b>
<b>A</b>	<b>Power spectrum of a simple mask</b>	<b>192</b>
A.1	Simple mask in the $\vartheta$ plane . . . . .	192
A.2	The convolution of power from masking . . . . .	195
<b>B</b>	<b>Dark energy, massive neutrinos, and their impact on cosmology</b>	<b>197</b>
B.1	Dark energy . . . . .	197
B.1.1	The distance-redshift relation . . . . .	199
B.1.2	Dark energy in weak lensing . . . . .	200
B.1.3	The lensing kernel . . . . .	200
B.1.4	The matter power spectrum . . . . .	202
B.1.5	The $A_s$ - $\sigma_8$ relation . . . . .	204
B.1.6	Cosmic shear angular power spectrum . . . . .	205
B.2	Neutrinos . . . . .	207
B.3	Summary . . . . .	207
	<b>References</b>	<b>209</b>



*We choose to go to the Moon! We choose to go to the Moon in this decade, not because it is easy, but because it is hard; because that goal will serve to organize and measure the best of our energies and skills, because that challenge is one that we are willing to accept, one we are unwilling to postpone, and one we intend to win.*

—John F. Kennedy

1

# Introduction

---

*Gentlemen, a short view back to the past.* I think every cosmology PhD student since the Big Bang has said something along the lines of ‘now is a very exciting time to be a cosmologist...’, however, as much as it is clichéd to say, *it really is an exciting time to be a weak-lensing cosmologist!* We are now in an era where the precision of the data that we are receiving really is *awesome*<sup>1</sup>. The exploration and exploitation of this data will allow us to test the fundamental properties of our Universe with a precision that has never been possible before. Hence, the statistical methods that are applied to this extremely exquisite data need to as accurate, precise, and robust as the data. It would be a travesty to spend billions of pounds and tens of millions of human-hours to send the finest telescopes into space, observe galaxies whose light has taken over ten billion years to get to us, only to analyse the data with sub-optimal statistical methods. Thus, the development and verification of these cosmic shear analysis methods is the fundamental driving force behind the work presented in this thesis. But before we get bogged down in *E-/B-modes*, the mixing matrix, baryonification methods, and what a ‘theoretical error’ is, it’s good to take stock of just how rapidly cosmology, astrophysics, and astronomy have become precision sciences in just over a century.

While humankind may have stared at the night sky and admired the wonders of the heavens that was laid out before them for a hundred millennia, it wasn’t until Isaac Newton’s *Principia Mathematica* of 1687 that we started to have the mathematical framework to describe the observed motion of the heavenly bodies [20]. It is almost remarkable that it took over two hundred years for us to advance beyond Newtonian theories of motion, requiring us to wait for the great Albert Einstein to develop his theory of general relativity (GR) in 1915 to describe the large-scale properties of our Universe [21].

The introduction of general relativity heralded the beginnings of modern cosmology, where now we could, for the first time, study the fundamental properties of our Universe, ask and answer questions such as: What was the history of our Universe? What is our Universe made of? And what will the future of our Universe be?

Most of these questions could be answered through the assumption of the *cosmological principle* and the subsequent development of the Friedmann-Lemaître-Robertson-Walker metric, which predicted a global expansion or contraction of the Universe that is governed by the contents within it. Such an expansion was in direct contradiction with the static

---

<sup>1</sup>And I mean this in the traditional dictionary definition: it inspires awe, and fills someone with reverential fear, wonder, or respect.

Universe theory, which was a widely held belief at the turn of the twentieth century that our Universe was infinite in space and eternal in time and was neither expanding nor contracting. Einstein constructed his static universe such that the free parameter  $\Lambda$ , present in his field equations, was such that it would oppose the gravitational attraction of the matter within our Universe, and we would be left with a static Universe [22, 23].

While there was no *a priori* theoretical reason not to include  $\Lambda$  in the field equations, there was a dearth of experimental evidence which could discriminate between a static or expanding Universe. This all changed when Vesto Slipher made observations of the spectral lines on extragalactic nebulae and found that they were slightly shifted to red or blue colours. These red- or blue-shifts in the spectra were correctly interpreted as resulting from the Doppler shift of the motion of the extragalactic nebulae with respect to us [24, 25]. These Doppler shifts could have just indicated that these galaxies just had large peculiar velocities, which is any motion not resulting from the large-scale bulk flow of the Universe, and so consistent with the static Universe model. In the next decade, Georges Lemaître derived that in an expanding spacetime, there is a simple direct proportionality between a distant galaxy’s recessional velocity and its distance from Earth [26]. Edwin Hubble was then able to get accurate distance measurements to Slipher’s receding galaxies through observations of Cepheid variable stars, building upon work by Henrietta Leavitt and Harlow Shapley [25, 27, 28]. In 1929, Hubble announced that he found a proportionality between the redshift of galaxies and their distance to us, thus forming Hubble’s law. When combined with the cosmological principle, the observations that distant galaxies were receding away from us with a velocity that was proportional to their distance, became observational unequivocal proof that our Universe was expanding [29, 30]. These observations signalled the end of the inclusion of  $\Lambda$  in the Einstein equations, since there was no desire to force a static universe anymore, though its death was rather short-lived. . .

While the derivation of the Friedmann equations and the observational verification of Hubble’s law was a powerful test of Einstein’s general relativity, perhaps the most famous ‘killer’ piece of evidence of Newtonian mechanics’ demise, and establishment of general relativity as the correct framework for our Universe’s dynamics, was the result from the Eddington expedition of 1919 [31]. Both general relativity and Newtonian mechanics predict that matter can deflect the path of light-rays, though the prediction for the deflection angle in general relativity is double that of Newtonian mechanics. Since this deflection of light by matter is equivalent to the presence of an optical lens along the light’s path, this phenomenon is called *gravitational lensing*. By measuring the slight shift in apparent positions of distant stars by our Sun during the eclipse of 1919, Eddington and collaborators confirmed that their deflection angles were consistent with the predictions of general relativity, ushering in the general relativistic age. What Eddington and his collaborators may not have been realised at the time is that their primitive observations to test general relativity will be re-employed a century later, with unimaginable precision, to yet again test the physical properties of our Universe [32, 33].

The first cosmic mystery that general relativity could not explain were the observations made by Fritz Zwicky who imaged the Coma cluster and, using the assumption of the virial theorem, found that the average density in the Coma cluster would have to be at least four hundred times larger than estimates based on the apparent luminous matter [34, 35]. This extra, non-luminous matter was dubbed ‘dark matter’ (originally ‘dunkle Materie’ in German) by Zwicky, and the name has stuck ever since. Zwicky’s findings of non-luminous dark matter were followed up by, among many other results, observations of galaxy rotation curves by Vera Rubin and collaborators. Their observations suggested that stars which were a large radial distance from their galaxy’s centre were orbiting too fast for the gravitational attraction of the apparent luminous matter [36]. This either suggests that either the Newtonian limit of general relativity does not hold on intra-

galactic scales, or that there is extra material within galaxies that exerts gravitational attraction without being luminous. Thanks to Zwicky, we still call this extra non-luminous gravitational material ‘dark matter’, and has become an accepted part of the modern standard cosmological model, even if we cannot explain its exact phenomenology.

The second cosmological mystery which was unravelled at the end of the twentieth century (a mere four months after my birth!) came from observations of high-redshift supernovae, and suggested that they were fainter than otherwise predicted for a matter-dominated Universe [37, 38]. This gave strong evidence that our Universe was not just expanding, as Hubble and co found, but *accelerating*. The only way to get accelerated expansion in general relativity is by having the cosmological constant being the dominant contribution to our Universe’s energy density. Hence, the cosmological constant  $\Lambda$  was back with a vengeance, but instead of forcing our Universe to be static, it was acting to accelerate its expansion!<sup>2</sup>

The detection of both dark matter and dark energy have been corroborated by numerous independent probes and observational groups, and form the foundations of our modern standard cosmological model [39]. But the physical properties of both dark matter and dark energy remain today as mysterious as their first detection: dark matter is some form of matter that only interacts gravitationally and contributes around 25 % of our Universe’s energy density today; dark energy can be perfectly described by the cosmological constant  $\Lambda$  in the Einstein equation, and contributes around 70 % of our Universe’s energy density today [40]. So we really don’t have much of a clue about what 95 % of our Universe is!

While our tried and tested method of investigating physical phenomena in our Universe of simply ‘looking at it’ might not work for dark matter and dark energy, it does not mean that we have no hope of constraining their behaviour. Since both interact gravitationally, we can use any probe that is sensitive to the total amount of matter present, not just the luminous stuff that we’re made from. Such a probe is gravitational lensing, first proved by Eddington and his collaborators, and experienced a great revival to test dark matter and dark energy in the late 1990s [32, 41]. It is the perfect probe of the dark sector, since lensing is sensitive to both the amount of matter and evolution of the energy densities over time, allowing us to constrain the time-evolution of the dark matter and dark energy fields – a key goal of the latest cosmic shear surveys [42].

Measurements of weak lensing by large-scale structure were first published by four independent groups in 2000 [43–46], which was made possible by improvements in CCD technology enabling much wider field of views and increased sensitivity, providing the ideal conditions for observing large quantities of distant galaxies. Further developments in telescope and detector technology have enabled weak lensing surveys to go from covering around  $1 \text{ deg}^2$  to nearly  $15\,000 \text{ deg}^2$  [33], and has evolved into one cosmology’s most precision sciences.

Hence, we are suitably motivated to go out looking into our cosmos and try to make measurements of gravitational lensing across the sky and across cosmic time. However, while Eddington’s observations were to measure the simple deflection in the light from a handful of stars, a modern weak lensing survey aims to measure the deflection of light from well over a billion galaxies, and fraught with intricacies and subtleties that need the correct modelling to ensure that we reach the correct conclusions from our data. In this thesis, we investigate the effect of power spectrum estimation techniques and the impact of baryonic feedback for weak lensing galaxy surveys such that we can maximise information from them.

---

<sup>2</sup>I was privileged to attend a talk given by Nobel laureate Brian Schmidt at the University of Southampton in November 2015. His talk came at a time when I considering university applications but was as yet undecided what to study between chemistry, mathematics, and physics. After his talk, I had no doubt that physics, and more specifically cosmology, was my natural calling. *The rest, as they say, is history.*

## Layout of the thesis

In Chapter 2 we present background material on modern cosmology, leading to a discussion of some of the current observational probes our Universe. This feeds into a detailed discussion of gravitational lensing and its application in cosmology in Chapter 3, and culminates in a short discussion about the state of weak lensing cosmology in 2024 in Chapter 4.

We then go on to present new work introducing a new cosmic shear power spectrum estimation technique in Chapter 5, and work on mitigating the effects of baryonic feedback physics on cosmic shear surveys through a theoretical error covariance in Chapter 6 and binary scale cuts in Chapter 7.

We end on a short discussion and conclusions about the work presented in this thesis with an outlook for the future in Chapter 8.

## Notation

In this thesis we use natural units, where  $c = \hbar = k_B = 1$ , and the ‘mostly negative’ metric signature  $(+, -, -, -)$  for coordinates  $(t, x_1, x_2, x_3)$ . Latin indices from the start of the alphabet ( $a, b, c, \dots$ ) represent space-time indices, while Latin indices from the middle of the alphabet ( $i, j, k, \dots$ ) represent spatial indices only.

Ah, shit,  
the shipping and receiving!

—Sips

Crabs are people,  
clams are people!

—Lewis Brindley

2

# Modern cosmology

**Outline.** In this chapter, I present a brief overview of the ideas and motivations of modern cosmology starting from general relativity, deriving various well-known results along the way, and ending with presentation and discussion of key results from several observational probes which form the foundation of modern cosmology. *Okay, we do it.*

## 2.1 Cosmology from general relativity

The era of modern cosmology started with the introduction of general relativity (GR) by Einstein in 1915 [21]. This provided insights into the underlying nature of our Universe, such as how energy, matter, and space-time are related, and that gravity is nothing more than the curvature of space-time. One of the key equations underpinning general relativity are the Einstein equations, which are a series of ten coupled non-linear partial differential equations, and can be written as [47]

$$R_{ab} - \frac{1}{2}Rg_{ab} + \Lambda g_{ab} = 8\pi G T_{ab}, \quad (2.1)$$

where  $g_{ab}$  is the space-time metric,  $R_{ab}$  is the Ricci tensor,  $R$  is the Ricci scalar (which are both built from derivatives of the metric),  $T_{ab}$  is the energy-momentum tensor, and  $\Lambda$  is a constant. This constant is the famous cosmological constant, or ‘fudge factor’, that Einstein introduced to make his model of the Universe static. The raw equations are agnostic to  $\Lambda$ ’s value; it could be zero, close to zero, or highly non-zero. From theory alone, there is no *a priori* constraint that can be placed on the value of  $\Lambda$ . Einstein, realising that his model of the Universe predicted one that expanded, refused to believe that such Universe existed, and so ansatzed<sup>1</sup> the value of  $\Lambda$  to be exactly that which gave a static evolution of the Universe. This static Universe was unstable with the dynamics of the Universe hanging in a delicate balance, with the slightest perturbation leading to expansion or contraction.

With Edwin Hubble’s 1929 work finding that the Universe was expanding, and thus not a steady-state solution [29], Einstein abandoned the cosmological constant as it was no longer necessary — dubbing his inclusion of it in the first place as his “greatest mistake”. However, this was not the end of the cosmological constant’s story as we will see shortly.

---

<sup>1</sup>Ansatz the answer

### 2.1.1 Ricci curvature

To start with our analysis of the Einstein field equations (Equation 2.1), let us look at the left-hand side of the equation. This is dubbed the ‘geometry side’, as it encodes the geometrical properties of a system. We start out with the Ricci scalar,  $R$ , which is a contraction of the Ricci tensor,

$$R \equiv R^a_a. \quad (2.2)$$

We can now go one step up and ask how do we define the Ricci tensor? We find that it is a contraction over the first and third indices of the Riemann tensor<sup>2</sup>  $R^a_{bcd}$  as

$$R_{ab} \equiv R^c_{acb}. \quad (2.3)$$

We now go one step higher and ask what the Riemann tensor is made out of, and we find that it’s built from products and derivatives of connection coefficients, or Christoffel symbols,  $\Gamma^a_{bc}$  as

$$R^a_{bcd} = \partial_c \Gamma^a_{bd} - \partial_d \Gamma^a_{bc} + \Gamma^a_{cf} \Gamma^f_{bd} - \Gamma^a_{df} \Gamma^f_{bc}. \quad (2.4)$$

We can *finally* ask what are the connection coefficients<sup>3</sup> made from, and we happily find that they’re computed from derivatives of the space-time metric as

$$\Gamma^a_{bc} = \frac{1}{2} g^{ad} [\partial_b g_{dc} + \partial_c g_{bd} - \partial_d g_{bc}]. \quad (2.5)$$

Thus, starting from a space-time metric, we can fully derive the geometry part of the Einstein equations. We are now lead down a new rabbit hole as we try to work out how to construct our space-time metric...

### 2.1.2 The space-time metric

As shown above, one attempts to solve the Einstein field equations to obtain the space-time metric  $g_{ab}$ . The metric,  $g_{ab}$ , is usually written as the space-time element,  $ds^2$ , of

$$ds^2 \equiv g_{ab} dx^a dx^b, \quad (2.6)$$

where  $dx$  are the infinitesimal elements of our chosen coordinate system. The space-time element is especially useful since it is an invariant and thus the same for all observers.

#### The Schwarzschild metric

For an arbitrary physical system, a general solution of the Einstein equations would be analytically intractable. To simplify the problem, one can place certain constraints, or symmetries, on the physical problem to arrive at solutions for the metric. The first such solution for the metric came from Karl Schwarzschild in 1916, arriving at the Schwarzschild metric for the gravitational field generated by a point mass of mass  $M$  [48]. This solution is obtained by noting that outside of the point mass, the region that we are interested in, the energy-momentum tensor  $T_{ab}$  is zero. Additionally, we note the spherical symmetry of the problem, and thus spherical coordinates  $(t, r, \vartheta, \phi)$  are the natural choice. In these coordinates, the Schwarzschild metric is given as [47]

$$ds^2 = \left(1 - \frac{2GM}{r}\right) dt^2 - \left(1 - \frac{2GM}{r}\right)^{-1} dr^2 - r^2 [d\vartheta^2 + \sin^2 \vartheta d\phi^2]. \quad (2.7)$$

<sup>2</sup>Yes, it is confusing having three different quantities all with the symbol  $R$ , however we can tell which one we are using by the number of indices each term is carrying.

<sup>3</sup>Despite having indices, the connection coefficients are not tensors since *they do not transform like a tensor*.

## The Friedmann-Robertson-Walker metric

While the Schwarzschild metric was solved in a vacuum, where the energy-momentum tensor vanishes ( $T_{ab} = 0$ ), one can try and find a solution to the Einstein equations where this condition is not true. This is motivated by the fact that our Universe is not totally empty and does feature stuff in it, such as me and you! As discussed above, a general solution for an arbitrary universe's energy distribution is totally intractable, so we need to place some constraints on our system if we are to obtain a solution.

The first such assumption is that we do not hold any special place in the Universe, and thus any such observations that we make could have been made from any other position in the Universe. This is the Copernican principle, or the modern assumption of *homogeneity*.

The second assumption is that when we make observations of the Universe, such as temperature maps of the cosmic microwave background (CMB), or the distribution of galaxies on the sky, the Universe appears to look very much the same in every direction. For example, the temperature of the CMB radiation was measured to be within one part in one hundred thousand by the FIRAS instrument on the *COBE* satellite [49]. This extreme uniformity across the entire sky gives rise to the assumption of *isotropy*. Though, of course, there is a significant dipole term which arises from the Solar System's movement through the universe, which has been measured to be around 370 km/s, which is a whopping 0.1 % of the speed of light, with respect to the CMB rest frame [50]. This dipole is almost always removed in any cosmological analyses using CMB data.

It is important to note that homogeneity and isotropy are different properties, and a system obeying one does not necessarily obey the other. For example, consider the electric field between two infinite plates with potential difference  $\Delta V$  and separation  $d$ . The electric field is then given by  $\vec{E} = \frac{\Delta V}{d} \hat{n}$ , where  $\hat{n}$  points towards the negative plate [51]. This is clearly homogenous everywhere between the two plates, but clearly not isotropic as the field gives rise to a preferential direction. Equally, we can consider the electric field of a point-charge  $q$  at the origin. As a function of radial distance  $r$ , the field is  $\vec{E}(r) = \frac{1}{4\pi\epsilon_0} \frac{q}{r^2} \hat{r}$ . At the origin, this is clearly an isotropic field as it looks the same in every direction, but is not homogenous. The observations that our Universe obeys *both* homogeneity and isotropy was a cornerstone of modern observational cosmology.

Together, the joint assumptions of homogeneity and isotropy form the modern *cosmological principle*, from which much of modern cosmology is built upon. Imposing this cosmological principle, with a non-zero energy density, gives rise to the Friedmann-Robertson-Walker (FRW) metric, written in spherical polars, of

$$ds^2 = dt^2 - a^2(t) \left( \frac{dr^2}{1 - kr^2} + r^2 [d\vartheta^2 + \sin^2\vartheta d\phi^2] \right), \quad (2.8)$$

where  $a(t)$  is the scale-factor (which describes the homogenous expansion of space with cosmic time  $t$ , normalised such that it is unity at present times:  $a(t_0) = 1$ ), and  $k$  is the curvature parameter which describes the spatial geometry of the universe: flat ( $k = 0$ ), closed ( $k > 0$ ), or open ( $k < 0$ ). A subtlety in our FRW metric of Equation 2.8 is that  $r$  is the dimensionful comoving coordinate. That is, objects that simply move with the bulk Hubble flow have fixed comoving coordinates. The physical distance at time  $t$  is  $a(t)r$ .

Since the radial element of our FRW metric changes depending on the value of the curvature of the universe, we can transform our FRW metric to one where the radial comoving coordinate is given by  $\chi$  and is independent of curvature. This gives [47]

$$ds^2 = dt^2 - a^2(t) \left( d\chi^2 + f_k^2(\chi) [d\vartheta^2 + \sin^2\vartheta d\phi^2] \right), \quad (2.9)$$



where the function  $r = f_k(\chi)$  is given by

$$f_k(\chi) = \begin{cases} \sin \chi & \text{for } k > 0, \\ \chi & \text{for } k = 0, \\ \sinh \chi & \text{for } k < 0. \end{cases} \quad (2.10)$$

### The perturbed metric

While the FRW metric is very useful to describe the large-scale homogenous properties of the universe, many of which will be derived just later, it is important to note that the Universe is *not* totally homogenous. For example, the air in the room that you are reading this thesis has an average density of  $1.2 \text{ kg m}^{-3}$  so when compared to the average density of the universe of approximately  $10^{-26} \text{ kg m}^{-3}$ , this represents an extraordinary perturbation of the order  $10^{26}$ . While none of the cosmological perturbations will come close to this size, we can extend the FRW metric to include perturbations as

$$ds^2 = (1 + 2\Psi) dt^2 - a^2(t) (1 - 2\Phi) d\vec{x}^2, \quad (2.11)$$

where  $\Psi$  and  $\Phi$  are the Bardeen potentials, and are functions of the four space-time coordinates, and describe the first-order perturbations to a homogenous universe, and  $d\vec{x}^2$  is the spatial-only FRW metric. We will revisit this perturbed metric when we consider space-time perturbations later.

### 2.1.3 The Friedmann equations

When we introduced the FRW metric in Equation 2.8, we introduced a function  $a(t)$  which we invoked was the scale-factor of the universe. We can now ask many questions about the properties of this scale-factor: How does it behave to different matter densities? How does curvature affect the evolution of the scale-factor? And what physical intuition can we obtain from the scale-factor?

To answer these questions, we turn to the Einstein field equations. Since we have the key ingredient, the metric, we can start solving these field equations. Recalling that the right-hand side of the field equations (Equation 2.1) was in terms of the energy-momentum tensor, we need to find such energy-momentum tensor that describes the Universe. While this may seem like another intractable question, we turn to a cosmologist's favourite activity: assumptions! Since we are only after the general solution for a homogenous and isotropic universe (remember we are ignoring perturbations for the time being), we can describe the Universe as being a perfect fluid. This perfect fluid is characterised by having an energy density  $\rho$  and pressure  $p$ , both of which are functions of cosmic time  $t$  alone, since we are following the cosmological principle. This perfect fluid yields an energy-momentum tensor of the form

$$T_{ab} = (\rho + p)u_a u_b + p g_{ab}, \quad (2.12)$$

where  $u_a$  is the four-velocity which, for a fluid at rest in our comoving coordinate basis, is simply  $u_a = (1, 0, 0, 0)$ . Since we are dealing with an FRW universe, no time or positional-dependence can be included in our energy-momentum tensor.

### The Friedmann equation

Now that we have both the metric and the energy-momentum tensor, we arrive at the first Friedmann equation (often called just the Friedmann equation) derived from the



$tt$ -component of the Einstein field equations of

$$3H^2 = 8\pi G \rho - \frac{3k}{a^2} + \Lambda, \quad (2.13)$$

where we have introduced the Hubble parameter  $H$  defined as  $H \equiv \dot{a}/a$ , which measures the relative expansion rate of the universe, where  $\dot{a} \equiv da/dt$  – the derivative of the scale-factor with respect to cosmic time.

### The acceleration equation

Differentiating the Friedmann equation, and using the conservation of mass and energy, yields the second Friedmann equation, called the acceleration equation, of

$$3\frac{\ddot{a}}{a} = -4\pi G (\rho + 3p) + \Lambda. \quad (2.14)$$

One immediate result of the acceleration equation is that clear to see, is that both the energy density  $\rho$  and pressure  $p$  of any matter in our Universe will act to decelerate the expansion of the universe, whereas the cosmological constant  $\Lambda$ , depending on its sign, can act to accelerate ( $\Lambda > 0$ ) or decelerate ( $\Lambda < 0$ ) the universe. Thus, the sign of  $\Lambda$  and its relative importance when compared to  $\rho$  and  $p$  are key to understanding the dynamics of a universe, which we will see shortly.

### The fluid equation

With our energy-momentum tensor of Equation 2.12, we can apply the conservation of energy-momentum ( $\nabla^a T_{ab} = 0$ , where  $\nabla^a$  is the covariant derivative), to find a third Friedmann equation, often called the fluid or continuity equation, of

$$\dot{\rho} + 3H(\rho + p) = 0. \quad (2.15)$$

It is important to note that the three Friedmann equations are not independent of each other, and so, in general, only two are used to obtain solutions for the dynamics of the scale-factor.

## 2.1.4 Solutions to the Friedmann equations

Now that we are armed with the Friedmann, acceleration, and continuity equations, we can investigate solutions to the Friedmann equations — that is, solving for the time evolution of the scale-factor  $a(t)$  — given different dominating components of our cosmological fluid. In our three scenarios, we will consider flat universes ( $k = 0$ ) only. A discussion on curvature will come thereafter.

### Cold matter dominated

The first solution that we will investigate is one of a universe that is dominated by a cold, pressureless matter. Here, the ‘pressureless’ qualifier gives us the condition that  $\rho_M \gg p_M$ , and thus we can ignore any pressure terms in the Friedmann equations for this matter. Solving the fluid equation, we arrive at

$$\rho_M(t) = \rho_{M,0} a^{-3}(t), \quad (2.16)$$

where  $\rho_{M,0}$  is the density of this matter today. It is important to note the triviality of this result, if energy is conserved (which it *always* is), then the energy density evolves with

time as the inverse of volume and thus we arrive at the negative cubic power present on the scale-factor.

With our solution for the evolution of our matter density, we can plug this into the Friedmann equation to obtain

$$a(t) = \left[ \frac{t}{t_0} \right]^{2/3}, \quad (2.17)$$

where  $t_0$  is the age of the universe today, and that we have normalised the scale-factor to be unity today ( $a(t_0) = 1$ ).

## Radiation dominated

Unlike our cold matter, radiation has a non-negligible pressure term which is related to its energy density through  $p_R = \rho_R/3$ . Again, solving the fluid equation we find the evolution of our radiation of

$$\rho_R(t) = \rho_{R,0} a^{-4}(t), \quad (2.18)$$

and so we find that the radiation energy density decays with an additional factor of  $1/a$  compared to our matter, this corresponds to the cosmological redshifting of the photons — a phenomena that we will investigate shortly.

Again, now what we have the time evolution of our fluid, the Friedmann equation gives the scale-factor evolution as

$$a(t) = \left[ \frac{t}{t_0} \right]^{1/2}, \quad (2.19)$$

and thus we see that a radiation-dominated universe expands slower than a matter-dominated one.

## $\Lambda$ dominated

A fairly ominous term that's been appearing in many of our equations thus far has been  $\Lambda$ , dubbed the cosmological constant<sup>4</sup>. But what are the properties of this cosmological constant, and what would the dynamics of a universe that is dominated by it look like?

If  $\Lambda$  is truly a constant, then  $\dot{\rho}_\Lambda$  would be zero, since there would be no evolution in its density  $\rho_\Lambda$ , given as  $\rho_\Lambda = \Lambda/8\pi G$ . Thus, when comparing to the fluid equation of Equation 2.15, we find that we require  $p_\Lambda + \rho_\Lambda = 0$ , or equally  $p_\Lambda = -\rho_\Lambda$ , for our constant. This has the odd physical property that our cosmological constant fluid has a *negative* pressure, akin to tension in a stretched rubber band, but nevertheless makes physical sense. For our cosmological constant dominated universe, the Friedmann equation becomes

$$\left( \frac{\dot{a}}{a} \right)^2 = \frac{\Lambda}{3}, \quad (2.20)$$

which has the simple exponential solution of

$$a(t) \propto \exp \left[ \sqrt{\frac{\Lambda}{3}} t \right]. \quad (2.21)$$

This solution is also called *de Sitter* space, and shows that a  $\Lambda$ -dominated universe will expand exponentially forever.

---

<sup>4</sup>Somehow, ~~Palpatine~~ the cosmological constant returned

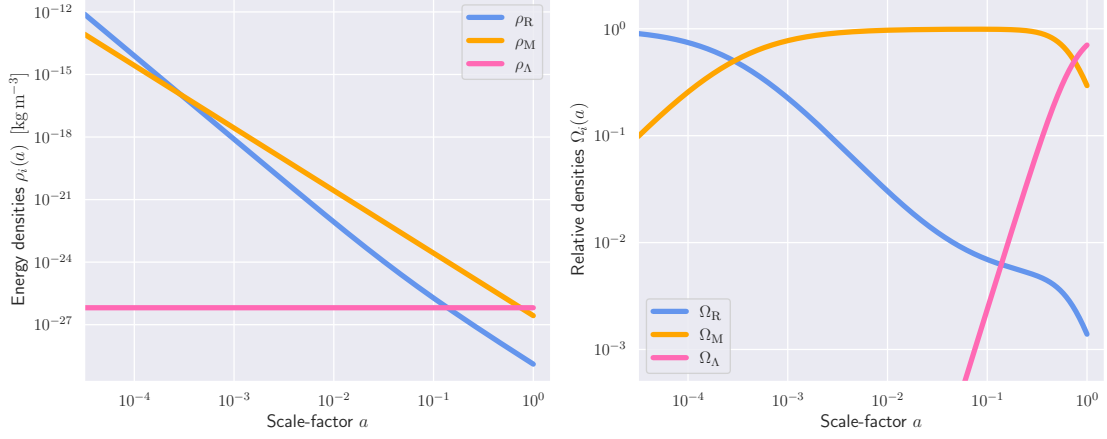


Figure 2.1: Evolution of the energy density (left panel) and relative density (right panel) of the three main components of our Universe: radiation, matter, and the cosmological constant. We see that at early times (small  $a$ ), the universe was radiation dominated. This was quickly redshifted away leading to an extended period of matter domination. It was only relatively recently that we entered the epoch of  $\Lambda$ -domination, and thus hit the turning point of accelerated exponential expansion.

### Arbitrary fluids

Looking at our three solutions for the scale-factor above, while the physical properties of our three cosmological fluids might be quite different, if one looks hard enough, they'll find only one common difference: the pressure term. We can express the pressure of a fluid in terms of its energy density through the equation of state

$$p_i = w_i \rho_i \quad (2.22)$$

for any arbitrary fluid  $i$ . Here,  $w$  is the *equation of state parameter*, which takes values for our three scenarios of

$$w_i = \begin{cases} w_M = 0 & \text{cold, pressureless matter,} \\ w_R = \frac{1}{3} & \text{radiation \& relativistic particles,} \\ w_\Lambda = -1 & \text{cosmological constant.} \end{cases}$$

If we now assume that the universe is dominated by our arbitrary fluid  $i$ , then we can re-write the acceleration equation (Equation 2.14) in terms of its equation of state  $w_i$ , to give

$$\frac{\ddot{a}}{a} = -\frac{4\pi G}{3}(1 + 3w_i)\rho_i, \quad (2.23)$$

and so we find that if our fluid's equation of state satisfies  $w_i < -\frac{1}{3}$  then  $\ddot{a} > 0$  and thus we get accelerated expansion.

### Dark energy equation of state

Thus far, we have been dealing with a static cosmological constant  $\Lambda$  present in the Einstein equations. Since this cosmological constant contributes around 70 % of our Universe's energy density, and cannot be directly observed, it was coined 'dark energy' to mimic the equally unobservable dark matter [52]. While  $\Lambda$  may be a constant in the Einstein equations, we can entertain the possibility that dark energy might not be a complete

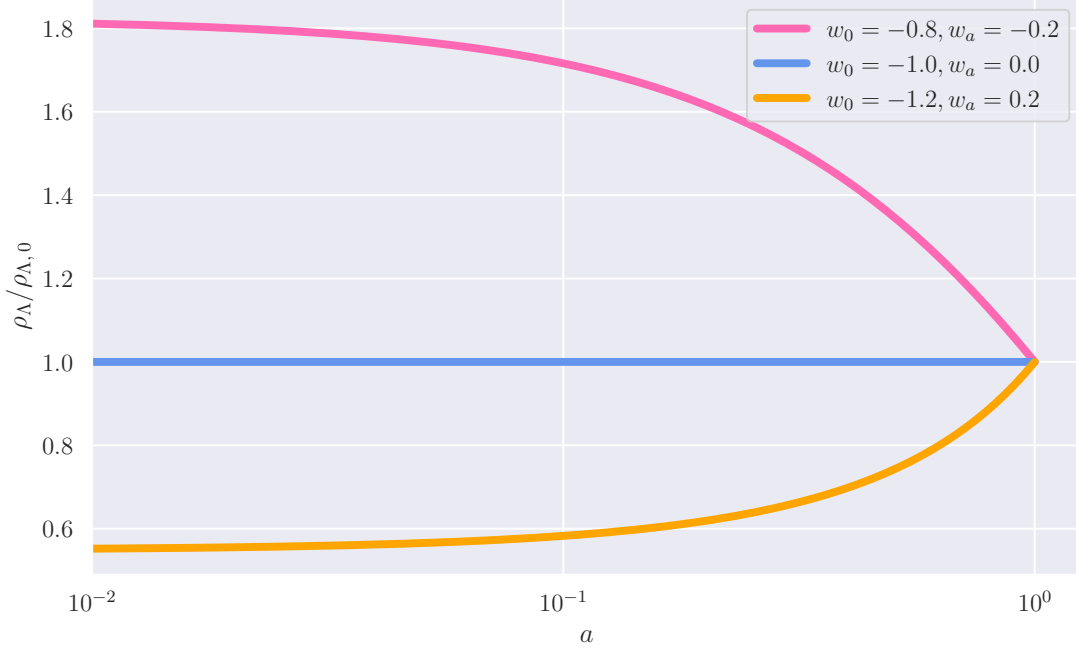


Figure 2.2: Evolution of the dark energy density for three different combinations of  $w_0$  and  $w_a$  values (Equation 2.24). The blue curve corresponds to the cosmological constant  $\Lambda$ , showing constant energy density over time. The non-constant curve's evolution can be explained through Equation 2.25.

constant. If we allow for dark energy to have a time dependence,  $w_\Lambda = w_\Lambda(t)$ <sup>5</sup>, a simple first-order linear expansion for its equation of state with cosmic expansion is [53, 54]

$$w_\Lambda(a) = w_0 + w_a(1 - a). \quad (2.24)$$

The cosmological constant then becomes a sub-class of our evolving dark energy model, and corresponds to  $w_0 = -1$  and  $w_a = 0$ . We plot three different combinations of  $(w_0, w_a)$  in Figure 2.2. We can explain the different evolution of our three curves by re-casting the fluid equation (Equation 2.15) into

$$\dot{\rho}_\Lambda = -3H\rho_\Lambda(1 + w_\Lambda), \quad (2.25)$$

and so if  $w = -1$ , then we arrive at our cosmological constant with its constant energy density. Likewise, we find that if  $w < -1$  then the dark energy density grows with time ( $\dot{\rho}_\Lambda > 0$ ), and if  $w > -1$  then the dark energy density decreases with time ( $\dot{\rho}_\Lambda < 0$ ). The dark energy field supports accelerated expansion as long as  $w_\Lambda < -\frac{1}{3}$ .

## Curvature

In our three scenarios above, we considered the case for a spatially flat universe (one where  $k = 0$ ). There is no *a priori* reason that we should consider flat universes only since the Einstein field equations are valid for all values of  $k$ . However, one can consider the properties of such a flat universe. If we impose that  $k = 0$  on the Friedmann equation of Equation 2.13, then we find that the total energy density  $\rho = \rho_M + \rho_R + \rho_\Lambda$  is constrained

<sup>5</sup>We shall use  $\Lambda$  to represent a generic dark energy fluid which acts to accelerate our Universe, even if it is not a complete constant.

to be that of the *critical density*  $\rho_{\text{CRIT}}$  of

$$\rho_{\text{CRIT}}(t) \equiv \frac{3H^2(t)}{8\pi G}. \quad (2.26)$$

Since the Hubble parameter  $H$  depends on time, so will the critical density. If we use that the Hubble parameter today is around  $H_0 \simeq 70 \text{ km/s Mpc}^{-1}$ , then we find that the Universe's critical density today is around  $9 \times 10^{-30} \text{ g cm}^{-3}$ , or about five hydrogen atoms per cubic metre.

From the critical density, one can define the *density parameters* of each component of the cosmological fluid  $\Omega_i$ , defined as

$$\Omega_i(t) \equiv \frac{\rho_i(t)}{\rho_{\text{CRIT}}(t)}. \quad (2.27)$$

From this, one can define a density parameter associated with the curvature of an arbitrary universe  $\Omega_k$ , defined as

$$\Omega_k(z) = -\frac{k}{a^2 H^2}, \quad (2.28)$$

such that the sum of the density parameters is defined to be unity

$$\Omega_{\text{TOT}} = \Omega_{\text{R}}(z) + \Omega_{\text{M}}(z) + \Omega_{\Lambda}(z) + \Omega_k(z) \equiv 1. \quad (2.29)$$

We measure values of  $\Omega_k$  that are consistent with a flat universe of  $\Omega_k = 0$  (see Figure 2.3), and thus most analyses specialise to the flat-only case. However, in general, it should be a free parameter in any cosmological model.

## A note on notation

The density parameter for each component of the cosmological fluid, the  $\Omega_i$ 's, are time / redshift / scale-factor dependent, and thus should be written as  $\Omega_i(t)$ . Their values today, at  $t = t_0$ , should be written as  $\Omega_{i0}$ , however since cosmologists are lazy people, the subscript zero is usually dropped and thus  $\Omega_{\text{M}}$  should be interpreted as the matter density parameter today, likewise for  $\Omega_{\text{R}}$  and  $\Omega_{\Lambda}$ .

## 2.1.5 Cosmological redshift

One of the most basic fundamentals to modern cosmology is our ability to collect photons of all different wavelengths and from different epochs in our Universe's history. Thus, understanding the physics of what happens to these photons between when they were emitted and detected by us is key to ensuring that we can deduce the correct properties of our Universe from these observations. One such key property to these propagating photons is the phenomena of cosmological redshift, which we will derive here.

Firstly, consider a source of photons at rest (in its reference frame) at fixed radial comoving distance  $\chi$ . Since photons travel along null geodesics ( $ds^2 = 0$ ), we find for a radially incoming photon that

$$dt = -a(t) d\chi \quad (2.30)$$

Integrating the total comoving distance from us (the observer at  $\chi = 0$ ) out to the source at  $\chi = \chi$ , we find

$$\chi = \int_0^\chi d\chi' = - \int_{t_2}^{t_1} \frac{dt}{a(t)} = \int_{t_1}^{t_2} \frac{dt}{a(t)}, \quad (2.31)$$

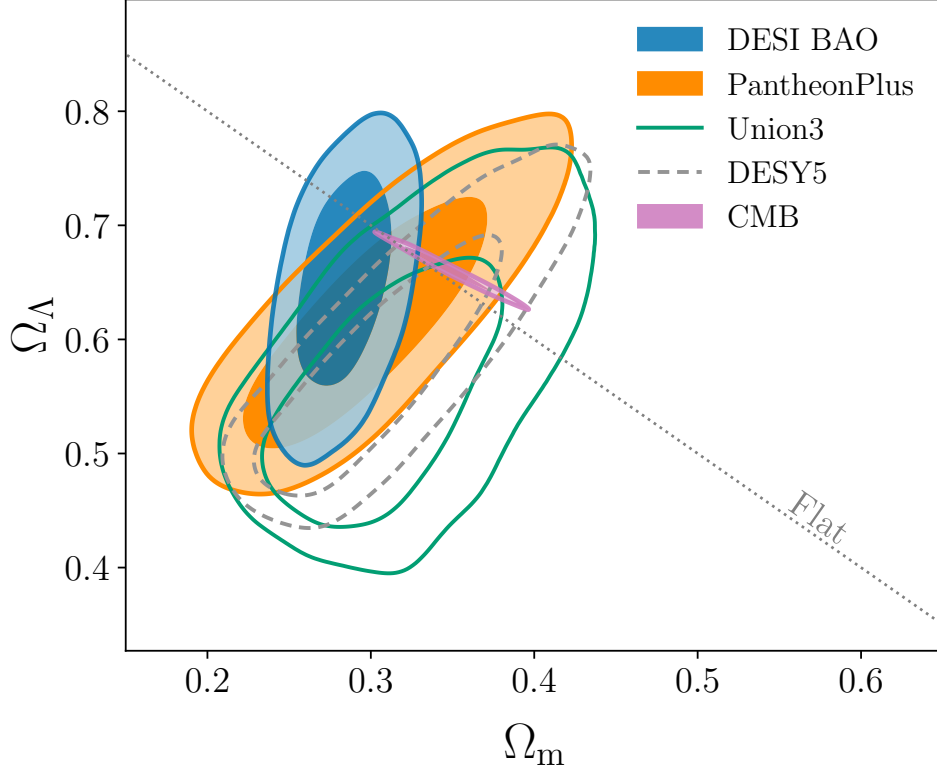


Figure 2.3: Parameter constraints on the matter ( $\Omega_m$ ) and dark energy densities ( $\Omega_\Lambda$ ) from a number of different cosmological probes. While each individual probe’s average value might vary from one another, all agree that  $\Omega_\Lambda > 0$ , we are living in an accelerating universe which is consistent with a flat universe of  $\Omega_k = 0$ . We introduce these cosmological probes in Section 2.7. Figure taken from the DESI 2024 release [55].

since the photon was emitted at time  $t = t_1$  and we observed the photon at  $t = t_2$  and  $\chi = 0$ . Thinking of photons not as of particles, but of continuous electromagnetic waves,  $t_1$  also corresponds to the time that a crest of the wave is emitted. A second crest of the wave will be emitted  $\delta t = 1/\nu_1$  later, where  $\nu_1$  is the frequency in the source rest frame. This will be detected by us at the origin at time  $t_2 + \delta t_2$ . Since the comoving radial distance is invariant, we find

$$\chi = \int_{t_1}^{t_2} \frac{dt}{a(t)} = \int_{t_1 + \delta t_1}^{t_2 + \delta t_2} \frac{dt}{a(t)}. \quad (2.32)$$

For this to hold true, we require that

$$\frac{\delta t_2}{a(t_2)} - \frac{\delta t_1}{a(t_1)} = 0. \quad (2.33)$$

This gives us the result for cosmological redshifting of

$$\frac{\delta t_2}{\delta t_1} = \frac{\nu_1}{\nu_2} = \frac{a(t_2)}{a(t_1)}. \quad (2.34)$$

Expressing this in terms of the wavelength of the light emitted ( $\lambda_1$ ) and detected ( $\lambda_2$ ), we find that the wavelength of the detected photons are given by

$$\lambda_2 = \lambda_1 \frac{a(t_2)}{a(t_1)}. \quad (2.35)$$

Thus, the properties of the detected light now depend on the evolution of the scale-factor of the universe. If, for example, a universe was expanding ( $a(t_2) > a(t_1)$ ), then the wavelength of the detected light will be larger than that of when it was emitted, i.e. it was shifted to the redder part of the electromagnetic spectrum – and thus the term redshift was born. If both  $\lambda_1$  and  $\lambda_2$  are known (say they correspond to a known elements emission line), then one can assign a *redshift* to the source of

$$1 + z = \frac{\lambda_2}{\lambda_1}. \quad (2.36)$$

Additionally, since we have normalised the scale-factor to be unity today (recall  $a(t_0) = 1$ ), then we find

$$a = \frac{1}{1 + z}, \quad (2.37)$$

a very useful relation between redshift and the scale-factor.

## 2.1.6 The generalised Hubble parameter

The density parameter for each component of the cosmological fluid introduced in Equation 2.27,  $\Omega_i$ , becomes extremely useful when we want to manipulate the first Friedmann equation (Equation 2.13) into the generalised Hubble parameter  $H(z)$ . By noting the redshift evolution of each individual component, we can write the Hubble parameter as

$$H^2(z) = H_0^2 \left( \Omega_{R0}(1+z)^4 + \Omega_{M0}(1+z)^3 + \Omega_{\Lambda0} + \Omega_{k0}(1+z)^2 \right). \quad (2.38)$$

This form of the Hubble parameter becomes incredibly useful when dealing with distances in cosmology, since it can be anchored to values observed today.

## 2.1.7 Cosmological distances

Large amounts of observational cosmology rely on us being able to measure accurate distances to objects, such as galaxies or galaxy clusters. While accurate measurements are essential, a solid theoretical understanding of these distances are also key to correctly interpret these distances. Measuring distances in a flat, Euclidean space-time are simple; we can produce different estimates for distance to an object using different methods and they will all agree, to within the measurement's statistical errors. However, when we go to an expanding space-time this no longer holds, and so different measurement techniques yield different result for distances to the same object. Here, we discuss different measurement techniques to astronomical and cosmological objects and how they are related to each other.

### Comoving distances

The comoving distance to an object at redshift  $z$  can be given in terms of an integral over the Hubble parameter as

$$\chi = \int_0^z \frac{dz'}{H(z')}, \quad (2.39)$$

and hence if one can accurately measure redshifts and comoving distances to objects, then one can constrain the evolution of the Hubble parameter – a key goal of modern cosmology.

## Hubble velocity distance

Another simple distance measure is the Hubble velocity distance ( $d_H$ ), which only works for local objects ( $z \ll 1$ ). Here, we can re-write Hubble's law to find

$$d_H = \frac{cz}{H_0}. \quad (2.40)$$

## Angular diameter distance

The angular diameter distance is useful when we measure objects that have a known physical size and want to relate it to the angular size that it appears from at Earth. If we have an object of proper length  $l$  at distance  $d$ , then the angle that it subtends on the sky would be given by  $\Delta\theta = l/d$  (in the limit  $d \gg l$ ) for flat Euclidean space. Using this relation, we can define the angular diameter distance  $d_A$  to satisfy

$$d_A \equiv \frac{l}{\Delta\theta}. \quad (2.41)$$

The solution to this can be given in terms of the comoving distance as

$$d_A = \frac{f_k(\chi)}{1+z}. \quad (2.42)$$

It is often useful to calculate the angular diameter distance between a source at redshift  $z_2$  and observer at redshift  $z_1$  ( $z_1 < z_2$ ), which is given by [56]

$$d_A(z_1, z_2) = \frac{1}{1+z_2} f_k(\chi(z_2) - \chi(z_1)). \quad (2.43)$$

We see that  $d_A(z_1, z_2) \neq d_A(z_2) - d_A(z_1)$ , which is an important result when we consider the equations of gravitational lensing shortly.

## Luminosity distance

Analogously, the luminosity distance ( $d_L$ ) can be defined from the classical luminosity-flux relation which follows an inverse-square law of

$$F = \frac{L}{4\pi d_L^2}, \quad (2.44)$$

where  $F$  is the flux received, and  $L$  is the luminosity of an object. Again, this can be written in terms of the comoving distance to give

$$d_L = (1+z)f_k(\chi) = (1+z)^2 d_A. \quad (2.45)$$

From this, we see that in an expanding universe, the distance inferred from measuring its luminosity alone would be larger than that from measuring its size and inferring its distance from that. This shows that objects in the sky appear fainter in an expanding universe than they otherwise would be in a static space-time, an important result of observational cosmology.

Figure 2.4 plots the luminosity, comoving, and angular diameter distances as a function of redshift. This demonstrates the differences between these three measurements, and why they're important.



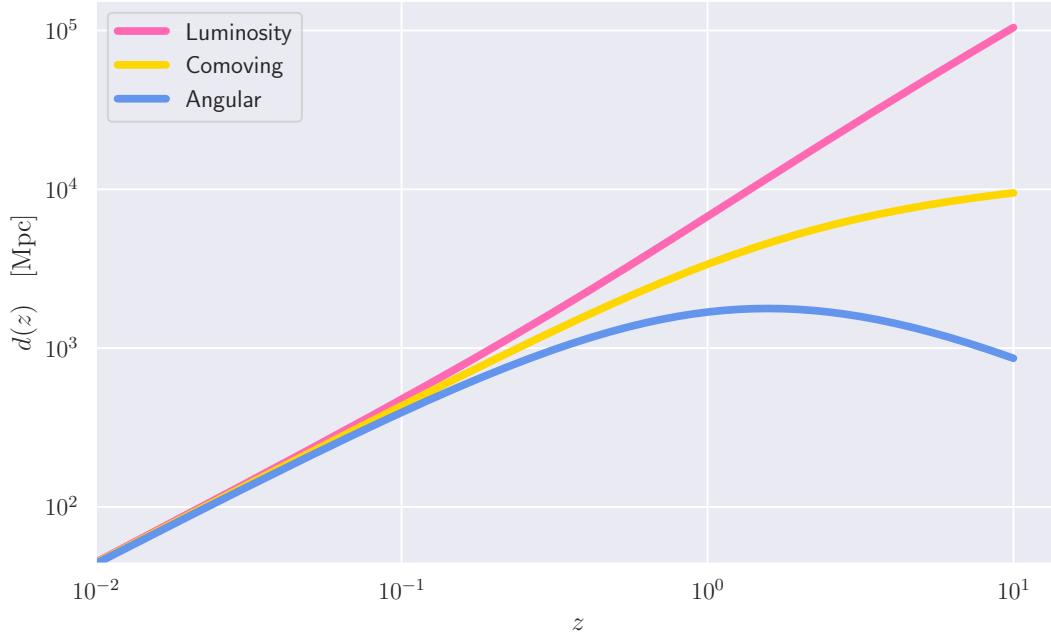


Figure 2.4: Plot of the different measurements of cosmological distances as a function of redshift. Here, we see that in an expanding universe objects are fainter, and thus appear further away than they actually are. We also see the peak in the angular diameter distance which is unique to an expanding space-time. For the best explanation of this effect, see [xkcd 2622](#).

## 2.2 Inflation & the early universe

In the beginning (queue *2001: A Space Odyssey* theme) there was nothing.... Then a wild Big Bang occurred! Much has happened to the universe in its (approximate) 13.6 billion years of evolution, and thus it's important to look across the universe's entire existence for us to start answering the fundamental questions: How did we get here? What's going to happen to the Universe? And what is the meaning of life? (Though that has a simple answer of 42.)

### 2.2.1 The hot Big Bang model

With Edwin Hubble's observations that distant objects were receding from us equally in all directions, one could wind the clock back in which one would predict that at the start of the universe, all matter was at one location and thus everything started from a single 'Big Bang'<sup>6</sup>. The Big Bang model got modified to the 'hot' Big Bang model by George Gamow's work on trying to explain the abundance of elements within the universe [57]. By proposing that the early universe at some point had sufficient energy to overcome the repulsive nature of the strong nuclear force, such that nuclear fusion reactions can occur, but not too high energy which would result in instant destruction of any newly created atoms from rouge high-energy photons, one can precisely calculate the exact ratios of elements formed in the early universe. This process of element creation is called Big Bang nucleosynthesis (BBN), lasting from about one second to three minutes after the initial

<sup>6</sup>It's interesting to note that British astronomer Fred Hoyle who coined this name, was actually trying to discredit the theory – favouring the steady state solution instead.

Big Bang, and created elements D,  $^3\text{He}$ ,  $^4\text{He}$ , and  $^7\text{Li}$  [58]. The famous ‘Alpha-Bethe-Gamow’, or  $\alpha\beta\gamma$ , paper [59] was one of the first attempts to calculate the abundances of such elements from BBN, with subsequent calculations being in very good agreement with observational data [58]. This agreement underpins our hot Big Bang model; that our Universe started out extremely hot and dense which rapidly expanded and cooled.

## 2.2.2 The Big Bang break down

While the hot Big Bang model has been very successful in providing many physical answers to many questions that arose, such as the relative abundances of elements (through primordial nucleosynthesis [57]) and the prediction of the cosmic microwave background [60], it is not an exhaustive theory. Such is life, you answer some questions only to be left with more that are unresolved. Why can’t it be turtles all the way down?

### Flatness problem

The flatness problem is a problem with the hot Big Bang model that when we observe the Universe on the large scales, we observe a universe that is consistent with being spatially flat. Some of the latest observational constraints on spatial curvature come from the *Planck* 2018 data release [40], which constrain the curvature density  $\Omega_k$  to be  $\Omega_k = (0.0007 \pm 0.0019)$ , which is very much consistent with a flat universe of  $k = 0$ .

One can now ask: Why is this a ‘problem’? Surely<sup>7</sup> we could just be living in a flat, or very close to flat universe. On the flip side, we could have been living in a very non-flat universe that experiences severe spatial curvature with no way for the Big Bang model to favour one of the other. Thus, for our theoretical model to match the experimental evidence, one needs to ‘fine-tune’ the curvature parameter such that it has the value that it has today, for which we have no *a priori* reason for doing so.

Furthermore, it should be noted that from the Friedmann equations, the evolution of the curvature density during matter domination (which is what the vast majority of the universe’s history has been in) scales as [61]

$$|\Omega_k(t)| \propto t^{\frac{2}{3}}. \quad (2.46)$$

Since this is an increasing function with time, if we observe  $\Omega_k$  to be very close to zero today, some 13.6 billion years after the Big Bang, then it must have been *exceedingly* close to zero at the start of the Universe. For example, during the period of nucleosynthesis, approximately one second after the Big Bang, then we require an upper limit on the curvature density of  $|\Omega_k| \lesssim 10^{-18}$  [61]. Since  $\Omega_k$  should be a free parameter in any cosmological model, requiring it to have such a tight constraint is highly unphysical. Thus, we would like to introduce some theoretically motivated mechanism for which the value of  $\Omega_k$  is driven to very small values, regardless of its initial value.

Note that if, for some reason,  $\Omega_k$  was *exactly* zero at the time of the Big Bang, then it would *always* be zero and thus there would be no flatness problem today.

### Horizon problem

When we look at the Universe on the largest scales, we see that it is very nearly isotropic (this was the motivation behind the cosmological principle, and the FRW metric). For example, since the level of temperature anisotropies in the cosmic microwave background are at the level of one in one hundred thousand, this prompts us to believe that any two points on the opposite side of the sky must have been in thermal equilibrium for them to

---

<sup>7</sup>I am serious, and don’t call me Shirley.

have such similar statistical properties. However, given that the Universe has a finite age, the hot Big Bang model predicts that these two vastly separated regions could not have been in causal contact for them to establish this equilibrium.

Therefore, in the framework of the hot Big Bang model, we require very nearly uniform initial conditions across the entire universe for us to observe such statistical isotropy. This requires additional ‘fine-tuning’ in the initial conditions, which again is dissatisfying and theoretically unmotivated.

## Cosmological perturbations

While the horizon problem looks at the large-scale statistical isotropies that we see on the sky, it is important to note that the Universe is *not* totally homogenous. For example, the existence of planets, stars, and galaxies all show that there are significant overdensities in the Universe – the formation and evolution of which need to be explained in our cosmological models. Thus, we require some mechanism in the early universe to ‘seed’ these perturbations, from which they can evolve to form structures, and you and me.

### 2.2.3 Inflate our problems away

As we’ve discussed, there are numerous ‘problems’ with the hot Big Bang model, namely that there involves much ‘fine-tuning’ of the initial conditions if we were to match up our experimental evidence to our theoretical models. Thus, we wish to introduce some physical mechanism that can solve many of these problems while also producing its own predictions which we can test to verify or nullify the theory.

The inflationary paradigm was introduced in Refs. [62, 63] as a period of rapid expansion in the *very* early universe, when it was only around  $10^{-34}$  seconds old. Inflation was introduced to solve many of the problems with the hot Big Bang model (namely the flatness and horizon problems), as noted by the title of Ref [62] “Inflationary universe: *A possible solution to the horizon and flatness problems*”. The principle of inflation is that the universe undergoes accelerated expansion, i.e.  $\ddot{a} > 0$ . As we will see, by postulating that there was this rapid expansion very early in the Universe’s evolution, it solves many of the problems that we have seen in the hot Big Bang model.

## Solving the flatness problem

Previously, we have seen that during matter domination the curvature density grows with time (Equation 2.46), and so a small perturbation from zero in the early universe would grow into a much larger value today. We can repeat this analysis during a period of inflation and see how the curvature density changes during this epoch.

If we assume the case of perfect exponential inflation, which is highly motivated as we will see later, then the evolution of the scale-factor evolves with time has the same functional form as our  $\Lambda$ -dominated universe of Equation 2.21. Using the Friedmann equations again, it can be shown that the curvature density changes with time as [61]

$$|\Omega_k(t)| \propto \exp\left(-\sqrt{\frac{4\Lambda}{3}} t\right). \quad (2.47)$$

Hence, no matter what the initial value of  $\Omega_k$  was from the initial conditions of the Big Bang singularity,  $\Omega_k$  is exponentially suppressed and the universe is rapidly forced to being spatially flat provided that there is sufficient inflation.

## Solving the horizon problem

Inflation also naturally solves the horizon problem, as the accelerated expansion allows for a, then small, patch of the Universe to reach thermal equilibrium before the exponential expansion kicks in to enlarge the patch to a size that is many times larger than our observable Universe. Hence, if we assume that the initial patch thermalised,<sup>8</sup> then the resulting expanded volume will also be in thermal equilibrium – matching the statistical isotropy that we see today.

## Solving the monopole problem

There also exists the ‘monopole problem’. This is where, as modern particle physics theory try to unify the electromagnetic, strong, and weak forces into a single ‘Grand Unified Theory’ (GUT), extraordinarily heavy particles are predicted to have numerous formed right after the Big Bang. Such particle could be a magnetic monopole, which are analogous to electric charge carries, such as quarks and electrons, but for the magnetic force and arise from such GUT theories [61, 64]. These magnetic monopoles would have had masses around the GUT scale,  $E_{\text{GUT}} \sim 10^{16}$  GeV, which when compared to the heaviest elementary particle found thus far, the top quark with mass around 173 GeV [65], shows that even if there were only very few of these magnetic monopole particles they would dominate the universe’s energy density contributions. This would significantly alter the previously well-understood dynamics of radiation domination in the early universe followed by matter domination, and thus would be incompatible with the hot Big Bang model.

Inflation solves this problem as the rapid, exponential expansions will serve to vastly dilute the abundances of relic particles. Thus with sufficient expansion, it could be probable that none of these particles would exist in an observable universe despite initially dominating the energy distribution of the pre-inflated universe [66].

## How much inflation

While inflation solves many of the problems that we have discussed, by postulating that the Universe underwent a rapid exponential expansion soon after it formed, it does not tell us exactly how long this expansion lasted. To quantify how long inflation went on for, we can introduce the idea of  $e$ -foldings,  $N$ , which are simply the number of times that the universe expanded by a factor of  $e$ . Mathematically, this is defined as the ratio of the scale-factors at the end ( $a_2$ ) to the beginning ( $a_1$ ) of inflation

$$N \equiv \ln \frac{a_2}{a_1} = \int_{t_1}^{t_2} dt H(t). \quad (2.48)$$

Estimates for this place the number of  $e$ -foldings around  $50 \lesssim N \lesssim 70$  to adequately explain the flatness, horizon, and monopole problems [67, 68]. For example, if we assume inflation started at the GUT scale, with a temperature  $T_{\text{GUT}} \sim 10^{28}$  K, and lasted for  $N = 65$   $e$ -foldings, then it would be driven to a temperature of  $T_2 \sim e^{-65} T_{\text{GUT}} \sim 0.6$  K [69]. Though due to the wide variety of inflationary models that have been studied in the literature, there exist many models where inflation lasts for much longer, such as models where  $N$  can be of the order one thousand or even larger than ten thousand [70, 71].

## Ending inflation and reheating

During inflation, all existing matter and radiation are rapidly expanded away with the universe rapidly cooling to a temperature of 1 K or less, as shown above. The entire energy

---

<sup>8</sup>Now there’s no particular reason for the initial patch to be in thermal equilibrium before inflation, which is one of the major criticisms of the inflationary paradigm.

density of the universe is now held in the inflaton field(s). Thus, to match the existing well-tested predictions of the hot Big Bang model, such as primordial nucleosynthesis [72], these inflaton fields will need to decay, creating the very many high-energy elementary particles that are present in the Standard Model [73]. This then allows the hot Big Bang to progress normally, with a hot radiation-dominated universe, though one with now the correct initial conditions to match the phenomena that we observe today.

It should be noted that the energy scale of reheating,  $T_R$ , should be large enough that it produces an abundance of highly energetic Standard Model elementary particles, but much smaller the GUT scale so as to not re-form troublesome particles, such as magnetic monopoles, that inflation was invoked to solve [61, 74].

## 2.2.4 The physics of inflation

While the exact physics of inflation is the subject of much lengthy discussion, we will only present a set of various key results and derivations. Many textbooks have been dedicated to inflation, with Refs. [72, 75, 76] covering the topic particularly well.

### Inflation, or dark energy?

While we are conceded with the primordial universe for the time being, it is important to note that the results that we derive here hold for any scalar field that is dominating the universe's energy density – irrespective of if its dynamics occur  $10^{-34}$  seconds after the Big Bang or after 13 billion years. Thus, these results also apply to dark energy domination period that our universe is currently experiencing.

### Inflating with scalar fields

Currently, the most accepted idea for what drove inflation was that there were some scalar field(s) active during the early universe whose dynamics gave rise to accelerated expansion. This is because, as we shall see, if the energy density is dominated by scalar fields, then the exponential expansion is a natural consequence. Furthermore, by quantising the scalar field to a quantum scalar field, we produce perturbations in the late-universe that are compatible with observations today.

Scalar fields exist in a wide range of physics, with an example of a classical scalar field being temperature – each point in spacetime has a specific value for the field, which may evolve with time. As we are dealing with relativistic quantum fields, we require that the scalar field is invariant under Lorentz transforms.

The idea of inflating with scalar fields is physically motivated from elementary particle physics, due to the fact that scalar fields are an established part of the Standard Model of particle physics, as one of its constituent particles, the Higgs boson, is a particle derived from a scalar field [77]. In the 1960s, the Englert-Brout-Higgs mechanism [78, 79] proposed to use scalar fields to help solve the *small* problem of particles having no mass! Weinberg then applied the mechanism to produce particle masses in the newly developed Standard Model [80]. With the detection of the Higgs boson in 2012 [81, 82], we have strong experimental evidence that scalar fields exist in nature, and so may be included in our cosmological models. Therefore, it is conceivable that some scalar fields were active during the early universe in such a way that can give rise to inflationary dynamics.

### Scalar field Lagrangian

To determine the dynamics of the scalar field during inflation, we can make use of Lagrangian mechanics. This introduces the concept of the Lagrangian density  $\mathcal{L}$  which

encodes the physical properties of the scalar fields. In classical mechanics, this is a function of the coordinates  $x^i$  and their derivatives  $\dot{x}^i$  (giving  $\mathcal{L} = \mathcal{L}(x^i, \dot{x}^i)$ ). This translates to field theory as a function of the field  $\phi$  and its derivatives  $\partial_a \phi$  (giving  $\mathcal{L} = \mathcal{L}(\phi, \partial_a \phi)$ ). Using our field theory Lagrangian, we find the action to be

$$S = \int d^4x \mathcal{L}(\phi, \partial_a \phi). \quad (2.49)$$

Using the calculus of variations, and applying the principle of least action – which states that the action is extremised such that  $\delta S = 0$  – gives rise to the Euler-Lagrange field equations of

$$\partial_a \left( \frac{\partial \mathcal{L}}{\partial (\partial_a \phi)} \right) - \frac{\partial \mathcal{L}}{\partial \phi} = 0, \quad (2.50)$$

which are analogous to the Euler-Lagrange equations for a system in classical mechanics.

Let us consider the simplest case: a single scalar field  $\phi$  (called the inflaton field). From field theory, the Lagrangian density for a free scalar field is [83]

$$\mathcal{L} = \frac{1}{2} g^{ab} (\partial_a \phi) (\partial_b \phi) - V(\phi), \quad (2.51)$$

where the first term is a generalised kinetic energy, and  $V(\phi)$  is the potential. Applying the Euler-Lagrangian equations, we find the field equation of motion to be

$$\nabla^a \nabla_a \phi + \frac{\partial V}{\partial \phi} = 0, \quad (2.52)$$

where  $\nabla_a$  is the covariant derivative ( $\nabla_a x^b = \partial_a x^b + \Gamma_{ca}^b x^c$ ) since we wish to include the properties of a non-trivial metric [47].

## The action in curved spacetime

So far, our discussion of scalar fields have been for the case of flat Minkowski spacetime, where the metric is  $g_{ab} = \eta_{ab}$ . However, since we know that the observable Universe can be accurately described by the FRW metric, we wish to understand how our scalar fields act in non-Minkowski spacetimes. Since the action should be invariant upon general coordinate transformations, the action in GR becomes [47]

$$S = \int d^4x \sqrt{|g|} \mathcal{L}(\phi, \partial_a \phi), \quad (2.53)$$

where  $g$  is the determinant of the metric. This gives an ‘effective Lagrangian’, which is now the correct term to use in the Euler-Lagrange equations, of  $\sqrt{|g|} \mathcal{L}(\phi, \partial_a \phi)$ .

If we now consider a FRW universe that is dominated by our single scalar field that is homogenous, we can neglect the spatial derivatives that feature in our field-space Lagrangian of Equation 2.51, to give simply

$$\mathcal{L}(\phi, \partial_a \phi) = \frac{1}{2} \dot{\phi}^2 - V(\phi). \quad (2.54)$$

The determinant of the FRW metric (Equation 2.8) is  $\sqrt{|g|} = a^3(t)$ , and thus we find the evolution of our scalar fields in FRW spacetime to be given by

$$\ddot{\phi} + 3H\dot{\phi} = -\partial_\phi V. \quad (2.55)$$

This can be recognised as a form of a damped harmonic oscillator, where the damping term ( $3H\dot{\phi}$ ) is analogous to the friction generated by an expanding universe – and is called the Hubble drag [75].

## The equation of state for a scalar field

Previously, in Equation 2.23, we saw that to get accelerated expansion, we required that the Universe be dominated by a fluid that has equation of state  $w$  such that  $w < -\frac{1}{3}$ . Hence, we need to verify that this condition on  $w$  can be satisfied by a scalar field.

The pressure and density of a scalar field can be found by coupling it to gravity through the Einstein-Hilbert action which, for a spatially homogenous field ( $\partial_i\phi = 0$ ), yields [47, 67]

$$P_\phi = \frac{1}{2}\dot{\phi}^2 - V(\phi), \quad (2.56a)$$

$$\rho_\phi = \frac{1}{2}\dot{\phi}^2 + V(\phi). \quad (2.56b)$$

Hence, the equation of state for a scalar field is

$$w_\phi = \frac{\frac{1}{2}\dot{\phi}^2 - V(\phi)}{\frac{1}{2}\dot{\phi}^2 + V(\phi)}, \quad (2.57)$$

which gives accelerated expansion provided that  $V(\phi) > \dot{\phi}^2$ . Additionally, we see that in the limit that the potential dominates over the kinetic term ( $V(\phi) \gg \dot{\phi}^2$ ), the equation of state is driven to negative one ( $w_\phi \rightarrow -1$ ), which is the limit of the classical cosmological constant.

## 2.2.5 The primordial perturbations

While inflation was largely motivated to solve the many problems with the hot Big Bang model (Section 2.2.3), one problem not yet addressed is the generation of perturbations in the early universe that are necessary for structure to grow, and thus result in the creation of you, dear reader, and I. This is where inflation provides perhaps its greatest success, a physical mechanism for how these primordial perturbations were produced. A full discussion of cosmological perturbation theory during inflation is outside the scope of this thesis, see Refs. [72, 75, 76] (yet again) for comprehensive descriptions, and reserve our discussion to some key results that will be needed later.

Nevertheless, we can at least start with a brief physical insight into the basic mechanisms that drove the primordial perturbations, which have subsequently evolved in the large-scale structure we see today some 13.6 billion years later. The foundation of the generation of inflationary perturbations come from the quantum fluctuations in the scalar field that drove inflation. Quantum field theory tells us that even in an empty vacuum, particle-antiparticle pairs are continually popping in and out of existence, so called ‘virtual particles’, whose energies and lifetimes are governed by Heisenberg’s uncertainty principle [47]. The effect of these virtual particles is that a small region of space will have a slightly higher energy than average and one with a correspondingly lower energy. In a non-inflationary spacetime, this has no macroscopic effects, as these virtual particle pairs are confined to the quantum realm and the overall average energy is conserved. However, when we subject our spacetime to the dramatic exponential expansion of inflation, these particle-antiparticle pairs are driven apart much faster than the speed of light, and so are out of causal contact [76].

Hence, the virtual particle pair cannot recombine since they are out of causal contact (outside of the horizon), and thus the under- and over-dense regions are ‘locked in’ by inflation. These quantum fluctuations then provide the seeds of structure formation during the decelerating periods of radiation- and then matter-domination of our Universe.



We can decompose our inflaton field  $\phi$  into a zeroth-order homogenous background  $\bar{\phi}$ , and a perturbative part,  $\delta\phi$ , to give [84]

$$\phi(t, \vec{x}) = \bar{\phi}(t) + \delta\phi(t, \vec{x}). \quad (2.58)$$

These perturbations in our scalar field during inflation give rise to the curvature perturbation  $\zeta$ , which has a general interpretation as the fractional perturbation in the scale factor  $\zeta = \delta a/a$ . It is an extremely useful quantity in inflationary cosmology since  $\zeta$  is conserved when perturbation modes move outside the horizon.

We now wish to investigate the statistical properties of  $\zeta$ , such that we can hope to obtain something that can be measured experimentally, and thus test our theories of inflation.

### The two-point function

Since we have constructed the curvature perturbation field  $\zeta$  to have a mean of zero,  $\langle \zeta(\vec{x}) \rangle = 0$ , the first non-zero statistical measure of  $\zeta$  will be the total variance of the perturbations. This is called the two-point function. If we consider the Fourier transform of  $\zeta$  into momentum-space, we get

$$\zeta(\vec{x}) = \int \frac{d^3\vec{k}}{(2\pi)^3} \zeta_{\vec{k}} e^{i\vec{k}\cdot\vec{x}}, \quad (2.59)$$

where we are integrating over all wavenumbers  $\vec{k}$ . If we now compute the variance of  $\zeta$  at point  $\vec{x}$  using the above Fourier transform, which is the definition of the variance of the field  $\zeta$ , we find

$$\langle \zeta^2(\vec{x}) \rangle = \int \frac{d^3\vec{k}}{(2\pi)^3} \frac{d^3\vec{k}'}{(2\pi)^3} \langle \zeta_{\vec{k}} \zeta_{\vec{k}'} \rangle e^{i\vec{x}\cdot(\vec{k}+\vec{k}')}. \quad (2.60)$$

Statistical homogeneity and isotropy (the cosmological principle) requires that this expectation value be position independent, i.e.  $\langle \zeta^2(\vec{x}) \rangle = \langle \zeta^2 \rangle$ . For this to hold, we require that  $\vec{k} + \vec{k}' = 0$ , and thus we find that the expectation value of our two  $\zeta$  terms in momentum-space are proportional to a  $\delta$ -function of the momenta:  $\langle \zeta_{\vec{k}} \zeta_{\vec{k}'} \rangle \propto \delta^{(3)}(\vec{k} + \vec{k}')$ . From this, we can *define* the primordial power spectrum  $P(k)$  such that

$$\langle \zeta_{\vec{k}} \zeta_{\vec{k}'} \rangle = (2\pi)^3 \delta^{(3)}(\vec{k} + \vec{k}') P_{\zeta}(k). \quad (2.61)$$

Using this definition of the power spectrum in Equation 2.60 gives

$$\begin{aligned} \langle \zeta^2 \rangle &= \int \frac{d^3\vec{k}}{(2\pi)^3} \frac{d^3\vec{k}'}{(2\pi)^3} (2\pi)^3 \delta^{(3)}(\vec{k} + \vec{k}') P_{\zeta}(k) e^{i\vec{x}\cdot(\vec{k}+\vec{k}')}. \\ &= \int \frac{d^3\vec{k}}{(2\pi)^3} P_{\zeta}(k) \\ &= \frac{1}{2\pi^2} \int dk k^2 P_{\zeta}(k). \end{aligned} \quad (2.62)$$

It is often useful to use the dimensionless power spectrum  $\mathcal{P}_{\zeta}(k)$  instead, which is related to  $P(k)$  through

$$\mathcal{P}_{\zeta}(k) = \frac{1}{2\pi^2} k^3 P_{\zeta}(k). \quad (2.63)$$



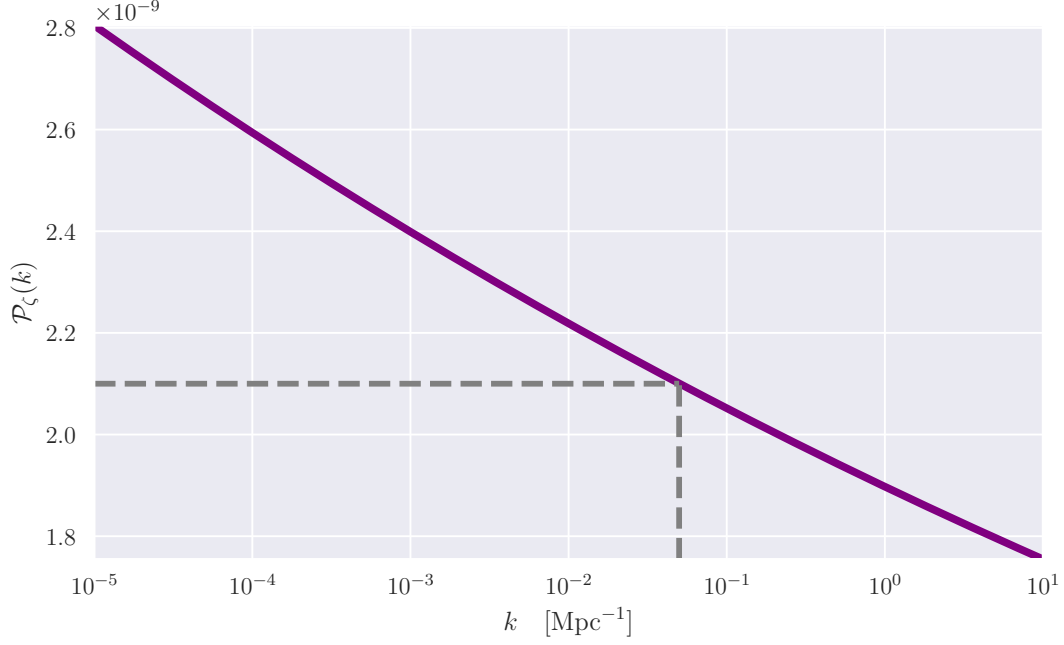


Figure 2.5: The dimensionless inflationary power spectrum plotted using the *Planck* 2018 values. Here, we show the ‘pivot’ scale of  $0.05 \text{ Mpc}^{-1}$  and the amplitude at this scale of  $2.1 \times 10^{-9}$ . Since  $n_s < 1$ , we have a ‘red’ spectrum giving more power<sup>9</sup> on larger physical scales than small scales, which propagates into the density contrasts that we see today.

This has the useful statistical property that it is the variance per logarithmic interval in  $k$ -space. The power spectrum can be parametrised as a power-law relation of [85]

$$\mathcal{P}_\zeta(k) = A_s \left( \frac{k}{k_*} \right)^{n_s - 1}, \quad (2.64)$$

where  $A_s$  is the scalar amplitude,  $n_s$  is the scalar spectral index – with  $n_s = 1$  giving a true scale-independent spectrum – and  $k_*$  is the ‘pivot’ scale, which characterises the observational scale of interest. The latest observational constraints on the power spectrum come from the 2018 *Planck* data release, placing  $\ln(10^{10} A_s) = 3.047 \pm 0.014$ , evaluated at the pivot scale  $k_* = 0.05 \text{ Mpc}^{-1}$ , and  $n_s = 0.9665 \pm 0.0038$  [40].

The inflationary power spectrum is plotted in Figure 2.5.

### The three-point function

For a pure Gaussian field, the two-point function encodes all the statistical properties about the field, since higher-order correlators are either zero (for an odd number of terms), or can be expressed entirely out of the two-point function (for an even number of terms). This arises from how a Gaussian distribution can be described using only two numbers: its mean and variance. However, while the curvature perturbations are thought to be heavily Gaussian, they may not be exactly Gaussian and thus have small non-Gaussianities. Thus, the first higher-order correlator up from the two-point function is the three-point function defined through [86, 87]

$$\langle \zeta_{\vec{k}_1} \zeta_{\vec{k}_2} \zeta_{\vec{k}_3} \rangle = (2\pi)^3 \delta^{(3)}(\vec{k}_1 + \vec{k}_2 + \vec{k}_3) B_\zeta(k_1, k_2, k_3), \quad (2.65)$$

---

<sup>9</sup>More power — Cyber-Leader

where  $B_\zeta(k_1, k_2, k_3)$  is the curvature bispectrum. The relative amplitude of the bispectrum compared to the power spectrum is parameterised through  $f_{\text{NL}}$ , defined as [75]

$$\frac{6}{5}f_{\text{NL}}(k_1, k_2, k_3) = \frac{B_\zeta(k_1, k_2, k_3)}{P_\zeta(k_1)P_\zeta(k_2) + P_\zeta(k_1)P_\zeta(k_3) + P_\zeta(k_2)P_\zeta(k_3)}. \quad (2.66)$$

Measuring a statistically significant value for  $f_{\text{NL}}$  has been the goal of very many experimental cosmologists for the last couple decades as vary many inflationary models could be ruled out by its value [88].

## 2.3 Evolution of structure across cosmic time

While we have seen that inflation can generate small perturbations in the very early universe, our next task is to find out how these small perturbations evolve into the large-scale structure that we see today.

### 2.3.1 Linear density evolution

Let us start with assuming that the density of the universe can be expressed as a homogeneous background  $\bar{\rho}$  and a spatially varying relative perturbative part  $\delta$ , to give

$$\rho(t, \vec{x}) \equiv \bar{\rho}(t) (1 + \delta(t, \vec{x})). \quad (2.67)$$

Since the density of the Universe is constrained to be non-negative,  $\delta$  is bound to be  $-1 \leq \delta < \infty$ . By construction, the average of  $\delta$  is zero,  $\langle \delta(t, \vec{x}) \rangle = 0$ . We now want to work out how the perturbations  $\delta$  evolve during the expanding evolution of our Universe. The first such equation that we will use is the Poisson equation of [72]

$$\vec{\nabla}^2 \Phi = 4\pi G \bar{\rho} \delta, \quad (2.68)$$

where  $\Phi$  is the Newtonian gravitational potential. This gives rise to the evolution of our perturbations  $\delta$  in an expanding space-time as

$$\ddot{\delta} + 2H\dot{\delta} - 4\pi G \bar{\rho} \delta = 0. \quad (2.69)$$

For approximately constant  $\bar{\rho}$  and small  $H$ , we find that the solution for the time-evolution of  $\delta$  is exponential growth. In this case, we find that an initially small overdensity would continuously grow as its gravitational potential continued to bring in nearby matter. However, the presence of the  $2H\dot{\delta}$  (the ‘Hubble drag’) term serves to slow this exponential growth, and thus we see that in an expanding space-time, the growth of

We now wish to go about solving this equation to obtain the evolution of  $\delta$  for different components of our Universe during its different epochs.

### 2.3.2 Matter perturbations during radiation domination

First, we shall consider the perturbations in the matter density  $\delta_{\text{M}}$  during the epoch of radiation domination – early on in our Universe’s evolution. Since we are considering the matter perturbations, we can transform Equation 2.69 into

$$\ddot{\delta}_{\text{M}} + 2H\dot{\delta}_{\text{M}} - \frac{3}{2}H^2(t)\Omega_{\text{M}}(t)\delta_{\text{M}} = 0, \quad (2.70)$$

where we have used the Friedmann equation to write the physical matter density in terms of the Hubble parameter and matter density parameter. During radiation domination, we

can approximate that  $\Omega_M(t) \rightarrow 0$ , and recalling that the time evolution of the scale factor was  $a(t) \propto \sqrt{t}$  (Equation 2.19) and thus the Hubble rate is given by  $H(t) = 1/2t$ , we find the evolution of the matter perturbations as

$$\ddot{\delta}_M + \frac{1}{t}\dot{\delta}_M = 0. \quad (2.71)$$

This has solutions of the form

$$\delta_M(a) = A \ln a + B, \quad (2.72)$$

and so we see that the matter perturbations during radiation domination grow with the logarithm of the scale factor.

### 2.3.3 Matter perturbations during matter domination

We can now repeat the same exercise, but ask how do the matter perturbations evolve during the matter dominated epoch of our Universe. Since we are now in matter domination, we can approximate  $\Omega_M(t) \rightarrow 1$ , the time evolution of the scale factor was  $a(t) \propto t^{2/3}$  (Equation 2.17) giving the Hubble rate as  $H = 2/3t$ . This gives the evolution of our matter perturbations to be governed by

$$\ddot{\delta}_M + \frac{4}{3t}\dot{\delta}_M - \frac{2}{3t^2}\delta_M = 0. \quad (2.73)$$

This has a solution of the form

$$\delta_M(a) = Aa + Ba^{-\frac{3}{2}}. \quad (2.74)$$

Hence, we see that during matter domination the matter perturbations grow as  $\delta_M(a) \propto a$  which is significantly faster than their growth during radiation domination of  $\delta_M(a) \propto \ln a$ . This shows the suppression in the growth of structure that arose during the radiation dominated epoch and is called the Mészáros effect [89].

### 2.3.4 Matter perturbations during $\Lambda$ domination

Since we currently observe that our Universe is undergoing accelerated expansion due to a non-zero cosmological constant, we can consider how the matter perturbations evolve during  $\Lambda$  domination. In this case, we can again approximate that  $\Omega_M(t) \rightarrow 0$  and that the Hubble rate tends to a constant,  $H(t) \rightarrow \text{const}$ . This gives a solution as  $\delta_M \rightarrow \text{const}$ , and thus during  $\Lambda$  domination the matter perturbations stop growing and become static. Hence, there will be no new large-scale structure in our Universe, and that everything that will ever form would have formed by now.

### 2.3.5 The Fourier underworld

We have already encountered the Fourier transform when looking at the curvature perturbation  $\zeta$  (Equation 2.59), and so we yet again turn to it when dealing with our density perturbation  $\delta$ . This is especially useful since we can now investigate how the perturbations evolve on different physical scales. We can define the Fourier components of the density perturbation  $\delta(t, \vec{k}) \equiv \delta_{\vec{k}}$  through

$$\delta_{\vec{k}} = \int d^3\vec{x} e^{-i\vec{k}\cdot\vec{x}} \delta(t, \vec{x}). \quad (2.75)$$

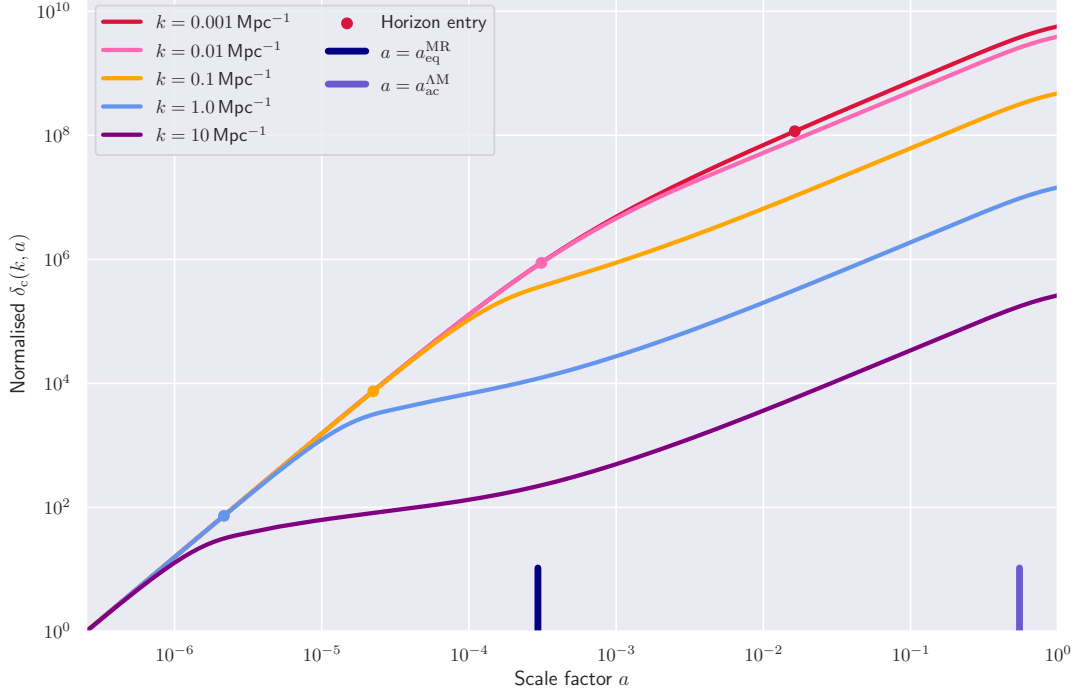


Figure 2.6: Evolution of the cold dark matter density perturbations for five different Fourier modes across the evolution of the Universe, normalised to their value on the left-hand side. The coloured circles represent the scale factor at which that coloured curve’s wavenumber re-enters the horizon (given when  $k = aH(a)$ ), and so undergo sub-horizon evolution again. We see that as the small-scale modes enter the horizon during radiation domination (up to matter-radiation equality of  $a_{\text{eq}}^{\text{MR}} \sim 10^{-3}$ , highlighted by the navy band), they undergo only logarithmic growth in their amplitudes, which suppresses power on the smallest scales today. As the Universe begins its epoch of matter domination (after the navy band), these modes then grow with the scale factor,  $\delta_{\text{M}} \propto a$ , as do the modes newly entering the horizon. We also see the effects of the current epoch of  $\Lambda$  domination towards the right-hand side of the plot (the Universe entering accelerated expansion at  $a_{\text{ac}}^{\text{AM}} \sim 0.5$ , highlighted by the light blue band), where the growth of the perturbations slows for all scales, and so will tend to a constant in the far future. These curves were computed using CAMB for a  $\Lambda$ CDM universe that is compatible with observations.

$\delta_{\vec{k}}$  are complex quantities, where the magnitude represents the amplitude of the perturbation and the phase represents its spatial dependence. Momentum-space is especially useful when considering that any spatial derivatives of the density perturbations become algebraic in Fourier-space:  $\partial_i \delta(t, \vec{x}) \rightarrow ik_i \delta(t, \vec{k})$ . Larger values of the wavenumber  $k$  represent smaller physical scales and vice-versa.

Figure 2.6 plots the evolution across the history of our Universe of the dark matter density perturbations for five physical scales, ranging from the largest scales that we can observe in the observable Universe today to the smallest scales. This clearly shows the suppression in the growth of perturbations during the radiation dominated epoch, how the perturbations grow with the scale factor during matter domination, and that the growth of perturbations is already being suppressed due to the cosmological constant – and will become static in the far future.

### 2.3.6 The photonic and baryonic perturbations

While investigating the evolution of the dark matter perturbations has given us vital insights into how these perturbations grow with the evolution of the Universe, which sow the seeds and form the large-scale structure that we see today, we do have to remember that our Universe isn't totally made of cold dark matter and that it has vital contributions from radiation and baryons! Working out the evolution of the dark matter perturbations were relatively easy since they simply evolve under gravity in an expanding spacetime and are decoupled with the rest of the goings-on in the Universe. In the early epochs of our Universe, radiation and baryons are coupled together and have a non-negligible self-pressure. This dramatically reduces their ability to clump together under gravity, and the perturbations have the ability to 'bounce' back out again due to their pressure. These physical effects making evaluating the evolution of the baryonic and photonic perturbations significantly more challenging, and so we leave the full derivation of these to other works (e.g. Refs. [72] and [90]).

As the photonic and baryonic fluids have non-zero self-pressure, these fluids have a non-zero sound speed,  $c_s$ , defined as

$$c_s^2 \equiv \frac{\partial p}{\partial \rho}. \quad (2.76)$$

This modifies the perturbation evolution equation to that of a damped harmonic oscillator,

$$\ddot{\delta} + 2H\dot{\delta} - \left(4\pi G\bar{\rho} - \frac{c_s^2 k^2}{a^2}\right)\delta = 0, \quad (2.77)$$

where we are already working in Fourier space. Hence, the wavenumber determines the evolution of that perturbation mode: long range modes (small  $k$ ) continue to grow, whereas short range modes (large  $k$ ) undergo damped oscillations. Specifically, if the physical wavelength is smaller than the Jeans length, given by [72]

$$\lambda_J = c_s \sqrt{\frac{\pi}{G\bar{\rho}}}, \quad (2.78)$$

then the perturbations will undergo oscillatory evolution. As the Universe expands and the average density  $\bar{\rho}$  decrease, this will increase the Jeans length and so longer range modes will start to oscillate. We also see that once recombination takes place and the baryonic fluid's sound speed drops to zero, then its oscillations will cease and ordinary gravitational attraction can continue.

Figure 2.7 plots the evolution of the baryonic and photonic perturbations for three physical scales across the evolution of our Universe. We see that prior to recombination these two fluids are highly coupled, and that both feature heavy oscillations in their amplitudes, as predicted from Equation 2.77. We also see that the frequency of oscillation is highly  $k$  dependent, with short-range modes exhibiting higher frequency oscillations. It also shows that the longer range modes start oscillating later on in the Universe's evolution, which is predicted from the Jeans length and the fact that these long-range modes re-entered the horizon significantly after the shorter-range modes. After recombination, the baryonic perturbations are free to catch up with the dark matter perturbations which is shown by their steep increase after  $a \sim 10^{-3}$ , while the photonic fluid which still features a self-supporting pressure term undergoes damped harmonic motion with an amplitude and frequency related to their physical scale.

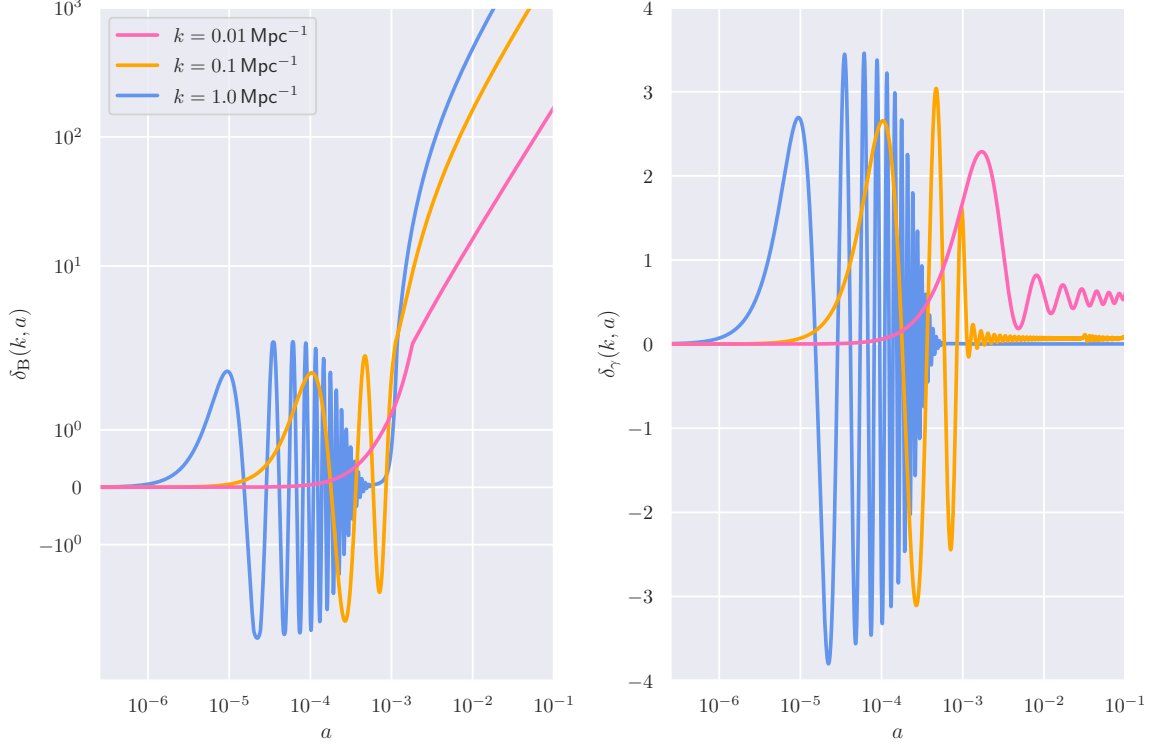


Figure 2.7: Evolution of the perturbations in the baryonic (left panel) and radiation (right panel) components of our Universe for three different scales. We see that prior to decoupling ( $a \sim 10^{-3}$ ), the baryons are highly coupled to the photonic fluid, which rapidly undergoes expansion and contraction due to its self-supporting pressure. This inhibits the gravitational collapse of the baryonic fluid, and forces their perturbations to oscillate. Once recombination has taken place and the baryons are no longer coupled to the photons, the baryonic perturbations can gravitationally collapse, ‘catching up’ with the dark matter perturbations which have been free to grow under gravity since the early Universe (Figure 2.6). These curves were computed using CAMB for a  $\Lambda$ CDM universe that is compatible with observations.

## 2.4 The matter power spectrum

Now that we have an understanding of how density perturbations evolve during the Universe’s evolution, we wish to use this to produce estimates for quantities that we hope are either directly observable, or lead to quantities that are. Hence, we want to consider statistics of the density perturbations  $\delta$ , just as how we looked into statistics of the curvature perturbation  $\zeta$  during inflation.

By construction, the spatial average of the density perturbation  $\delta$  is zero at any given time (cf. Equation 2.67)

$$\langle \delta \rangle = \left\langle \frac{\rho}{\bar{\rho}} - 1 \right\rangle = \frac{\langle \rho \rangle}{\bar{\rho}} - 1 = 0, \quad (2.79)$$

and thus the first non-zero statistic is the two-point correlation function  $\xi$ , defined through

$$\xi(t, \vec{x}, \vec{y}) = \langle \delta(t, \vec{x}) \delta(t, \vec{y}) \rangle. \quad (2.80)$$

However, due to our assumptions of homogeneity and isotropy (the cosmological principle), should not depend on the exact positions  $\vec{x}$  and  $\vec{y}$ , but of the magnitude separation vector  $\vec{r}$  between the two  $r \equiv |\vec{x} - \vec{y}|$  giving  $\xi$  as  $\xi(t, r)$ .

We can now consider the Fourier transform of our correlation function, to find the two-point function for the momenta of

$$\langle \delta(t, \vec{k}_1) \delta(t, \vec{k}_2) \rangle = \iint d^3\vec{x} d^3\vec{y} e^{i\vec{k}_1 \cdot \vec{x}} e^{i\vec{k}_2 \cdot \vec{y}} \langle \delta(t, \vec{x}) \delta(t, \vec{y}) \rangle. \quad (2.81)$$

Since we know that this should not depend on the raw values of  $\vec{x}$  and  $\vec{y}$ , we can use that  $\vec{y} = \vec{x} - \vec{r}$ , to give

$$\langle \delta(t, \vec{k}_1) \delta(t, \vec{k}_2) \rangle = \iint d^3\vec{x} d^3\vec{r} e^{i(\vec{k}_1 + \vec{k}_2) \cdot \vec{x}} e^{-i\vec{r} \cdot \vec{k}_2} \xi(t, r) \quad (2.82)$$

$$= \int d^3\vec{x} e^{i(\vec{k}_1 + \vec{k}_2) \cdot \vec{x}} \int d^3\vec{r} e^{-i\vec{r} \cdot \vec{k}_2} \xi(t, r) \quad (2.83)$$

Thus, we can evaluate the  $\vec{x}$  integral, to give out two-point function as

$$\langle \delta(t, \vec{k}_1) \delta(t, \vec{k}_2) \rangle = (2\pi)^3 \delta^{(3)}(\vec{k}_1 + \vec{k}_2) P(k), \quad (2.84)$$

where we have defined the power spectrum  $P(k)$  as

$$P(k) \equiv \int d^3\vec{r} e^{-i\vec{r} \cdot \vec{k}_2} \xi(t, r). \quad (2.85)$$

It can often be convenient to work in the dimensionless power spectrum  $\Delta(k)$  defined through

$$\Delta(k) \equiv \frac{k^3}{2\pi^2} P(k), \quad (2.86)$$

since it is related to the total variance of the density perturbation field,  $\sigma^2$ , though

$$\sigma^2 \equiv \int d^3\vec{x} \langle \delta^2(\vec{x}) \rangle, \quad (2.87)$$

$$\begin{aligned} &= \int \frac{d^3\vec{k}}{(2\pi)^3} |\delta_{\vec{k}}|^2, \\ &= \int d \ln k \frac{k^3}{2\pi^2} P(k), \end{aligned} \quad (2.88)$$

and thus  $\Delta(k)$  is the contribution to the total variance per logarithmic interval in  $k$ .

## 2.4.1 $\sigma_8$

Equation 2.87 gives the total variance of the density perturbation field, however it can be useful to consider the variance smoothed by a filter of comoving radius  $R$ . This smoothed variance is therefore given as

$$\sigma^2(R) = \int d \ln k \Delta(k) W^2(kR), \quad (2.89)$$

where  $W$  is a window function. This is usually chosen to be a spherical top-hat profile given by [91]

$$W(x) = \frac{3}{x^3} [\sin x - x \cos x]. \quad (2.90)$$

From our spatially smoothed variance, by choosing a fixed scale, we can define a parameter that allows for easy comparison for the amplitude of the power spectrum between

different models and for comparison between theory and experiment. For historical reasons, this scale was chosen to be  $8 h^{-1} \text{Mpc}$ <sup>10</sup>, and thus we find the smoothed variance to be  $\sigma_8$  as

$$\sigma_8^2 = \int d \ln k \Delta_{\text{LIN}}(k) W(k 8 h^{-1} \text{Mpc}), \quad (2.91)$$

where we are explicitly using the *linear* dimensionless power spectrum.

## 2.4.2 Evolution of the matter power spectrum

Now that we have the tools to investigate the matter power spectrum, we can look at how it changes during the Universe's evolution and for different scales. Schematically, we can write the evolution of the Newtonian potential as a  $k$ -dependant transfer function  $T(k)$ , and an overall scaling/growth function  $D_+(k)$  to give [84]

$$\Phi(k, a) = \frac{3}{5} \zeta(k) \times [\text{Transfer function}(k)] \times [\text{Growth function}(a)]. \quad (2.92)$$

The transfer functions are defined to ‘transfer’ the perturbation of a given wavenumber  $k$  from an initial time  $t_i$  to a later time  $t_f$ ,

$$\Phi(t_f, k) = T(k) \Phi(t_i, k). \quad (2.93)$$

These transfer functions depend on their wavenumber compared to the wavenumber of the horizon during matter-radiation equality ( $z \sim 3400$  [93])

$$k_{\text{EQ}} \equiv (aH)|_{\text{EQ}}, \quad (2.94)$$

and thus modes smaller than this ( $k > k_{\text{EQ}}$ ) entered the horizon during radiation domination, while larger modes ( $k < k_{\text{EQ}}$ ) entered the horizon during matter domination. We have seen in Sections 2.3.2 and 2.3.3 that the matter perturbations,  $\delta_{\text{M}}$ , grow with different rates in radiation domination and matter domination, respectively. Hence, the evolution of these density perturbation modes will be determined by when that mode enters the horizon (which is in turn is determined by its wavenumber  $k$ ). Thus, different modes will have different different transfer functions.

The transfer functions can be computed, and are

$$T(k) \propto \begin{cases} 1 & k < k_{\text{EQ}}, \\ k^{-2} & k > k_{\text{EQ}}. \end{cases} \quad (2.95)$$

Recalling the definition of our primordial power spectrum, Equation 2.64, we find the linear matter power spectrum at late times to be

$$P_{\text{LIN}}(k, a) = A_{\text{s}} T^2(k) \left( \frac{k}{k_*} \right)^{n_{\text{s}}}, \quad (2.96)$$

and thus we find the overall  $k$ -scaling to be

$$P_{\text{LIN}}(k) \propto \begin{cases} k^{n_{\text{s}}} & k < k_{\text{EQ}}, \\ k^{n_{\text{s}}-4} & k > k_{\text{EQ}}. \end{cases} \quad (2.97)$$

<sup>10</sup>The value of  $R = 8 h^{-1} \text{Mpc}$  was chosen as when we look into our local Universe, the relative fluctuations of the number density of galaxies are order unity on this scale, and thus  $\sigma_8$  will be of order unity without having to do any complicated cosmology. A value of order unity is nice property for our cosmological parameter [32, 92].



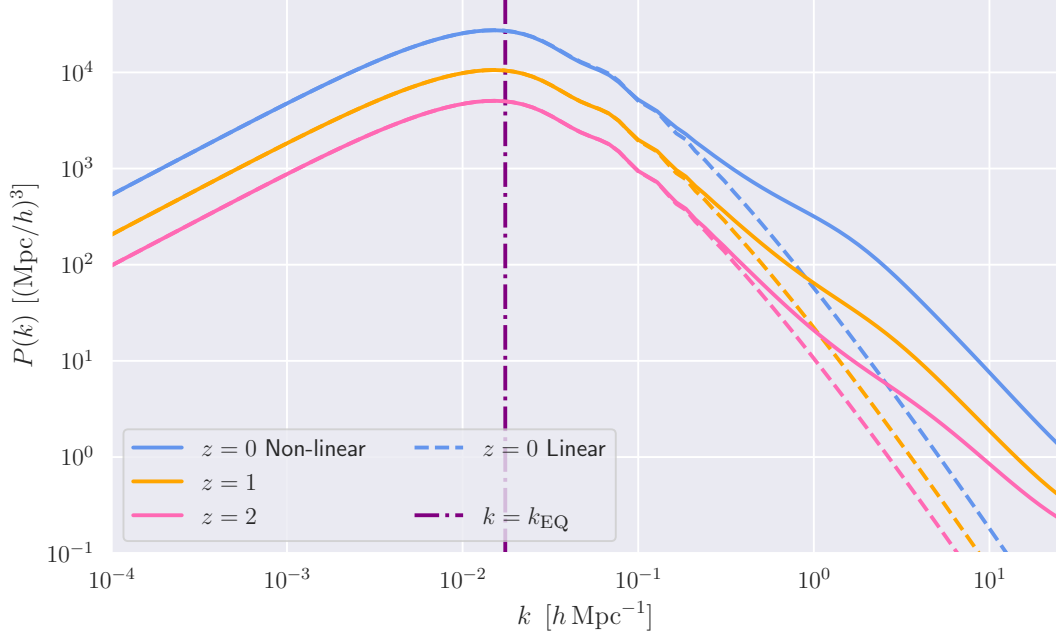


Figure 2.8: Linear and non-linear matter power spectrum evaluated at redshifts 0, 1, and 2 using CAMB [9, 10] with the approximate  $k$ -scale of matter-radiation equality ( $k_{\text{EQ}} \simeq 1.7 \times 10^{-2} h \text{ Mpc}^{-1}$ ) [95] plotted as the dashed vertical line. This shows the extremely strong break in the linear matter power spectrum around  $k_{\text{EQ}}$  as predicted from Equation 2.97, which is a direct result of how perturbations grow more slowly in radiation domination (scales smaller than  $k_{\text{EQ}}$ ) and so the growth of structure is suppressed on small scales. This also shows the small oscillations in the power spectrum around  $k \sim 10^{-1} h \text{ Mpc}^{-1}$ , which arises from the oscillations in the photonic and baryonic density perturbations prior to recombination (see Figure 2.77), and are called baryonic acoustic oscillations (BAO). We also see the significant boost in the power on small scales from non-linear effects, and thus accurate determination of the non-linear effects are crucial for the correct evaluation of  $P(k)$  at small-scales.

### 2.4.3 Non-linear evolution

So far, we have concerned ourselves with linear perturbations where they have been described using perturbation theory with linearised equations. However, this is only applicable for small fluctuations, where  $\delta \ll 1$ . Thus, when these fluctuations start to become order unity,  $\delta \sim 1$ , perturbation theory breaks down, and thus the evolution of perturbations are described by solving the fully-coupled differential equations in an expanding FRW spacetime. These calculations are extremely complex, and even non-linear perturbation theory fails to properly describe the perturbations in the densest and smallest-scales [94].

Hence, we are forced to turn to numerical methods in order to correctly determine the behaviour of the matter power spectrum on the smallest scales, the scales that hold a huge amount of cosmological information. This is because there are very many more small-scale modes than large-scales for a given volume of a cosmological survey. Hence, as the amplitude of shot noise is inversely proportional to the number of modes, the small-scale modes inherently carry more cosmological information.

The linear and non-linear matter power spectrum is plotted in Figure 2.8 which shows the clear break in the power spectrum around the  $k_{\text{EQ}}$  scale, and the effects of the non-linear effects on small-scale  $k$  modes.

## 2.5 The halo model

As we have already touched upon, non-linear perturbation theory is both extremely analytically complex and fails to describe the proper dynamics of the scales in the matter power spectrum. Thus, to accurately obtain predictions for the matter power spectrum in the non-linear regime, we turn to numerical tools as our saviour. However, these numerical  $N$ -body simulations are extremely computationally expensive to run, especially for a wide range of cosmological parameters that we want to test in our analyses of data.  $N$ -body simulations capture the non-linear gravitational clustering and dynamics of dark matter only, which can produce estimates for the non-linear matter power spectrum down to very small physical scales (large  $k$ ). From these  $N$ -body simulations, physically-motivated semi-analytic models for the non-linear spectra can be constructed, with values for free-parameters obtained by fitting the models to the  $N$ -body simulations. Using a suite of such  $N$ -body simulations allows for the comparison and benchmarking of these semi-analytic models. Note that  $N$ -body simulations produce predictions for the non-linear dark matter power spectrum only, without any baryonic feedback present.

It was suggested in Refs. [96, 97] that clustering on highly non-linear scales could be understood through assuming that regions of large overdensities undergo virialisation and detach from the expanding FRW background. This then evolved into the halo model [98–101], which models the total non-linear matter power spectrum as a sum of two components

$$P_{\text{NL}}(k) = P_{2\text{H}}(k) + P_{1\text{H}}(k), \quad (2.98)$$

where  $P_{2\text{H}}(k)$  is the two-halo term, which is a quasi-linear term that represents the power generated by the large-scale distribution of dark matter haloes throughout the universe, and  $P_{1\text{H}}(k)$  is the one-halo term which describes the power contributions from the dark matter clustering within a single halo. By choosing physically motivated functions for the one- and two-halo terms, one can fit the free parameters of the model to  $N$ -body simulations to provide accurate results for the non-linear matter power spectrum. This approach was first taken in Ref. [102] to form the **HaloFit** model, and was extended in Ref. [103] which increased the accuracy of the fitting-functions from the increase in accuracy from  $N$ -body simulations in the intervening decade. Further improvements were made in Refs. [104–106] culminating in the **HMCode-2020** software package which claims to have an RMS error of less than 2.5 % across a range of cosmologies for scales  $k < 10 \, h\text{Mpc}^{-1}$  and redshifts  $z < 2$ .

Figure 2.9 plots the total non-linear matter power spectrum along with the one- and two-halo terms. We see how the two-halo term dominates the linear spectrum, since these wavenumbers correspond to distances much greater than the size of a typical halo, whereas the one-halo term describes the non-linear dynamics of the power spectrum on the smallest scales, since these wavenumbers are probing the dynamics of individual haloes.

## 2.6 Baryon feedback in the matter power spectrum

In our solutions to the background Friedmann equations (Section 2.1.4), we had that the matter density  $\Omega_{\text{M}}$  was simply the sum of the cold dark matter density ( $\Omega_{\text{C}}$ ) and the baryonic matter density ( $\Omega_{\text{B}}$ ), since in the late-time Universe the baryonic fluid can be considered pressureless and so its dynamics are governed from gravitational attraction only. Thus, on large scales the Universe’s dynamics is driven by only the total matter density  $\Omega_{\text{M}}$ , not the individual values of  $\Omega_{\text{B}}$  and  $\Omega_{\text{C}}$ . This also holds true for the matter power spectrum, where on scales larger than  $k_{\text{EQ}}$  it is only sensitive to  $\Omega_{\text{M}}$ , whereas on smaller scales the physics of baryons becomes sufficiently different from the physics of dark matter such that the degeneracy breaks and is sensitive to both  $\Omega_{\text{B}}$  and  $\Omega_{\text{C}}$ .

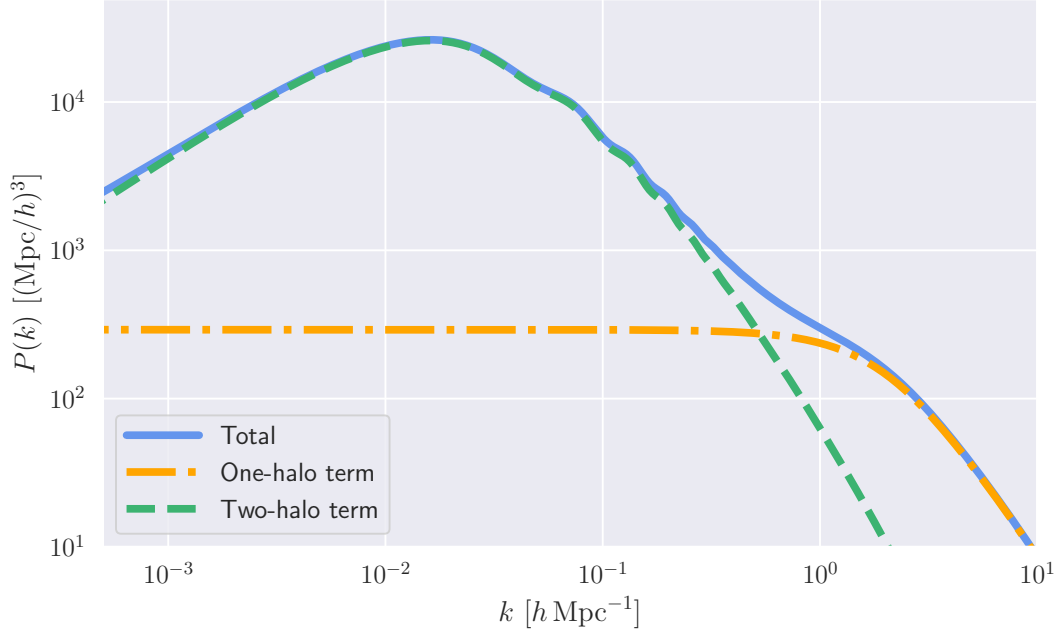


Figure 2.9: Total matter power spectrum with the one- and two-halo terms from the halo model computed at redshift  $z = 0$  using `PyHaloModel` [101]. This shows that the two-halo term dominates the linear power spectrum, with the one-halo term dominating the non-linear dynamics.

We have already seen the first of these different physical processes: during the radiation dominated era, the baryonic matter was coupled to the radiation and thus supported from gravitational collapse through radiation pressure. However, the dark matter has no such coupling to the radiation, and thus it is free to condense into gravitational potentials, growing them further. Thus, in a universe with more dark matter, its gravitational potentials can grow much faster in the primeval universe than one with more baryonic matter. This produces an increased amplitude in the matter power spectrum on scales smaller than  $k_{\text{EQ}}$ .

Baryons have many other ways in which they can affect the matter power spectrum on small scales, which we describe below.

### 2.6.1 Supermassive black holes and active galactic nuclei

In order to explain supermassive black holes, let us first take a detour to explain ‘ordinary’ stellar black holes<sup>11</sup>. These are formed by the gravitational collapse of a dying star, when the gravitational pull of its matter is greater than what the repulsive force of the Pauli exclusion principle can even provide, thus collapsing the star to a single point in spacetime [110]. While, in theory, general relativity does not place any constraints on the masses of black holes, since stellar remanent black holes are the result of the collapse of a dying star, their masses are restricted to those above the Chandrasekhar limit (about  $1.4 M_{\odot}$ ) up to the mass limit for which stars can form (which is of the order  $100 M_{\odot}$  [111]). Gravitational wave signals from inspiralling black hole binaries have been confirmed by the LIGO and Virgo detectors [112, 113], confirming the GR prediction of both the existence of black holes and the propagation of gravitational waves.

<sup>11</sup>Given the nature of black holes, with how they represent an unphysical singularity within the laws of general relativity, there is nothing ordinary about any type of black hole.



Figure 2.10: Image of the Milky Way’s central supermassive black hole Sagittarius A\* with magnetic field lines overlaid, taken by the Event Horizon Telescope collaboration released in 2024 [107, 108]. Sgr A\* was discovered in 1974 by Balick and Brown [109], with the 2020 Nobel physics prize being awarded to Genzel and Ghez for showing that it was a single compact object.

Supermassive black holes are extraordinarily massive black holes which can be found in the centre of galaxies, with typical masses of millions to billions of solar masses. The black hole at the centre of our galaxy, Sagittarius A\*, has an estimated mass of  $4.2 \times 10^6 M_\odot$  [114], with the one at the centre of Messier 87 having a mass of approximately  $6.5 \times 10^9 M_\odot$  [115]. Both of these supermassive black holes have been imaged by the Event Horizon Telescope collaboration, with Figure 2.10 showing an image of Sagittarius A\* with polarisation field lines overlaid. What we see here is the electromagnetic radiation emitted from the accretion disk that surrounds the supermassive black hole. The formation of these supermassive black holes are not yet completely understood. Observations of quasars with masses around  $10^{10} M_\odot$  at redshift  $z \sim 6$  (when the universe was less than 1 Gyr old) presents a challenging puzzle for how these objects grew so large so quickly [116].

New observations from the James Webb Space Telescope (JWST) further strengthen our understanding that supermassive black holes formed during the primeval universe ( $z > 6$  [117]), at which point the Universe was only 800 million years old [118]. Spectroscopic observations from JWST have confirmed the presence of such a supermassive black hole at  $z = 7.0848$  having mass  $M = (1.52 \pm 0.17) \times 10^9 M_\odot$ , estimated from observations of the  $H\alpha$  emission line [118], and eight objects at redshift  $z > 6.5$  with masses  $M \sim 10^9 M_\odot$  using  $H\beta$  and [Fe II] emission lines [119]. As JWST continues to perform exquisite observations of the primeval universe, it will undoubtedly find more high-redshift objects which challenge our theoretical understanding of how these objects got so massive so quickly.

The accretion of the surrounding interstellar gas onto the supermassive black hole causes the matter to emit huge amounts of energy across the entire electromagnetic spectrum, from radio to  $\gamma$ -rays [120]. These powerful emissions from the galactic centre are called active galactic nuclei (AGN, plural AGNi [121]). These emissions energises the in-

terstellar medium, having the effect of moving baryons from high-density to lower-density regions [122]. Additionally, the supermassive black hole may power two perpendicular, highly columnated jets of relativistic matter which spew forth into the interstellar medium, further displacing the baryons out to very large distances [123].

We have detected the presence of such thermal and jet emission from AGN through high-resolution X-ray observations of galaxy clusters [124]. These observations have revealed the existence of giant cavities within clusters, which disrupts the ordinary gravitational collapse of gas, and thus suppressing or even terminating star formation and the growth of luminous galaxies [125]. AGN feedback is also essential for reproducing the observed stellar luminosity function. In particular, we observe a sharp decrement in the luminosity function of massive galaxies which can only be reproduced through the inclusion of gas heating from AGN feedback in our theoretical models [126].

Additionally, measurements of the thermal Sunyaev-Zeldovich effect of the cosmic microwave background allows the probing of the thermodynamics of hot gas in massive galaxies, galaxy groups and clusters [127]. This allows us to probe the physics of AGN feedback, and the comparison of observational data to simulated models [128, 129].

## 2.6.2 Supernovae

The baryons in galaxies can condense under gravity to form stars, some of which undergo violent supernova explosions at the end of their life. These explosions expel huge amounts of matter at extremely high velocities into the interstellar medium, further disrupting its original structure. Supernovae are also major sources of heavy elements, which alters the chemical composition of the interstellar medium, which changes the physics of baryonic cooling [130]. Supernovae can also trigger star formation via compression of the interstellar medium from their shock waves, thus increasing clustering on very small scales [131].

Supernovae feedback can particularly affect small, or dwarf, galaxies by driving out large quantities of interstellar gas from these dwarf galaxies. This dramatically quenches their star formation rates [132, 133], with JWST again providing recent high-quality data on these low-mass quiescent galaxies [134].

## 2.6.3 Modelling baryon feedback

As we have seen, baryonic physics can have an extremely large effect on the matter distribution within the interstellar medium, and thus a strong effect on the matter power spectrum. Since the evaluation of the matter power spectrum is crucial for many cosmological analyses, the accurate determination of baryonic effects within it is essential to ensure unbiased cosmological constraints [123]. While pure analytic models, in the form of a Taylor expansion in powers of  $k$ , have been attempted [130], more accurate methods in the form of semi-analytic models have had more success in matching results from fully hydrodynamical simulations (hydro-sims). These hydro-sims are much more complex than  $N$ -body simulations, since they aim to implement full prescriptions for baryonic feedback, such as AGN and supernovae feedback, radiative heating and cooling, chemical processes in the intergalactic and interstellar mediums, and galaxy formation, in addition to the usual gravitational dynamics [135].

Such semi-analytic model including baryonic feedback is **HMCode-2020** [106], which can either have one or three physical parameters that quantify the strength and effect of baryonic feedback. The underlying halo model is modified to change the halo concentration ( $B$ ) and gas content ( $M_b$ ) of haloes, which accounts for how mass is removed from halo centres due to feedback, and the inclusion of a central mass term ( $f_\star$ ) which corresponds to the presence of stars in the centres of haloes [106]. Figure 2.11 plots the ratio of the

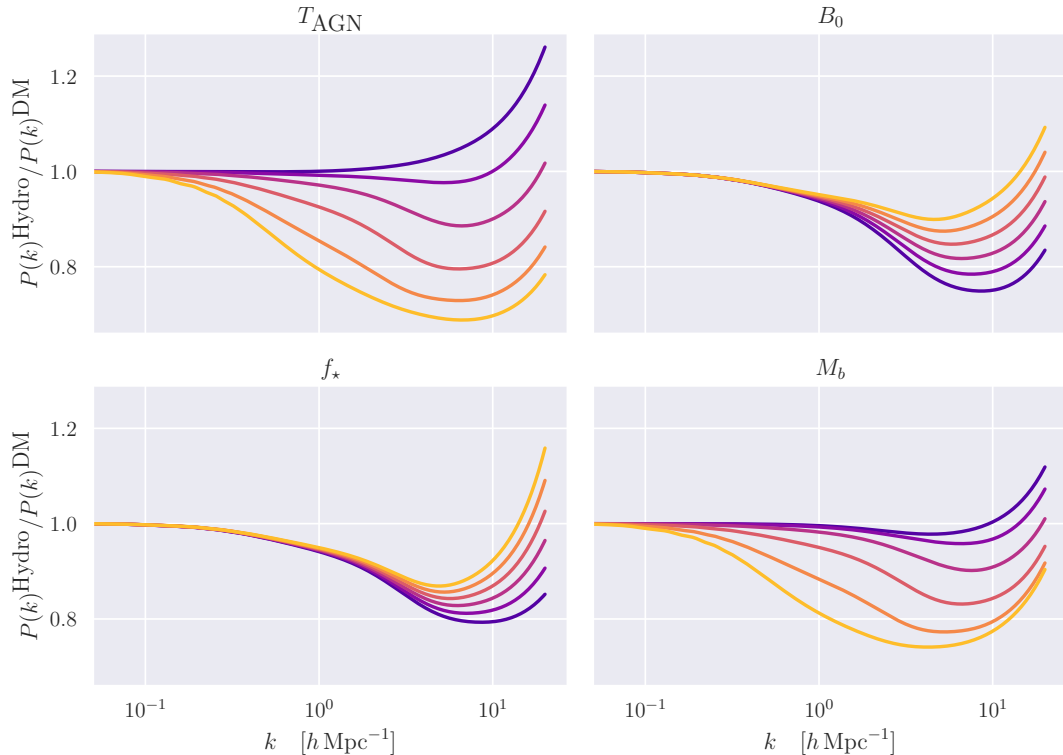


Figure 2.11: Ratios of matter power spectra for models with baryon feedback to no feedback at redshift  $z = 0$  when varying feedback parameters (with smaller values in blue and larger values in yellow for each parameter). We see that in the single-parameter model,  $T_{\text{AGN}}$  both the amplitude of the suppression and the scale at which the suppression starts to take place (with larger values shifting to larger scales). In the three-parameter model, we see that  $B_0$ , which is the halo concentration parameter, mainly changes the depth of the suppression, with smaller values leading to more suppression since more gas has been expelled from haloes.  $f_*$  accounts for the presence of stars within haloes, and thus we see larger values corresponds to an increase in power on very small scales.  $M_b$  controls the break-scale which modifies the Navarro-Frenk-White (NFW) window function [136] to account for gas expulsion from the halo, and changes both the amplitude and starting scale of the suppression. Note that we start plotting the ratios from  $k \sim 10^{-1} h\text{Mpc}^{-1}$ , and so the linear spectrum down to  $k \sim 10^{-4} h\text{Mpc}^{-1}$  is unaffected by baryonic feedback.

matter power spectrum with baryonic feedback to that of dark matter only clustering for a range of different values for each HMCode-2020 astrophysical parameter, at redshift zero.

## 2.7 Probes of the large-scale structure

Thus far, we have built up a physical picture of how quantum fluctuations generated in the inflationary universe seeded slight regions of under- and over-densities right at the beginning of our Universe. These perturbations then grow in an expanding radiation-, matter-, and then a cosmological constant-dominated universe where the perturbation dynamics are governed by the dominating fluid. Thus, by probing the large-scale structure throughout the Universe’s history, we can constrain the physics and contents of our Universe. Since different probes are sensitive to different types of physics, we find that our overall picture of the universe today is formed from the combination of many individual probes<sup>12</sup>, many of which we will describe here.

<sup>12</sup> *What? No, not the mind probe.*



### 2.7.1 Supernovae and the distance-redshift relation

As described above in Section 2.6.2, supernovae explosions can occur at the end of a massive star's life and emit enormous amounts of electromagnetic radiation, often outshining their entire host galaxy. Since they are only observable for a short period of time, they are classified as transient objects. Despite the low chance of any star undergoing a supernova explosion, we are now observing upwards of ten supernovae per day [137]. Due to their extreme brightness, supernovae have been observed as far back as 185 A.D. [138]. There exists many different classes of supernova explosions, of which the 'Type Ia', which originate from the thermonuclear explosions of white dwarfs, are most applicable to cosmological analyses. This is because their explosions can be thought of as a 'standardisable candle', and thus their absolute magnitude is approximately the same between all supernovae Ia explosions – up to empirical corrections [139]. This makes them prime candidates to test the distance-redshift relation, which constrains the present-day energy densities and Hubble expansion rate [137].

In the low redshift limit, Hubble's law of the expanding universe can be written as<sup>13</sup>

$$v = H_0 d, \quad (2.99)$$

where  $H_0$  is the present expansion rate. Transforming this to a source's redshift, we find Hubble's law to be

$$z = H_0 d. \quad (2.100)$$

Thus, a measurement of both the redshift and distance to supernovae will allow the constraint on the Hubble rate, though this approximation only holds for low redshift sources.

For sources at larger redshifts ( $z \gtrsim 0.1$ ), we turn to the full distance-redshift relation for the luminosity distance of Equation 2.45. Specialising for a flat universe consisting of matter and a cosmological constant only (a suitable approximation for any late-universe study, since any contributions from radiation and relativistic particles have long since been redshifted away), we find the luminosity distance to be

$$d_L(z) = \frac{1+z}{H_0} \int_0^z \frac{dz'}{\sqrt{\Omega_M(1+z')^3 + \Omega_\Lambda}}. \quad (2.101)$$

If one is able to measure the apparent magnitude  $m$  of a source, one can define the *distance modulus*  $\mu$  of a source as  $m - M$ , where  $M$  is its absolute magnitude. It is given in terms of the logarithm of the luminosity distance as

$$\mu = 5 \log_{10} \left[ \frac{d_L(z)}{1 \text{ Mpc}} \right] + 25. \quad (2.102)$$

Thus, by making measurements of the distance modulus and redshift of many sources, one can constrain the evolution of the Hubble parameter – both determining the value of  $H_0$  and the density parameters  $\Omega_i$ . Such example is in Figure 2.12, which clearly shows that supernovae data supports  $\Omega_\Lambda \neq 0$ .

---

<sup>13</sup>If my calculations are correct, when an object hits 560 parsecs away, you're gonna see some serious shit.  
— Dr Emmett Brown (probably).

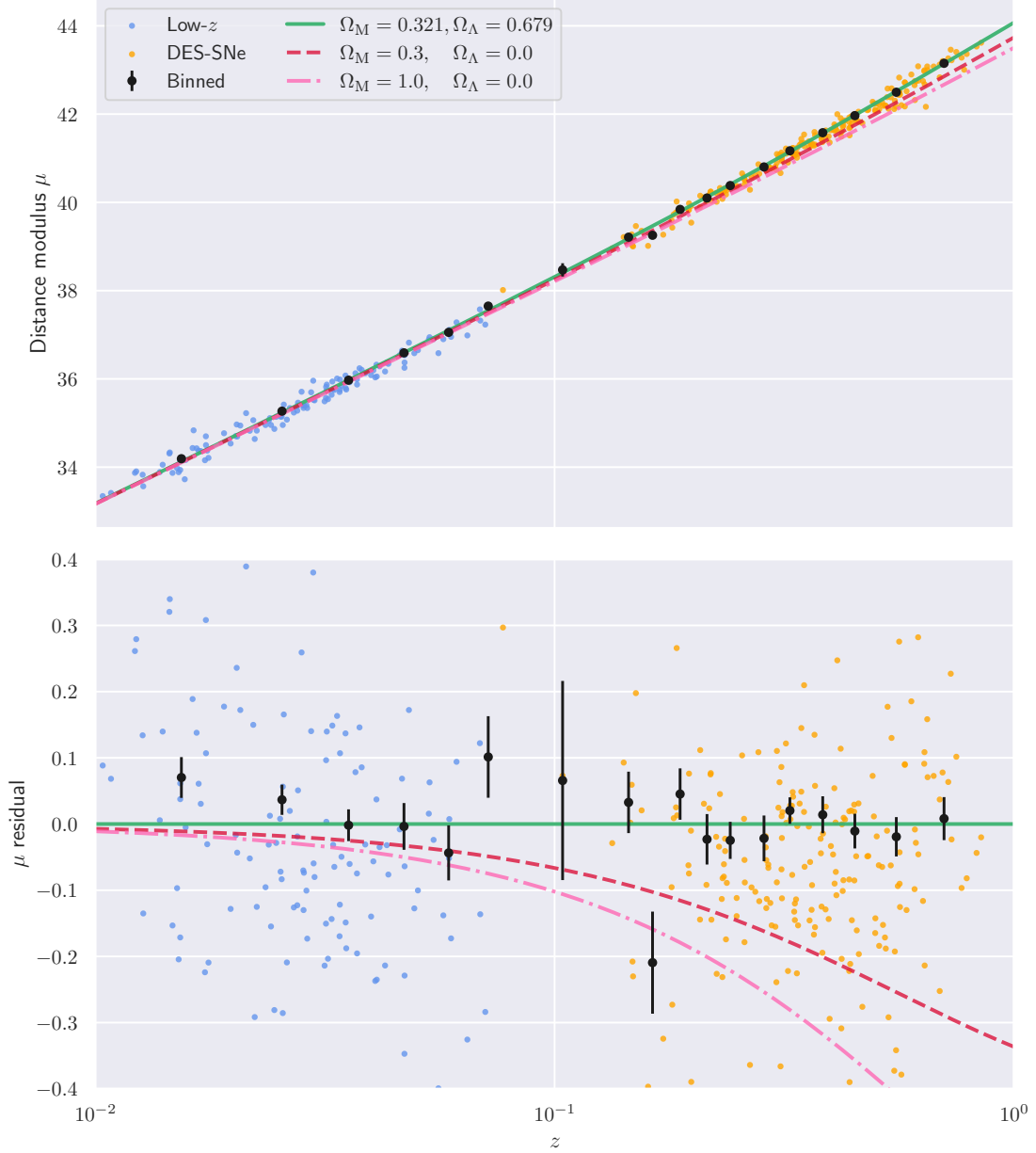


Figure 2.12: Hubble diagram created using high-redshift supernovae data from the Dark Energy Survey (DES) [140, 141] and low-redshift supernovae from the Harvard-Smithsonian Center for Astrophysics surveys [142, 143] and Carnegie Supernova Project [144, 145]. We plot the distance modulus to redshift relation for the observed Type Ia supernovae, along with binned data-points. Plotted in the solid, dotted, and dashed-dotted lines are predictions for this relation for three different cosmologies – where the solid green line represents the best-fit cosmology from the data. These results are consistent with first precision observations of supernovae from the late 1990s [38], showing that we live in a universe with a non-zero cosmological constant  $\Omega_\Lambda \neq 0$ , which was a major advancement in observational cosmology.



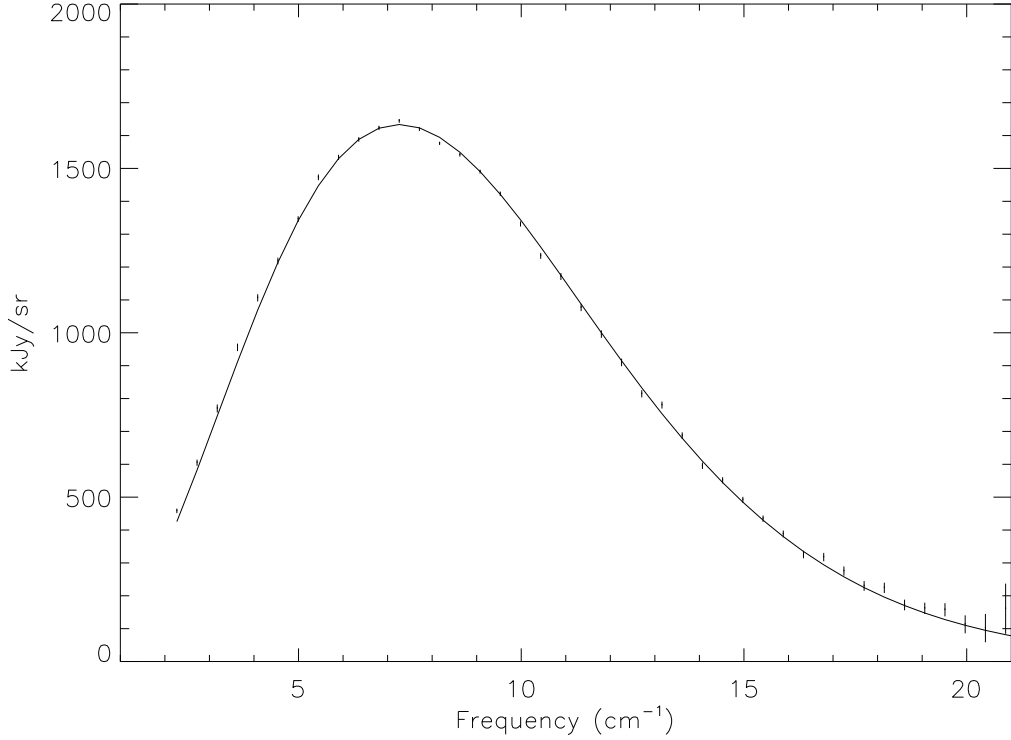


Figure 2.13: Plot of the CMB black-body spectrum, as measured by the *FIRAS* experiment on the *COBE* satellite. Here, the points represent the observed values, and the line is a fitted black-body spectrum. We see that the black-body spectrum is an excellent fit to the data, providing one of the best-fits in all of cosmology and a core proponent of the hot Big Bang model. Plot taken from Ref. [146].

## 2.7.2 The cosmic microwave background

The cosmic microwave background (CMB) is another hugely powerful probe of the large-scale structure of our Universe. It has been measured by very many experiments over many decades, starting with the initial detection by Penzias & Wilson in 1965 [147]. They were trying to measure the radio emission of our galaxy, the Milky Way. However, what they found was a persistent signal was present no matter where they pointed their radio telescope and did not depend on the days or the seasons. They initially believed that this low-level signal was the result of a pair of pigeons making the 6-metre reflector their home, leaving the reflector coated in “a white dielectric material” [25]. After thorough checks of their experiment, they concluded that their radio signal, which they estimated to be between 2.5 K and 4.5 K, was of extragalactic origin. These observations were accompanied by theoretical predictions that such microwave spectra should exist in our Universe today, if the early Universe was hot and filled with radiation [60]. These observations and accompanying theoretical derivations started the era of cosmic microwave background cosmology, and has evolved to be one of the most precise measurements in all of cosmology.

The first accurate, all-sky CMB survey was performed by NASA’s *Cosmic Background Explorer (COBE)* satellite. Figure 2.13 shows the spectrum of the CMB as measured by its *FIRAS* (Far InfraRed Absolute Spectrophotometer) instrument with a black-body spectrum at  $T = 2.728$  K plotted on top. This shows that the CMB follows an almost exact black-body spectrum, which is the equilibrium distribution for photons of frequency  $\nu$  at temperature  $T$  of

$$f_{\gamma}(\nu) = \frac{2}{(2\pi)^3} \frac{1}{\exp(\nu/T) - 1}, \quad (2.103)$$

where the factor of two arises from the two polarisation states for photons. Thus, the energy density distribution for photons following a black-body distribution is given as

$$\epsilon_\gamma(\nu) = \frac{8\pi \nu^3}{\exp(\nu/T) - 1}. \quad (2.104)$$

Since we observe the CMB to be an almost perfect black-body today, we can ‘rewind’ the universe backwards to find out the properties of the CMB at much earlier times. As photons get redshifted due to the expansion of the universe, we find  $\nu \propto 1/a$ . Thus, the CMB at earlier times will still be a black-body spectrum, but one with a shifted temperature of

$$T(z) = (1+z)T_0, \quad (2.105)$$

where  $T_0$  is the temperature of the CMB observed today.

## Anisotropies in the CMB

While the initial studies of the CMB confirmed the existence of the CMB and that it followed a black-body spectrum, which is an extremely useful probe of the thermal history of the Universe, the study of the background alone cannot help us in understanding the origin and evolution of perturbations in the Universe that we see today in galaxies and superclusters. To investigate these perturbations, we turn to the *anisotropies* in the CMB, which are the small deviations from the average temperature over a specific patch of sky.

In the early universe, photons were in thermal equilibrium with the matter, and thus the study of anisotropies in the CMB will allow us to probe the inhomogeneities in the matter density field. The all-sky study of these CMB anisotropies were initially led by the Wilkinson Microwave Anisotropy Probe (*WMAP*), and then followed up by the *Planck* satellite, as shown in Figure 2.14. Since the temperature anisotropies are expected to closely follow a Gaussian distribution (stemming from how the curvature perturbations from inflation should be largely Gaussian), the first non-zero statistical tool for studying the anisotropies is the two-point function.

## Cosmology on the sphere

Since we observe the CMB anisotropies as a function of angular direction only, as we can assume that all photons originate from the surface of last-scattering, we can treat the anisotropies as a function of angular size on a 2D sphere instead of physical wavenumber size, as was done for the inflationary perturbations. Thus, we can perform an expansion in terms of spherical harmonics  $Y_{\ell m}$ , which satisfy the eigenvalue equation for the two-dimensional Laplacian of

$$r^2 \vec{\nabla}^2 Y_{\ell m} = -\ell(\ell+1)Y_{\ell m}. \quad (2.106)$$

Thus, we can expand the temperature anisotropy at a specific angular point,  $\Delta T(\hat{n})$ , defined as  $\Delta T(\hat{n}) \equiv T(\hat{n}) - \langle T \rangle$  where  $\langle T \rangle$  is the average CMB temperature, as [153]

$$\Delta T(\hat{n}) = \sum_{\ell=0}^{\infty} \sum_{m=-\ell}^{\ell} a_{\ell m} Y_{\ell m}(\hat{n}), \quad (2.107)$$

where  $a_{\ell m}$  are the expansion coefficients and  $\hat{n}$  is the unit vector on the sky. The  $a_{\ell m}$ ’s can be found by inverting the above equation, and using the orthonormality of the spherical harmonics, to obtain

$$a_{\ell m} = \int d\Omega(\hat{n}) \Delta T(\hat{n}) Y_{\ell m}^*(\hat{n}), \quad (2.108)$$

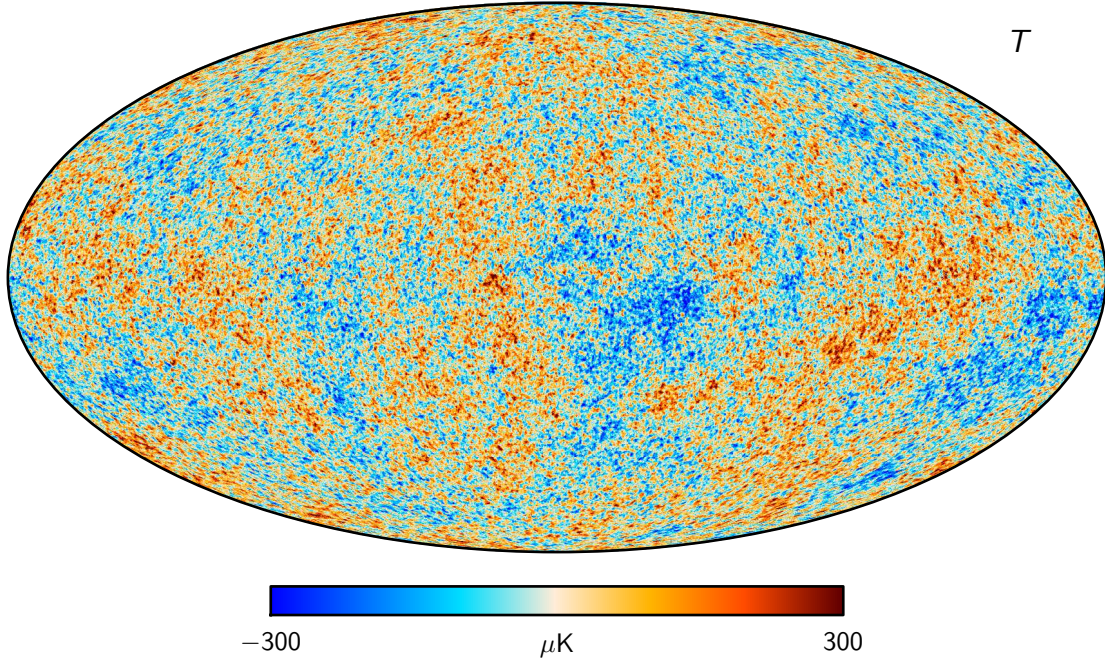


Figure 2.14: Map of the CMB temperature anisotropies, as measured by the *Planck* satellite and taken from their 2018 data release [148]. Here, we see the exquisite precision to which *Planck* observed the CMB over its five-year lifetime. Thus, *Planck* has provided some of the most stringent tests of the general relativity,  $\Lambda$ CDM, and hot Big Bang model yet. The quality of the data is such that *Planck* has almost saturated the information content from the primary temperature anisotropies, and so future CMB experiments, such as the Simons Observatory [149, 150] and CMB-S4 [151, 152], aim to measure the polarisation of the CMB to unprecedented accuracy.

where  $d\Omega$  is the area element on a 2-sphere. The  $\ell$  index determines the angular size of the anisotropy on the sky, where small  $\ell$  corresponds to large angular scales, and vice versa. The  $\ell = 0$  term corresponds to the monopole which, for a correctly normalised  $\Delta T$ , should be zero. The  $\ell = 1$  term is the dipole, of which the primary contribution is due to the Earth's motion. Therefore,  $\ell \geq 2$  modes give us information about the intrinsic CMB anisotropies.

Invariance under rotations impose that  $\langle a_{\ell m} \rangle = 0$ , and also leads to the two-point function of the  $a_{\ell m}$  to be given as

$$\langle a_{\ell m} a_{\ell' m'}^* \rangle = \delta_{\ell\ell'} \delta_{mm'} C_\ell, \quad (2.109)$$

where  $C_\ell$  is the power spectrum of the CMB anisotropies.

### Relating the CMB to inflation

Since we can make accurate measurements of the anisotropies in the cosmic microwave background, we want to form a theoretical prescription for the angular power spectrum, such that it can be predicted from a theory of cosmology. Using Equations 2.108 and 2.109, we find the angular power spectrum as

$$C_\ell = 4\pi \int d \ln k \, T_\ell^2(k) \mathcal{P}_\zeta(k), \quad (2.110)$$

where  $T_\ell(k)$  are the CMB transfer functions and  $\mathcal{P}_\zeta$  is the dimensionless inflationary power spectrum (Equation 2.63).

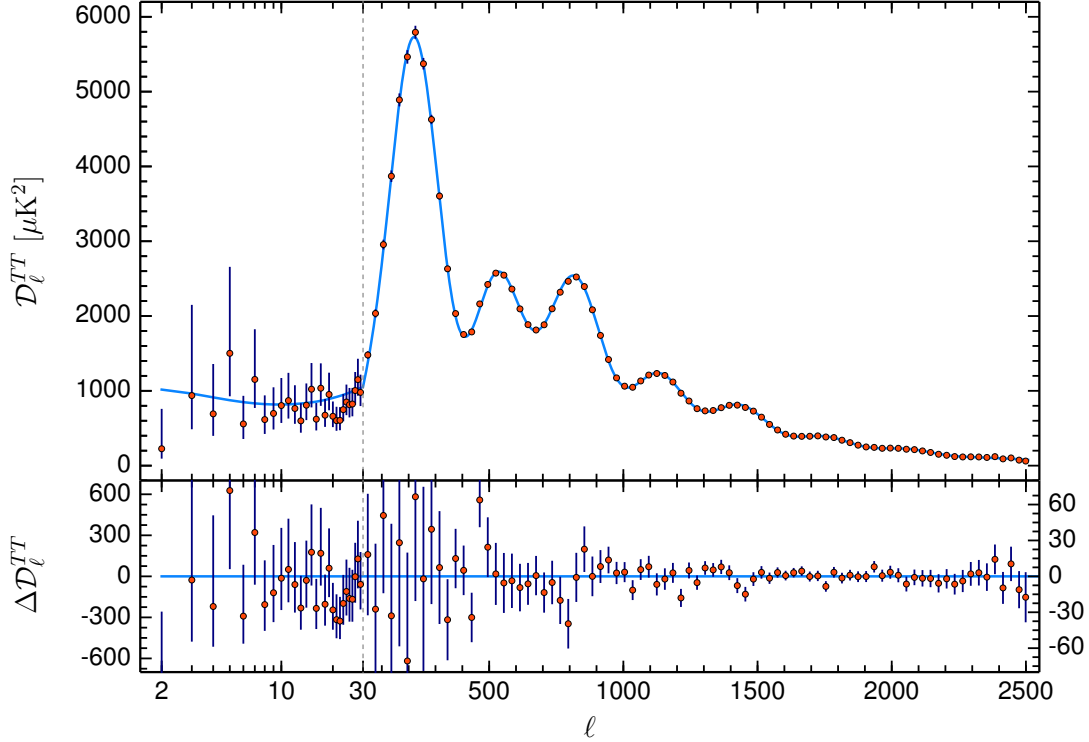


Figure 2.15: The measured CMB temperature power spectrum performed by the *Planck* satellite, taken from their 2018 data release [40]. The red dots are the measured values, with  $\pm 1\sigma$  errors, and the blue curve is the best-fit for the  $\Lambda\text{CDM}$  model. This demonstrates the remarkable success of the  $\Lambda\text{CDM}$  model in describing our Universe using just six free parameters:  $\Omega_{\text{B}}$ ,  $\Omega_{\text{C}}$ ,  $H_0$ ,  $A_{\text{s}}$ ,  $n_{\text{s}}$ , and  $\tau$ . The *Planck* results are a real triumph of both observational and theoretical cosmology since they produce such amazing agreement over across all scales. Note that what is plotted is  $D_\ell \equiv \ell(\ell + 1) C_\ell / 2\pi$ .

We can now investigate the nature of the theoretical CMB power spectrum to see if we can gain any physical intuition about either the properties or physics of our Universe which can then be matched to observational data.

### The Sachs-Wolfe effect

If we consider very large angular scales, then the CMB anisotropies are determined by large-scale modes that have entered the horizon very recently. This provides a great way of directly measuring the initial conditions from the CMB [84]. This is because the large-scale modes have only just undergone sub-horizon evolution, and so are mostly fixed to when they left the horizon during inflation. In this large-scale limit, the transfer functions reduce to  $-\frac{1}{5}j_\ell(k\eta_*)$ , where  $j_\ell$  are the spherical Bessel functions, and  $\eta_*$  is the comoving distance to recombination. Thus, we find that the CMB anisotropies on the largest-scales reduce to a simple form, which, for a scale-invariant primordial power spectrum of  $n_{\text{s}} = 1$ , is approximately

$$\frac{\ell(\ell + 1)}{2\pi} C_\ell \simeq \frac{A_{\text{s}}}{25}, \quad (2.111)$$

where  $A_{\text{s}}$  was the amplitude of the primordial power spectrum. This holds for angular scales  $\ell \lesssim 40$  [69] and can be verified by comparing to Figure 2.15 which measured a roughly constant Sachs-Wolfe plateau from which we can read off a value of  $D_\ell \sim 1000 \mu\text{K}^2$ , yielding a value of  $A_{\text{s}} \sim 3 \times 10^{-9}$ , correct to within a factor of two.

### Acoustic peaks

Looking at the CMB temperature power spectrum of Figure 2.15, it is clear that there are several strong peaks in the power spectrum. These are called the acoustic peaks and arise from the photon-baryon interactions in the early Universe, which we discussed in Section 2.3.6. Prior to photon decoupling, the photon-baryon fluid energy density was only about forty percent of the dark matter energy density [69]. Thus, the dynamics of the photon-baryon fluid are mostly dominated by gravitational interactions of the dark matter. This dark matter, interacting only gravitationally, is free to clump together and form deep potential wells in the matter-dominated era, with growth suppressed in the radiation-dominated era. The photon-baryon fluid will then try to condense within these potential wells, increasing its pressure as it is compressed by gravity. This self-interaction pressure eventually grows to a point where it is greater than the gravitational attraction, and so causes the photon-baryon fluid to expand outwards. As the fluid expands, the self-interaction pressure decreases until it starts to fall back into the potential wells. The cycle of infalling and expulsion is called acoustic oscillations and are what cause the acoustic peaks in the CMB power spectrum.

The primary acoustic peak occurs at around  $\ell \simeq 220$  [69] and corresponds to potential wells where the photon-baryon fluid reached maximum compression at the time of decoupling. The subsequent peaks represent integer multiples of the compression peaks for the photon-baryon fluid.

Since the location of these acoustic peaks in multipole-space strongly depend on the angular diameter distance to the surface of last scattering, which in-turn depends on the spatial curvature of the Universe, measurements of the acoustic peaks provide strong constraints on the curvature of our Universe.

Additionally, measurements of the relative amplitudes of the acoustic peaks provide strong constraints on the ‘physical’ baryon density,  $\Omega_{\text{B}} h^2$ .

### 2.7.3 Baryonic acoustic oscillations

As we have seen in the cosmic microwave background above, the acoustic oscillations in the photon-baryon fluid causes detectable acoustic peaks in the photon temperature anisotropies. These oscillations also perturb the baryonic density distribution, resulting in the creation of baryon acoustic oscillations (BAO). The primary peak in the baryon fluid can be translated from the angular scale used in the CMB to a comoving distance at the redshift of last-scattering, which gives the acoustic scale of around  $r_{\text{BAO}} \approx 100 \text{ Mpc}/h$  [69].

To see if we can detect this peak in the baryonic fluid, we can measure the correlation function of galaxies,  $\xi(r)$ . If you chose any random galaxy, the correlation function quantifies, on average, how many galaxies are likely to be found at a comoving distance  $r$  away from it. Thus, if these baryonic acoustic oscillations caused an increase in the baryonic density on the  $r_{\text{BAO}}$  scale, then we would find a small increase in the galaxy density correlation function around the BAO scale,  $r_{\text{BAO}}$ .

This increase in the correlation function is exactly what has been measured by various galaxy surveys, such as the *Baryon Oscillation Spectroscopic Survey* (BOSS) from the Sloan Digital Sky Survey (SDSS), and in the *Dark Energy Spectroscopic Instrument* (DESI) data release one, as plotted in Figure 2.16. Since this BAO scale acts as a ‘standard ruler’, measuring its location provides very tight constraints on the evolution of the angular diameter distance, and thus on the geometry of the universe.



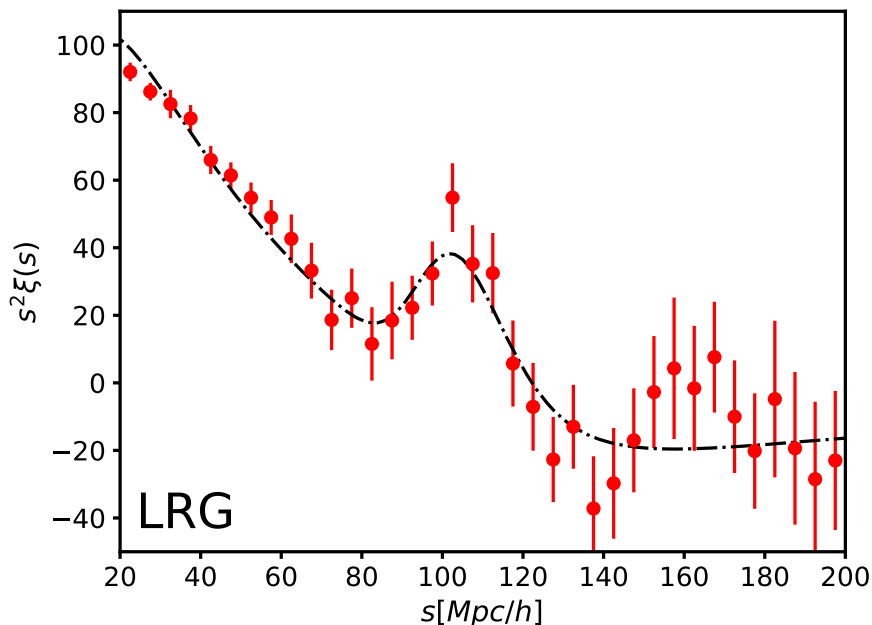


Figure 2.16: Measurements of the BAO signal from the DESI early data release one [154]. This shows a strong and significant increase in the clustering of galaxies around the 100 Mpc/h scale, which is in perfect agreement with the theory (the dashed black line).

### 2.7.4 Why use different probes?

It is a natural question to ask why do we have so many different independent probes of the structure and properties of our Universe? Wouldn't a single, high-quality survey provide us with all the information that we could possibly want about our Universe? To answer this, we must consider that each cosmological survey that we have discussed (along with many others) probe slightly different physical processes within our Universe, and at different times within its evolution. Thus, we find that different probes have different degeneracy directions between cosmological parameters. For example, the amplitude of the high- $\ell$  CMB power spectra constrains the combination of  $A_s e^{-2\tau}$ , thus having a significant degeneracy between the amplitude  $A_s$  and the optical depth  $\tau$ . Similarly, there is a degeneracy between the value of  $H_0$  and the absolute magnitude  $M$  when analysing supernovae data. Furthermore, measurements of BAO alone are only able to measure  $\Omega_M$  and  $H_0 r_d$ <sup>14</sup>, and thus information from Big Bang nucleosynthesis is needed to provide constraints on the physical baryon density  $\Omega_B h^2$ , and thus break the degeneracy between  $H_0$  and  $r_d$ .

Thus, by using and combining different probes of our Universe, we extract much more information about the physics and properties of our Universe than any single experiment can.

<sup>14</sup> $r_d$  is the distance travelled by sound waves between the end of inflation and the decoupling of baryons from photons after recombination.

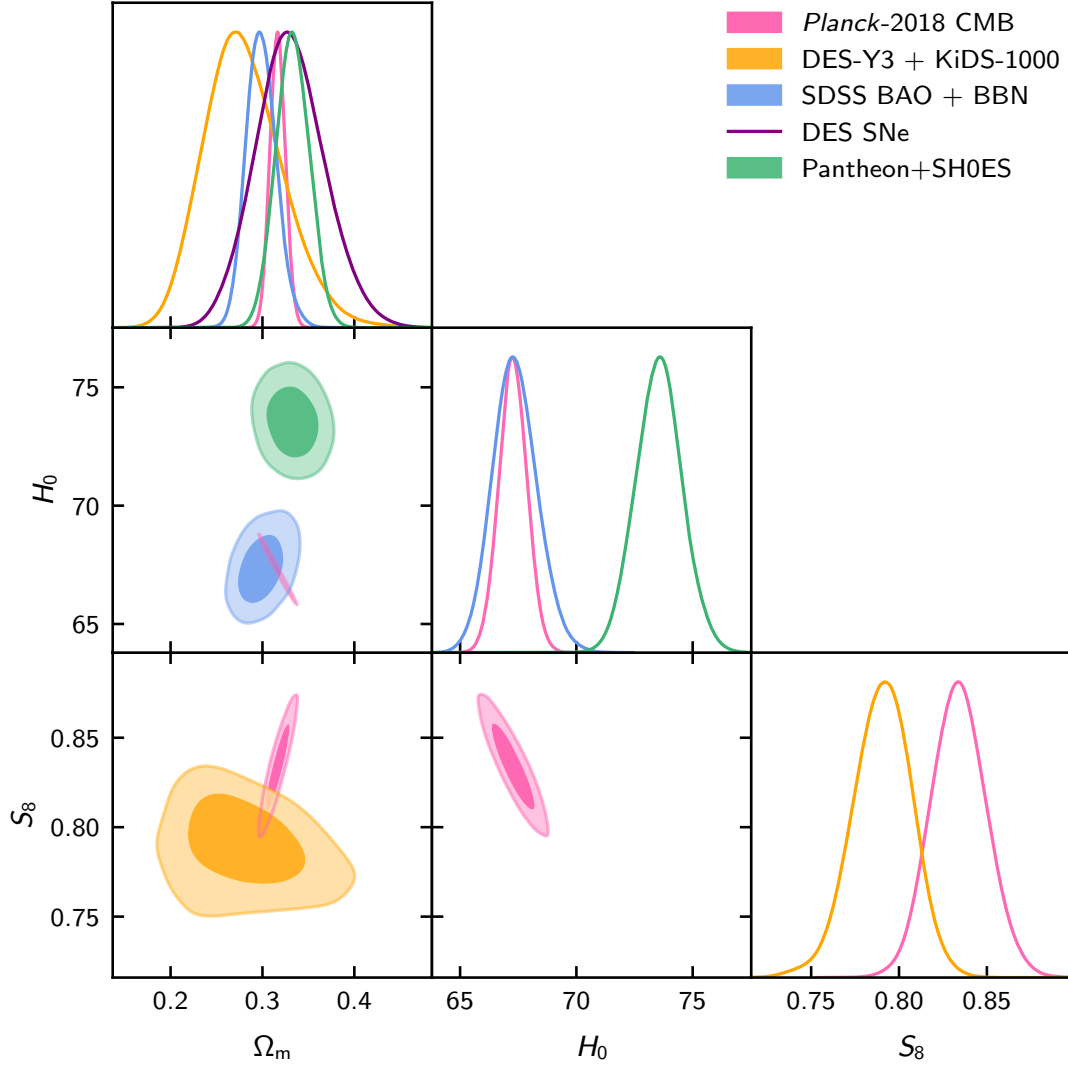


Figure 2.17: Triangle plot showing the results for three key cosmological parameters (the overall matter density today  $\Omega_m$ , the Hubble parameter today  $H_0$  [in units of  $\text{km/s Mpc}^{-1}$ ] and the clustering of matter  $S_8$ ) that are well-measured by a variety of experimental probes. We see that since each probe measures a different physical process within our Universe, this leads to different degeneracy directions within the parameter-space. We also see that some probes show non-overlapping contours for certain cosmological parameters...

*Science knows it doesn't know everything,  
otherwise it'd stop.*

—Dara Ó Briain

# 3

## Gravitational lensing analysis

**Outline.** In this chapter, I review the basic formalism and derive the gravitational lensing effect from general relativity. I then go on to explain how gravitational lensing can be used in an analysis to constrain the properties and content of our Universe.

### 3.1 Gravitational lensing from a point-mass

Since we wish to gain a physical understanding of the gravitational lensing phenomena, we can start with the simplest example in general relativity: a light-ray being deflected by a point mass  $M$  surrounded by empty space. For this case, the spacetime metric is the Schwarzschild geometry (Equation 2.7), which we had as

$$ds^2 = \left(1 - \frac{2GM}{r}\right) dt^2 - \left(1 - \frac{2GM}{r}\right)^{-1} dr^2 - r^2 [d\vartheta^2 + \sin^2 \vartheta d\phi^2]. \quad (3.1)$$

To solve for how light propagates through this spacetime, we need to solve the GR equivalent of Newton's second law of classical mechanics ( $F = ma$ ), which is the geodesic equation. This can be written as

$$\frac{d^2 x^a}{d\lambda^2} + \Gamma_{bc}^a \frac{dx^b}{d\lambda} \frac{dx^c}{d\lambda} = 0, \quad (3.2)$$

where  $\lambda$  is an affine parameter used to parametrise the particle's path, and  $\Gamma_{bc}^a$  are the Christoffel symbols, which can be computed from the metric through

$$\Gamma_{bc}^a = \frac{1}{2} g^{ad} [\partial_b g_{dc} + \partial_c g_{bd} - \partial_d g_{bc}]. \quad (3.3)$$

This is quite an involved approach, and thus to gain additional physical insight into the process of gravitational lensing, we can instead consider the use of calculus of variations.

#### 3.1.1 Lagrangians

The fundamental quantity when using the calculus of variations is the Lagrangian  $\mathcal{L}$ , which is defined as

$$\mathcal{L}(x^a, \dot{x}^a, \lambda) = g_{ab} \dot{x}^a \dot{x}^b, \quad (3.4)$$



where

$$\dot{x}^a \equiv \frac{dx^a}{d\lambda}. \quad (3.5)$$

Since we have a diagonal metric, computing our Lagrangian is straightforward, giving

$$\mathcal{L} = \left(1 - \frac{2GM}{r}\right) \dot{t}^2 - \left(1 - \frac{2GM}{r}\right)^{-1} \dot{r}^2 - r^2 \left[\dot{\vartheta}^2 + \sin^2 \vartheta \dot{\phi}^2\right]. \quad (3.6)$$

To obtain the geodesic equation, we can simply apply the Euler-Lagrange equations of

$$\frac{d}{d\lambda} \left[ \frac{\partial \mathcal{L}}{\partial \dot{x}^a} \right] - \frac{\partial \mathcal{L}}{\partial x^a} = 0. \quad (3.7)$$

Noting that our Lagrangian is independent of  $t$  and  $\phi$ , depending only on their derivatives, we find their associated Euler-Lagrange equation is that of a conserved quantity

$$\left(1 - \frac{2GM}{r}\right) \dot{t} = k, \quad (3.8)$$

$$r^2 \sin^2 \vartheta \dot{\phi} = h, \quad (3.9)$$

where  $k$  and  $h$  are constants. Unfortunately, the Lagrangian depends explicitly on  $r$  and  $\vartheta$ , and thus their Euler-Lagrange equations give

$$\left(1 - \frac{2GM}{r}\right)^{-1} \ddot{r} + \frac{GM}{r^2} \dot{t}^2 - \left(1 - \frac{2GM}{r}\right)^{-2} GM \frac{\dot{r}^2}{r^2} - r \left[\dot{\vartheta}^2 + \sin^2 \vartheta \dot{\phi}^2\right] = 0, \quad (3.10)$$

$$\ddot{\vartheta} + 2 \frac{\dot{r}}{r} \dot{\vartheta} - \sin \vartheta \cos \vartheta \dot{\phi}^2 = 0. \quad (3.11)$$

Equation 3.11 provides an immediate solution for  $\vartheta$  as  $\vartheta = \frac{\pi}{2}$ , which allows us to restrict the light-ray's path to the equatorial plane with no loss of generality. However, Equation 3.10 provides no such trivial answer.

To continue, we recall that photons propagate along null geodesics ( $ds^2 = 0$ ), and thus we find the line element as

$$\left(1 - \frac{2GM}{r}\right) \dot{t}^2 - \left(1 - \frac{2GM}{r}\right)^{-1} \dot{r}^2 - r^2 \dot{\phi}^2 = 0, \quad (3.12)$$

where we have specialised to the case where  $\vartheta = \frac{\pi}{2}$ . To obtain the light-ray's trajectory, we wish to solve this equation for a function of the form  $r(\phi)$ . Using our two conserved quantities (Equations 3.8 and 3.9), and implementing a coordinate transform of  $u \equiv \frac{1}{r}$ , we find the light-ray's propagation to be given by

$$k^2 - h^2 \left[ \frac{du}{d\phi} \right]^2 - (1 - 2GMu) h^2 u^2 = 0, \quad (3.13)$$

where now we have an equation containing only  $\phi$  and  $u$  (and thus  $r$ ).

By performing a  $\phi$  derivative, we find our final form to be

$$\frac{d^2 u}{d\phi^2} + u - 3GMu^2 = 0, \quad (3.14)$$

which can be solved to find a solution for  $u(\phi)$ .

This can be solved by considering a zeroth-order solution and then perturbing it. To zeroth-order, there is no point mass ( $M = 0$ ), and thus our light-ray propagates along a straight line. In this case, our differential equation becomes

$$\frac{d^2 u}{d\phi^2} = -u, \quad (3.15)$$

which has a solution of

$$u(\phi) = \frac{\sin \phi}{b}, \quad (3.16)$$

where  $b$  is the *impact parameter* and is the radial distance to the point-mass at closest approach. Thus, our general solution becomes

$$u(\phi) = \frac{\sin \phi}{b} + \Delta u(\phi), \quad (3.17)$$

where  $\Delta u(\phi)$  is our perturbation. Solving for the full solution gives

$$u(\phi) = \frac{\sin \phi}{b} + \frac{3GM}{2b^2} \left[ 1 + \frac{1}{3} \cos(2\phi) \right]. \quad (3.18)$$

To find the deflection angle of our light-ray due to our point mass, we can consider the angle in the limit  $r \rightarrow \infty$  (thus  $u \rightarrow 0$ ) and double it. Since we expect the angle to be small, we can apply the small-angle approximations ( $\sin \phi \approx \phi$  and  $\cos \phi \approx 1$ ) to Equation 3.18 to find  $\phi$  as

$$\phi \simeq \frac{-2GM}{b}, \quad (3.19)$$

and thus the total deflection angle is

$$|\Delta\phi| \simeq \frac{4GM}{b}. \quad (3.20)$$

This is exactly *double* the expected deflection when calculated from Newtonian mechanics, and thus an accurate measurement of the deflection angle would be able to discern between the Newtonian and Einsteinian theories of gravity.

### 3.1.2 The Eddington expedition

With the announcement of Einstein's general theory of relativity at the Prussian Academy of Sciences in 1915, cosmologists were eager to test this new theory. Since many of the predictions from Einstein's general relativity required incredible observational precision, such as it requiring over a century of technological advances to measure the gravitational waves predicted from GR [112], the additional factor of two in the deflection angle over the Newtonian prediction, which could be measured terrestrially and occurred within our Solar System, became the perfect test-bed for GR.

Astronomer Royal Frank Watson Dyson and director of the Cambridge Observatory Arthur Stanley Eddington realised that the total solar eclipse of 1919 would be the perfect opportunity to test the deflection angle and thus sought to lead an expedition to make measurements during the eclipse. Since the eclipse's path was from northern Brazil to west Africa, measurements from the UK were not possible. Thanks to the recent ending of World War One, international travel was now possible, with Eddington leading a group to the west African island of Príncipe, and fellow astronomer Andrew Crommelin from the Royal Observatory Greenwich led a group to the north-eastern Brazilian town of Sobral [155].

Figure 3.1 shows a modern restoration of one of Eddington's plates that recorded the position of stars in the Taurus constellation during the eclipse. The results of the expedition gave a result for the deflection angle that was consistent with the GR prediction, and thus was one of the first major confirmations of GR over Newtonian gravity [31].

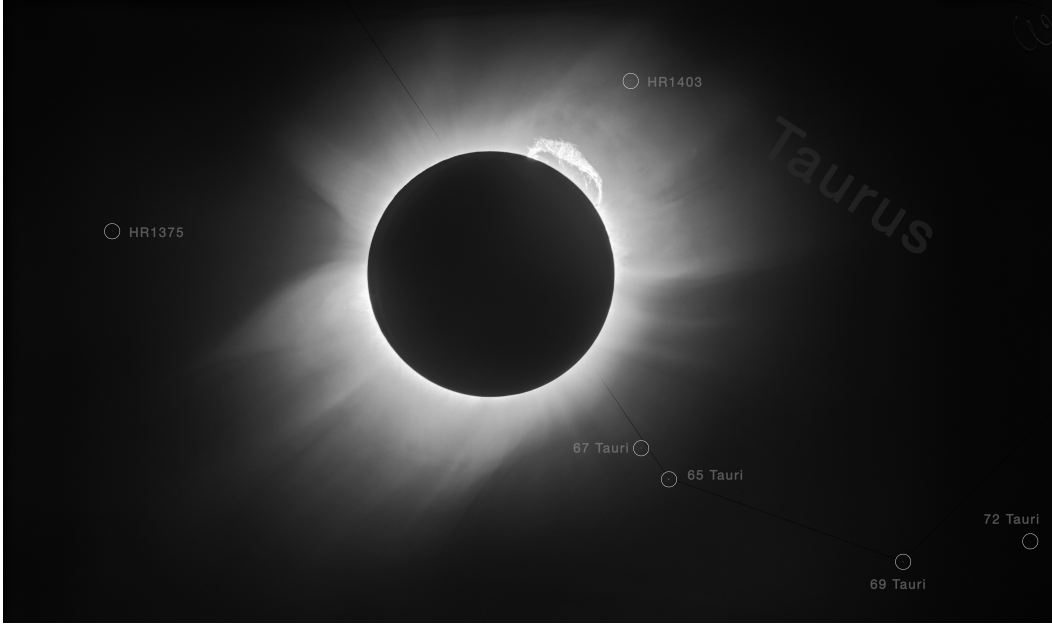


Figure 3.1: Modern restoration of an original plate as measured by Eddington and collaborators during the 1919 Solar eclipse, with the position of stars in the Taurus cluster labelled. It was plates like these that allowed the astronomers to measure the gravitational deflection angle from the sun, and confirm that Einsteinian gravity more accurately predicts the angle over Newtonian mechanics. Credit: European Southern Observatory / Landessternwarte Heidelberg-Königstuhl / F. W. Dyson, A. S. Eddington, & C. Davidson.

## 3.2 Weak gravitational lensing

In Section 3.1, we saw how point masses can deflect light-rays propagating through space-time. The effect of this is that when we observe the angular positions of objects on the sky, this may not be their true positions, since their light-rays could have been deflected by massive objects located between us (the observer) and the source. Thus, gravitational lensing creates a map between the observed angular positions and the true angular positions of objects on the sky. Figure 3.2 shows a typical singular-lensed configuration, where light rays are emitted from an object located on the source plane, which are then deflected by masses in the lens plane, and then detected by the observer. Here, we are assuming that the deflections occur over a much shorter distance in the lens plane than the distance between the source and lens and lens and observer planes (the thin-lens approximation). Using some geometry, we can relate the observed angular separation  $\vec{\theta}$ , the true angular separation  $\vec{\beta}$  and the deflection angle  $\hat{\alpha}$  through

$$\vec{\eta} = \vec{\beta}D_s = \vec{\theta}D_s - \hat{\alpha}D_{ds}, \quad (3.21)$$

where  $D_s$  and  $D_{ds}$  are the angular diameter distance between the observer and source, and source and lens, respectively, and  $\vec{\eta}$  is the angular separation in the source plane. Defining the reduced deflection angle as  $\vec{\alpha} \equiv (D_{ds}/D_s) \hat{\alpha}$ , we find that the lens equation is given as

$$\vec{\beta} = \vec{\theta} - \vec{\alpha}(\vec{\theta}). \quad (3.22)$$

If the lens equation has more than one solution for fixed source position  $\vec{\beta}$ , then the same source can be seen by the observer at multiple angular separations  $\vec{\theta}$  and thus the source is multiply-imaged. This can happen for the cases where the lenses are ‘strong’.

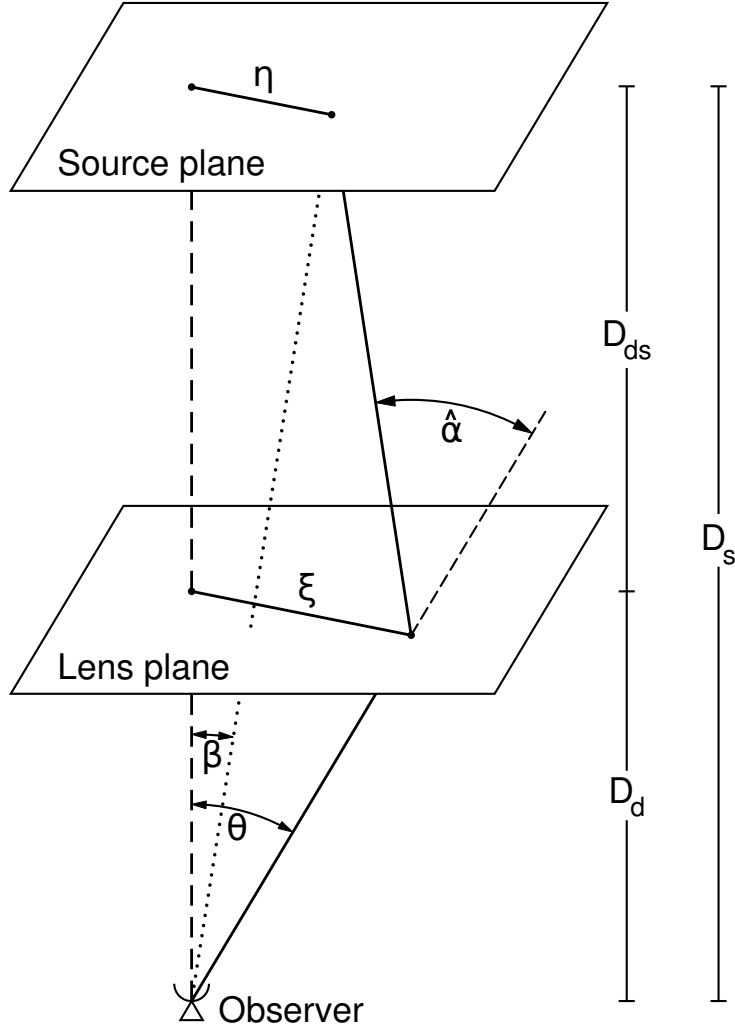


Figure 3.2: Simplified diagram of a typical lensing scenario: we have a source located on the source plane at an angular diameter distance  $D_s$  from the observer, whose light gets deflected by a lens in the lens plane at an angular diameter distance  $D_d$  from the observer. The lens acts to move the observed position of the source from the undeflected angle  $\beta$  to the lensed angle  $\theta$ , and so  $\hat{\alpha}$  becomes the deflection angle. Figure taken from Ref. [32].

The strength of lenses is characterised by the dimensionless surface mass density  $\kappa(\vec{\theta})$ , which is given as

$$\kappa(\vec{\theta}) = \frac{\Sigma(\vec{\theta} D_d)}{\Sigma_{\text{CR}}}, \quad (3.23)$$

where  $\Sigma_{\text{CR}}$  is the critical surface mass density and given as

$$\Sigma_{\text{CR}} = \frac{1}{4\pi G} \frac{D_s}{D_d D_{ds}}. \quad (3.24)$$

Thus, as  $\Sigma_{\text{CR}}$  is a function of distances, it is therefore a function of redshifts of the sources and lenses. A lens plane which has  $\kappa \geq 1$  can produce multiple images for some positions  $\vec{\beta}$ , and thus the condition of  $\kappa \geq 1$  distinguishes sources between ‘weak’ and ‘strong’. Though, while images where  $\kappa < 1$  may be considered weak, the sources used in real weak lensing analyses feature  $\kappa \ll 1$  [32].

### 3.2.1 Propagation of light through the Universe

Now that we know how light-rays react to the presence of both point masses and thin lenses, we wish to extend our discussions to deflections of light from the large-scale structure of the Universe, not singular lenses. Since large-scale structures are scattered throughout a photon's path, we need to consider how the photon propagates through this perturbed spacetime. In Equation 2.11, we introduced the perturbed FRW metric of

$$ds^2 = (1 + 2\Psi) dt^2 - a^2(t) (1 - 2\Phi) d\vec{x}^2,$$

where  $\Psi$  and  $\Phi$  are our perturbation potentials. Under Einsteinian gravity, and where there are no anisotropic stresses in the energy-momentum tensor  $T_{ab}$ , we find that they are equal,  $\Psi = \Phi$ . Since photons propagate along null geodesics ( $ds^2 = 0$ ), we find that the time taken for a general photon's path through our perturbed spacetime to be

$$t = \int (1 - 2\Phi) dr, \quad (3.25)$$

where the integral is in physical coordinates,  $r$ . This is analogous to light propagating through a medium with a variable refractive index given by  $n = 1 - 2\Phi$ . We can now apply Fermat's principle, that light takes the path of minimum time, thus  $\delta t = 0$  [33, 92]. This gives us the Euler-Lagrange equations for the light ray, and thus can be integrated to find the deflection angle  $\hat{\alpha}$  (cf. Figure 3.2) can be written as

$$\hat{\alpha} = -2 \int \nabla_{\perp} \Phi dr, \quad (3.26)$$

where the gradient and integral are both evaluated in physical coordinates. Since deflections in the photon's path arise from the gradient of the gravitational potential perpendicular to the photon's path (parallel gradients simply change the arrival time of a photon for a source at fixed distance), this is why we take the two-dimensional gradient only. Again, this factor of two exists only in Einsteinian gravity and not in Newtonian dynamics.

To see how light-rays are deflected as they travel through spacetime on cosmological scales, let us consider two light rays that separated by a comoving distance  $\vec{x}$ . This separation will change as the two light rays encounter slightly different gradients in the gravitational potential as they propagate through spacetime. In a completely homogenous universe, one where there are no perturbations, then the comoving separation between the two light rays are given by the zeroth-order solution  $\vec{x}_0$  of

$$\vec{x}_0 = f_k(\chi) \vec{\theta}. \quad (3.27)$$

However, in a non-homogenous universe where perturbations are present, we find that these perturbations induce lensing deflections along the line-of-sight. For this case, the separation can be written as an integral along the line-of-sight of the photon, where the superscript zero corresponds to the fiducial ray from which the separation vector  $\vec{x}$  is defined from, to give

$$\vec{x}(\chi) = f_k(\chi) \vec{\theta} - 2 \int_0^\chi d\chi' f_k(\chi - \chi') [\nabla_{\perp} \Phi(\chi', \vec{x}) - \nabla_{\perp} \Phi^0(\chi')], \quad (3.28)$$

where  $\vec{\theta}$  is the angle subtended by the two light rays for the observer, and the source is at some comoving distance  $\chi$ . The second, fiducial ray  $\Phi^{(0)}$  does not require a second argument since we have defined it to travel along  $\vec{x} = 0$ .

Applying the lens equation, we find that we can write the comoving separation  $\vec{x}$  in terms of the observed angle ( $\vec{x}(\chi) = f_k(\chi) \vec{\beta}$ ), and thus we find the reduced deflection angle  $\vec{\alpha}$  as

$$\vec{\alpha} = 2 \int_0^\chi d\chi' \frac{f_k(\chi - \chi')}{f_k(\chi)} [\nabla_{\perp} \Phi(\chi', \vec{x}) - \nabla_{\perp} \Phi^0(\chi')]. \quad (3.29)$$

### 3.2.2 The amplification matrix

The lens equation (Equation 3.22) provided us with a relation between the lensed (observed) coordinates  $\vec{\theta}$  to the original (source) coordinates  $\vec{\beta}$ . Alternatively, we can express this mapping through the differential Jacobian transformation matrix  $\mathbf{A}$ , given as

$$\mathbf{A} \equiv \frac{\partial \vec{\beta}}{\partial \vec{\theta}}, \quad (3.30)$$

where  $\mathbf{A}$  is our amplification matrix. Taking components of this matrix, we find that they can be written as

$$A_{ij} = \frac{\partial \beta_i}{\partial \theta_j} = \delta_{ij} - \frac{\partial \alpha_i}{\partial \theta_j}, \quad (3.31)$$

$$= \delta_{ij} - 2 \int_0^\chi d\chi' \frac{f_k(\chi - \chi') f_k(\chi')}{f_k(\chi)} \frac{\partial^2}{\partial x_i \partial x_j} \Phi(\chi', f_k(\chi') \vec{\theta}), \quad (3.32)$$

where we have used the zeroth-order approximation for  $\vec{x}$  as  $\vec{x}_0 = f_k(\chi) \vec{\theta}$ , which in differential form gives  $\partial x_i = f_k(\chi') \partial \theta_i$ , and dropped the term proportional to the gradient of  $\Phi^{(0)}$  since it does not depend on the angle  $\theta$ . Here  $\delta_{ij}$  is the Kronecker- $\delta$  symbol which is either one or zero.

Using our amplification matrix, we can define a scalar lensing potential  $\psi$  such that it satisfies

$$A_{ij} = \delta_{ij} - \partial_i \partial_j \psi, \quad (3.33)$$

where the partial derivatives are with respect to  $\vec{\theta}$ . This definition gives  $\psi$  as

$$\psi(\chi, \vec{\theta}) = 2 \int_0^\chi d\chi' \frac{f_k(\chi - \chi')}{f_k(\chi) f_k(\chi')} \Phi(\chi', f_k(\chi') \vec{\theta}). \quad (3.34)$$

The amplification matrix  $\mathbf{A}$  can be parameterised in terms of a scalar field, the convergence  $\kappa$ , and a spin-2 field, the shear  $\gamma = (\gamma_1, \gamma_2)$ , as

$$\mathbf{A} = \begin{pmatrix} 1 - \kappa - \gamma_1 & -\gamma_2 \\ -\gamma_2 & 1 - \kappa + \gamma_1 \end{pmatrix}. \quad (3.35)$$

This assumes that the amplification matrix is symmetric, which is a very good assumption as galaxies are only very weakly lensed,  $|\gamma|, |\kappa| \ll 1$ , and thus we can ignore higher-order terms in the expansion. Comparing our definition of  $\mathbf{A}$  in terms of  $\gamma$  and  $\kappa$  to our definition of the lensing potential, as given in Equation 3.33, we find that the shear and convergence are given in terms of derivatives of the potential  $\psi$  as

$$\kappa = \frac{1}{2} (\partial_1 \partial_1 + \partial_2 \partial_2) \psi = \frac{1}{2} \vec{\nabla}^2 \psi, \quad (3.36a)$$

$$\gamma_1 = \frac{1}{2} (\partial_1 \partial_1 - \partial_2 \partial_2) \psi, \quad (3.36b)$$

$$\gamma_2 = \partial_1 \partial_2 \psi. \quad (3.36c)$$

Hence, both the convergence  $\kappa$  and shear  $\gamma$  are related to the lensing potential  $\psi$ , which allows us to transform between these quantities, such as using the Kaiser-Squires reconstruction method [42].

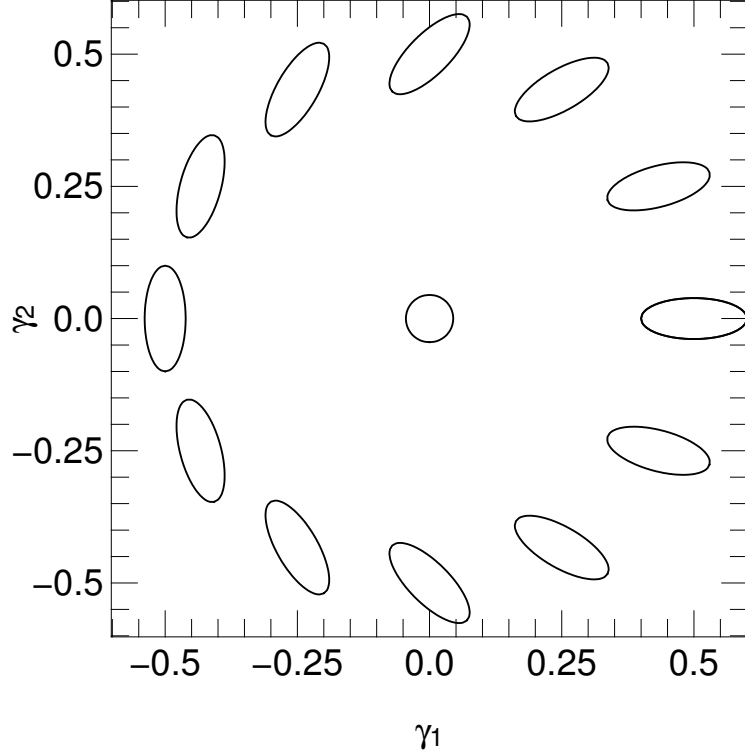


Figure 3.3: Figure showing that if we started out with a perfectly circular original image, the action of  $\gamma_1$  and  $\gamma_2$  on it serves to distort our image into an ellipse, with the orientation of the ellipse as a function of the shear components  $\gamma_1$  and  $\gamma_2$ . We note that the distortions from  $\gamma_1$  are offset  $\frac{\pi}{4}$  from  $\gamma_2$ , such is the nature of the spin-2 field. Taken from Ref. [33].

### 3.2.3 Physical interpretation of shear and convergence

Introduced in Equation 3.35, we can characterise the distortions in galaxy images through a spin-0 (scalar) field the convergence  $\kappa$ , and a spin-2 (tensor) field the shear  $\gamma$ . Physically, the convergence corresponds to an isotropic increase or decrease in the size of observed images when compared to their undistorted original size. This isotropic stretching is called the magnification,  $\mu$ , and is the determinant of the inverse amplification matrix,  $\mathbf{A}^{-1}$ . Thus, it is given as

$$\mu \equiv \det \mathbf{A}^{-1}, \quad (3.37)$$

$$= \left[ (1 - \kappa)^2 - |\gamma|^2 \right]^{-1}, \quad (3.38)$$

$$\simeq 1 + 2\kappa, \quad (3.39)$$

where the last approximation is taken in the weak-field limit [33]. Thus,  $\kappa < 0$  is a demagnification, whereas  $\kappa > 0$  is a magnification in this limit. The shear field  $\gamma$  corresponds to the anisotropic stretching of images on the sky, turning circular objects into elliptical images, as shown in Figure 3.3.

The shear is called a spin-2 field since the rotation of an ellipse of  $\pi$  radians returns the original ellipse, as demonstrated in Figure 3.3. With this, it is convenient to express shear in terms of a polar complex number:  $\gamma = \gamma_1 + i\gamma_2 = |\gamma| \exp(2i\varphi)$ , where  $\varphi$  is the angle between the two shear components. From this definition, it is immediately obvious that a rotation of  $\pi$  in  $\varphi$  returns the original shear  $\gamma$ .

### 3.2.4 Overdensity projections

Equation 3.36a relates the convergence  $\kappa$  to a Poisson equation for the lensing potential  $\psi$ , and thus the convergence can be interpreted as a projected surface density. We now wish to use this relation to find an equation for  $\kappa$  in terms of the density perturbation  $\delta$  (Equation 2.67). To do so, we can ‘add’ a second-order derivative of the comoving distance  $\chi$ ,  $\frac{\partial^2}{\partial \chi^2}$ , which, to good approximation, integrates to zero along the line-of-sight. This then gives us a 3D Laplacian acting on the Newtonian potential  $\Phi$ ,  $\vec{\nabla}^2 \Phi$ , and so we can use the gravitational Poisson equation (Equation 2.68) to relate the Laplacian to the density contrast  $\delta$ . Thus, we find the convergence field out to a conformal distance  $\chi$  to be

$$\kappa(\chi, \vec{\theta}) = \frac{3H_0^2 \Omega_M}{2} \int_0^\chi \frac{d\chi'}{a(\chi')} \frac{f_k(\chi - \chi') f_k(\chi')}{f_k(\chi)} \delta(\chi', f_k(\chi') \vec{\theta}), \quad (3.40)$$

where we have used that  $\bar{\rho} \propto a^{-3}$ .

Here, we see that our convergence field is a projection of the density contrast along the line-of-sight in comoving coordinates, weighted by some geometrical factors involving distances between the source, lenses, and observer. For the case of a flat universe, where  $f_k(\chi) = \chi$ , then we find the geometrical weight to be  $(\chi - \chi')\chi'$  which is a parabola with a maximum at  $\chi' = \frac{\chi}{2}$ , and thus lensing structures around halfway between the source and observer are the most efficient at generating lensing perturbations.

In practice, we have a distribution of source galaxies in redshift,  $n(z)$ , and thus we wish to find the average convergence for these sources. This requires an additional weighting with respect to this  $n(z)$  in our line-of-sight integral. A typical distribution for  $n(z)$  is the Smail distribution [156, 157] of

$$n(z) \propto \left(\frac{z}{z_0}\right)^n \exp \left[ - \left(\frac{z}{z_0}\right)^{\frac{3}{2}} \right], \quad (3.41)$$

where  $z_0$  is given in terms of the median redshift  $z_{\text{MED}}$  by  $z_0 = z_{\text{MED}}/\sqrt{2}$ . For the *Euclid* survey,  $z_{\text{MED}} = 0.9$  [158]. We can relate this galaxy distribution in redshift-space to comoving distance-space by noting that the number of galaxies are conserved, and thus  $n(z)dz = n(\chi)d\chi$ . Thus, the convergence from a distribution of source galaxies is given by

$$\kappa(\vec{\theta}) = \int_0^{\chi_{\text{MAX}}} d\chi \, n(\chi) \kappa(\chi, \vec{\theta}). \quad (3.42)$$

where we integrate out to the limiting comoving distance of our galaxy distribution  $\chi_{\text{MAX}}$ . Inserting our equation for  $\kappa(\chi, \vec{\theta})$  of Equation 3.40, we find

$$\kappa(\vec{\theta}) = \frac{3H_0^2 \Omega_M}{2} \int_0^{\chi_{\text{MAX}}} d\chi \, g(\chi) \frac{f_k(\chi)}{a(\chi)} \delta(\chi, f_k(\chi) \vec{\theta}), \quad (3.43)$$

where we have defined  $g(\chi)$  as the lensing efficiency kernel, and is given as

$$g(\chi) = \int_\chi^{\chi_{\text{MAX}}} d\chi' n(\chi') \frac{f_k(\chi' - \chi)}{f_k(\chi')}. \quad (3.44)$$

The lensing kernel represents the efficiency of a lens at distance  $\chi$  combined with the source galaxy distribution. We plot the distribution of source number densities  $n(z)$  and their associated lensing kernels  $g(z)$  in Figure 3.4.



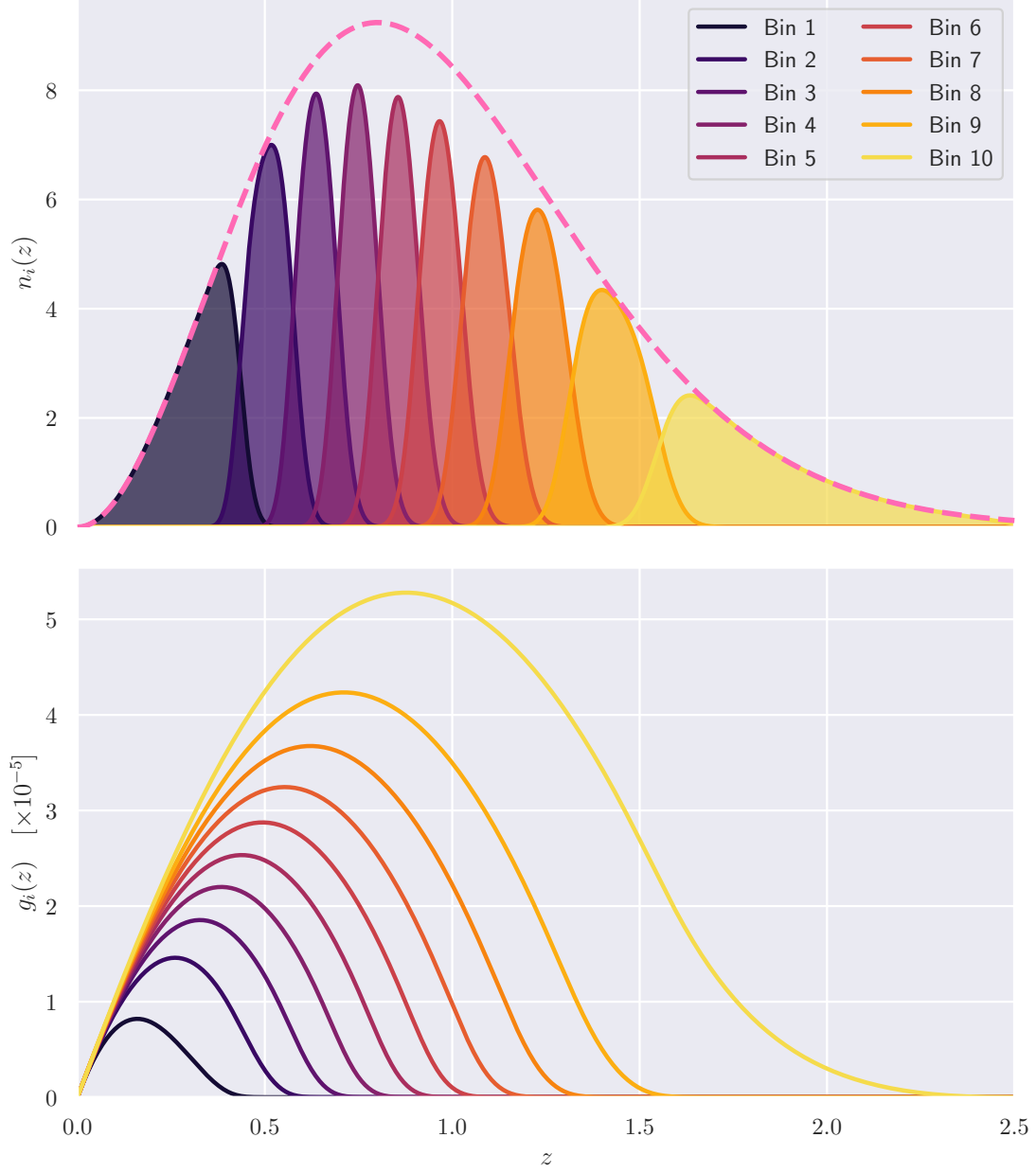


Figure 3.4: *Top panel:* An example Smail distribution (Equation 3.41) for the total source galaxy number density, in dashed pink, which is then split into ten equally-populated tomographic redshift bins (the coloured curves), computed using the GLASS public code [14]. *Bottom panel:* The lensing kernels computed for each of the corresponding photometric redshift bins in the top panel. We see that the lensing kernels peak at around half the redshift of the number density peak, which follows from the lens equation, and that higher redshift bins have large support in their kernels over a wide range of redshifts.

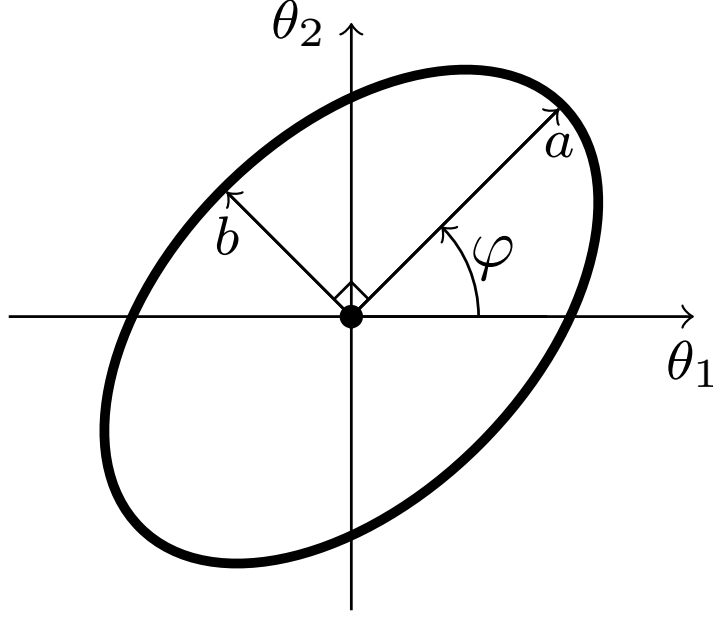


Figure 3.5: An image of a galaxy can be approximated by an ellipse, characterised by its semi-major axis  $a$ , semi-minor axis  $b$ , and orientation  $\varphi$ .

### 3.2.5 Measuring shear

To measure the shear field, we first need to measure the ellipticity of galaxies on the sky. A galaxy can be approximated by an ellipse, which is characterised by its semi-major axis  $a$ , semi-minor axis  $b$ , and orientation  $\varphi$  (see Figure 3.5). This allows us to quantify each galaxy with a (complex) ellipticity  $\varepsilon$ , defined as

$$\varepsilon = \frac{a - b}{a + b} e^{2i\varphi}. \quad (3.45)$$

Now, it is highly unlikely that every galaxy is perfectly spherical in its source plane (e.g. galaxy morphology and classifications from the Hubble tuning fork [159]), and thus we can assume that every galaxy has some intrinsic ellipticity in its source plane,  $\varepsilon^s$ . Thus the observed ellipticity will be its source ellipticity convoluted with gravitational lensing, to give

$$\varepsilon = \frac{\varepsilon^s + g}{1 + g^* \varepsilon^s}, \quad (3.46)$$

where  $g$  is the reduced shear, defined as

$$g \equiv \frac{\gamma}{1 - \kappa}. \quad (3.47)$$

In the weak lensing limit, where  $\kappa \ll 1$ , then Equation 3.46 reduces to

$$\varepsilon \simeq \varepsilon^s + \gamma. \quad (3.48)$$

If the original intrinsic ellipticities of galaxies are randomly oriented on the sky, then the average of  $\varepsilon^s$  is zero,  $\langle \varepsilon^s \rangle = 0$ . Thus, the average of the observed ellipticity of galaxies over a small patch of sky is an unbiased estimator for the shear field in that patch

$$\langle \varepsilon \rangle = \gamma. \quad (3.49)$$

### 3.3 Estimating source galaxy redshift

A major source of information from weak lensing is our ability to perform redshift tomography on our data, that is to split our sheared, source galaxies into different redshift bins which allows us to measure the *evolution* of the shear signal with redshift, and increases the number of data-points in our data-vectors [160]. Thus, to perform a tomographic analysis, we need estimates of the source galaxies redshifts. The most accurate estimates for the redshifts of extragalactic objects come from spectroscopy, which can measure the wavelength of individual atomic emission and absorption lines, such as:  $H\alpha$ ,  $H\beta$ ,  $H\gamma$ , [OII], [OIII], and [NeIII] [161]. These observations can be compared to measurements performed at-rest in a laboratory, and so the redshift can be easily computed from the increase in wavelength from the Doppler shift (Equation 2.36).

Exceedingly high-quality spectroscopic redshifts of distant galaxies have been observed using the Near-Infrared Spectrograph (NIRSpec) instrument on the James Webb Space Telescope [161, 162]. While we would love to perform spectroscopy on our weak lensing source galaxies, the amazingly long exposure times required for spectroscopy, which can be of the order ten thousand seconds [161], makes spectroscopy absolutely prohibitively expensive for over the billion galaxies whose shapes we wish to include in our tomographic analyses. Hence, we are forced to use alternative methods to estimate galaxy redshifts that can still deliver (somewhat) accurate results, but with much reduced observation time.

Photometric redshifts work by imaging a galaxy in multiple colours (band-filters) which can approximately recover the galaxy’s spectral energy distribution (SED), and by comparing this to simulated galaxies SED’s at known redshifts an estimate for the photometric redshift can be obtained (SED fitting [163]). Figure 3.6 plots the transmission profile curves for *Euclid*’s VIS instrument, the three filters associated with its NISP instrument [164], the five filters to be used by the LSST survey at the *Rubin* observatory [165], and an example galaxy SED located at  $z = 1$  created using the BAGPIPES code [166]. The full SED is hugely complicated, featuring many emission and absorption lines, which is what allows for precision spectroscopic redshifts to be obtained. The solid circles in Figure 3.6 shows the photometric measurements of the SED in the nine filters (excluding the broad VIS filter), and is what would be used to estimate this galaxies redshift photometrically. We see that by using the combination of these nine filters, we can obtain information about a galaxy’s SED from the near-ultraviolet into the near-infrared which can approximate spectroscopic information – though is, of course, far coarser in wavelength than spectroscopy.

*Euclid* alone will be unable to accurately determine photometric redshifts, and so needs combining with ground-based optical measurements – these measurements will come from LSST for the southern sky and the UNIONS collaboration for the northern sky.

By performing a tomographic analysis of cosmic shear, that is to utilise the auto- and cross-correlations of our galaxy shapes at different redshifts, we can directly constrain the growth and evolution of structure across cosmic time. This will allow us to place tight constraints on the properties of dark energy, since it directly affects the background evolution and growth of structure in our Universe – with the end goal to determine if dark energy is compatible with the cosmological constant  $\Lambda$  or is some new time-evolving field.

The uncertainties in the estimates of photometric redshifts is a leading source of systematic uncertainty for current weak lensing surveys [167]. Hence, we require extremely accurate assessment of photometric redshifts for any forthcoming weak lensing survey which aim to significantly reduce statistical and systematic uncertainties. Thus, considerable efforts have been spent to optimise the estimation of photometric redshifts [168, 169].

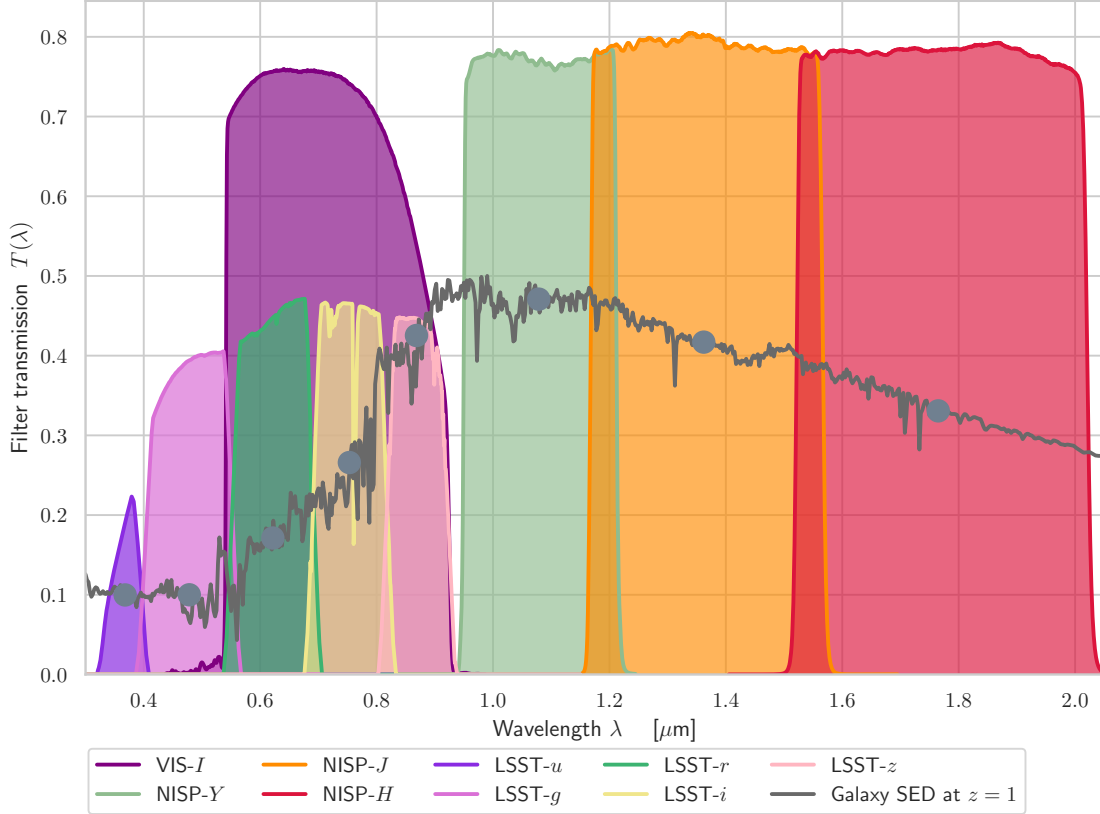


Figure 3.6: Plot of filter transmission profiles for the space-based *Euclid* VIS and NISP instruments [164], along with the ground-based LSST survey at the *Rubin* observatory [165]<sup>1</sup>, and an example galaxy spectral energy distribution created using the BAGPIPES code [166] where the galaxy is located at redshift  $z = 1$  (the SED is normalised to 0.5 for easier comparison to the filter profiles). The photometric measurements using these nine filters for this SED is shown in the grey circles. *Euclid* is able to image in the infrared since there is no atmosphere in space that absorbs these wavelengths as for Earth-based observatories, which is seen by the lower transmission amplitude for the five LSST curves. By complementing space-based infrared measurements with ground-based optical measurements, higher accuracy photometric redshifts can be obtained for the source galaxies, thus optimising the weak lensing analysis pipeline.

## 3.4 Estimators of weak lensing

Now that we have built up a solid theoretical understanding of cosmic shear, we can look at how it is actually measured in practice.

### 3.4.1 Lensing power spectrum

Since galaxy images are observed on the sky, though unlike the CMB we *can* obtain radial information of galaxies through their redshift, we are motivated to express the statistics of cosmic shear through the angular power spectrum  $C_\ell$ , analogous to the CMB. Here, we wish to derive the angular power spectrum for cosmic shear. Equation 3.43 gave us the angular convergence field as a line-of-sight integral over the density perturbation  $\delta$ ,

<sup>1</sup>*Euclid* data taken from <https://euclid.esac.esa.int/msp/refdata/nisp/NISP-PHOTO-PASSBANDS-V1> [170], LSST data taken from [https://github.com/LSSTDESC/SN-PWV/tree/main/data/filters/lsst\\_baseline](https://github.com/LSSTDESC/SN-PWV/tree/main/data/filters/lsst_baseline) [165].

weighted with some geometrical factors. To start our derivation, we consider the Fourier transform of the density perturbation field into momentum-space of

$$\delta(\chi, \chi\vec{\theta}) = \int \frac{d^3\vec{k}}{(2\pi)^3} \delta_{\vec{k}} e^{i\vec{k}\cdot\vec{x}}, \quad (3.50)$$

where  $\vec{x} \equiv (\chi, \hat{\vartheta}\chi)$ . Thus, the convergence field on the sky can be written as

$$\kappa(\vec{\theta}) = \frac{3H_0^2\Omega_M}{2} \int d\chi \frac{g(\chi) f_k(\chi)}{a(\chi)} \int \frac{d^3\vec{k}}{(2\pi)^3} \delta_{\vec{k}} e^{i\vec{k}\cdot\vec{x}}, \quad (3.51)$$

$$= \Upsilon \int d\chi \Gamma(\chi) \int \frac{d^3\vec{k}}{(2\pi)^3} \delta_{\vec{k}} e^{i\vec{k}\cdot\vec{x}}, \quad (3.52)$$

where we have defined  $\Upsilon$  as the cosmological prefactors, and  $\Gamma(\chi)$  as the collection of geometrical functions for convenience. Now, using the Rayleigh plane-wave expansion, we can express the complex exponential into a decomposition of spherical harmonics and spherical Bessel functions  $j_\ell(x)$  [171], as

$$e^{i\vec{k}\cdot\vec{x}} = 4\pi \sum_{\ell, m} i^\ell j_\ell(k\chi) Y_{\ell m}(\hat{k}) Y_{\ell m}^*(\vec{\theta}). \quad (3.53)$$

Thus, the angular convergence field becomes

$$\kappa(\vec{\theta}) = 4\pi\Upsilon \sum_{\ell, m} i^\ell \int d\chi \Gamma(\chi) \int \frac{d^3\vec{k}}{(2\pi)^3} j_\ell(k\chi) Y_{\ell m}(\hat{k}) Y_{\ell m}^*(\vec{\theta}) \delta_{\vec{k}}. \quad (3.54)$$

We can now compare this formula with that of a spherical harmonic expansion on a function of the sphere (Equation 2.107), to find the expansion coefficients  $a_{\ell m}$  of the convergence field as

$$a_{\ell m} = 4\pi\Upsilon i^\ell \int d\chi \Gamma(\chi) \int \frac{d^3\vec{k}}{(2\pi)^3} j_\ell(k\chi) Y_{\ell m}(\hat{k}) \delta_{\vec{k}}. \quad (3.55)$$

Recalling that the definition of the power spectrum arose from the expectation value of two  $a_{\ell m}$  values (Equation 2.109), we can take this expectation value to find

$$\langle a_{\ell m}, a_{\ell' m'}^* \rangle = (4\pi\Upsilon)^2 i^\ell (-i)^{\ell'} \times \int d\chi d\chi' \frac{d^3\vec{k}}{(2\pi)^3} \frac{d^3\vec{k}'}{(2\pi)^3} \Gamma(\chi)\Gamma(\chi') j_\ell(k\chi) j_{\ell'}(k'\chi') Y_{\ell m}(\hat{k}) Y_{\ell' m'}^*(\hat{k}') \langle \delta_{\vec{k}} \delta_{\vec{k}'}^* \rangle. \quad (3.56)$$

Now recalling our definition of the matter power spectrum as (Equation 2.84)

$$\langle \delta_{\vec{k}} \delta_{\vec{k}'}^* \rangle = (2\pi)^3 \delta^{(3)}(\vec{k}_1 - \vec{k}_2) P(k), \quad (3.57)$$

we find that we require  $\vec{k}' = \vec{k}$ , and so we can immediately perform the  $\vec{k}'$  integral, to give

$$\langle a_{\ell m}, a_{\ell' m'}^* \rangle = (4\pi\Upsilon)^2 i^\ell (-i)^{\ell'} \times \int d\chi d\chi' \frac{d^3\vec{k}}{(2\pi)^3} \Gamma(\chi)\Gamma(\chi') j_\ell(k\chi) j_{\ell'}(k\chi') Y_{\ell m}(\hat{k}) Y_{\ell' m'}^*(\hat{k}) P(k) \quad (3.58)$$

We can now express our  $d^3\vec{k}$  volume element as  $k^2 dk d\Omega$ , where  $d\Omega$  is the volume element on the sphere, to give

$$\langle a_{\ell m}, a_{\ell' m'}^* \rangle = \frac{(4\pi\Upsilon)^2}{(2\pi)^3} i^\ell (-i)^{\ell'} \int d\chi d\chi' dk \Gamma(\chi)\Gamma(\chi') j_\ell(k\chi) j_{\ell'}(k\chi') k^2 P(k) \times \int d\Omega Y_{\ell m}(\hat{k}) Y_{\ell' m'}^*(\hat{k}). \quad (3.59)$$

Thus, using the orthonormality of the spherical harmonics over the complete sphere, we can evaluate the angular integral to find

$$\langle a_{\ell m}, a_{\ell' m'}^* \rangle = \frac{2\Upsilon^2}{\pi} i^\ell (-i)^{\ell'} \delta_{\ell\ell'} \delta_{mm'} \int d\chi d\chi' dk \Gamma(\chi) \Gamma(\chi') j_\ell(k\chi) j_{\ell'}(k\chi') k^2 P(k). \quad (3.60)$$

Since the Kronecker- $\delta$  forces  $\ell' = \ell$ , we find that  $i^\ell (-i)^\ell = 1$  for all  $\ell$ . Thus, we find

$$\langle a_{\ell m}, a_{\ell' m'}^* \rangle = \frac{2\Upsilon^2}{\pi} \delta_{\ell\ell'} \delta_{mm'} \int d\chi d\chi' dk \Gamma(\chi) \Gamma(\chi') j_\ell(k\chi) j_\ell(k\chi') k^2 P(k). \quad (3.61)$$

## The Limber approximation

Thus far, we have been performing an exact calculation with no approximations yet. So, if we wish to keep our derivation of the angular power spectrum coefficients to be exact, then this would be where our derivation ends with our  $C_\ell$  values given by Equation 3.61. However, this is not such a nice equation for the  $C_\ell$  values since it is a triple integral over  $\chi$ ,  $\chi'$ , and  $k$ , and involves two spherical Bessel functions which are highly oscillatory, especially for large  $\ell$  values, and thus challenging to numerically evaluate to make theoretical predictions for the  $C_\ell$  values.

Hence, we can employ Limber's approximation of the spherical Bessel functions, which allows us to re-write the spherical Bessel functions as Dirac- $\delta$  functions in the following way [172]

$$j_\ell(x) \Rightarrow \sqrt{\frac{\pi}{2\alpha}} \delta(\alpha - x), \quad (3.62)$$

where  $\alpha$  is determined by the  $\ell$  index. Originally,  $\alpha$  was taken to be  $\alpha = \ell$ , however  $\alpha = \ell + \frac{1}{2}$  has been found to increase the accuracy of the approximation for smaller values of  $\ell$ , where it is accurate down to  $\ell \simeq 10$  [173]. An even further improvement can be made by using  $\alpha = \sqrt{\ell(\ell+1)}$  [174]. For simplicity, we will be using  $\alpha = \ell$  in the continuing derivation since it is trivial to replace it with either of the two approximations in the final result.

Returning to Equation 3.61, we can employ Limber's approximation on the  $j_\ell(k\chi')$  term to eliminate the  $k$  integral as

$$j_\ell(k\chi') \Rightarrow \sqrt{\frac{\pi}{2\ell}} \delta(\ell - k\chi'), \quad (3.63)$$

and thus enforces that  $k = \ell/\chi'$ . This gives our integral<sup>2</sup> as

$$\langle a_{\ell m}, a_{\ell' m'}^* \rangle \simeq \frac{2\Upsilon^2}{\pi} \sqrt{\frac{\pi}{2\ell}} \delta_{\ell\ell'} \delta_{mm'} \int d\chi d\chi' \Gamma(\chi) \Gamma(\chi') j_\ell\left(\frac{\ell}{\chi'}\chi\right) \left[\frac{\ell}{\chi'}\right]^2 \frac{1}{\chi'} P(k). \quad (3.65)$$

Thus, we can use our remaining spherical Bessel function to eliminate the  $\chi'$  integral through

$$j_\ell\left(\frac{\ell}{\chi'}\chi\right) \Rightarrow \sqrt{\frac{\pi}{2\ell}} \delta\left(\ell - \frac{\ell\chi}{\chi'}\right), \quad (3.66)$$

<sup>2</sup>It is important to remember that when evaluating an integral of the  $\delta$ -function when it is scaled by a constant  $\beta$ , the integral gives

$$\int dx \delta(\beta x) = \frac{1}{\beta} \quad (3.64)$$

since the integral is required to be normalised, and thus we pick up a  $1/\chi'$  term in our integrand.

which enforces that  $\chi' = \chi$ . This gives our remaining 1D integral as

$$\langle a_{\ell m}, a_{\ell' m'}^* \rangle \simeq \frac{2\Upsilon^2}{\pi} \sqrt{\frac{\pi}{2\ell}} \delta_{\ell\ell'} \delta_{mm'} \int d\chi \Gamma^2(\chi) \left[ \frac{\ell}{\chi} \right]^2 \frac{1}{\chi} \frac{\chi}{\ell} P(k). \quad (3.67)$$

Simplifying terms, and substituting in  $\Upsilon$  and  $\Gamma$ , we find the angular power spectrum of convergence to be [33]

$$\kappa\kappa C_\ell^{ab} = \frac{9\Omega_M^2 H_0^4}{4} \int_0^{\chi_{\text{MAX}}} d\chi \frac{g_a(\chi) g_b(\chi)}{a^2(\chi)} P_\delta \left( k = \frac{\ell}{f_k(\chi)}, z = z(\chi) \right), \quad (3.68)$$

where now  $g_a$  is the lensing kernel associated with the distribution of source galaxies,  $n_a(z)$ , in redshift bin  $a$ .

## ***E*- and *B*-modes**

So far, we have been concerned with the statistics of the convergence field  $\kappa$ . However, this is not directly observable, what is observable is the shapes of galaxies and thus we make measurements of the spin-2 field shear  $\kappa$ . Because shear is a spin-2 field, when we decompose it into power spectra, we actually get three unique spectra: *EE*, *EB*, and *BB* modes which are analogous to the same three mode decomposition from the polarisation of the CMB (also a spin-2 field). This arises from Helmholtz's decomposition theorem, which states that any vector field can be written as the gradient of a scalar potential ( $\vec{\nabla}\Phi$ ) plus the curl of a vector potential ( $\vec{\nabla} \times \vec{A}$ ) [175]. The *E*-modes subsequently correspond to the gradient-like term, and the *B*-modes correspond to the curl-like term of our shear fields. Hence, the *EE* and *BB* modes are the auto-correlation of the *E*- and *B*-modes, respectively, with the *EB* mode being the cross-correlation.

Since Equation 3.36 relates convergence and shear to derivatives of the same lensing potential  $\psi$ , we find that the shear-*EE* power spectrum can be written as

$$C_\ell^{EE} = \frac{(\ell-1)(\ell+2)}{\ell(\ell+1)} C_\ell^{\kappa\kappa}, \quad (3.69)$$

and due to parity considerations under Einsteinian gravity  $C_\ell^{EB} = 0$  for all  $\ell$ . For spherically-symmetric mass distributions, the induced deflections are aligned tangentially and so we expect zero *B*-mode power ( $C_\ell^{BB} = 0$ ) from cosmic shear [92].

## **Cosmic variance & noise**

In Section 3.2.5, we argued that while every galaxy has an intrinsic shape, if we average over enough galaxies then the observed ellipticities are an unbiased estimator of the intrinsic shear field. These intrinsic ellipticities contribute to a white-noise effect on the power spectrum of the form

$$N_\ell^{ab} = \frac{\sigma_\epsilon^2}{\bar{n}} \delta_{ab}, \quad (3.70)$$

where  $\sigma_\epsilon$  is the standard deviation of the intrinsic galaxy ellipticity dispersion per component, and  $\bar{n}$  is the expected number of observed galaxies per steradian per redshift bin.  $\bar{n}$  depends on the specifics of the galaxy survey, for the main *Euclid* survey it is expected to observe 30 galaxies per square arcminute, divided into ten redshift<sup>3</sup> bins gives

<sup>3</sup>Generally, the more tomographic redshift bins that the observed source galaxy distribution is divided into provides additional information from the increased number of cross-correlations of the angular power spectrum. However, by splitting the source galaxy distribution into more bins decreases the number density of each bin  $\bar{n}$ , increasing the noise level of each bin. This reduces the amount of information that can be extracted at small-scales. Thus, detailed investigations were required to establish the optimal number of bins to split the source galaxies into. It has been suggested that the first *Euclid* data release (DR1) be split into six tomographic bins [176], and *Euclid*'s final data release (DR3) using either ten or thirteen bins [164] for optimal constraints on the dark energy equation of state.

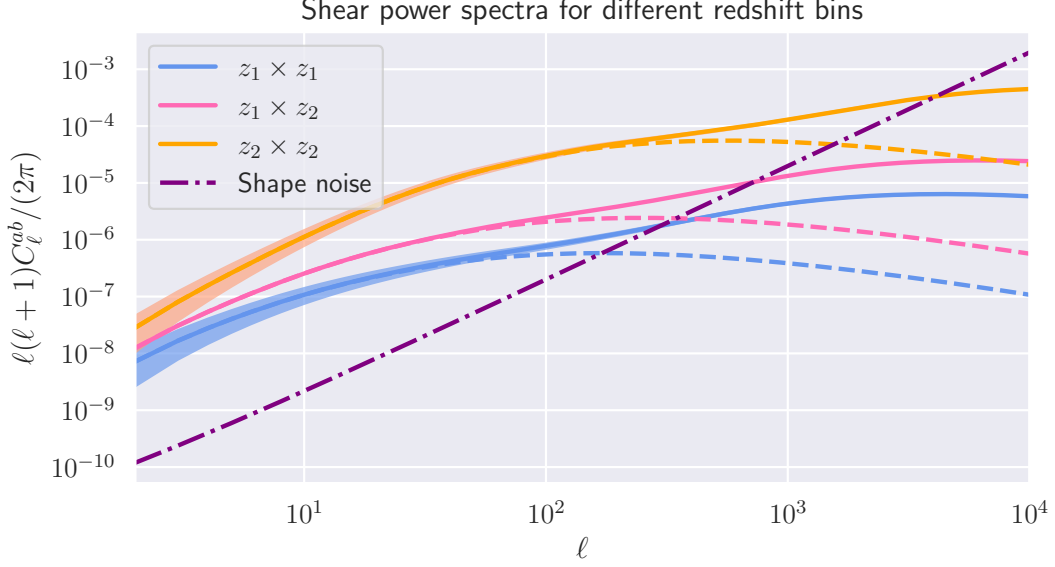


Figure 3.7: Plot of the auto and cross shear power spectrum for two Gaussian redshift bins with centres  $z_1 = 0.5$  and  $z_2 = 2.0$  and widths of  $\sigma_z = 0.25$ . Dashed lines indicate where the linear matter power spectrum has been used instead of the full non-linear prescription. The shaded regions on the auto-spectra indicate the  $1\sigma$ -width of the cosmic variance. The dashed purple line corresponds to the shape noise amplitude expected for *Euclid* [158].

$\bar{n} = 3 \text{ gals / arcmin}$ , with  $\sigma_\epsilon = 0.21$  [158].

While shape noise primarily reduces the information content at small-scales, the effect of cosmic variance impacts at large-scales. This is because each  $\ell$ -mode is only estimated from  $2\ell + 1$   $m$ -modes, and so each  $C_\ell$  mode has a variance of  $2/(2\ell + 1)$ . This significantly affects the precision of which large-scale  $C_\ell$  modes can be measured, and is a result of us only being able to make measurements from one point in the Universe.

The shear power spectrum is plotted in Figure 3.7 for two Gaussian redshift bins. We plot the logarithmic derivatives of the angular power spectrum with respect to the underlying cosmological parameters in Figure 3.8. We see that cosmic shear is generally sensitive to the density perturbation amplitude  $A_s$  and matter density  $\Omega_c$  (which combine to form the lensing amplitude parameter  $S_8$  [177]), with weaker dependency on the dark energy equation of state ( $w_0$  and  $w_a$ ) and the neutrino masses ( $m_\nu$ ), and so require large quantities of accurate and precise statistical measurements of cosmic shear to place tight constraints on these less well constrained cosmological parameters.

### 3.4.2 Real-space correlation functions & COSEBIs

An alternative statistical quantity to the power spectrum is the angular two-point correlation function  $\hat{\xi}_\pm$ . This can be estimated from the same set of galaxy images and can be written as (for redshift bins  $a$  and  $b$ ) [179]

$$\hat{\xi}_\pm^{ab}(\theta) = \frac{\sum w_i w_j [\varepsilon_T^a(\vec{x}_i) \varepsilon_T^b(\vec{x}_j) \pm \varepsilon_\times^a(\vec{x}_i) \varepsilon_\times^b(\vec{x}_j)]}{\sum w_i w_j}, \quad (3.71)$$

where  $w_i$  are the individual weights of each galaxy, the sum is taken over pairs of galaxies with angular separation  $|\vec{x}_i - \vec{x}_j| = \theta$ , and  $\varepsilon_T$  and  $\varepsilon_\times$  are the tangential and cross-ellipticity parameters, respectively. Galaxy weights are used as, for example, one might want to



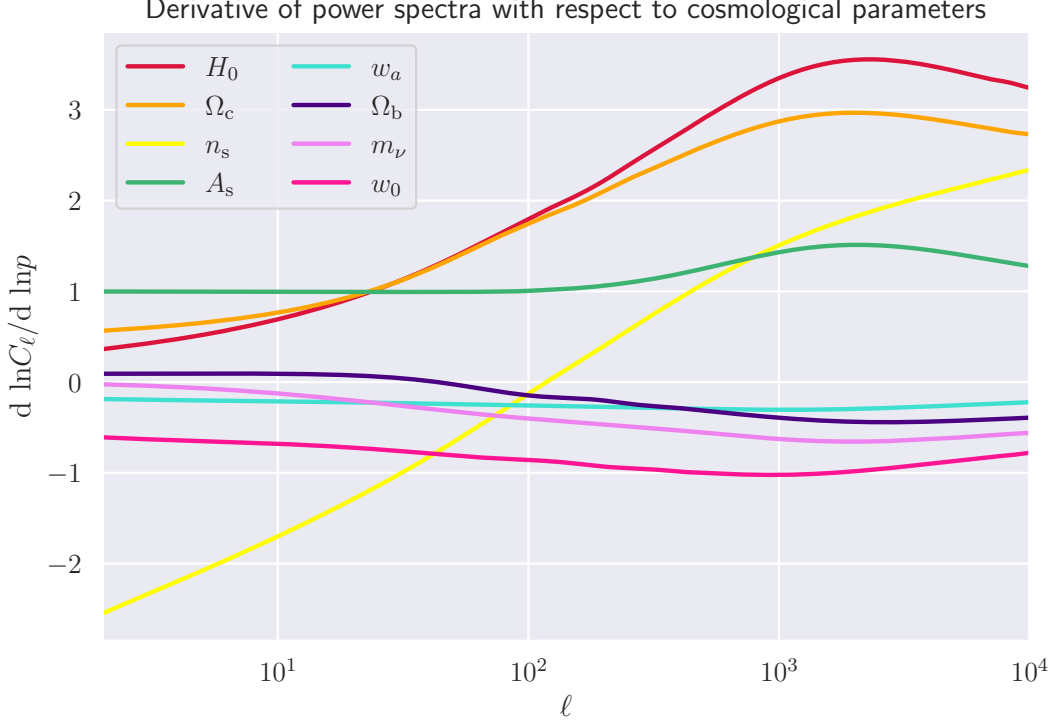


Figure 3.8: Derivatives of the shear power spectrum with respect to input cosmological parameters,  $d \ln C_\ell / d \ln p$ , except for the  $m_\nu$ ,  $w_0$ , and  $w_a$  curves which are  $d \ln C_\ell / dp$ . The curves are coloured and ordered by their amplitude on the right-hand side. Derivates were evaluated for the Gaussian redshift bin located at  $\bar{z} = 2.0$ , and a fiducial cosmology of  $A_s = 2.1 \times 10^{-9}$ ,  $n_s = 0.96$ ,  $H_0 = 70 \text{ km/s Mpc}^{-1}$ ,  $\Omega_c = 0.25$ ,  $\Omega_b = 0.046$ ,  $w_0 = -1$ ,  $w_a = 0$ , and  $m_\nu = 0.06 \text{ eV}$ . We can understand the nature of these curves by recalling that the angular power spectra is the Limber integral over the matter power spectrum weighted by the lensing kernels (Equation 3.68).  $A_s$  and  $n_s$  are the amplitude and tilt of the primordial perturbation power spectrum (Equation 2.64), which then directly feed into the amplitude and tilt of the matter power spectrum (Equation 2.97). Thus, we see that  $A_s$  provides an overall scaling (save for the small non-linear increase) of the  $C_\ell$  values, and that increasing  $n_s$  produces a bluer spectrum – providing the tilt seen above. Increasing the cold dark matter density  $\Omega_c$  increases the gravitational clustering of matter in our Universe, which increases the lensing signal, particularly on smaller-scales. Increasing the baryon density  $\Omega_b$  serves to increase the effect of baryonic feedback processes, and thus suppresses power on smaller-scales. In our lensing integral, have a prefactor of  $H_0^4$  which is then modulated by a  $\mathcal{O}(h^{-3.5})$  term in the matter power spectrum on the largest physical scales [177], which combine for form the  $H_0$  dependence shown. Neutrinos serve to wash out clustering on small-scales thanks to their free-streaming effects, with an increased neutrino mass increasing this suppression of small-scale clustering [178]. More positive values of the dark energy equation of state parameters  $w_0$  and  $w_a$  require that dark energy had a larger physical density in the past (Equation 2.25 and Figure 2.2) and so suppresses the gravitational attraction of matter, decrease the clustering of matter and thus decreasing the lensing angular power spectrum amplitudes. A more thorough discussion about the impacts of time evolving dark energy ( $w_0$  and  $w_a$ ) and massive neutrinos on the weak lensing power spectrum is presented in Appendix B.

down-weight galaxies that have poor or noisy shape measurements, but still include them in the analysis.

The two-point correlation functions can be predicted from the cosmic shear angular power spectrum through [180]

$$\xi_+^{ab}(\theta) = \sum_{\ell} \frac{2\ell + 1}{4\pi} \left[ {}_{EE}C_{\ell}^{ab} + {}_{BB}C_{\ell}^{ab} \right] d_{22}^{\ell}(\theta), \quad (3.72a)$$

$$\xi_-^{ab}(\theta) = \sum_{\ell} \frac{2\ell + 1}{4\pi} \left[ {}_{EE}C_{\ell}^{ab} - {}_{BB}C_{\ell}^{ab} \right] d_{2-2}^{\ell}(\theta), \quad (3.72b)$$

where  $d_{mn}^{\ell}$  are the reduced Wigner  $D$ -matrices, and we have generalised to a case where  $C_{\ell}^{BB} \neq 0$ .

A further statistic can be derived from the correlations in the form of the COSEBIs (Complete Orthogonal Sets of E/B-mode Integrals) statistics which provide a set of  $E_n$  and  $B_n$  values for the  $E$ - and  $B$ -mode shear statistics, respectively, where larger values of  $n$  are typically more sensitive to small-scale information. In terms of the two-point correlation functions, the COSEBI statistics are given as [181, 182]

$$E_n^{ab} = \frac{1}{2} \int_{\theta_{\min}}^{\theta_{\max}} d\theta \, \theta \left[ T_{+n}(\theta) \xi_+^{ab}(\theta) + T_{-n}(\theta) \xi_-^{ab}(\theta) \right], \quad (3.73a)$$

$$B_n^{ab} = \frac{1}{2} \int_{\theta_{\min}}^{\theta_{\max}} d\theta \, \theta \left[ T_{+n}(\theta) \xi_+^{ab}(\theta) - T_{-n}(\theta) \xi_-^{ab}(\theta) \right], \quad (3.73b)$$

where  $T_{\pm n}(\theta)$  are the COSEBI filter functions.

Since the angular power spectrum values are related to the underlying geometry and clustering of our Universe through a single integral (Equation 3.68), rather than two or three sums/integrals for the case of the correlation functions and COSEBIs, the angular power spectrum can be much simpler to model – and thus will be our cosmic shear summary statistic of choice throughout this thesis.

## 3.5 Parameter estimation

Thus far, we have laid down a large amount of theoretical background for modern cosmology. We started with some fundamental theories about the nature of the Universe, and developed them into predictions for physical phenomena that we can go out and measure. While all of our theories are precisely calculated and well-motivated, we still have numerous unknown parameters in our models that we would like to constrain, along with the fundamental assumptions that allowed us to develop these theoretical models. This is where we use our very expensive telescopes and instruments to go looking into our Universe to measure physical properties via physical processes (Section 2.7). Since every measurement comes with it an associated uncertainty, the propagation of uncertainties from our measurements to the parameters that we aim to measure is just as, if not more, important than the measurement of the parameter’s value itself.

This is because a measurement without an uncertainty is no measurement at all; we have no idea if the measurement is important or not and to which degree the new measurement agrees or disagrees with existing values. Thus, the determination of cosmological parameter values and their uncertainties underpin all of modern experimental observational cosmology.

Bayesian statistics form the heart of our parameter estimation statistical analyses, since Bayesian statistics naturally incorporate the degree of *certainty* that we have in our

measurements. The foundation of Bayesian statistics is Bayes' theorem, which is often stated in terms of events  $A$  and  $B$  as

$$P(A|B) = \frac{P(B|A) P(A)}{P(B)}, \quad (3.74)$$

where  $P(A)$  and  $P(B)$  are the probabilities of events  $A$  and  $B$ , respectively, and  $P(A|B)$  and  $P(B|A)$  are the condition probabilities of event  $A$  occurring given that event  $B$  happened, and vice-versa. While this form is useful for dealing with discrete events  $A$  and  $B$ , and their probabilities associated with these events, it becomes less useful when applying it to a cosmological analysis.

Therefore, we shall introduce the idea that we have some data vector  $\vec{x}$ , which has been derived from some observations (e.g. the CMB power spectrum), and a model with some parameters  $\vec{\theta}$  that we want to estimate from our observations. In this case, Bayes' theorem becomes

$$P(\vec{\theta}|\vec{x}) = \frac{P(\vec{x}|\vec{\theta}) P(\vec{\theta})}{P(\vec{x})}. \quad (3.75)$$

Since each term is important in its own right, we have

- $P(\vec{\theta}|\vec{x})$  is the *posterior* for our parameters, and is what we are trying to estimate.
- $P(\vec{x}|\vec{\theta})$  is the *likelihood* and is often denoted by its own symbol  $\mathcal{L}(\vec{x}|\vec{\theta})$  because of its importance.
- $P(\vec{\theta})$  is the *prior* and quantifies our level of certainty in the values of our model, and may encode information from previous results.
- $P(\vec{x})$  is the *evidence* which acts to normalise the posterior, and is mostly ignored in cosmological analyses since the relative probabilities of parameters do not change.

### 3.5.1 Likelihoods

The key to evaluating the posterior distribution of Equation 3.74 is the likelihood. It turns out that the log-likelihood  $\mathcal{L}$  is often the more useful quantity, defined as

$$\mathcal{L} \equiv -\ln \mathcal{L}. \quad (3.76)$$

Unfortunately, for such an important quantity, the likelihood is rarely known exactly for an arbitrary data-set and has to be approximated.

Due to the central limit theorem, the principal likelihood is that of a Gaussian distribution. It is quantified by the mean of the observables (which are a function of the model parameters)  $\vec{\mu}(\vec{\theta})$ , its covariance matrix  $\mathbf{C}$ , and number of observables  $N$ . Here, probability density function is given as

$$p(\vec{x}|\vec{\mu}, \mathbf{C}) = \frac{1}{(2\pi)^{N/2} \sqrt{|\mathbf{C}|}} \exp\left(-\frac{1}{2} [\vec{x} - \vec{\mu}]^T \mathbf{C}^{-1} [\vec{x} - \vec{\mu}]\right), \quad (3.77)$$

and thus we can see that the  $\chi^2$  for the Gaussian distribution is given by

$$\chi^2 = [\vec{x} - \vec{\mu}(\vec{\theta})]^T \mathbf{C}^{-1} [\vec{x} - \vec{\mu}(\vec{\theta})]. \quad (3.78)$$

If each observable is independent of each other, then we have a diagonal covariance matrix where the entries are the variances of each observable  $\sigma_i^2$ , and thus the  $\chi^2$  becomes

$$\chi^2 = \sum_{i=1}^N \frac{1}{\sigma_i^2} [x_i - \mu_i(\vec{\theta})]^2. \quad (3.79)$$

### 3.5.2 Likelihood of $C_\ell$ values

Since having the correct form of the likelihood is essential for any cosmological analysis, we can look at the distribution of the  $C_\ell$  values, which are the observables that we are interested in. Since the underlying  $a_{\ell m}$  values follow a Gaussian distribution of mean zero and variance  $C_\ell$ , we have that their distribution is given by [183]

$$p(a_{\ell m}|C_\ell) = \frac{1}{\sqrt{2\pi C_\ell}} \exp\left[-\frac{|a_{\ell m}|^2}{2C_\ell}\right], \quad (3.80)$$

which gives our previous result of  $\langle |a_{\ell m}|^2 \rangle = C_\ell$  (Equation 2.109). We have that the *estimator* of the power spectrum,  $\tilde{C}_\ell$ , is the average over the  $a_{\ell m}$  values as

$$\tilde{C}_\ell = \frac{1}{2\ell + 1} \sum_m |a_{\ell m}|^2. \quad (3.81)$$

This gives that the  $C_\ell$  values are distributed as the sum of  $\nu \equiv 2\ell + 1$  squared Gaussian distributions, which is a  $\Gamma$  distribution [183] of the form

$$p(\tilde{C}_\ell|C_\ell) \propto C_\ell \left[\frac{\tilde{C}_\ell}{C_\ell}\right]^{\frac{\nu}{2}-1} \exp\left[-\frac{\nu}{2} \frac{\tilde{C}_\ell}{C_\ell}\right]. \quad (3.82)$$

This distribution has a mean of  $C_\ell$  and a variance of  $2C_\ell^2/\nu$  (this factor of  $2/\nu$  is the cosmic variance that we saw in Section 3.4.1). The maximum of this distribution occurs not at the mean value, but instead at  $\tilde{C}_\ell = C_\ell(\nu - 2)/\nu$ . In the high- $\ell$  limit ( $\nu \rightarrow \infty$ ), we find this distribution tends to the Gaussian distribution, due to the central limit theorem<sup>4</sup>.

Figure 3.9 shows this  $\Gamma$  distribution of the estimated  $C_\ell$  values through their relative differences to the mean  $C_\ell$ . This clearly shows that for low  $\ell$  values, the distribution is significantly non-Gaussian and as  $\ell$  increases the distribution tends to a Gaussian due to the central limit theorem.

For the case where we have more than one redshift bin, we find that we have a mix of auto- and cross-spectra for each  $\ell$  value. For the case of two redshift bins, we find the signal matrix for each  $\ell$ -mode,  $\mathbf{S}_\ell$ , to be

$$\mathbf{S}_\ell = \begin{pmatrix} \tilde{C}_\ell^{11} & \tilde{C}_\ell^{12} \\ \tilde{C}_\ell^{12} & \tilde{C}_\ell^{22} \end{pmatrix}, \quad (3.83)$$

where we have used that  $C_\ell^{12} = C_\ell^{21}$  from symmetry arguments. The corresponding theory matrix, at each  $\ell$ -mode, is  $\mathbf{W}_\ell$  given as

$$\mathbf{W}_\ell = \frac{1}{2\ell + 1} \begin{pmatrix} C_\ell^{11} & C_\ell^{12} \\ C_\ell^{12} & C_\ell^{22} \end{pmatrix}. \quad (3.84)$$

These combine to form the Wishart likelihood of [183]

$$\mathcal{L}(\mathbf{S}_\ell|\mathbf{W}_\ell) = \frac{|\mathbf{S}_\ell|^{(\nu-p-1)/2} \exp\left[-\text{Tr}\left(\mathbf{W}_\ell^{-1}\mathbf{S}_\ell/2\right)\right]}{2^{p\nu/2} |\mathbf{W}_\ell|^{\nu/2} \Gamma_p(\nu/2)}, \quad (3.85)$$

where  $\mathbf{S}_\ell$  and  $\mathbf{W}_\ell$  are positive-definite symmetric  $p \times p$  matrices,  $\nu > p$ , and  $\Gamma_p$  is the multivariate Gamma function. In the high- $\ell$  limit, this Wishart distribution tends towards the multivariate Gaussian distribution [184].

<sup>4</sup>Unless, of course, if the limit does not exist.

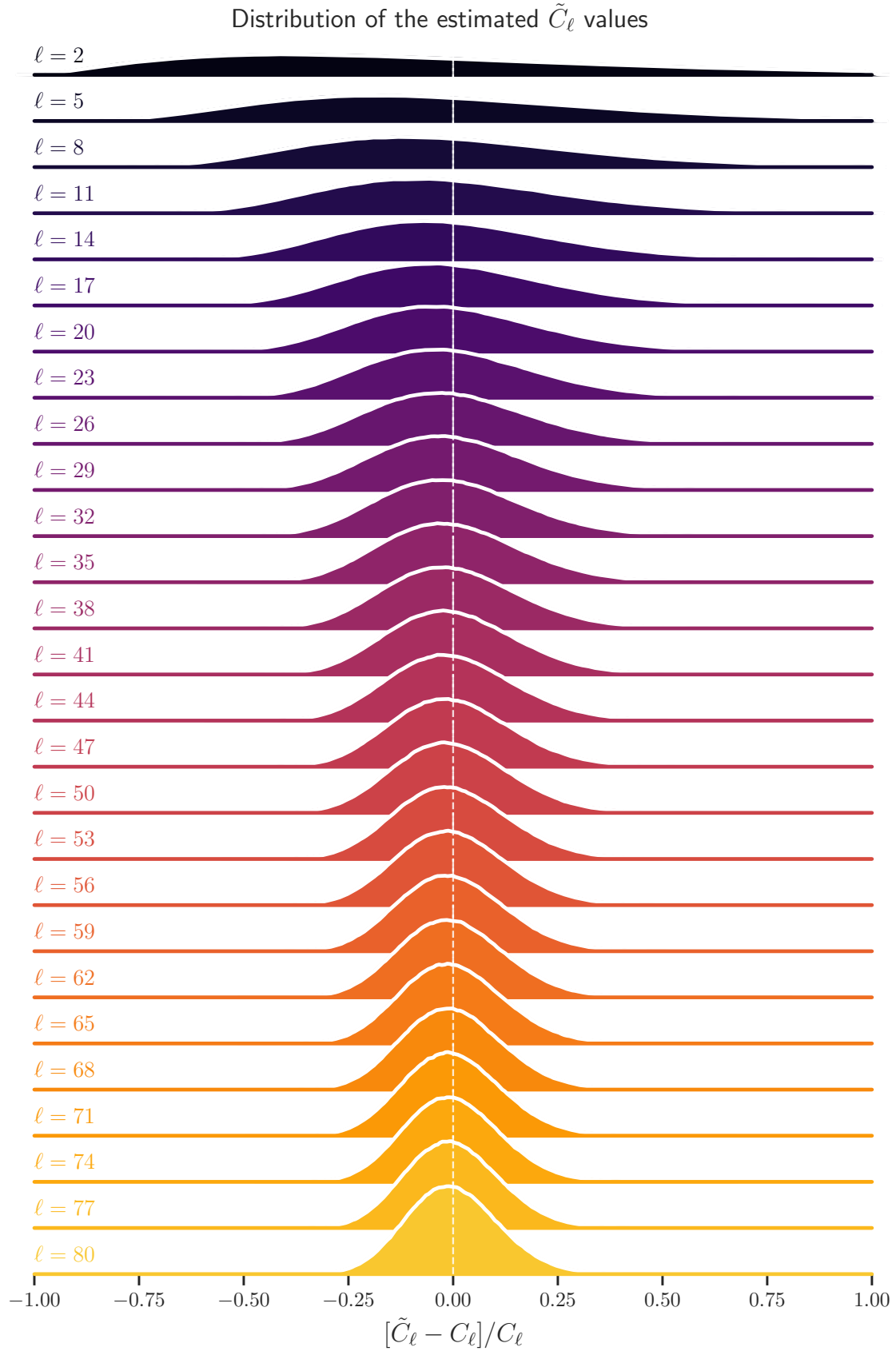


Figure 3.9: Relative distribution of the estimated power spectrum coefficients,  $\tilde{C}_\ell$ , with respect to their average value,  $C_\ell$ , for an ensemble of one million realisations. We can see that for low  $\ell$  values, the distribution is significantly non-Gaussian, where the  $C_\ell$  distributions exhibit significant skewness and excess kurtosis, since they follow the  $\Gamma$  distribution. Once the  $\ell$  value becomes significantly large ( $\ell \gtrsim 50$ ), their distribution can be well-approximated by a Gaussian.

### 3.5.3 Priors

The fundamental philosophy of Bayesian parameter estimation is that we evaluate the posterior distribution using Bayes’ theorem (Equation 3.75) to ‘update’ our knowledge about some parameters or models as more information is gained about the system. With zero evaluations of the posterior, the initial knowledge about the system comes from the prior distribution  $P(\vec{\theta})$ . This distribution is usually informed by existing experiments and measurements of our parameters, or by physical constraints (e.g. the sum of neutrino masses being non-negative).

#### Flat priors

A weakly-informative prior is the flat, or uniform, prior. For a single parameter  $\theta$ , its flat prior is defined as

$$P(\theta) = \begin{cases} \frac{1}{\theta_{\text{MAX}} - \theta_{\text{MIN}}} & \text{for } \theta_{\text{MIN}} \leq \theta \leq \theta_{\text{MAX}}, \\ 0 & \text{otherwise.} \end{cases} \quad (3.86)$$

Thus, with a flat prior, the posterior is simply directly proportional to the likelihood.

While flat priors may appear harmless since they just provide lower and upper bounds on the parameter’s value, in high dimensional spaces the very many 1D flat priors serve to cause samplers to concentrate on a thin shell of a  $D$ -dimensional hypercube [185]. To obtain a truly uninformative prior, one must use the Jeffreys prior, which partially mitigates the impact of volume effects and is insensitive to model parametrisations [186, 187].

### 3.5.4 Markov chain Monte Carlo

Thus far, we have seen that the posterior distribution is incredibly useful for parameter estimation problems in cosmology. Hence, we wish to have numerical tools which allow us to form estimates of the posterior, and thus form constraints on our parameters. The main numerical tool of choice are Markov chain Monte Carlo<sup>5</sup> (MCMC) which aims to generate a series of points whose distribution is the same as the posterior, and thus an unbiased estimator for the posterior.

#### Metropolis-Hastings algorithm

The simplest MCMC algorithm is the Metropolis-Hastings algorithm which gives the acceptance probability of a new point in the chain with parameters  $\vec{\theta}'$  over the existing set of parameters  $\vec{\theta}$  as [188]

$$P(\text{acceptance}) = \min \left[ \frac{P(\vec{\theta}'|\vec{x})}{P(\vec{\theta}|\vec{x})}, 1 \right]. \quad (3.87)$$

This probability is then compared to a uniform random number  $\alpha$  in the interval  $[0, 1)$  and accept the new parameters if  $P > \alpha$ , otherwise the new parameters are rejected and the existing ones are written into the chain with the algorithm starting again with a new set of proposed points.

---

<sup>5</sup>Name comes from the Monte Carlo Casino in Monaco and the random nature of the gambling within it.

## Nested samplers

An alternative method to chain-based MCMC algorithms are the nested samplers, which directly evaluates the evidence and is advantageous in high-dimensional parameter spaces and complex likelihood surfaces [189, 190]. Popular implementations of nested sampling algorithms are MultiNest [191–193] and PolyChord [194, 195].

### 3.5.5 Fisher matrix formalism

The Fisher matrix formalism provides an alternative method to obtaining cosmological parameter covariances from MCMC simulations, thus saving significant computational costs since MCMC analyses require significantly many evaluations of the likelihood ( $10^5$  to  $10^6$  evaluations). The Fisher matrix formalism has primarily been used to derive parameter covariance estimates, not for parameter values which requires us to fall-back to MCMC analyses. The Fisher matrix is formally defined as the second derivative of the log-likelihood ( $\mathcal{L}$ ) with respect to our parameters of a model ( $\vec{\vartheta}$ ). The Fisher matrix for parameters  $\alpha$  and  $\beta$  is

$$F_{\alpha\beta} \equiv - \left\langle \frac{\partial^2 \mathcal{L}}{\partial \vartheta_\alpha \partial \vartheta_\beta} \right\rangle, \quad (3.88)$$

and thus for an  $N$ -parameter model, its corresponding Fisher matrix is an  $N \times N$  matrix [196]. We can directly obtain parameter standard deviations from the Fisher matrix by taking the diagonal of its inverse matrix which gives the Cramér-Rao inequality of

$$\sigma_\alpha \geq \sqrt{[\mathbf{F}^{-1}]_{\alpha\alpha}} \quad (3.89)$$

which gives the minimum 1- $\sigma$  marginalised error bars for any unbiased estimator of the parameters from the data [197].

If we assume that our data follows a multivariate Gaussian distribution, then it is simply characterised by the mean vector  $\vec{\mu}$  and covariance matrix  $\mathbf{C}$ . In this case, we can analytically calculate the Fisher matrix, which is a function of these two objects only, as [196]

$$\mathbf{F}_{\alpha\beta} = \frac{1}{2} \text{Tr} \left[ \mathbf{C}^{-1} \frac{\partial \mathbf{C}}{\partial \vartheta_\alpha} \mathbf{C}^{-1} \frac{\partial \mathbf{C}}{\partial \vartheta_\beta} \right] + \frac{\partial \vec{\mu}}{\partial \vartheta_\alpha} \mathbf{C}^{-1} \frac{\partial \vec{\mu}}{\partial \vartheta_\beta}. \quad (3.90)$$

Since the mean of the cosmic shear field is zero, we are free to transform our Fisher matrix into one for the power spectrum coefficients, in which case the cosmological dependence of the covariance matrix drops out and we are left with [157]

$$\mathbf{F}_{\alpha\beta} = \frac{\partial \vec{C}_\ell}{\partial \vartheta_\alpha} \mathbf{C}^{-1} \frac{\partial \vec{C}_\ell}{\partial \vartheta_\beta}, \quad (3.91)$$

which is analogous to the Gaussian likelihood, but now we're inverse covariance weighting the derivatives of the power spectra, not the differences between data and theory.

Since we can easily compute the partial derivatives of the power spectrum coefficients with respect to parameters and form a fiducial covariance matrix, the estimation of the Fisher matrix becomes straightforward and thus parameter constraints are readily computed.

## The figure of merit

When comparing different models with different Fisher matrices, it is often useful to see how constraining each model is for a sub-set of two parameters. This can be done through the figure of merit (FoM), which is inversely proportional to the area of the  $2\text{-}\sigma$  marginalised contour for two parameters  $\vartheta_\alpha$  and  $\vartheta_\beta$ . The figure of merit for any two parameters is given as in terms of the sub-Fisher matrix  $\tilde{\mathbf{F}}$  as [157]

$$\text{FoM}_{\alpha\beta} = \sqrt{\det [\tilde{\mathbf{F}}_{\alpha\beta}]}. \quad (3.92)$$

## The figure of bias

Using the Fisher matrix, we can also compute the level of expected bias in the cosmological parameters when using a different model for the recovery of parameters to one that was used to generate the original data. This is useful since we can see how changing models affects the bias in the parameters, hopefully optimising the models to have the smallest possible biases. The bias on parameter  $\vartheta_\alpha$ ,  $\delta\vartheta_\alpha$ , is given by [198]

$$\delta\vartheta_\alpha = [\mathbf{F}^{-1}]_{\alpha\beta} \left( \vec{C}_\ell^{\text{true}} - \vec{C}_\ell^{\text{model}} \right) \mathbf{C}^{-1} \frac{\partial \vec{C}_\ell}{\partial \vartheta_\beta}. \quad (3.93)$$

The figure of bias (FoB), which is an overall summary statistic quantifying how biased the parameters are overall, can then be computed from the combination of individual parameter biases though [199]

$$\text{FoB} = \sqrt{\delta\vec{\vartheta}_\alpha \tilde{\mathbf{F}}_{\alpha\beta} \delta\vec{\vartheta}_\beta}. \quad (3.94)$$

Thus, with the Fisher matrix, we can provide both constraints on both the size and offset of parameter contours for different models, thus enabling us to select the most optimal methods for a given data-set.

## 3.6 $C_\ell$ Covariance matrix

Core to the accurate and precise measurement of cosmological parameters through MCMC methods is the data covariance matrix,  $\mathbf{C}$ . The incorrect specification of this matrix could lead to parameter constraints that are either off-set from their true values, and/or contours that are too large or small, neither of which are desirable outcomes from the data. Thus, correct evaluation of the covariance matrix is critical for any cosmological survey.

There exists two broad categories from which a covariance matrix can be estimated from: analytically, and numerically. Analytic methods aim to provide the covariance matrix in closed-form expressions, usually as a function of the underlying power spectra. Numerical methods aim to produce very many realisations of the underlying fields, and then take a numerical covariance of the resulting observables. Both methods provide a useful cross-check of the other, and we expand on these methods significantly in Chapter 5, however a small discussion of analytic methods is presented here.

### 3.6.1 Gaussian covariance

While the proper distribution of the  $C_\ell$  values follow a Wishart distribution (Equation 3.85), this can be accurately approximated to the Gaussian distribution for cosmic



shear [184]. In the full-sky limit, the covariance of two power spectra  $C_\ell^{ab}$  and  $C_{\ell'}^{cd}$ , including the effects of shape noise, is given by the four-point function of

$$\text{Cov} [C_\ell^{ab}, C_{\ell'}^{cd}] = \frac{\delta_{\ell\ell'}}{(2\ell+1)} (C_\ell^{ac} C_\ell^{bd} + C_\ell^{ad} C_\ell^{bc}). \quad (3.95)$$

This can be modified to account for the effects of the cut-sky through the scaling relation approximation of

$$\text{Cov} [C_\ell^{ab}, C_{\ell'}^{cd}] = \frac{\delta_{\ell\ell'}}{(2\ell+1) f_{\text{sky}}} (C_\ell^{ac} C_\ell^{bd} + C_\ell^{ad} C_\ell^{bc}), \quad (3.96)$$

where  $f_{\text{sky}}$  is the fraction of sky observed. Thus, the error on a single power spectrum is

$$\Delta C_\ell = \sqrt{\frac{2}{(2\ell+1) f_{\text{sky}}}} [C_\ell^{EE} + N_\ell], \quad (3.97)$$

where  $N_\ell$  is the noise spectrum, given by Equation 3.70. Thus, there are three regimes to the errors on the cosmic shear power spectrum:

1. **Cosmic variance limited.** Here, the  $1/\sqrt{\ell}$  term dominates the errors, since for low multipoles there are only a limited number of  $a_{\ell m}$  modes that can contribute to each  $C_\ell$ . Thus, cosmic shear is not particularly sensitive to the largest angular scales.
2. **Signal dominated.** In this region, we have enough  $a_{\ell m}$  modes per  $C_\ell$  such that each measurement is statistically significant, and that our cosmic shear signal dominates over the shape noise - and thus we are able to extract maximum information from our shape measurements.
3. **Shape noise dominated.** Here, the shape noise spectrum is much larger than the cosmic shear signal ( $N_\ell \gg C_\ell^{EE}$ ), which holds on the smallest scales. Thus, to adequately probe the smallest scales, large numbers of galaxies are needed to be observed over the sky, which requires deep and precise measurements.

### 3.6.2 Super-sample and non-Gaussian covariances

In addition to the simple Gaussian term, there exists the residual covariance from the non-Gaussianity of the underlying field, which generates higher-order correlations and forms the non-Gaussian covariance term. There also exists the super-sample covariance, which arises from the correlation between modes within the survey and those on larger scales than the survey footprint. Both the non-Gaussian and super-sample covariance terms contribute significantly to the overall covariance matrix, particularly for the off-diagonal terms [200, 201]. If these additional terms are not present, then this can lead to an underestimate in the uncertainties on cosmological parameters of up to 70%. Thus, it is essential that any cosmic shear survey include these terms in their covariance matrices to ensure accurate parameter constraints.

While these additional covariance terms are important to keep in a full cosmic shear analysis, we are going to neglect them — opting for a Gaussian-only covariance matrix for the rest of this thesis — for the sake of simplicity.

## 3.7 Information gain at high redshift

When discussing the Gaussian covariance matrix, Section 3.6.1, we noted that there were three regions in which the errors on the power spectrum fall into - with the signal dominated region driving the constraining power of cosmic shear. Thus, we would like to have

the signal-dominated region to be as large as possible, which requires that  $C_\ell \gg N_\ell$  for a wide range of  $\ell$  values. Since the angular power spectra values increase as we observe galaxies at higher redshift, due to their light rays passing through more of the Universe's large-scale structure (see Figure 3.7), galaxies at higher redshifts have more statistical power than those at low redshifts

We can quantify this statistical power through the signal-to-noise (S/N). For a signal vector  $\vec{d}$  with covariance matrix  $\mathbf{C}$ , its signal-to-noise is defined as

$$\text{S/N} \equiv \sqrt{\vec{d}^T \mathbf{C}^{-1} \vec{d}}. \quad (3.98)$$

Applying this to a single cosmic shear power spectrum bin, and using the fact that the inverse of a diagonal matrix is a matrix of the reciprocal values along the diagonal, we find its signal-to-noise to be given by

$$[\text{S/N}]^2 = \sum_{\ell=2}^{\ell_{\text{MAX}}} \frac{(2\ell+1) f_{\text{sky}}}{2} \frac{[C_\ell^{EE}]^2}{[C_\ell^{EE} + N_\ell]^2}, \quad (3.99)$$

$$= \sum_{\ell=2}^{\ell_{\text{MAX}}} \frac{(2\ell+1) f_{\text{sky}}}{2} \left[ 1 + \frac{N_\ell}{C_\ell^{EE}} \right]^{-2}. \quad (3.100)$$

We can now study how this signal-to-noise changes as a function of the maximum multipole ( $\ell_{\text{MAX}}$ ) considered.

In Figure 3.10 we plot the signal-to-noise for the auto-correlations of eight Gaussian redshift bins centred at  $\bar{z} = \{0.25, 0.50, 0.75, 1.00, 1.25, 1.50, 1.75, 2.00\}$ , all with widths  $\sigma_z = 0.15$ . We see that due to the increasing amplitude of the shear power spectrum with redshift, the further away bins have a significantly greater signal-to-noise than the close redshift bins. Additionally, the lower redshift bins saturate their information content around  $\ell_{\text{MAX}} \sim 2000$ , providing very little benefit to measuring the power spectrum beyond that, whereas the higher redshift bins still gain information even down to an  $\ell_{\text{MAX}}$  of 5000.

### 3.7.1 Including cross-correlations

So far, we have been looking at the signal-to-noise of a single bin's auto spectra as a function of redshift. In a real cosmic shear survey, not only do we have access to the auto-spectra, but we can cross-correlate these bins to obtain cross-spectra. This has the powerful advantages of both dramatically increasing the number of spectra in our data-vector (the number of spectra scales as  $n_{\text{spectra}} = n_{\text{bins}}[n_{\text{bins}} + 1]/2$ ), but also having the property that the variances of the cross-spectra feature a reduced impact from contributions from shape noise (though while their power spectrum coefficients  ${}_{EE}C_\ell^{ab}$  [ $a \neq b$ ] do not feature any shape noise, their covariances are still partially dependent on shape noise). This can be seen by specialising our Gaussian covariance (Equation 3.96) to that of a cross-correlation (where  $ab = cd$ ,  $a \neq b$ ),

$$\text{Cov} [C_\ell^{ab}, C_{\ell'}^{ab}] = \frac{\delta_{\ell\ell'}}{(2\ell+1) f_{\text{sky}}} \left( [{}_{EE}C_\ell^{aa} + N_\ell] [{}_{EE}C_{\ell'}^{bb} + N_{\ell'}] + [{}_{EE}C_\ell^{ab}]^2 \right), \quad (3.101)$$

Thus, when considering the covariances of the cross-spectra, we find that the impact of shape noise is reduced when compared to the auto-spectra. This reduces the effect of the shape-noise dominated region at high  $\ell$ , and so we can extract more information from this region due to the larger signal-to-noise than from auto-spectra, which motivates us to measure the shear power spectrum to large  $\ell$  values (small angular scales).

Now, while it is true that the signal-to-noise will be higher for the cross-spectra, to properly model them we need to build a full covariance matrix featuring both auto- and

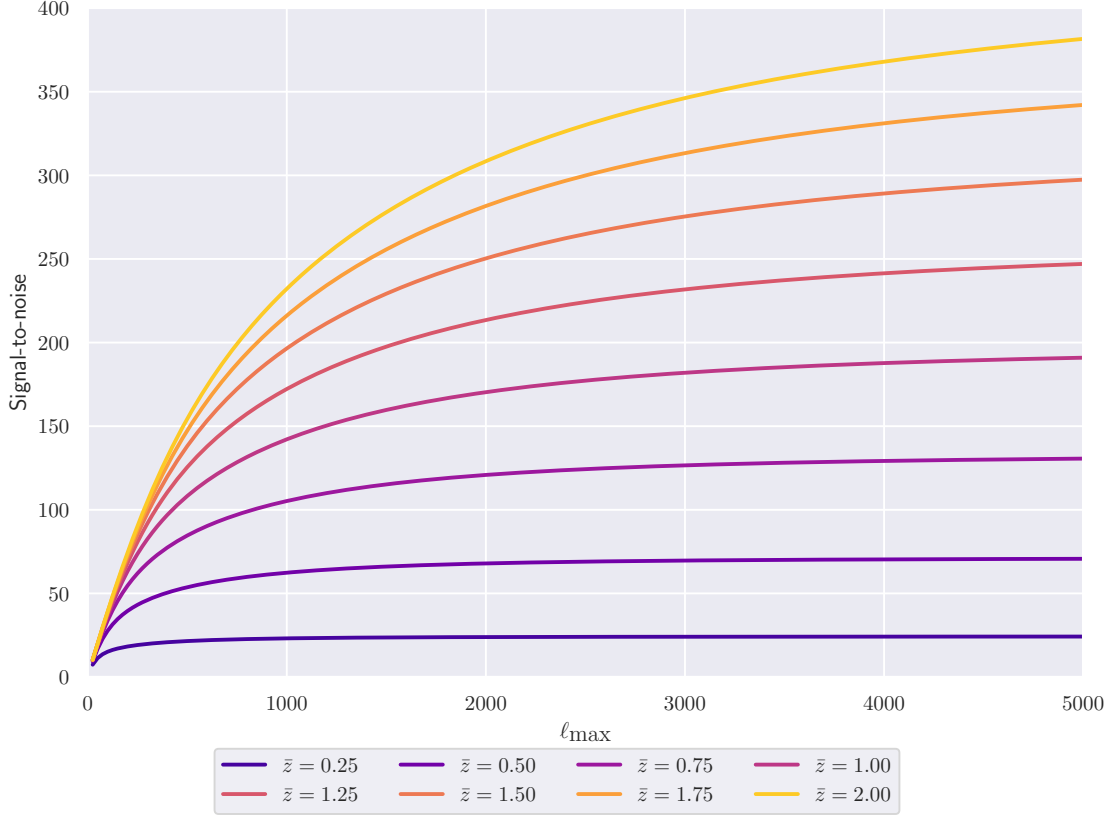


Figure 3.10: The signal-to-noise of the auto-correlation for eight different Gaussian redshift bins with centres  $\bar{z}$ , as a function of the maximum multipole considered. We see that the signal-to-noise amplitude and profile is highly bin dependent. The low-redshift bins have both an intrinsically smaller signal-to-noise and saturate around  $\ell_{\text{MAX}} \sim 1000$ . In contrast, the higher redshift bins, which have a larger cosmic shear signal, have a larger signal-to-noise, and do not saturate until around  $\ell_{\text{MAX}} \sim 4000$ . Thus, the optimal cosmic shear survey would probe the smallest scales at the highest redshifts possible.

cross-spectra. Let us consider the case for two photometric redshift bins, which gives us three unique spectra:  $1 \times 1$ ,  $1 \times 2$ , and  $2 \times 2$ . Thus, the full covariance matrix will be made out of nine sub-blocks, as follows

$$\mathbf{C} = \begin{pmatrix} \mathbf{C}_{11 \times 11} & \mathbf{C}_{11 \times 12} & \mathbf{C}_{11 \times 22} \\ \mathbf{C}_{12 \times 11} & \mathbf{C}_{12 \times 12} & \mathbf{C}_{12 \times 22} \\ \mathbf{C}_{22 \times 11} & \mathbf{C}_{22 \times 12} & \mathbf{C}_{22 \times 22} \end{pmatrix}, \quad (3.102)$$

where each sub-block  $\mathbf{C}_{ab \times cd}$  can be computed using Equation 3.96. Hence, when we invert this covariance matrix, the sub-blocks get convoluted with each other, and so even though the cross-spectra have a reduced impact from shape noise, they still get additional contributions to their (inverse) covariances arising from the mixing from the auto-spectra.

We can now repeat the same exercise as shown in Figure 3.10, but now including the effects of cross-spectra in the signal-to-noises. Figure 3.11 plots the signal-to-noise of the auto- and cross-correlations, along with the total signal-to-noise of the entire data-vector. Here, we see the same trend with higher redshift bins having larger signal-to-noise, but we also see how the suppression of shape noise in the cross-correlations leads to higher signal-to-noise for these spectra. Furthermore, we see the total signal-to-noise (plotted in the pink dot-dashed curve) continues to grow even for our maximum multipole of 5000. Thus, probing the smallest scales with cosmic shear continues to provide valuable information content and constraining power here.

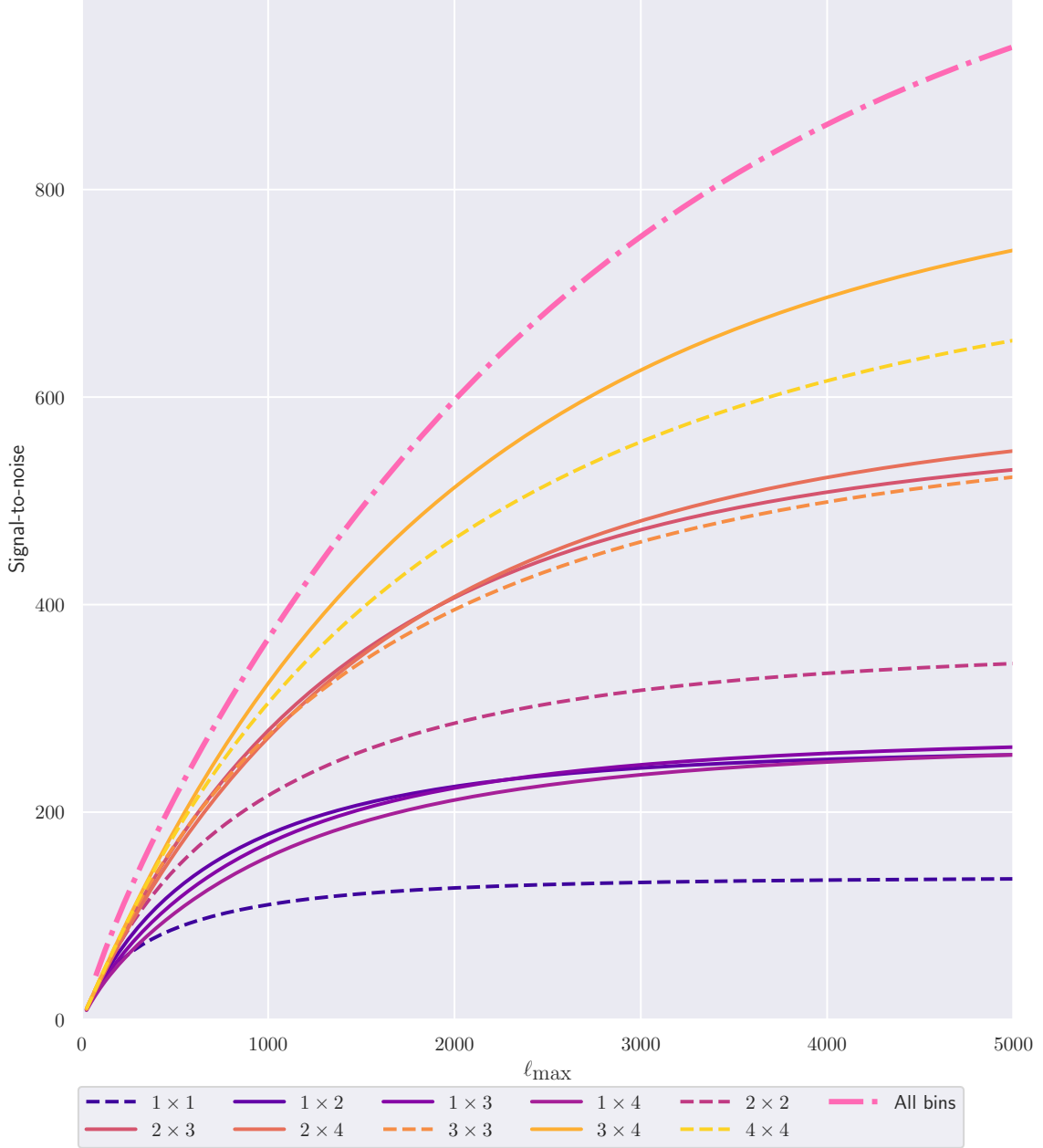


Figure 3.11: The signal-to-noise of the auto- and cross-correlations for four different Gaussian redshift bins, as a function of the maximum multipole considered, along with the total signal-to-noise of all bin combinations in dot-dashed pink. We see that the signal-to-noise amplitude and profile is still highly bin dependent, with low-redshift bins having a smaller signal-to-noise than higher redshift bins. We also see that the cross-correlations (plotted in the solid curves) have systematically larger signal-to-noises than the auto-correlations (plotted in the dashed lines), which reflects the reduced impact of shape noise in their covariances since the cross-correlations lack shape noise contributions in their data-vectors. The total signal-to-noise of the entire data-vector (dot-dashed pink curve) still increases even as we approach an  $\ell_{\text{MAX}}$  of 5000. Hence, while many of the individual spectra appear to saturate on these small-scales, we still gain considerable overall constraining power on the smallest scales. It is also important to note that the total signal-to-noise is not just the sum of the individual signal-to-noises. This is because there is significant correlation between the higher and lower redshift curves, which reduces the total overall information content available [160].

### 3.8 Baryonic feedback in the angular power spectrum

Since the cosmic shear angular power spectrum is a Limber integral of the matter power spectrum, weighted by the lensing kernels, any baryonic feedback effects that alter the matter power spectrum (see Section 2.6.3) will also alter the observed angular cosmic shear power spectrum. As baryonic feedback mostly impacts the small-scale clustering, that is large wavenumbers ( $k \gtrsim 1 \, h\text{Mpc}^{-1}$ ), this will propagate into contaminating our small-scale angular modes ( $\ell \gtrsim 100$ ) – modes provide significant contributions to the signal-to-noise, particularly for the dark energy equation of state parameters  $w_0$  &  $w_a$  and the neutrino masses  $m_\nu$ .

Since we are aiming to measure the angular power spectrum down to small-scales with high precision, in order to place tight constraints on the values of  $w_0$ ,  $w_a$ , and  $m_\nu$ , baryonic feedback could catastrophically bias our results for these parameters (along with measurements of the lensing amplitude  $S_8$  and matter density  $\Omega_M$ ). Hence, we are driven to apply our models of baryonic feedback in the matter power spectrum to our cosmic shear analyses. Else, we would be forced to discard all data which is contaminated by baryonic feedback, leaving only a tiny number of data-points from our original observations, a highly unsatisfactory process.

Using the HMCode-2020 model of baryonic feedback, Figure 3.12 plots the ratio of the angular power spectrum values obtained using the model of baryonic feedback to that without baryonic feedback in, and for the four different astrophysical parameters of the model (by row). This is broadly analogous to Figure 2.11, but now we are comparing the effects of baryonic feedback on the angular scales, which is the observable. Additionally, we plot the ratio for two Gaussian redshift bins, one centred at  $\bar{z} = 0.5$  and one at  $\bar{z} = 2.0$ , which shows that the effects of baryonic feedback changes with redshift.

HMCode-2020 is only one model of baryonic feedback and while its functional form and values of its astrophysical parameters have been motivated from hydrodynamical simulations, there is no guarantee that it can reproduce the exact form of baryonic feedback that takes place within our Universe. Hence, while it is an extremely useful model that allows our analyses to probe much smaller angular scales than otherwise possible, we should remember that it's only a model and thus susceptible to errors, as *any* model is.

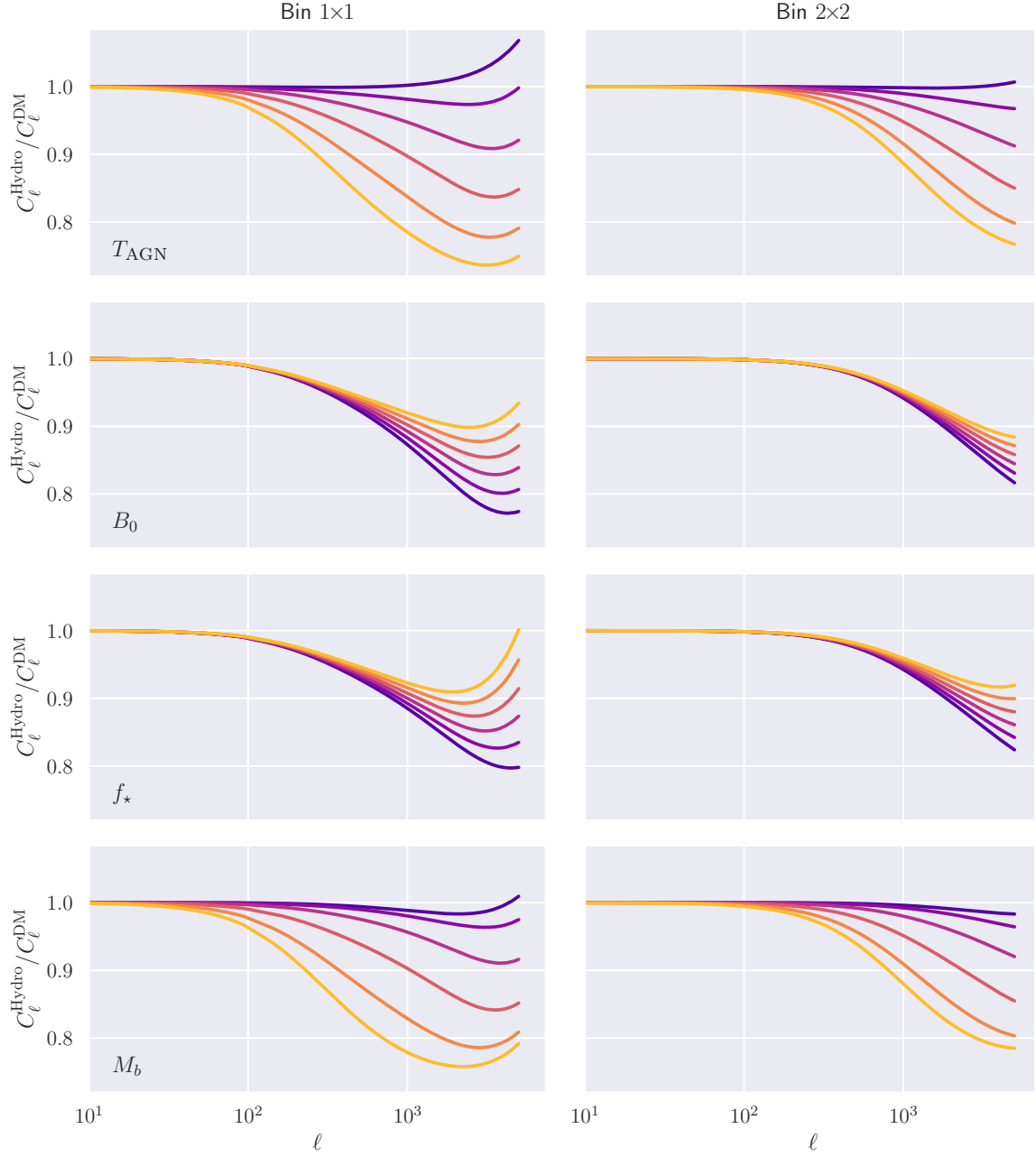


Figure 3.12: Ratio of the cosmic shear angular power spectrum for the case with baryonic feedback ( $C_{\ell}^{\text{Hydro}}$ ) to that without any feedback present ( $C_{\ell}^{\text{DM}}$ ), for two Gaussian redshift bins, one centred at  $\bar{z} = 0.5$  and one at  $\bar{z} = 2.0$  (the columns), and for a range of the four astrophysical parameters present in the HMCode-2020 model (by row, where the blue [yellow] curve represents a smaller [larger] value of that parameter). We plot the ratios out to an  $\ell_{\text{MAX}}$  of 5000, the optimistic target for Stage-IV cosmic shear surveys, such as *Euclid* [164].

*I think we agree,  
the past is over*

—George W. Bush

# 4

## Concordance cosmology in 2024

**Outline.** I briefly overview some of the challenges and outlook for cosmology in 2024<sup>a</sup>.

<sup>a</sup>I am aware that this chapter will probably age horribly; *Tempora mutantur, nos et mutamur in illis*.

### 4.1 Current tensions in cosmology

I’m sure that every cosmology PhD since the dawn of science have said something along the lines of “Now is a very exciting time to be a cosmologist”, but we are living in an era of precision cosmology such that it’s an entirely different kind of science, altogether!<sup>1</sup> With the dramatic increase in the precision of data, and thus cosmological constraints, any small disagreement between data sets becomes increasingly large as the error bars on the measurements decrease. We measure the disagreement between two values through their  $\sigma$  significance. Assuming Gaussian errors, then two measurements that have a  $2\text{-}\sigma$  tension have a 2.3 % one-sided probability of being a statistical fluctuation which, while somewhat significant, is still unsatisfactory to call this a genuine discrepancy.

#### 4.1.1 The $H_0$ tension

The Hubble rate  $H$  was defined through Equation 2.13 as  $H \equiv \dot{a}/a$ , where  $\dot{a} \equiv da/dt$ , and measures the rate of expansion in the Universe. The Hubble constant  $H_0$  is the present expansion rate of our Universe today, given as  $H_0 \equiv H(t = t_0)$ , and is an important observational quantity for any cosmological survey to measure,

Measurements of  $H_0$  fall into two broad categories: direct and indirect measurements, as described below.

#### Direct measurements

We call direct measurements anything that does not need to infer the  $H_0$  value through a cosmological model and instead measures the  $H_0$  value directly. Such example is the

---

<sup>1</sup>*It’s an entirely different kind of science*

measurements of the recessional velocity of supernovae through the distance-redshift relation, as seen in Section 2.7.1. Some of the tightest direct measurements on  $H_0$  using Type Ia supernovae come from the SH0ES collaboration using measurements from the *Hubble* space telescope, finding a value of  $H_0 = (73.04 \pm 1.04) \text{ km/s Mpc}^{-1}$  [202].

### Indirect measurements

Indirect measurements differ by requiring a model, usually the  $\Lambda$ CDM model, and a number of assumptions to relate quantities that were measured in the earlier universe to the Hubble constant today. The leading constraint from the indirect measurements come from the CMB anisotropy measurements (Section 2.7.2) from the *Planck* 2018 data release finding  $H_0 = (67.36 \pm 0.54) \text{ km/s Mpc}^{-1}$  using their ‘TT,TE,EE+lowE+lensing’ dataset [40].

### Tensions

If we compare the *Planck* 2018 and latest SH0ES results, then we find a  $5\text{-}\sigma$  discrepancy between their two  $H_0$  values, which is highly statistically significant. This tension extends beyond these two individual results, as Figure 4.1 shows a summary of results of various direct and indirect measurements showing that *in general* indirect measurements predict a low  $H_0$  value whereas direct measurements find a high  $H_0$  value. The nature of this tension has been extensively discussed in the literature but with no solid theoretical framework in place, much of the discussion have been speculation with no concrete results thus far.



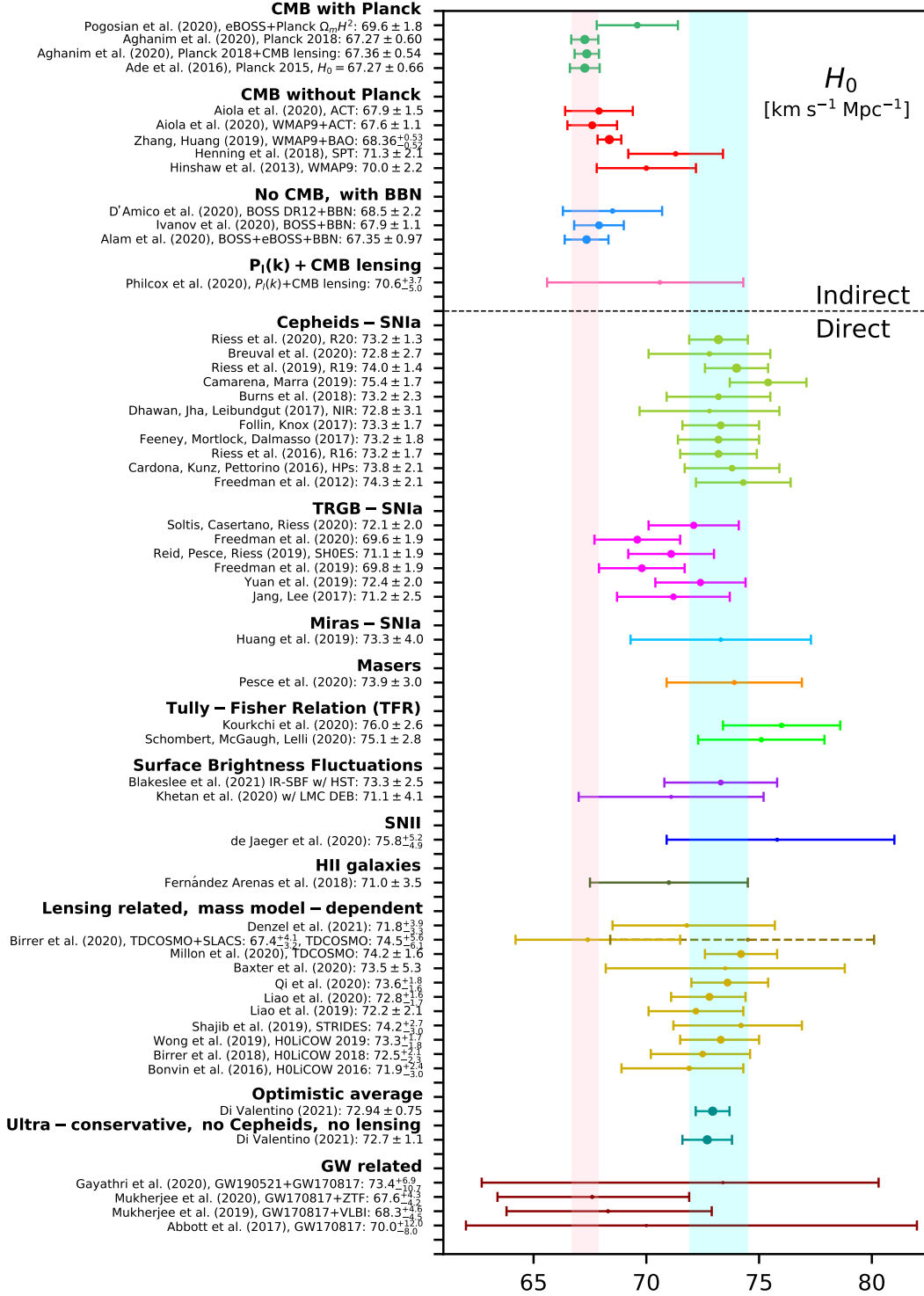


Figure 4.1: Whisker plot showing the different  $1-\sigma$  (68 %) widths on  $H_0$  results from different probes and analyses choices. This shows a clear distinction between results obtained from direct and indirect means. Figure taken from Ref. [203].

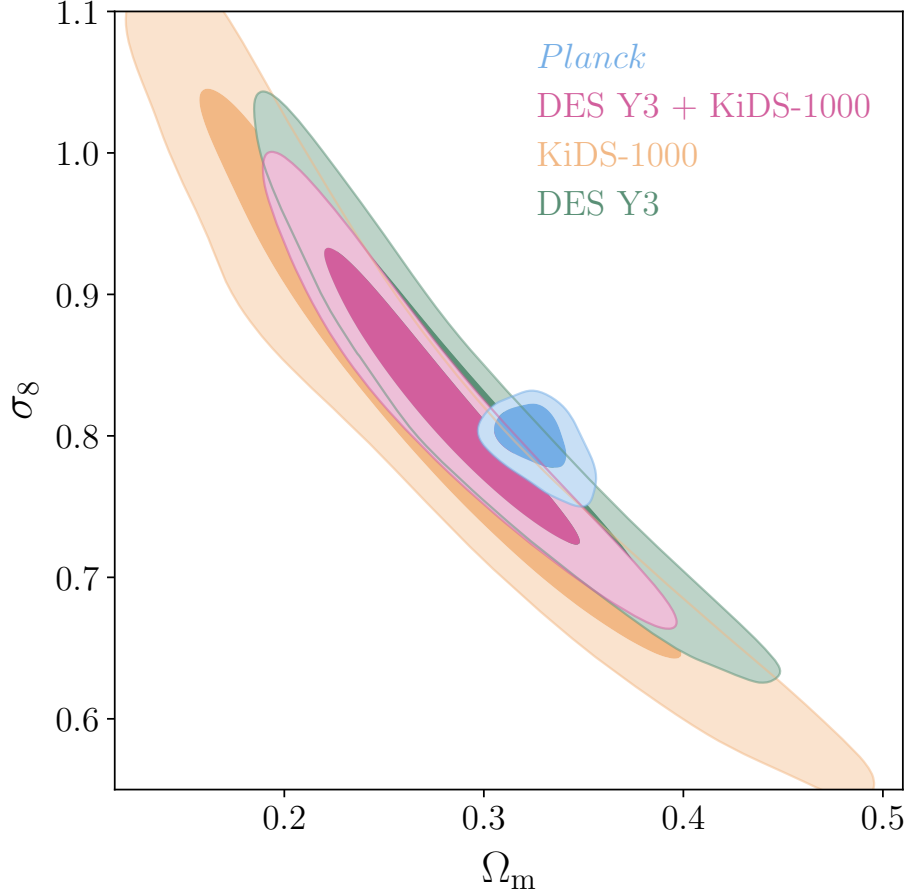


Figure 4.2: Joint  $\sigma_8 - \Omega_M$  constraints from the *Planck* 2018 results [40], the individual KiDS-1000 and DES Y3 results, and the joint KiDS-DES analysis [204] showing the distinctive ‘lensing bananas’ from the weak lensing analyses, how the CMB constraints are not subject to this degeneracy, and showing the approximately  $1.7\sigma$  discrepancy between the cosmic shear and CMB constraints. Figure taken from Ref. [204].

#### 4.1.2 The $S_8$ tension

While not as statistically significant as the  $H_0$  tension at present, a tension in the value of  $S_8$  has been lurking in the literature for a number of years and is a significant target for current and future cosmological surveys. The  $S_8$  parameter roughly approximates the amplitude of weak lensing distortions, and is defined as  $S_8 \equiv \sigma_8 \sqrt{\Omega_M/0.3}$  where  $\sigma_8$  is defined through Equation 2.91. This was chosen as  $S_8$  is related to the width of the ‘lensing bananas’ from weak lensing studies in the  $\sigma_8 - \Omega_M$  plane. Here, we find large degeneracies in the joint  $\sigma_8 - \Omega_M$  distribution, but the width of this degeneracy is tightly constrained by weak lensing (see Figure 4.2).

Again, this tension arises between the late universe (weak lensing and galaxy clustering) and early universe (CMB) measurements. The tightest CMB constraints again come from the *Planck* 2018 release using their ‘TT,TE,EE+lowE+lensing’ dataset finding an  $S_8$  value of  $0.832 \pm 0.013$  [40]. The tightest weak lensing constraints come from the joint analyses of the KiDS-1000 and DES Y3 datasets finding an  $S_8$  value of  $0.790^{+0.018}_{-0.014}$  [204]. This gives an agreement at approximately  $1.7\sigma$  which, while not totally consistent, is not large enough to say that there is a significant deviation between the two results at the moment.

Figure 4.3 presents a summary of current  $S_8$  results, again broken down into early and late universe measurements, where the early universe results preferring a slightly higher  $S_8$  value and late universe results preferring a lower  $S_8$  value.

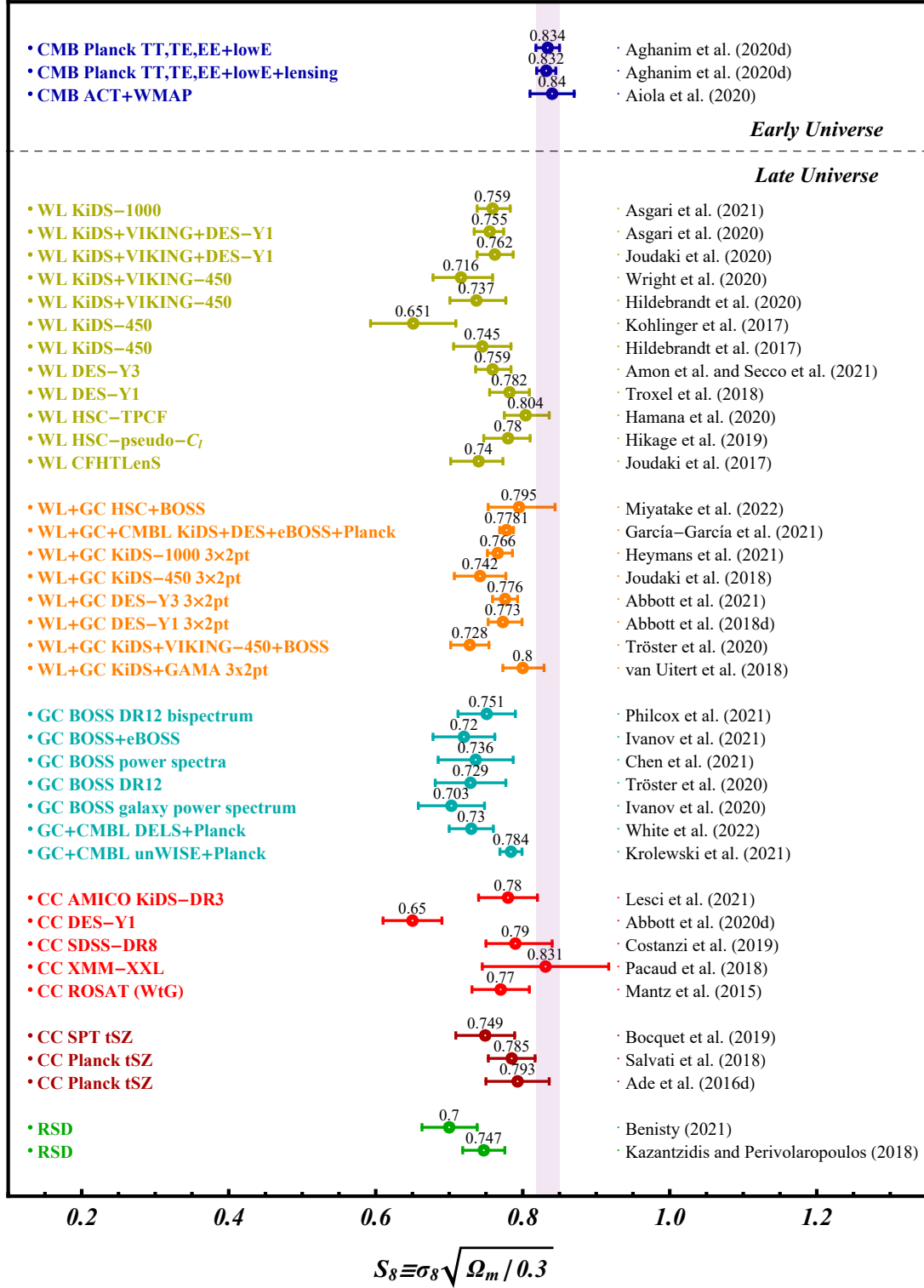


Figure 4.3: Whisker plot showing the different  $1-\sigma$  (68 %) widths on  $S_8$  results from different probes and analyses choices. We see that late-time measurements, such as weak lensing and galaxy clustering, are systematically lower than early-Universe measurements, principally *Planck*’s observations of the CMB. The further narrowing down of the uncertainties on  $S_8$  are one of the key goals of the Stage-IV cosmic shear surveys. Figure taken from Ref. [203].



Figure 4.4: The *Euclid* satellite atop a SpaceX Falcon 9 rocket launching off from the Kennedy Space Centre on 1<sup>st</sup> July 2023<sup>4</sup>. Credit: ESA/SpaceX/J.-C. Cuillandre

## 4.2 The Next Generation™

Figure 4.3 summarises our current best constraints on  $S_8$  using existing cosmic shear surveys: the Kilo Degree Survey (KiDS), Dark Energy Survey (DES), and Hyper Suprime-Cam (HSC) – the so called ‘Stage III’<sup>2</sup> cosmic shear surveys [205]. We are now entering the next level of cosmic shear surveys, the ‘Stage IV’<sup>3</sup> surveys of: the *Euclid* space telescope, the Legacy Survey of Space and Time (LSST) at the Vera Rubin Observatory, and the *Roman* space telescope.

As I write (November 2024), *Euclid* has been at  $L_2$  for approximately sixteen months after launching in July 2023 on a SpaceX Falcon 9 rocket (Figure 4.4). While it is already taking incredible data, for example Figure 4.5 showing a *Euclid* image of spiral galaxy IC 342, it will take time for *Euclid* to complete its planned six-year survey [164] and provide us with its fully complete cosmological data.

All three surveys promise to deliver cosmic shear data that is unprecedented in terms of its quality and quantity. This will produce a significance reduction in error bars for observed quantities, in particular  $S_8$ , and so we want to develop tools that allow us to extract the maximum amount of information possible from these new awesome observatories. This will be the theme of the rest of my thesis: Chapter 5 discusses a new implementation of a power spectrum estimator to minimise error bars, and Chapters 6 and 7 discussing modelling of baryonic feedback induced scale cuts to maximise information gain.

<sup>2</sup> *Revenge of the Sithematics* 🌌

<sup>3</sup> *A New Telesc(h)ope* 🌌

<sup>4</sup> *Euclid*’s launch certainly went better than any of my many attempts in *Kerbal Space Program*! *Bon voyage, Jeb, Val, Bill, and Bob. Bon voyage.* 🚀





Figure 4.5: An image of nearby spiral galaxy IC 342 taken by the *Euclid* satellite as part of its early release observations scheme. *Euclid*'s VIS camera ordinarily takes black and white images for maximum signal-to-noise, however this colour image was taken by combining VIS data and NISP photometry. We see spectacular sub-structure within this spiral galaxy, the precision shown here will allow us to execute cosmic shear measurements for far fainter galaxies with unprecedented precision. Credit: ESA/Euclid Consortium, data processed by J.-C. Cuillandre

---

*And now excuse me while I interrupt myself,  
With half the thesis gone, there is still half the thesis to go!*

—Murray Walker

*Whoa, we're half way there*

—Bon Jovi

---

Remember kids, the only difference  
between science and screwing around  
is writing it down


—Adam Savage

5

# Testing quadratic maximum likelihood estimators for forthcoming Stage-IV weak lensing surveys

---

This chapter was published in *Monthly Notices of the Royal Astronomical Society* as Maraio, Hall, and Taylor (2023) [1].

**Outline.** Headline constraints on cosmological parameters from current weak lensing surveys are derived from two-point statistics that are known to be statistically sub-optimal, even in the case of Gaussian fields. We study the performance of a new fast implementation of the Quadratic Maximum Likelihood (QML) estimator, optimal for Gaussian fields, to test the performance of Pseudo- $C_\ell$  estimators for upcoming weak lensing surveys and quantify the gain from a more optimal method. Through the use of realistic survey geometries, noise levels, and power spectra, we find that there is a decrease in the errors in the statistics of the recovered  $E$ -mode spectra to the level of  $\sim 20\%$  when using the optimal QML estimator over the Pseudo- $C_\ell$  estimator on the largest angular scales, while we find significant decreases in the errors associated with the  $B$ -modes. This raises the prospects of being able to constrain new physics through the enhanced sensitivity of  $B$ -modes for forthcoming surveys that our implementation of the QML estimator provides. We test the QML method with a new implementation that uses conjugate-gradient and finite-differences differentiation methods resulting in the most efficient implementation of the full-sky QML estimator yet, allowing us to process maps at resolutions that are prohibitively expensive using existing codes. In addition, we investigate the effects of apodisation,  $B$ -mode purification, and the use of non-Gaussian maps on the statistical properties of the estimators. Our QML implementation is publicly available and can be accessed from [GitHub](#) .

## 5.1 Introduction

Cosmic shear is the study of the coherent distortion in the shapes of background galaxies due to the matter distribution of the intervening large-scale structure [32, 33, 206]. Since these distortions are sensitive to the total matter distribution, with contributions from both ordinary baryonic matter and non-luminous dark matter, cosmic shear is a powerful probe of dark matter. By measuring the cosmic shear signal in multiple redshift bins, we can place constraints on the evolution of structure in the Universe, ultimately placing constraints on the properties of dark energy – a key goal for cosmology in the current decade. See Appendix B for a detailed discussion on why cosmic shear is sensitive to the evolution of dark energy, and the observational prospects of measuring it.

Given the large quantity of high-precision cosmic shear data that forthcoming Stage-IV weak gravitational lensing surveys, such as the *Euclid* space telescope [158], the Legacy Survey of Space and Time (LSST) at the *Rubin* observatory [207], and the *Roman* space telescope [208], are expected to take, it is important to ensure that we are using the most optimal methods possible throughout the data analysis pipeline. Given that each of these observatories will observe and measure the shear of well over one billion galaxies, it is unfeasible to perform data analysis on each of these individual galaxies. Hence, some form of data compression steps are needed to make the data processable. Here, we have investigated the process of compressing maps of the observed ellipticities of galaxies into two-point summary statistics, namely the power spectrum. The use of two-point statistics is well motivated because for Gaussian fields the power spectrum contains all of the information about the field, and two-point statistics have been extensively studied leading to the development of robust, well-tested models. The estimation of two-point statistics from data is an important process as it allows comparisons between observations and values predicted from cosmological theories to be performed. These comparisons allow us to constrain the cosmological parameters that feature in the models, and the cosmic shear power spectrum has been used to obtain competitive results [209–211]. Recent works have suggested that there could be a possible tension to the level of  $\sim 3\sigma$  in the value for the structure of growth parameter,  $S_8 \equiv \sigma_8 \sqrt{\Omega_M/0.3}$ , measured between data from cosmic shear surveys and those from cosmic microwave background experiments [e.g. 203, 209]. Therefore, to help determine if this tension has physical origins or not, it is essential to ensure that our analysis methods are as optimal as possible.

The process of compressing maps into two-point summary statistics is crucial, and so naturally a number of competing methods to do so have been developed and applied to cosmic shear data. Most notably are the two-point correlation functions (2PCF)  $\xi_{\pm}(\theta)$  [212, 213], the Complete Orthogonal Sets of E-/B-mode Integrals (COSEBIs) [181, 214], and the power spectrum coefficients  $C_{\ell}$  [215–217]. In this work, we focus on analysing cosmic shear maps using the power spectrum. The power spectrum has the advantage that it provides the most direct comparison between theory- and data-vectors, without the need to perform any additional transformations when comparing them, as is required for analyses using correlation functions [213]<sup>1</sup>. Additionally, the power spectrum provides a

<sup>1</sup>The cosmic shear angular power spectrum is a simple Limber integral over the matter power spectrum weighted by the lensing kernels (Equation 6.4). Many methods have been developed to ensure that this integral step is as fast and accurate as possible. If we now wish to use another estimator, say the two-point correlation functions or COSEBIs, then one or two additional summation steps are necessary, respectively (Equations 3.72 and 3.73). This also requires the angular power spectrum coefficients to be computed to much larger  $\ell$  values than when using the angular power spectrum natively. This further evaluation of the  $C_{\ell}$  values and the additional summation steps significantly slows down the application of 2PCF and COSEBIs to cosmic shear analyses using Markov chain Monte Carlo methods – which are the baseline choice for any cosmic shear survey. Thus, we are motivated to use the  $C_{\ell}$  values as our theoretical data-vector, and so we are tasked with finding the most-optimal experimental  $C_{\ell}$  estimator.



cleaner separation between linear and non-linear scales, which aids the investigation of biases from the non-linear modelling of the matter power spectrum and intrinsic alignments [210], and the scale-dependent signatures in the power spectrum – for example arising from the properties of massive neutrinos and baryonic effects. We note that none of the methods discussed in this work employ the flat-sky approximation, with all quantities being evaluated on the full, curved-sky.

While power spectrum estimators are a sub-set of two-point correlators, we can further break down this category of estimators into two main methods: the Pseudo- $C_\ell$  method [216, 218], and the quadratic maximum likelihood method (QML) [219, 220]. In addition, there is the **PolSpice** algorithm which uses the correlation functions to produce estimates of the power spectrum, and is statistically equivalent to the Pseudo- $C_\ell$  method [221, 222]. The Pseudo- $C_\ell$  class of estimators work in harmonic-space and utilise very efficient spherical harmonic transformation algorithms which makes this class of estimator extremely numerically efficient even for high-resolution maps [15, 218]. Alternatively, the QML method works in pixel-space, which results in a much larger computational demand when compared to Pseudo- $C_\ell$  method for the same resolution maps. Traditionally, this has limited analyses using the QML method to low-resolution maps only, and thus confined the values for the recovered power spectrum to low multipoles. Hence, when power spectrum methods have been applied to existing weak lensing data, the Pseudo- $C_\ell$  estimator has been the method of choice for the vast majority of weak lensing analyses [210, 214, 223–225], primarily using the **NaMaster** code which is a fast implementation of the Pseudo- $C_\ell$  estimator that can be easily applied to weak lensing analyses [17]. The Pseudo- $C_\ell$  estimator will form part of the analysis pipeline for upcoming weak lensing surveys [226]. However, it has been shown that while the QML estimator is optimal, in the sense that it estimates a power spectrum with the minimal possible errors [219], it is known that the Pseudo- $C_\ell$  method is not optimal [227], and thus could be introducing additional errors into the data.

Another aspect of the data analysis expected to benefit significantly from the application of an optimal estimator is in  $B$ -mode measurement. In the limit of weak gravitational lensing, the produced signal should form a curl-free field, and thus the predicted  $B$ -mode signal for cosmic shear should be zero. This is because the distortion in the shapes of galaxies due to cosmic shear should be tangentially aligned to spherical distributions of mass, which galaxies and galaxy clusters can be approximated as [92]. Thus, the rotated deflections to induce a  $B$ -mode signal must come from non-cosmic shear sources, such as unaccounted detector systematics [228], the presence of intrinsic alignments [229], or physics beyond general relativity. Traditionally, a statistically significant detection of  $B$ -modes would indicate the presence of unaccounted systematic effects present in the data. However, with the increased precision of forthcoming Stage-IV experiments, the  $B$ -mode signal will be treated as a potential signal that could give hints of new physical phenomena. An application of using  $B$ -modes to constrain novel cosmological models was presented in Ref. [230]. Hence, ensuring that the  $B$ -mode errors are as small as possible (to help determine if any residual  $B$ -mode signal is statistically significant, and to distinguish between systematic effects and a cosmological  $B$ -mode signal) is another key feature for any power spectrum estimation technique that would be applied to upcoming experimental data.

Additionally, in a power spectrum analysis a choice for how the survey mask should be modelled is present. Either the effects of the mask can be deconvolved from the observed values, giving predictions for the full-sky power [217], or the effects of the mask can be convolved into the theory predictions, the so-called ‘forward-modelling’ approach [226]. Here, we focus on the full-sky predictions, which the QML estimator naturally produces, as this allows for the most straightforward comparisons between experimental results and theoretical predictions to be made. This is because there is no need to convolve the

theory data-vector with the mask at every step in an analysis chain when using Monte Carlo Markov Chain methods, and thus reducing the per-step computational requirements resulting in faster run-times. We also note that by producing estimates of the full-sky power spectra, our covariance matrix is less affected by the mask on large scales.

Previous attempts at applying QML methods to existing weak lensing surveys have found little differences in results when compared to other analysis techniques. Ref. [231] applied a QML implementation to estimate band powers from the data from the Canada-France-Hawaii Telescope Lensing Survey (CFHTLenS) finding general consistency between their QML analysis and all other studies using CFHTLenS data. This implementation was then applied to data from the first data release from the Kilo Degree Survey (KiDS-450) in Ref. [232]. Here, they again found broadly consistent results between their analysis and previous works, though finding a slightly smaller value for  $S_8$  which could be explained by their work using a slightly smaller range of  $\ell$  multipole values [233]. Quadratic and Pseudo- $C_\ell$  estimators were applied to cosmic shear measurements performed by the Sloan Digital Sky Survey in Ref. [234], again finding strong consistency between the two methods. This demonstrates that analysing weak lensing data using QML methods provides a strong consistency check between different two-point estimators and ensuring that results are robust to the different analysis choices that are required for the different methods. While these previous analyses of weak lensing data using QML methods have shown strong consistencies in the main cosmological results, though their application as a cross-check remains an important use case, we note that the CFHTLenS and KiDS-450 surveys covered about  $154 \text{ deg}^2$  and  $450 \text{ deg}^2$  of sky, respectively. These sky areas are around two orders of magnitude smaller than the expected sky area that forthcoming Stage-IV experiments are expected to cover. While it has been shown that the QML and Pseudo- $C_\ell$  estimators are statistically equivalent in the high noise regime [227, 235], the expected noise levels for forthcoming surveys will be much lower than CFHTLenS and KiDS. Therefore, the huge increase in statistical precision that forthcoming Stage-IV surveys will bring means that the use of non-optimal methods (the Pseudo- $C_\ell$  estimator) needs to be reassessed and their affects on cosmological constraints quantified.

Despite the advantages of quadratic estimators, the development of maximum likelihood estimators, and in particular their applications to cosmic shear, has traditionally been less explored than other techniques because of their computational complexity and associated slowness. In general, they require the computation and inversion of a dense pixel-space covariance matrix of the map(s) which is a slow and inefficient process when compared to other analysis methods. Recent theoretical developments presented in Refs. [236] and [237], along with using methods presented in Ref. [238], have provided a set of key tools that has allowed us to build a new novel QML implementation that is highly efficient. We note that the construction of the QML estimator is very analogous to the Wiener filtering of the data, for which fast implementations have been recently developed and applied to CMB data-sets [239–241]. We also note that recent works have applied quadratic estimators to galaxy clustering in Refs. [242] and [243] applying their quadratic estimators to data from the VIPERS and BOSS surveys, respectively.

This Chapter is structured as follows: in Section 5.2 we present a review of both the QML and Pseudo- $C_\ell$  estimators, including a detailed derivation of the QML method in Section 5.2.1. Then in Sections 5.2.2 and 5.2.3 we present our new highly efficient implementation of the QML estimator. Section 5.3 outlines our methodology for generating mock weak lensing data, which is used for our results that we present in Section 5.4. Our conclusions are presented in Section 5.5.

## 5.2 Power spectrum estimators

As discussed in Section 5.1, there exists two broad classes of power spectrum estimation techniques. Here, we first derive the set of key results for the QML method, and then present a brief review of the Pseudo- $C_\ell$  method.

### 5.2.1 The quadratic maximum likelihood estimator

Consider a spin<sup>2</sup>-0 input map as a data-vector  $\vec{x}$  (which may be complex, such as for real-space shears) that has zero mean, an example of such a map would be convergence estimates in pixels over the sky, and covariance  $\mathbf{C}$ . This data-vector has a length equal to the number of pixels in the map  $N_{\text{pix}}$ . We can write it as

$$\vec{x} = \vec{s} + \vec{n}, \quad (5.1)$$

where  $\vec{s}$  and  $\vec{n}$  are the signal and noise data-vectors, respectively. Assuming that the signal and noise data-vectors are uncorrelated and both follow the Gaussian distribution, then the likelihood function for the power spectrum coefficients recovered from the map,  $\tilde{C}_\ell$ , is given by

$$\mathcal{L}(\vec{x} | \tilde{C}_\ell) = \frac{\exp\left(-\frac{1}{2}\vec{x}^\dagger \mathbf{C}^{-1} \vec{x}\right)}{(2\pi)^{N_{\text{pix}}/2} |\mathbf{C}|^{1/2}}, \quad (5.2)$$

where  $\mathbf{C}$  is the total pixel-covariance matrix, given as

$$\mathbf{C} = \langle \vec{x} \vec{x}^\dagger \rangle = \mathbf{S}(C_\ell) + \mathbf{N}, \quad (5.3)$$

where  $\mathbf{S}$  is the signal covariance matrix,  $\mathbf{N}$  is the noise matrix, and  $C_\ell$  are the fiducial power spectrum coefficients. The signal covariance matrix can be written as

$$\mathbf{S}(C_\ell) = \sum_{\ell} \mathbf{P}_\ell C_\ell, \quad (5.4)$$

where the  $\mathbf{P}_\ell$  matrices are defined, in pixel-space, as

$$\mathbf{P}_\ell \equiv \frac{2\ell + 1}{4\pi} P_\ell(\hat{r}_i \cdot \hat{r}_j), \quad (5.5)$$

where  $P_\ell$  are the Legendre polynomials, and  $\hat{r}_i$  is the unit vector for pixel  $i$ . This matrix can be decomposed into spherical harmonics through the addition theorem, giving

$$\mathbf{P}_\ell = \sum_{m=-\ell}^{\ell} Y_{\ell m}(\hat{r}_i) Y_{\ell m}^*(\hat{r}_j). \quad (5.6)$$

We note an important result of

$$\frac{\partial \mathbf{C}}{\partial C_\ell} = \mathbf{P}_\ell. \quad (5.7)$$

In harmonic-space, these  $\mathbf{P}_\ell$  matrices are simply zeros with ones along the diagonal corresponding to their  $\ell$  value. This makes evaluating the signal matrix very easy in spherical-harmonic space.

For uncorrelated noise, the noise matrix  $\mathbf{N}$  in pixel-space is simply given by the noise variance of the  $i$ -th pixel along the diagonal with zeros elsewhere. This makes evaluating the noise matrix very easy in pixel-space. We note that the QML method may require the

---

<sup>2</sup>Pronto, Sebastian? innala.

manual insertion of a small level of white noise into the covariance matrix to ensure that it is invertible, as in some extreme cases the covariance matrix can be singular [244].

A minimum-variance quadratic estimator of the power spectrum can be formed as [219]

$$y_\ell \equiv s_\ell - b_\ell = \vec{x}^\text{T} \mathbf{E}_\ell \vec{x} - b_\ell, \quad (5.8)$$

where the  $\mathbf{E}_\ell$  matrices are given by

$$\mathbf{E}_\ell = \frac{1}{2} \mathbf{C}^{-1} \frac{\partial \mathbf{C}}{\partial C_\ell} \mathbf{C}^{-1} = \frac{1}{2} \mathbf{C}^{-1} \mathbf{P}_\ell \mathbf{C}^{-1}, \quad (5.9)$$

and the noise bias terms  $b_\ell$  are given as

$$b_\ell = \text{Tr}[\mathbf{N} \mathbf{E}_\ell]. \quad (5.10)$$

Arranging our  $y_\ell$  and  $C_\ell$  values into vectors  $\vec{y}$  and  $\vec{C}$ , respectively, we can relate our quadratic estimator to the true power spectrum as

$$\langle \vec{y} \rangle = \mathbf{F} \vec{C}, \quad (5.11)$$

where  $\mathbf{F}$  is the Fisher matrix. Formally, this is defined through the likelihood as [245]

$$\mathbf{F}_{\ell_1 \ell_2} = - \left\langle \frac{\partial^2 \ln \mathcal{L}}{\partial C_{\ell_1} \partial C_{\ell_2}} \right\rangle. \quad (5.12)$$

When applying the likelihood of Equation 5.2, we find the Fisher matrix can be written as

$$\begin{aligned} \mathbf{F}_{\ell \ell'} &= \frac{1}{2} \text{Tr} \left[ \mathbf{C}^{-1} \frac{\partial \mathbf{C}}{\partial C_\ell} \mathbf{C}^{-1} \frac{\partial \mathbf{C}}{\partial C_{\ell'}} \right], \\ &= \frac{1}{2} \text{Tr} \left[ \mathbf{C}^{-1} \mathbf{P}_\ell \mathbf{C}^{-1} \mathbf{P}_{\ell'} \right]. \end{aligned} \quad (5.13)$$

Assuming that  $\mathbf{F}$  is regular, and thus can be inverted, we can form an estimator for the recovered power spectrum from our map,  $\tilde{\vec{C}}$ , as

$$\tilde{\vec{C}} = \mathbf{F}^{-1} \vec{y}. \quad (5.14)$$

This estimator is unbiased in the sense that its average is the true, underlying spectrum [219],

$$\langle \tilde{\vec{C}} \rangle = \vec{C}, \quad (5.15)$$

and it is optimal in the sense that its covariance matrix of our estimator is the inverse Fisher matrix  $\mathbf{F}^{-1}$ ,

$$\langle (\tilde{\vec{C}} - \vec{C})(\tilde{\vec{C}} - \vec{C})^\text{T} \rangle = \mathbf{F}^{-1} \quad (5.16)$$

and thus satisfies the Cramér-Rao inequality [197].

## Extension to spin-2 fields

Above, we have derived a set of key-results of the QML estimator applied to a scalar spin-0 field. These set of equations can be extended to cover spin-2 fields, as presented in Ref. [220]. Such spin-2 field is cosmic shear, of which the observed field can be decomposed into two components through  $\gamma(\hat{n}) = \gamma_1(\hat{n}) + i\gamma_2(\hat{n})$ . The data-vector will now have length  $2N_{\text{pix}}$ , where it will be given by  $\vec{x} = \{\vec{\gamma}, \vec{\gamma}^*\}$ , where  $\vec{\gamma}$  is the values of the complex shears

at each pixel, and the covariance matrix (and other associated pixel-space matrices) have dimensions  $2N_{\text{pix}} \times 2N_{\text{pix}}$ , where their block structure will be given by

$$\mathbf{C} = \begin{pmatrix} \langle \vec{\gamma} \vec{\gamma}^\dagger \rangle & \langle \vec{\gamma} \vec{\gamma}^{\text{T}} \rangle \\ \langle \vec{\gamma}^* \vec{\gamma}^\dagger \rangle & \langle \vec{\gamma}^* \vec{\gamma}^{\text{T}} \rangle \end{pmatrix}. \quad (5.17)$$

Similarly, the Legendre polynomial matrix  $\mathbf{P}_\ell$  will have a structure for the spin-2 case of [220]

$$\mathbf{P}_\ell = \begin{pmatrix} \sum_m {}_2Y_{\ell m}(\hat{r}_i) {}_2Y_{\ell m}^*(\hat{r}_j) & \sum_m {}_2Y_{\ell m}(\hat{r}_i) {}_2Y_{\ell m}^*(\hat{r}_j) \\ \sum_m {}_2Y_{\ell m}^*(\hat{r}_i) {}_2Y_{\ell m}(\hat{r}_j) & \sum_m {}_2Y_{\ell m}^*(\hat{r}_i) {}_2Y_{\ell m}(\hat{r}_j) \end{pmatrix}, \quad (5.18)$$

and the signal covariance matrix is given by

$$\mathbf{S} = \begin{pmatrix} \sum_\ell [C_\ell^{EE} + C_\ell^{BB}] \mathbf{P}_\ell^{(1,1)} & \sum_\ell [C_\ell^{EE} - C_\ell^{BB}] \mathbf{P}_\ell^{(1,2)} \\ \sum_\ell [C_\ell^{EE} - C_\ell^{BB}] \mathbf{P}_\ell^{(2,1)} & \sum_\ell [C_\ell^{EE} + C_\ell^{BB}] \mathbf{P}_\ell^{(2,2)} \end{pmatrix}, \quad (5.19)$$

where  ${}_sY_{\ell m}$  are the spin-weighted spherical harmonics.

The observed spin-2 shear field can be decomposed on the full-sky into a curl-free  $E$ -mode and divergence-free  $B$ -mode fields through [216]

$$(\gamma_1 \pm i\gamma_2)(\hat{n}) = \sum_\ell \sum_{m=-\ell}^\ell [a_{\ell m}^E \pm ia_{\ell m}^B] {}_{\pm 2}Y_{\ell m}(\hat{n}). \quad (5.20)$$

This relation can be inverted to give the  $a_{\ell m}$  coefficients on the full-sky as

$$a_{\ell m}^E \pm ia_{\ell m}^B = \int d\Omega (\gamma_1 \pm i\gamma_2)(\hat{n}) {}_{\pm 2}Y_{\ell m}^*(\hat{n}). \quad (5.21)$$

These  $a_{\ell m}$  coefficients can then be combined to form values for the all-sky power spectrum through

$$C_\ell^{XY} = \frac{1}{2\ell+1} \sum_{m=-\ell}^\ell a_{\ell m}^X [a_{\ell m}^Y]^*, \quad (5.22)$$

where  $X, Y$  denote either  $E$  or  $B$ .

## Affect of the fiducial cosmology

We note that to construct the covariance matrix, we have to provide our estimator with a set of fiducial  $C_\ell$  values. Given that the whole point of the estimator is to estimate the  $C_\ell$  values from map(s), of which their underlying power spectrum are unknown prior to the analysis, it may appear that the estimated power spectrum will somehow depend on the input cosmology. However, provided that the same fiducial power spectrum is applied consistently to the estimator, it will still produce unbiased estimates, but ones that may not necessarily be truly optimal. An iterative scheme where the results of the estimator are fed back into the construction of the covariance matrix, with this process repeating for a number of times, was investigated in Ref. [246].

## 5.2.2 Inverting the pixel covariance matrix

To evaluate our quadratic estimator, we need an efficient way to evaluate the set of  $y_\ell$  values for a given map. These in turn require efficient evaluation of the inverse-covariance weighted map,  $\mathbf{C}^{-1}\vec{x}$ . Naïvely, one may want to compute these terms through first evaluating the total covariance matrix  $\mathbf{C}$  and then inverting it. However, as we have seen

through Equation 5.3,  $\mathbf{C}$  is made up of both the signal and noise covariance matrices, resulting in there not being a single efficient basis to evaluate  $\mathbf{C}$  in without having to resort to using expensive massive matrix multiplications using matrices of spherical harmonics,  $\mathbf{Y}$ . Since these operations scale as  $\mathcal{O}(N_{\text{pix}}^3)$ , this is an important limiting factor to the resolution that can be obtained with traditional QML estimation techniques.

An alternative approach that negates the need to evaluate the total covariance matrix is required to obtain competitive resolution results using QML methods. Previous attempts at this problem have used either Newton-Raphson iteration techniques to find the root of  $\partial\mathcal{L}/\partial C_\ell = 0$  [215, 245, 247], or alternatively used conjugate gradient techniques [238], both of which avoid the need to directly evaluate and invert the covariance matrix and thus offers significantly better computational performance. Alternative techniques also include an iterative scheme presented in Ref. [248] and renormalisation-inspired methods presented in Refs. [249, 250]. Here, we employ the conjugate gradient approach, although minimisation approaches have also been shown to give good results [236].

The conjugate gradient method [238] utilises a converging iterative scheme to find a best-fitting solution vector  $\vec{z}$  such that it satisfies the linear equation

$$\mathbf{C}\vec{z} = \vec{x} \quad (5.23)$$

for a given covariance matrix and input maps. Using the conjugate gradient method allows us to only compute the action of a trial-vector on the covariance matrix instead of the traditional approach of computing the full form of the covariance matrix and inverting it. As this is an iterative approach to finding the best-fitting vector  $\vec{z}$ , the value of  $\mathbf{C}\vec{z}$  needs to be computed many times. Therefore, an efficient numerical approach to computing this is required. This is achieved through the use of splitting the pixel covariance matrix into a signal part, which is best suited to harmonic-space, and a noise part, which is best represented in pixel-space. Hence, this allows us to rapidly compute the action of our trial vector  $\vec{z}$  on the covariance matrix through

$$\mathbf{S}\vec{z} + \mathbf{N}\vec{z} = \vec{x}. \quad (5.24)$$

We can rapidly transform our trial vector  $\vec{z}$  between pixel- and harmonic-space through efficient spherical harmonic transform functions `map2alm` & `alm2map` from the `HEALPix` library [15]. Qualitatively, the per-iteration computation of  $\mathbf{C}\vec{z}$  proceeds along the following steps:

1. Convert our map-based trial-vector  $\vec{z}$  into a set of  $a_{\ell m}^E$  and  $a_{\ell m}^B$  values through the use of `map2alm` which implements Equation 5.21,
2. Re-scale the  $a_{\ell m}$  values with the input fiducial power spectrum  $C_\ell^{EE}$  and  $C_\ell^{BB}$ , respectively,
3. Generate a new set of spin-2 maps with these new  $a_{\ell m}$  coefficients to obtain the contribution from the cosmological signal using `alm2map` which implements Equation 5.20,
4. Take our original trial-vector  $\vec{z}$  and multiply all elements by the noise variance in the respective pixel to obtain the noise contribution,
5. Finally sum the signal and noise contributions giving a final set of two maps in pixel space.

With this efficient computation of  $\mathbf{C}\vec{z}$  in place, we can use standard implementations of the conjugate gradient algorithm to find  $\vec{z}$ . We used the `Eigen`<sup>3</sup> C++ linear algebra

---

<sup>3</sup><https://eigen.tuxfamily.org>

package to perform our conjugate gradient computations resulting in a quick and efficient numerical implementation.

Since we are now only computing the action of the covariance matrix on our trial vector, instead of explicitly computing the full form of the covariance matrix, we find that our method provides much better scaling to higher map resolutions than previous implementations. We explore the speed and memory performance of our new estimator in Section 5.4.1. In our analysis, we used map resolutions of  $N_{\text{side}} = 256$ , which compares to a maximum of  $N_{\text{side}} = 64$  that was explored in previous QML implementations [246].

In general, the conjugate gradient technique can benefit greatly from an appropriate choice of matrix preconditioner [238]. Given a linear system  $\mathbf{A}\vec{x} = \vec{b}$ , the preconditioner matrix  $\tilde{\mathbf{A}}$  should be such that  $\tilde{\mathbf{A}}^{-1}\mathbf{A} = \mathbf{I} + \mathbf{R}$ , where  $\mathbf{I}$  is the identity matrix and  $\mathbf{R}$  is a matrix whose eigenvalues are all less than unity. This minimises the number of iterations required for the conjugate gradient method to converge, and thus can offer significant performance improvements if properly set. Since our method requires a strictly diagonal preconditioner, this placed strict constraints on the form and values of the preconditioner. We investigated the use of different values for the diagonal of the preconditioner finding little change in the performance of the iterative method. Thus we used the identity matrix as our preconditioner.

We also note that we have free choice over the initial guess  $\vec{z}_0$  in the conjugate-gradient method. An educated ansatz for the choice of  $\vec{z}_0$  will dramatically speed up the iterative method, since there will be less work that the numerical method needs to perform. Approximating the Legendre polynomial matrix ( $\mathbf{P}_\ell$ ) as diagonal values of unity in pixel-space, the signal covariance matrix will be given by  $\mathbf{S} = \text{diag}(\Sigma_\ell C_\ell)$ . Since our noise matrix  $\mathbf{N}$  is already diagonal in pixel-space, we can form a zeroth-order inverse of our map  $\vec{x}$  such that it is given by  $\vec{z}_0 = \vec{x} / [\Sigma_\ell C_\ell + N]$ . This choice dramatically speeds up the convergence, particularly in the noise-dominated regime.

### 5.2.3 Forming the Fisher matrix

Since the covariance matrix of our quadratic estimator is the inverse Fisher matrix, we can get estimates for the estimator's errors through computation of this Fisher matrix. Direct computation of the Fisher matrix through Equation 5.13 requires many massive  $2N_{\text{pix}} \times 2N_{\text{pix}}$  matrix multiplications and inversions, which has  $\mathcal{O}(N_{\text{pix}}^3)$  scaling, even for efficient implementations of this technique [246]. Thus, this direct-evaluation technique becomes unfeasible for map resolutions above about  $N_{\text{side}} = 64$  for Stage-IV cosmic shear experiments. Hence, to get power spectrum estimates for higher-resolution maps, which increases the range of  $\ell$ -values that we can estimate the power spectrum over, an alternative method to direct computation is needed.

We note that the Fisher matrix is related to the second-order derivative of the likelihood function through Equation 5.12. Taking a single derivative of the likelihood yields

$$\frac{\partial \ln \mathcal{L}}{\partial C_\ell} = s_\ell - b_\ell - \text{Tr}[\mathbf{S} \mathbf{E}_\ell] \quad (5.25)$$

where  $s_\ell$  is our quadratic form of the map as introduced in Equation 5.8. Therefore, to evaluate our Fisher matrix, we wish to take a further derivative of the above quantity, which yields

$$\left\langle \frac{\partial^2 \ln \mathcal{L}}{\partial C_\ell \partial C_{\ell'}} \right\rangle = -\text{Tr}[\mathbf{C}^{-1} \mathbf{P}_\ell \mathbf{C}^{-1} \mathbf{P}_{\ell'}] + \frac{1}{2} \text{Tr}[\mathbf{C}^{-1} \mathbf{P}_\ell \mathbf{C}^{-1} \mathbf{P}_{\ell'}], \quad (5.26)$$

$$= -\frac{1}{2} \text{Tr}[\mathbf{C}^{-1} \mathbf{P}_\ell \mathbf{C}^{-1} \mathbf{P}_{\ell'}], \quad (5.27)$$



where the first trace term comes from the differentiation of the quadratic term  $s_\ell$  and the second trace arises from the differentiation of the other two terms in Equation 5.25. Since we note that the differentiation of just the  $s_\ell$  term alone yields twice the negative Fisher matrix, we can form an estimator for the Fisher matrix using just this term. Therefore, we can use the method of finite differences to differentiate  $s_\ell$  to give [236, 237]


$$F_{\ell\ell'} \Delta C_{\ell'} = -\frac{1}{2} \left[ \langle s_\ell(C_\ell^{\text{fid}} + \Delta C_{\ell'}) \rangle - \langle s_\ell(C_\ell^{\text{fid}}) \rangle \right]. \quad (5.28)$$

Here, we are manually injecting power into a specific  $\ell$ -mode (given as  $\Delta C_{\ell'}$ ), generating a map with the modified power spectrum, and recovering the set of  $s_\ell$  values. This gives the estimate of our Fisher matrix associated where we are averaging over many realisations of maps generated with the specified power spectrum, and  $C_{\text{fid}}$  is our original best-guess for the power spectrum coefficients used when building the covariance matrix  $\mathbf{C}$ .

This approach of using finite-differences to estimate the Fisher matrix performs much faster than the brute-force calculation, as described in Equation 5.13, due to our ability to estimate the Fisher matrix directly from the  $s_\ell$  values, which are vector quantities and for which we already have an efficient method to compute through the conjugate gradient method, and so we avoid having to compute the matrices and matrix products of Equation 5.13.

Here, the amount of power injected into the maps at the specific  $\ell$ -mode is a free parameter of the method. We used a value of  $\Delta C_\ell = 10^7 C_\ell^{\text{fid}}$  and verified that our results were insensitive to the choice of this value, provided that it is sufficiently large.

Note that in our analysis presented in this paper, we are not able to recover any of the covariances associated with any of the  $EB$  modes. This is because these modes are not linearly independent of either the  $EE$  or  $BB$  spectra, and thus with our choice of fiducial spectrum containing zero  $B$ -modes we cannot inject power into the  $EB$  modes.  $EB$ -spectra can be obtained by setting the fiducial  $B$ -mode power to small non-zero values, for example [236] use a  $B$ -mode spectra that has the same shape as their  $E$ -mode spectra but has an amplitude that is  $10^{-5}$  times smaller. Since we used zero  $B$ -mode power as our fiducial model, we are unable to report on any  $EB$  results in this work.

Our new code implementing these approaches is publicly available and can be downloaded from GitHub: <https://github.com/AlexMaraio/WeakLensingQML> .

## 5.2.4 Review of the Pseudo- $C_\ell$ estimator

We refer the reader to [17, 251], and references therein, for detailed reviews of the Pseudo- $C_\ell$  method, but here we discuss the key features of the estimator.

Since we cannot observe the shear field on the full-sky, our observed field is modulated through some window function,  $\mathcal{W}(\hat{n})$ , through  $\tilde{\gamma}(\hat{n}) = \mathcal{W}(\hat{n})\gamma(\hat{n})$ . Throughout this work, we consider binary masks only, and thus  $\mathcal{W}(\hat{n})$  is either zero or one. This turns the recovered harmonic modes into ‘pseudo modes’, given as

$$\tilde{a}_{\ell m}^E \pm i\tilde{a}_{\ell m}^B = \int d\Omega \mathcal{W}(\hat{n}) (\gamma_1 \pm i\gamma_2)(\hat{n}) {}_{\pm 2}Y_{\ell m}^*(\hat{n}), \quad (5.29)$$

where we are denoting quantities evaluated on the cut-sky with a tilde. These pseudo-modes are related to the underlying modes through

$$\tilde{a}_{\ell m}^E \pm i\tilde{a}_{\ell m}^B = \sum_{\ell', m'} (a_{\ell' m'}^E \pm ia_{\ell' m'}^B) {}_{\pm 2}W_{mm'}^{\ell\ell'}, \quad (5.30)$$

where  ${}_{\pm 2}W_{mm'}^{\ell\ell'}$  is the convolution kernel for our window function, which can be written as [216]

$${}_{\pm 2}W_{mm'}^{\ell\ell'} = \int d\Omega {}_{\pm 2}Y_{\ell' m'}(\hat{n}) \mathcal{W}(\hat{n}) {}_{\pm 2}Y_{\ell m}^*(\hat{n}). \quad (5.31)$$



Expanding the window function in spherical harmonics and evaluating the integrals yields

$$\begin{aligned} {}_{\pm 2}W_{mm'}^{\ell\ell'} = \sum_{\ell'', m''} (-1)^m \sqrt{\frac{(2\ell+1)(2\ell'+1)(2\ell''+1)}{4\pi}} \mathcal{W}_{\ell''m''} \\ \times \begin{pmatrix} \ell & \ell' & \ell'' \\ \pm 2 & \mp 2 & 0 \end{pmatrix} \begin{pmatrix} \ell & \ell' & \ell'' \\ \pm m & \mp m' & m'' \end{pmatrix}, \end{aligned} \quad (5.32)$$

where  $\mathcal{W}_{\ell''m''}$  is the spin-0 spherical harmonic transform of the mask and the terms in brackets are the Wigner-3j symbols.

When forming the pseudo-multipoles, there is a freedom to add pixel weights through the window function, for example using inverse-variance weighting scheme, though this is typically not done in large-scale structure applications.

Combining the three shear spectra into a single vector,  $\vec{C}_\ell = (C_\ell^{EE}, C_\ell^{EB}, C_\ell^{BB})$ , we find that the cut-sky power spectrum can be written in terms of the full-sky power spectrum through [216, 217]

$$\tilde{\vec{C}}_\ell = \sum_{\ell'} \mathbf{M}_{\ell\ell'} \vec{C}_{\ell'}, \quad (5.33)$$

where  $\mathbf{M}_{\ell\ell'}$  is the mode coupling matrix. Provided that  $\mathbf{M}_{\ell\ell'}$  is invertible, which is only the case when there is enough sky area such that the two-point correlation function  $C(\theta)$  can be evaluated on all angular scales [252], we can invert this relationship to give an estimate of the full-sky spectra from the pseudo-modes,

$$\vec{C}_\ell = \sum_{\ell'} \mathbf{M}_{\ell\ell'}^{-1} \tilde{\vec{C}}_{\ell'}. \quad (5.34)$$

This is the final expression for the estimated power spectrum of a map using the Pseudo- $C_\ell$  method. An alternative strategy that avoids this inversion is the forward-modelling of the mask's mode-coupling matrix into the theory power spectrum values through Equation 5.33.

Since our analysis was focused on the *errors* associated with the recovered power spectrum, a detailed description of the covariance matrix associated with the Pseudo- $C_\ell$  estimator is worthy of discussion. In general, the exact analytic covariance of two Pseudo- $C_\ell$  fields involve terms of the form [200, 216]

$$\text{Cov}[\tilde{C}_\ell, \tilde{C}_{\ell'}] \sim \sum_{\ell_1, \ell_2} C_{\ell_1} C_{\ell_2} \sum_{\substack{m, m', \\ m_1, m_2}} W_{mm_1}^{\ell\ell_1} \left(W_{m'm_1}^{\ell'\ell_1}\right)^* W_{m'm_2}^{\ell'\ell_2} \left(W_{mm_2}^{\ell\ell_2}\right)^* \quad (5.35)$$

Computing this involves summing  $\mathcal{O}(\ell_{\text{MAX}}^6)$  terms which becomes computationally intractable for even moderate-resolution maps. Hence, certain assumptions are used to speed up this calculation. The principle of these is the narrow-kernel approximation, which assumes that the power spectrum of the mask has support only over a narrow range of multipoles when compared to the power spectrum [225, 227]. This involves making substitutions of the form  $\{C_{\ell_1}, C_{\ell_2}\} \rightarrow \{C_\ell, C_{\ell'}\}$ , and so the power spectrum terms in Equation 5.35 can be extracted, and then the symmetric properties of the convolution kernels can be used to simplify the summations. This approximation is known to be inaccurate on large scales, though it has been shown that this has negligible impact on parameter constraints, and for power spectra that contain *B*-modes [225]. Alternatively, Gaussian covariances can be estimated from an ensemble of realisations. While this produces a more accurate estimate of the covariance matrix, especially for low multipoles, it is much more computationally demanding due to the large number of realisations required in the ensemble - especially for accurately determining the off-diagonal elements of the covariance matrix.

## 5.3 Methodology

Our aim is to investigate to what extent that QML estimators can give improved statistical errors on the recovered shear power spectra compared to Pseudo- $C_\ell$  methods. We will test the estimators on a set of mock shear maps. In this section, we describe the fiducial setup of these mocks.

### 5.3.1 Theory power spectrum

For our analysis, we used a single redshift bin with sources following a Gaussian distribution centred at  $z = 1$  with standard deviation of  $\sigma_z = 0.15$ . We used fiducial cosmological values of  $h = 0.7$ ,  $\Omega_c = 0.27$ ,  $\Omega_b = 0.045$ ,  $\sigma_8 = 0.75$ ,  $n_s = 0.96$ , and massless neutrinos.

The cosmic shear theory signal for this distribution of sources was calculated using the Core Cosmology Library (CCL) [12]. This implements the standard prescription for the weak lensing power spectrum [32, 33, 206], where the convergence power spectrum can be written in natural units where  $c = 1$  as

$$C_\ell^{\kappa\kappa} = \frac{9}{4} \Omega_m^2 H_0^4 \int_0^{\chi_h} d\chi \frac{g(\chi)^2}{a^2(\chi)} P_\delta\left(k = \frac{\ell}{f_K(\chi)}, \chi\right), \quad (5.36)$$

where  $a(\chi)$  is the scale factor,  $P_\delta$  is the non-linear matter power spectrum,  $f_K$  is the comoving angular diameter distance, and  $g(\chi)$  is the lensing kernel given as

$$g(\chi) = \int_\chi^{\chi_h} d\chi' n(\chi') \frac{f_K(\chi' - \chi)}{f_K(\chi')}, \quad (5.37)$$

where  $n(\chi)$  is the number density of source galaxies. The convergence power spectrum can be transformed into values for the  $E$ -mode power through [253]

$$C_\ell^{EE} = \frac{(\ell - 1)(\ell + 2)}{\ell(\ell + 1)} C_\ell^{\kappa\kappa}. \quad (5.38)$$

A plot of the  $C_\ell^{EE}$  power spectrum used, including the contribution from shape noise (described below), is shown in Figure 5.1.

Shape noise from the intrinsic ellipticity dispersion of galaxies is an important factor in cosmic shear analyses. We modelled it as a flat power-spectrum with value  $N_\ell$  given as

$$N_\ell = \frac{\sigma_\epsilon^2}{\bar{n}}, \quad (5.39)$$

where  $\sigma_\epsilon$  is the standard deviation of the intrinsic galaxy ellipticity dispersion per component, and  $\bar{n}$  is the expected number of observed galaxies per steradian. For our main analysis, we assume *Euclid*-like values where it is expected that 30 galaxies per square arcminute will be observed and divided into ten equally-populated photometric redshift bins, giving  $\bar{n} = 3 \text{ gals/arcmin}^2$  [158]. We investigate the effect of not splitting the sources into different bins, giving rise to a much lower noise level where  $\bar{n} = 30 \text{ gals/arcmin}^2$ , in Section 5.4.3. We take  $\sigma_\epsilon = 0.21$ .

The shape noise spectrum produces a noise matrix with components given by

$$N_{ij} = \frac{\sigma_\epsilon^2}{n_i} \delta_{ij}, \quad (5.40)$$

where  $i, j$  are pixel indices, and  $n_i$  is the expected number of galaxies in the  $i$ -th pixel, which we are assuming is constant and related to  $\bar{n}$  through the area of each pixel.

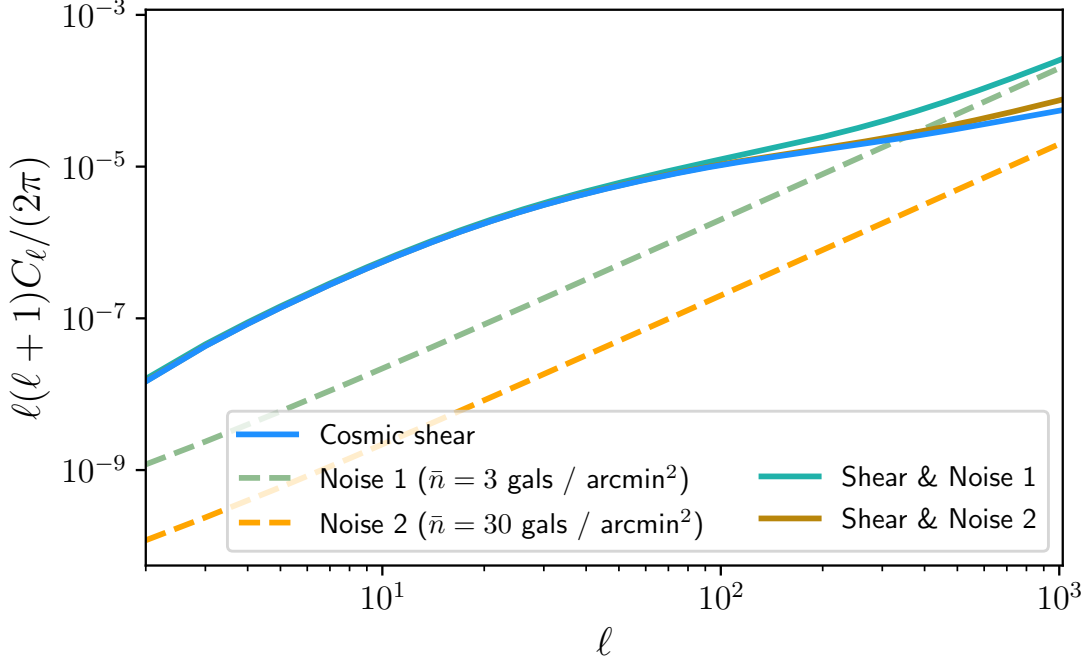


Figure 5.1: Plot of the fiducial power spectrum values for the cosmic shear signal for our single bin of source galaxies (blue curve) that we model as following a Gaussian distribution centred at  $z = 1$  and width  $\sigma_z = 0.15$ . We also plot the power spectrum of the shape noise corresponding to number densities of  $\bar{n} = 3$  gals / arcmin<sup>2</sup> (dashed green curve) and  $\bar{n} = 30$  gals / arcmin<sup>2</sup> (dashed orange curve), and the combined signal and noise spectra (solid green and orange curves).

Figure 5.1 shows the contribution to the total signal from cosmic shear alone and the shape noise. For the case where we consider an observed source galaxy density of  $\bar{n} = 3$  gals / arcmin<sup>2</sup>, we see three distinct regions: the first is for  $\ell \lesssim 200$  where the cosmic shear signal dominates, and thus the uncertainties are dominated by cosmic variance, the second is an intermediate set of scales where the cosmic shear and noise have roughly equal amplitude, and the third is for scales above  $\ell \gtrsim 400$  where the noise dominates. Since we consider the statistics of our estimators up to a maximum multipole of  $\ell_{\text{MAX}} = 512$ , this choice of noise level allows us to test the behaviour of our estimators in these three regions. Hence, we are sensitive to any differences in the statistics that might arise in the different regimes. For the case where  $\bar{n} = 30$  gals / arcmin<sup>2</sup>, we see that we are signal-dominated over our entire multipole range.

### 5.3.2 Survey geometry

Since much of the comparison between our two power spectrum estimation techniques will depend on the specific geometry of the sky mask used, we needed to use a single, generic mask that can be applied consistently to both estimators to highlight the effects of the estimators only. For our analysis, we generated a custom mask that would be applicable to a space-based full-sky weak lensing observatory. This comprises of a main cut that corresponds to the galactic-plane combined with a slightly narrower cut that corresponds to the ecliptic-plane. These two features alone capture the majority of features that are expected for a *Euclid*-like survey and so our simple model for the mask will yield representative results.

In a weak lensing analysis, stars that are present in the data need to be masked out

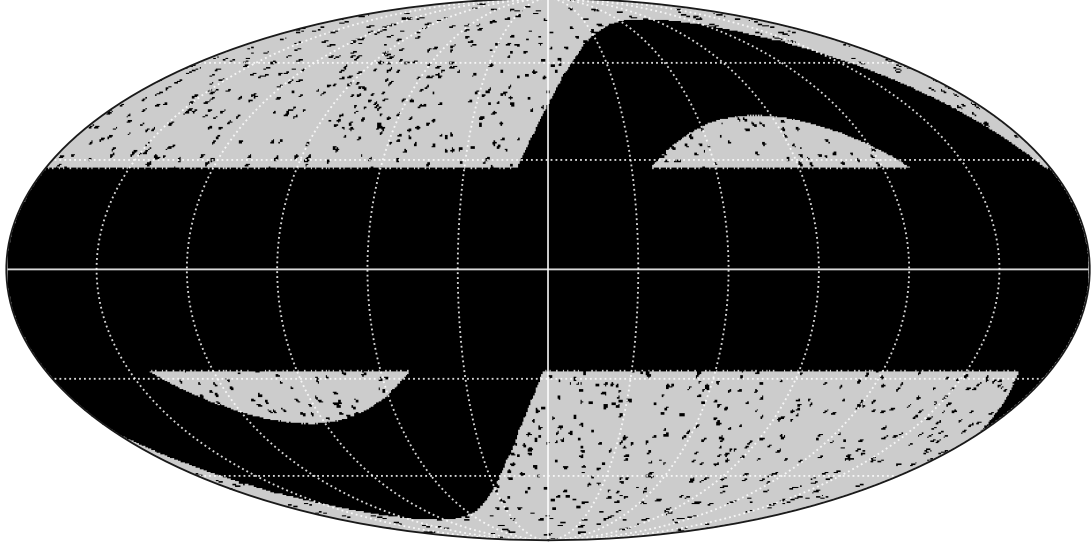


Figure 5.2: Plot of the sky mask used in our analysis applicable for a space-based weak lensing experiment. Here we see the main galactic-cut as the thick horizontal band, the ecliptic-cut as the slightly thinner sinusoidal band, and our star mask consisting of random circular cut-outs that were generated through the prescription of Section 5.3.2. The galactic- and ecliptic- cuts dominate the large-scale behaviour of the mask, whereas the star mask introduces strong small-scale effects.

due to their detrimental effects on determining the shapes of the lensed galaxies. In our analysis, we looked at the effects of our estimators with and without stars to see if the inclusion of stars makes any meaningful difference in either the errors or induced mode-coupling of the recovered power spectra.

The sky masked used in our analyses is shown in Figure 5.2.

### Star mask generation

We investigated the statistics of our estimators at a map resolution of  $N_{\text{side}} = 256$ . This corresponds to a pixel angular scale of 14 arcmin. The prescription described in Ref. [254] can be followed to generate a realistic *Euclid*-like star mask. This involves modelling stars as disks that are distributed randomly on the sky and that have a radii drawn from a random uniform distribution taking values between 0.29 arcmin and 8.79 arcmin. For a galaxy survey such as *Euclid*, stars can be considered point-sources, which are then broadened through the telescope’s optical system point-spread function (PSF) into disks which are then recorded on its CCD detector, and masked over to remove their effect [164]. Stars can be placed on a map until the desired sky area covered by stars is reached. However, we note that this distribution of radii of stars is smaller than the pixel scale for our map resolution, and so a star mask generated using such values as presented in Ref. [254] would give rise to under-sampling in the star mask produced, as all stars would be single pixels, which was found to induce errors in the Pseudo- $C_\ell$  estimator.

Since we are not after an exact realistic distribution of stars in our analysis, we can instead base our star mask on the distribution of ‘blinding stars’, or avoidance areas, that are expected to be encountered for a space-based observatory [255]. These avoidance areas are expected to have an average area of  $0.785 \text{ deg}^2$  and total an area of  $635 \text{ deg}^2$  over the

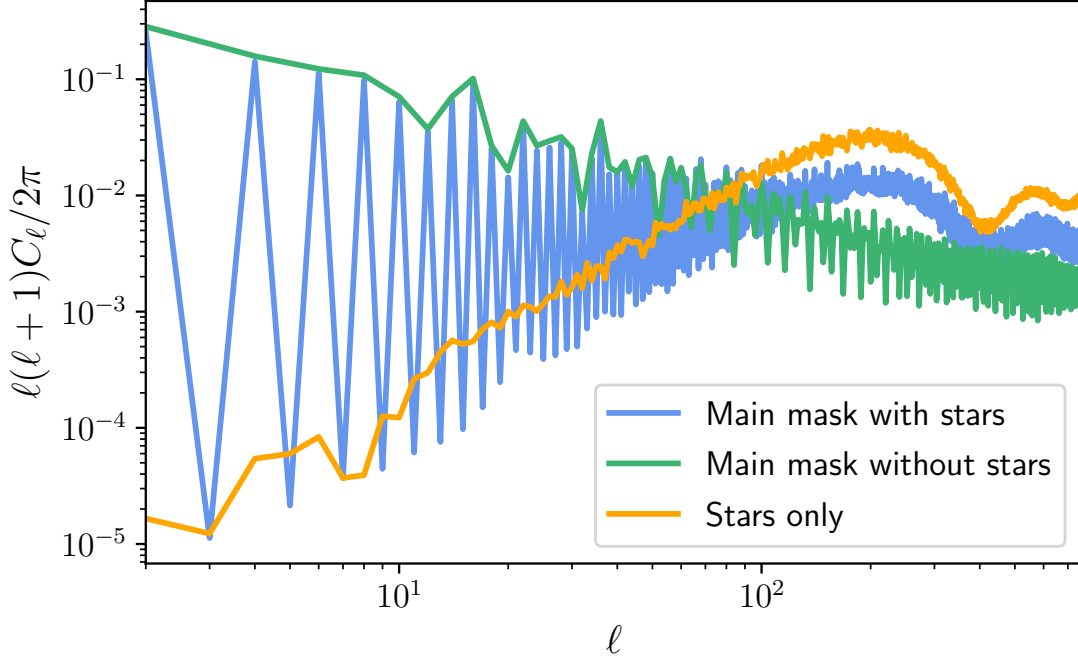


Figure 5.3: Power spectrum of the sky masks used in our analysis. Note that for the ‘main cuts without stars’ curve we plot the even  $\ell$ -modes only due to the very small values that odd  $\ell$ -modes take, arising from the parity of the mask.

expected survey area. Assuming that these avoidance areas can be modelled as disks, this corresponds to an average radii of 30 arcmin, and so is large enough to cover multiple pixels in our limited resolution maps. This approximate treatment should capture the main features brought to the analysis by a more realistic star mask.

We used an edited version of the `GenStarMask` utility as provided with the `Flask`<sup>4</sup> code [13] to generate our star mask using the avoidance area specification. Our edits were made to draw the radii from a uniform distribution rather than a log-normal. To add some scatter to our avoidance area mask, we generated the disks with radii between 25 arcmin and 35 arcmin. To match the desired total avoidance area, avoidance areas were added until they covered 5 % of the full-sky.

### Power spectrum of mask

Since the exact form of Pseudo- $C_\ell$  mixing matrix is highly sensitive to the power spectrum of the mask used, through Equation 5.32, we computed the spherical harmonic transform of our generated mask. This is shown in Figure 5.3.

We plot the power spectrum for our main galactic- and ecliptic- cuts only, the two cuts with added star mask, and star mask only. For the case without stars added, we plot the  $C_\ell$  values for even  $\ell$ -modes only. This is due to the very small values for odd- $\ell$  modes arising from the parity of the mask. Here, we see that the power spectrum for our main mask with stars added has two distinct regions: dominated by the two main cuts for  $\ell \lesssim 10^2$ , and dominated by the star mask above this threshold.

We can understand the primary behaviour of the mask’s power spectrum through computing the analytic power spectrum for a simple mask that is comprised of a single horizontal cut ranging from  $\theta = A$  to  $\theta = B$ . Doing so, we find that the  $C_\ell$  values are

<sup>4</sup><https://github.com/ucl-cosmoparticles/flask>

given by

$$C_\ell = \frac{\pi}{(2\ell + 1)^2} [P_{\ell+1}(\cos A) - P_{\ell-1}(\cos A) - P_{\ell+1}(\cos B) + P_{\ell-1}(\cos B)]^2. \quad (5.41)$$

The full derivation of this result can be found in Appendix A. Enforcing that the mask is symmetric around  $\theta = \pi/2$ , and using the parity of the Legendre polynomials, we find that the analytic prediction for the odd  $\ell$ -modes are zero. The addition of a second cut of equal width, for example the ecliptic-cut, keeps the reflective symmetry. While we use a slightly thinner ecliptic-cut, we still keep this approximate symmetry. Propagating these suppressed odd- $\ell$  modes into the mixing matrix through Equation 5.32 explains why we see strong coupling in the covariance matrices between  $C_\ell$  values that have even- $\ell$  offsets, and little coupling between odd differences.

We also see that the amplitude of the power spectrum coefficients for the mask without stars generally decreases at larger multipole values, where the  $C_\ell$  values roughly scale as  $\ell^2 C_\ell \propto 1/\ell$ . This arises from the large- $\ell$  behaviour of the Legendre polynomials, where they scale as  $P_\ell \propto 1/\sqrt{\ell}$  [256].

The behaviour of the power spectrum of the star mask can also be broadly split into two distinct regions. The first is for multipoles  $\ell \lesssim 200$  where the  $C_\ell$  values are constant, which is a result of the random scatter of the stars on the sphere resulting in a noise-like signal. The second is for multipoles larger than  $\ell \gtrsim 200$  where the  $C_\ell$  values start to oscillate in a sinc-like behaviour, which is where the features of the individual circular disks dominate.

### 5.3.3 Pseudo- $C_\ell$ implementation

An essential part of our work is the accurate computation of the  $C_\ell$  covariance matrices both for our new QML implementation and its comparison to results obtained using the Pseudo- $C_\ell$  method. Here, we used the NaMaster<sup>5</sup> code to produce all estimates for the Pseudo- $C_\ell$  method [17].

In general, the computation of the exact Gaussian covariance is a difficult problem that has been discussed extensively in previous literature. In our work, we employed the narrow kernel approximation as presented in Ref. [225] to compute this Gaussian approximation. However, it should be noted that the narrow kernel approximation overestimates the variances for the lowest  $\ell$  multipoles. Since it is these exact multipoles that we are most interested in, we instead opt to estimate the covariance from an ensemble of 5 000 maps when investigating the raw variances. However, as the estimation of the off-diagonal elements of the covariance matrix are highly sensitive to the number of realisations in the ensemble, when we investigate parameter constraints that are derived from the  $C_\ell$  covariance matrix, we use the ‘analytic’ result as returned from the narrow kernel approximation. In the limit of using large numbers of realisations in the ensemble, at the cost of extensive run-time, Ref. [225] demonstrated that these two estimation techniques are consistent.

## 5.4 Results

### 5.4.1 Benchmark against existing estimators

In this section, we present the results of a comparative study between our new QML implementation and the Pseudo- $C_\ell$  method. First, we wish to investigate how using the

<sup>5</sup><https://github.com/LSSTDESC/NaMaster>

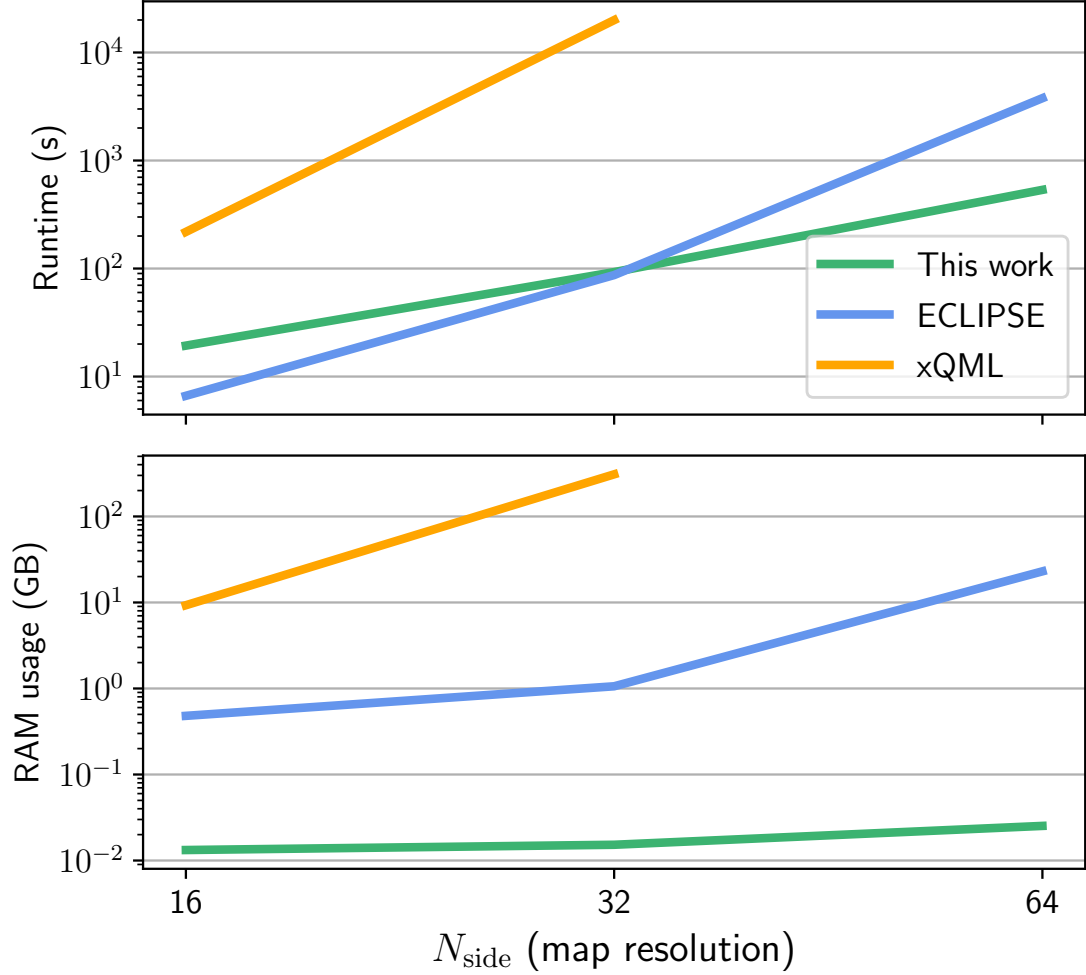



Figure 5.4: Comparison of RAM usage and run-time for different implementations of the QML estimator. We show that our new method has significantly reduced RAM usage compared to existing estimators, which is why we can extend our method to increased map resolutions that the other methods cannot process. Results were obtained using an average over ten maps for our method, and averaged over three runs for each method at each resolution. Computations were performed using 32 cores of an Intel Cascade Lake processor.



novel techniques employed by our new estimator impacts the ability to recover the power spectrum when compared to existing QML implementations. We compare with two leading public implementations of the QML estimator:

- **xQML**<sup>6</sup> as presented in Ref. [257]. This is a straightforward implementation of the QML method as presented in [219] and [220] that has been generalised to cross-correlations between maps. It is written primarily in Python with small parts written in C.
- **ECLIPSE**<sup>7</sup> as presented in Ref. [246]. This is a more numerically efficient implementation of the QML estimator compared to the original prescription and thus exhibits somewhat better performance scaling with resolution over the naive method. It is written in FORTRAN.

We wish to compare the performance of our new code, written in C++, with these existing methods. In Figure 5.4, we present a comparison for the total run-time and RAM usage for the two codes described above and our new method described in this work for a range of map resolutions pushing to the highest  $N_{\text{side}}$  possible with these codes and the computational resources available to us. Here, we see that while our new code is competitive in total run-time when compared to ECLIPSE, we see many orders of magnitude improvement in the total RAM usage for our method over the other two methods. This is because we never have to explicitly store, invert, and compute the product of any of the massive  $N_{\text{pix}} \times N_{\text{pix}}$  matrices that the other two methods employ. Since we are only interested in computing the action of the covariance matrix on a trial pixel-space vector, we keep all of our working-quantities as  $\mathcal{O}(N_{\text{pix}})$  which clearly have much better RAM scaling with resolution over the pixel-space matrices. It is this vastly reduced RAM usage requirement that allows us to push our method to resolutions that are simply not possible on standard high performance clusters using the two previously discussed methods. It is important to note that our new implementation is now only run-time limited, and thus can be pushed to even higher resolutions than have been considered in this work if more extensive computing resources are available. The time-limiting steps to our implementation is the transformations of the trial vector between pixel- and harmonic-space through the use of the `HealPix` functions `alm2map` & `map2alm`. Since both of these functions are implemented using `OpenMP` parallelism, faster run-times can be achieved through simply running our code on higher core count processors.

Our code is publicly available and can be downloaded from GitHub at <https://github.com/AlexMaraio/WeakLensingQML> .

## 5.4.2 Accuracy of numerical Fisher matrix

As explained in Section 5.2.3, we use finite-differences to compute the approximate form of the Fisher matrix from a set of  $s_\ell$  values estimated using conjugate gradient techniques. To validate the accuracy of these methods we compared our estimates of the Fisher matrix with the ‘analytic’ result as computed using the formalism presented in [246]. While this is still a ‘brute-force’ QML implementation, where the covariance matrix still needs to be computed and stored in full, their method allows many quantities to be expressed in terms of the spherical harmonic transform matrix  $\mathbf{Y}$  and thus reduce the computational demands of the estimator. This comparison was performed at a map resolution of  $N_{\text{side}} = 64$ , which was the maximum resolution possible for the computation of the analytic result. Note that at this resolution, the typical pixel scale is larger than the angular size of our cut-outs generated for our star mask, and so this comparison was computed for the case without the

<sup>6</sup><https://gitlab.in2p3.fr/xQML/xQML>

<sup>7</sup><https://github.com/CosmoTool/ECLIPSE/>



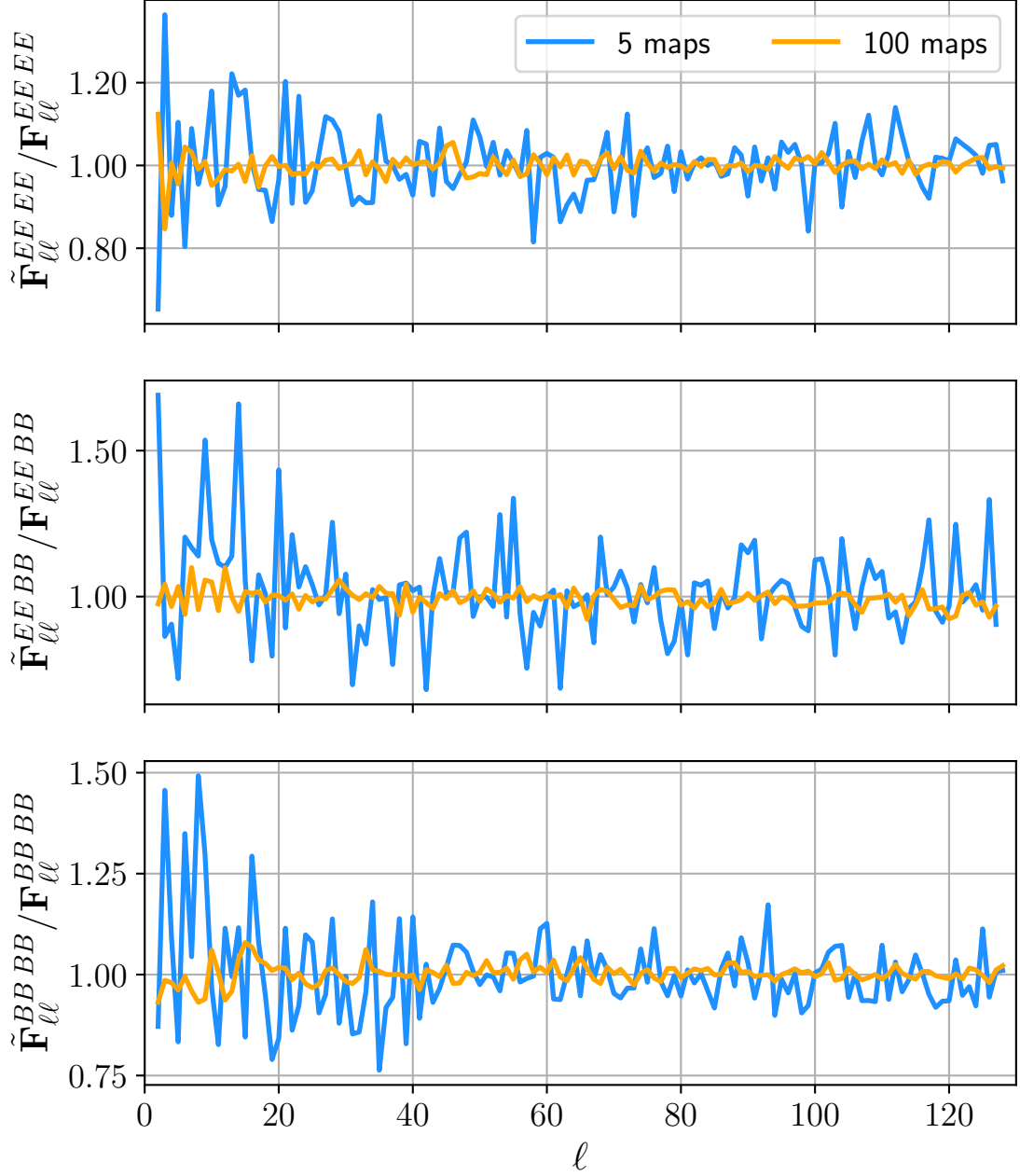


Figure 5.5: Ratio of our numerical Fisher matrix with respect to the analytic result for a map resolution of  $N_{\text{side}} = 64$ . Here, we plot the diagonal of the  $EE$ - $EE$ ,  $EE$ - $BB$ , and  $BB$ - $BB$  components. All three components show good consistency with unity regardless of the number of maps averaged over when computing the Fisher matrix through Equation 5.28, with the amplitude of the scatter decreasing with increasing number of maps.

star mask added to the main cuts. The result of this comparison is presented in Figure 5.5, where we plot the ratio of the diagonal of the  $EE-EE$ ,  $EE-BB$ , and  $BB-BB$  components of the Fisher matrix. We plot the cases for where we average over five and one hundred maps when injecting power into the generated maps when estimating the Fisher matrix (see Equation 5.28). Figure 5.19 shows this ratio extended to several of the off-diagonal strips, specifically for the cases with  $\Delta\ell = 2, 8, 32$ . Both figures show that while the amplitude of the random scatter in the ratio decreases significantly when averaging over more maps, both cases are simply random scatter around unity - and thus our numerically obtained Fisher matrix is a true representation of the actual Fisher matrix. Propagating the two different numerical and analytical  $C_\ell$ -Fisher matrices to parameter constraints using Fisher forecasts shows negligible differences in parameter contours which again highlights our trust in our new method to estimate the  $C_\ell$ -Fisher matrix at any resolution. Hence, we are free to use our validated method to reliably increase the resolution of our implementation beyond what is possible with current implementations. In our analysis, we averaged over twenty five random realisations which provided a good compromise between run-time and numerical accuracy.

### 5.4.3 Comparing $C_\ell$ variances of QML to Pseudo- $C_\ell$

With our new implementation, we can extend the analysis of the properties of the QML estimator to map resolutions of  $N_{\text{side}} = 256$ , which allows us to accurately recover the power spectrum up to a maximum multipole of  $\ell_{\text{MAX}} = 512$ . At this resolution, the storage of the full pixel covariance matrix alone would require approximately 5 TB of RAM, which is clearly an unfeasible requirement for any current computer and thus any analysis at this resolution is not achievable using current QML implementations.

We generate maps of the weak lensing shear through producing Gaussian realisations with the power spectrum described in Section 5.3.1 (see Figure 5.1). We then add shape noise to these maps according to Equation 5.39. We generate twenty five such maps for each power spectrum multipole that we are injecting power into ( $EE$  and  $BB$ , from  $\ell = 2$  to  $\ell = 767$ ) and compute the QML power spectrum ( $EE$  and  $BB$ ) from each. We estimate the QML covariance matrix using the fact that for Gaussian maps the inverse Fisher matrix is the covariance matrix. The methods described in Section 5.2.3 were used to estimate the Fisher matrix, where we average over twenty five maps per multipole when evaluating Equation 5.28. The Pseudo- $C_\ell$  covariance matrix was computed using the methods described in Section 5.3.3, and was constructed from an ensemble of 5 000 maps. We do not bin in  $\ell$  either of our QML or Pseudo- $C_\ell$  estimators, noting that our mask is small enough that the Pseudo- $C_\ell$  mixing matrix is invertible without binning as we are able to reconstruct all modes that we have generated. We note that our results were robust to different binning strategies that were applied though not used in our final results. We remind the reader that we are interested in estimates of the deconvolved full-sky Pseudo- $C_\ell$  values, not forward modelling of the mask into the original power spectrum. While this deconvolution could introduce additional sub-optimality over forward modelling through the inversion of the mixing matrix, for the types of mask that a forthcoming Stage-IV galaxy survey will typically use this should not be an issue. Appendix 5.A shows that the means of the two estimators applied to an ensemble of maps are consistent with the input spectra. Hence, this demonstrates that both estimators are unbiased in their means, and thus any differences in their variances are a result of the intrinsic properties between the two estimators.

In Figure 5.6 we plot the ratio of the standard deviations associated with the Pseudo- $C_\ell$  estimator with respect to our QML implementation for the diagonal values associated with the  $EE-EE$  and  $BB-BB$  block of the covariance matrix. Here, we see that the

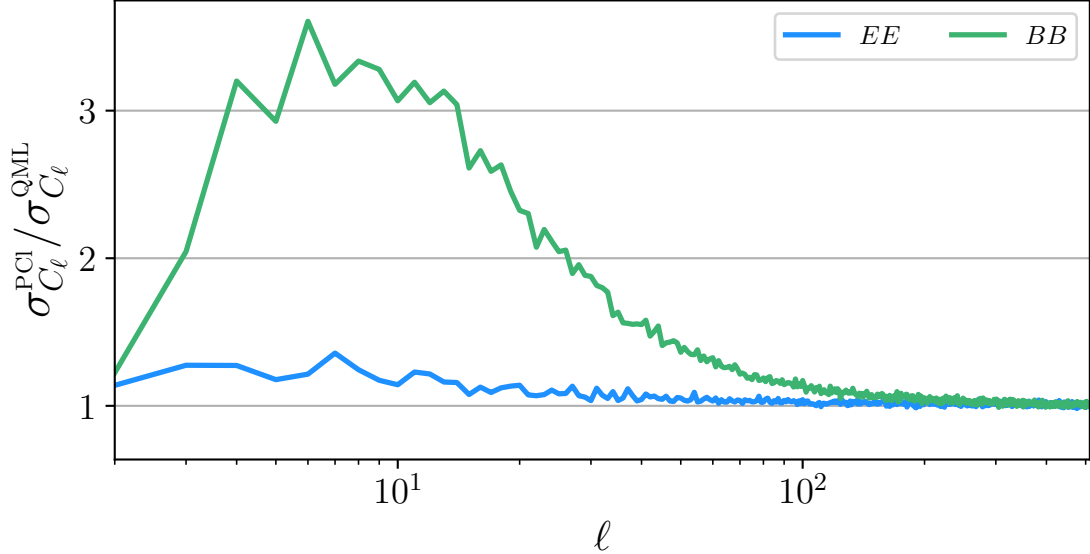


Figure 5.6: Ratio of standard deviation of the  $C_\ell$  values (top curve  $C_\ell^{BB}$ , bottom curve  $C_\ell^{EE}$ ) obtained using the deconvolved Pseudo- $C_\ell$  method using **NaMaster** to those obtained using our new QML implementation. We see that the QML estimator provides the largest improvements over the Pseudo- $C_\ell$  method on the largest angular scales, with a very significant improvement for the  $B$ -modes.

Pseudo- $C_\ell$  estimator is sub-optimal to the level of  $\sim 20\%$  for  $\ell \lesssim 50$  for the  $EE$  spectra. This corresponds to an equivalent increase in the survey area of around 40% on these scales, which is a massive increase in equivalent area considering that forthcoming Stage-IV surveys are expected to maximise the possible sky area that is observable for ground- or space-based cosmic shear surveys [255]. Hence, getting this additional area ‘for free’ by analysing the data through QML methods demonstrates the advantages of using such methods and such investigations into their behaviour for cosmic shear analyses. For the  $BB$  spectra, we find that the Pseudo- $C_\ell$  estimator produces errors that are many times that of the optimal QML estimator, peaking at over three times the standard deviation for the Pseudo- $C_\ell$  estimator with respect to our QML method. This ratio remains significantly above unity for multipoles that are well above one hundred, which shows that there is a huge advantage to be gained in  $B$ -mode precision when using QML methods over the Pseudo- $C_\ell$  estimator. We find that the ratio for both sets of spectra decays to unity (with some random scatter) for larger  $\ell$  values. This matches previous QML studies, which have principally been conducted in the context of the CMB and ground-based galaxy clustering surveys, which found that the Pseudo- $C_\ell$  estimator is close to optimal on small scales and for homogenous noise, and we find similar results here in the weak lensing context [227, 251].

Figure 5.6 also shows that the statistical precision of the  $B$ -mode power spectrum is significantly higher for the QML method compared with Pseudo- $C_\ell$  method. This is relevant because cosmic shear theory predicts zero  $C_\ell^{BB}$  modes and so any detection of a non-zero  $C_\ell^{BB}$  signal would prompt a thorough investigation of the data [33]. Potential sources of  $B$ -mode power include residual point-spread function uncertainties, telescope detector defects, and intrinsic alignments, all of which should be investigated if non-zero  $B$ -mode power was found to be statistically significant. The Pseudo- $C_\ell$  estimator is very sub-optimal on large scales, and so this loss of sensitivity to the  $B$ -modes can arise from contamination leakage from the  $E$ -modes into the  $B$ -modes due to the nature of the cut-sky. Since the QML estimator is derived from the likelihood for the maps, which depends

on the input fiducial power spectrum which contains zero  $B$ -mode power, any  $B$ -mode power present in the masked maps must arise from leakage from the  $E$ -modes, and thus the estimator can weight the data optimally through the covariance matrix to minimise the variance from the  $E$ -modes contributing to the  $B$ -modes. For the Pseudo- $C_\ell$  estimator, this leakage can be mitigated through the map-level procedure of  $B$ -mode purification [258–260] and has been shown to decrease dramatically the associated  $B$ -mode errors, particularly at low  $\ell$  multipoles [17]. However, a requirement for purification to work is that the mask must be differentiable along its edges. This can be achieved through the apodisation of the mask which convolves the mask with some smoothing window function that ensures differentiability. This has most commonly been applied to cosmic microwave background experiments where their masks are generally formed of a single much simpler cut applied to the sky [148]. This allows apodisation to work effectively on the mask without significant reduction to  $f_{\text{sky}}$ . However as previously discussed, a weak lensing experiment also needs to mask out small regions corresponding to bright stars or other objects that need removing from the data, or areas that feature no galaxies due to limitations in depth and/or pixel size. These small regions cause significant issues with the apodisation process as the convolution with the smoothing function serves to dramatically increase their apparent area - producing a significant reduction in  $f_{\text{sky}}$ . We investigate the effects of apodising our mask in Appendix 5.C. We find that while apodisation strongly reduces widely separated mode coupling arising from the suppression in small-scale power of the mask (as now the shape edges from our star-like disks are smoothed out), this could not offset the significant reduction in sky area (from  $f_{\text{sky}} = 33\%$  to  $f_{\text{sky}} = 22\%$ ) that apodisation brought about. This resulted in apodisation providing looser parameter constraints than for the case without apodisation. A key advantage of the QML estimator is the natural  $E/B$ -mode separation without a loss in sky area [240].

### Varying noise levels

Thus far, we have assumed a noise level corresponding to an experiment that has observed thirty galaxies equally divided into ten redshift bins, giving  $\bar{n} = 3 \text{ gals/arcmin}^2$ . Here, we wish to investigate the statistics of our estimators for the case where the observed galaxies are combined into a single redshift bin, giving a much lower noise level of  $\bar{n} = 30 \text{ gals/arcmin}^2$ . Performing this comparison produced results as shown in Figure 5.7. Here, we see that while there are negligible differences in the relative statistics between the  $E$ -modes, there was a large increase in ratio between our two estimators for the  $B$ -modes. We can investigate this large difference in the  $B$ -mode ratios by plotting the raw errors of the  $B$ -mode spectra for our two estimators for the two noise cases, which is shown in Figure 5.8.

Here, we see that for low multipoles there is a large difference in the errors for the QML estimator between the two noise levels whereas the errors for the Pseudo- $C_\ell$  estimator remains relatively unchanged. At this decreased noise level, the noise is subdominant to the cosmic variance from the  $E$ -modes on large-scales. Hence, the QML estimator can vastly outperform the Pseudo- $C_\ell$  method on these large-scales because the QML likelihood can efficiently minimise the cosmic variance from the  $E$ -modes leaking into the  $B$ -modes through the cut-sky. The increased noise level corresponds to a genuine increase in  $B$ -mode power which the QML estimator cannot suppress as efficiently as the  $E$ -mode cosmic variance leakage. Hence, we see an associated decrease in the ratio between its errors and that of the Pseudo- $C_\ell$  estimator.

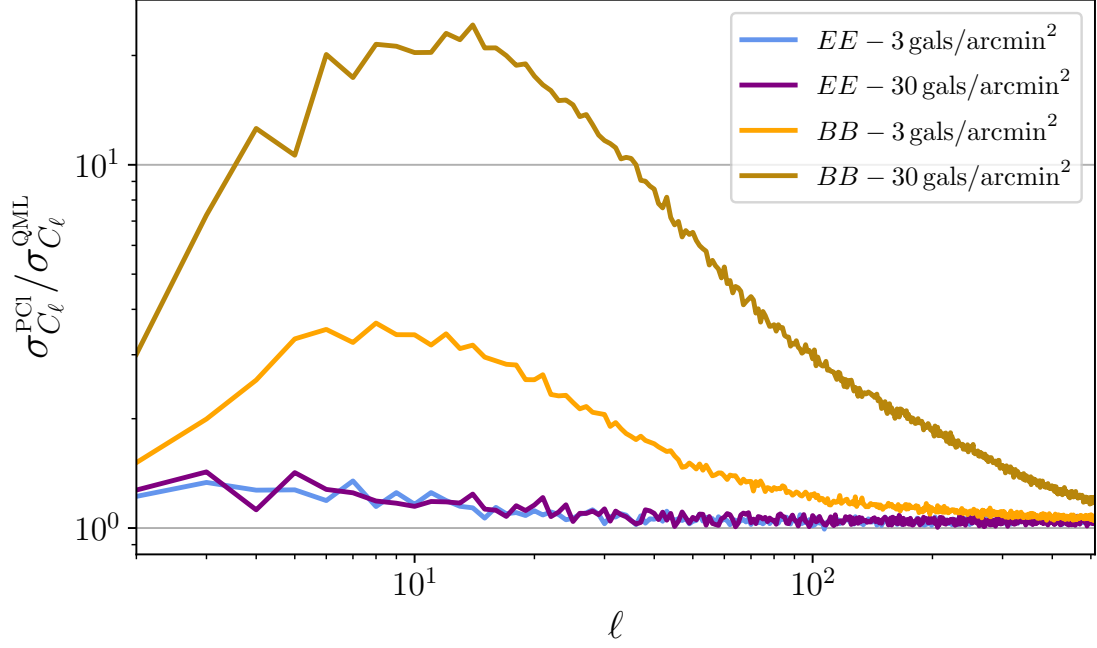


Figure 5.7: Ratio of the errors on the power spectrum for the Pseudo- $C_\ell$  estimator with respect to the QML estimator for the case of two different noise levels of  $\bar{n} = 3 \text{ gals / arcmin}^2$  and  $\bar{n} = 30 \text{ gals / arcmin}^2$ . Here, we see the decreased noise level for the curves for the case of  $\bar{n} = 3 \text{ gals / arcmin}^2$  has negligible effect on the errors associated with the  $EE$ -spectra, whereas there is a large increase in the ratio for the  $BB$ -spectra.

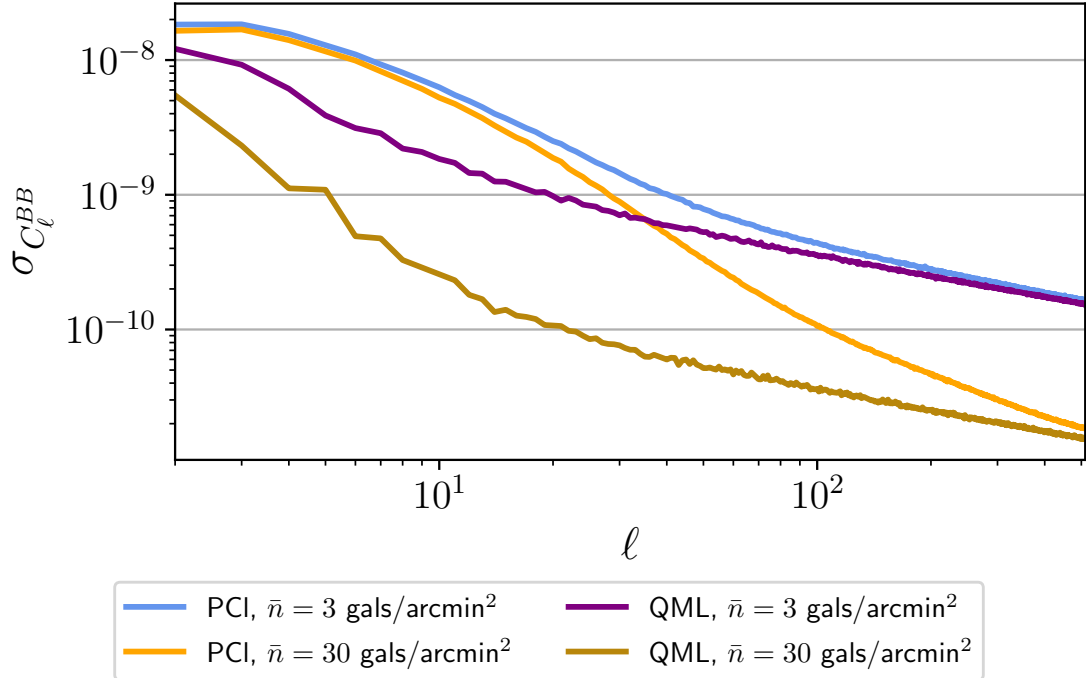


Figure 5.8: Errors on the  $BB$ -spectra for the two different noise levels considered. Here, we see that the errors for the Pseudo- $C_\ell$  estimator remain relatively unchanged for the lowest multipoles, whereas the errors for the QML estimator decrease dramatically when the amplitude of the noise is reduced.

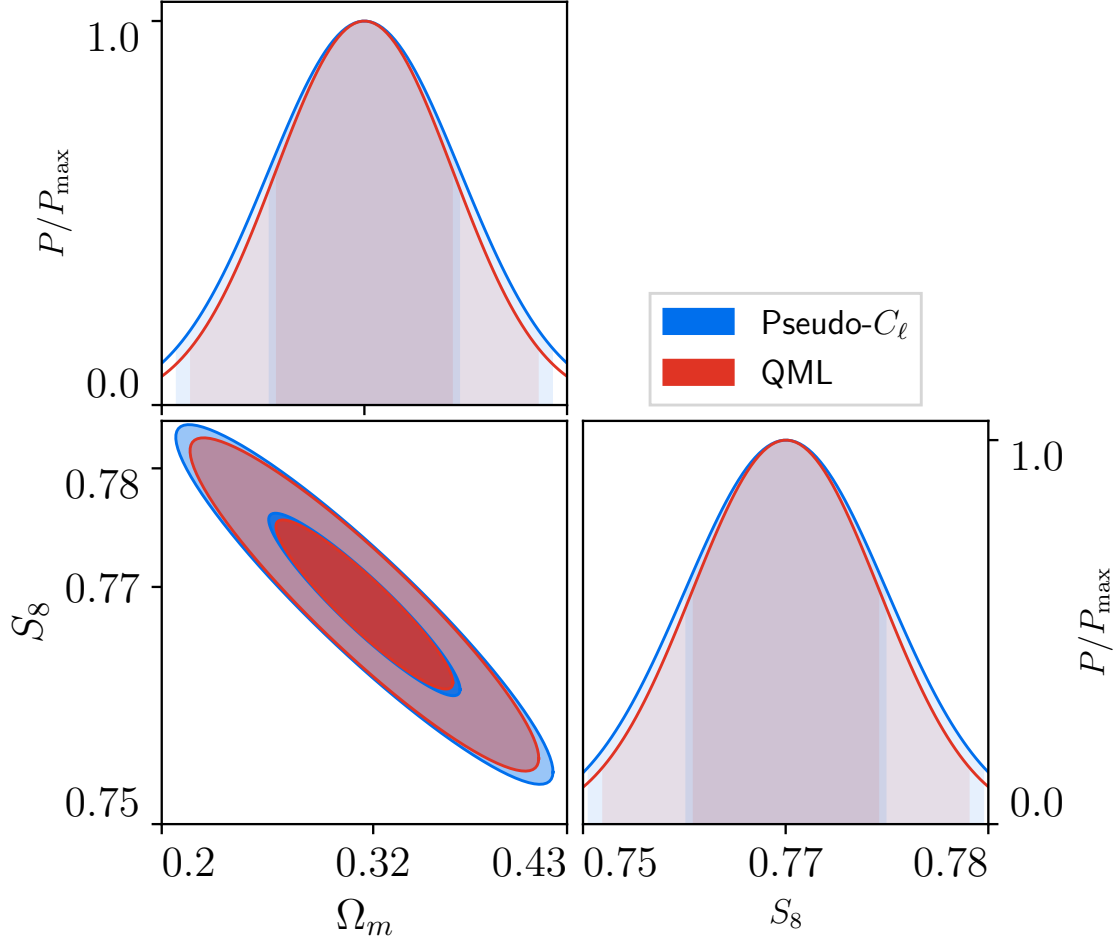


Figure 5.9: Parameter constraints on  $S_8$  and  $\Omega_m$  obtained from a Fisher matrix analysis up to a maximum multipole of  $\ell_{\text{MAX}} = 512$  for our two estimators. Here, we see that the increased errors associated with the Pseudo- $C_\ell$  method propagate through to slightly broadened parameter contours.

#### 5.4.4 Cosmological parameter inference

A Fisher matrix forecast was used to propagate our estimated  $C_\ell$  covariance matrices into parameter constraints. For an arbitrary set of cosmological parameters  $\vartheta_\alpha$  and  $\vartheta_\beta$ , the corresponding Fisher matrix element is given by [197]

$$\mathcal{F}_{\alpha\beta} = \sum_{\ell, \ell'} \frac{\partial C_\ell}{\partial \vartheta_\alpha} \mathbf{C}_{\ell\ell'}^{-1} \frac{\partial C_{\ell'}}{\partial \vartheta_\beta}, \quad (5.42)$$

where  $\mathbf{C}$  is the  $C_\ell$  covariance matrix. In our analysis, we focused on the two parameters that cosmic shear places the tightest constraints on: the clustering amplitude  $S_8$  and the total matter density  $\Omega_m$ . Figure 5.9 shows a comparison of the derived constraints for these two parameters between our two estimators. Here, we see the effect of the slightly increased errors associated with the Pseudo- $C_\ell$  estimator have propagated into slightly increased contours for these two parameters when compared to the QML estimator's contours. This result could have been anticipated from Figure 5.6, since most of the information on these parameters originates from small scales where the ratio of the errors approaches unity. In contrast, parameters affecting large angular scales, such as local primordial non-Gaussianity, are expected to benefit substantially from an optimal method.

The figure of merit, which quantifies how well constrained parameters are, is related

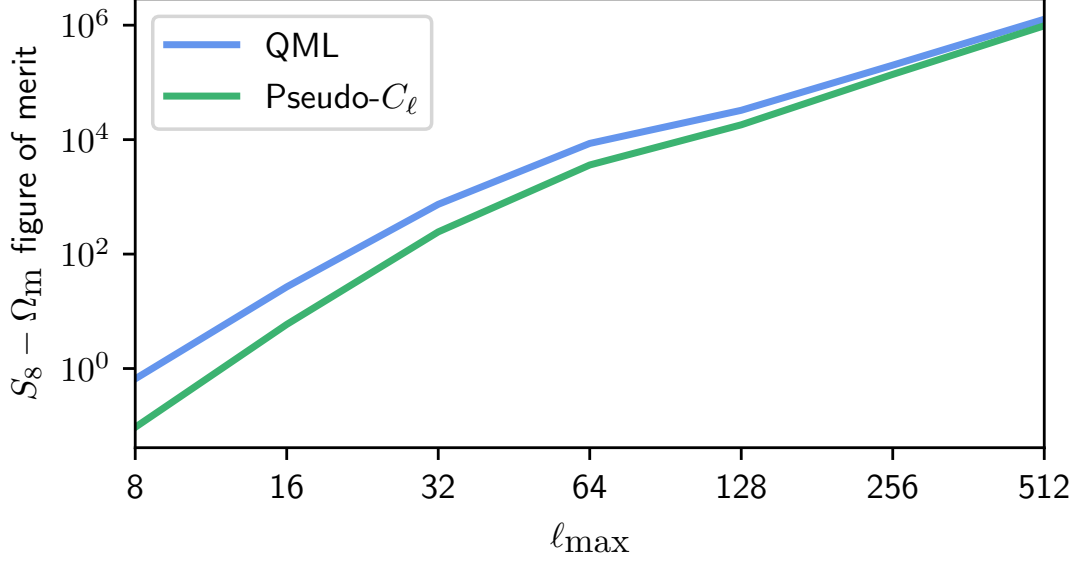


Figure 5.10: Values for the figure of merit for the combination of  $S_8$  and  $\Omega_M$  as a function of the maximum  $\ell$  multipole used in the analysis. We see that as the maximum multipole increases, the relative sub-optimality of the Pseudo- $C_\ell$  estimator decreases and results from the two estimators converge.

to the Fisher matrix through [157]

$$\text{FoM}_{S_8\Omega_M} = \sqrt{\det(\mathcal{F})}. \quad (5.43)$$

A plot of the figure of merit for the combination of  $\Omega_M$  and  $S_8$  as a function of maximum multipole is shown in Figure 5.10. Here, we see that the sub-optimality of the Pseudo- $C_\ell$  method is most apparent when we are limited to low multipoles. As the maximum multipole increases we see that the figures of merits converge, however showing that the QML method consistently out performs the Pseudo- $C_\ell$  method.

The application of Fisher forecasting to predict parameter constraints from the covariance matrix is done under the assumption that the  $C_\ell$  values recovered from the estimators can be described by a Gaussian likelihood. While it has been shown that for the full sky case, an analytic calculation of the likelihood of the power spectra can be computed [261], which can be accurately modelled as a Gaussian on small scales, the exact likelihood of the recovered power spectrum using either the QML or Pseudo- $C_\ell$  estimators is still unknown. Previous works have simply used the Gaussian approximation citing the central limit theorem [237], though the exact likelihood on large scales remains unknowns for both the QML and Pseudo- $C_\ell$  estimators.

### Inclusion of stars

Our results presented thus far have been all for the case where we have applied a star mask to a large-scale mask featuring ecliptic and galactic cuts, as shown in Figure 5.2. Here, we wish to investigate the detailed effects on the covariances of our estimators when we apply the star mask to our main two cuts. All results here are presented for the case without any mask apodisation applied.

The ratio of the Pseudo- $C_\ell$  covariance matrix for the cases with and without stars is presented in Figure 5.11. Here, we see that the primary effect of the addition of stars into the mask is to increase the correlation between widely separated  $\ell$ -modes, while leaving the values close to the diagonal in the covariance matrix relatively unchanged.



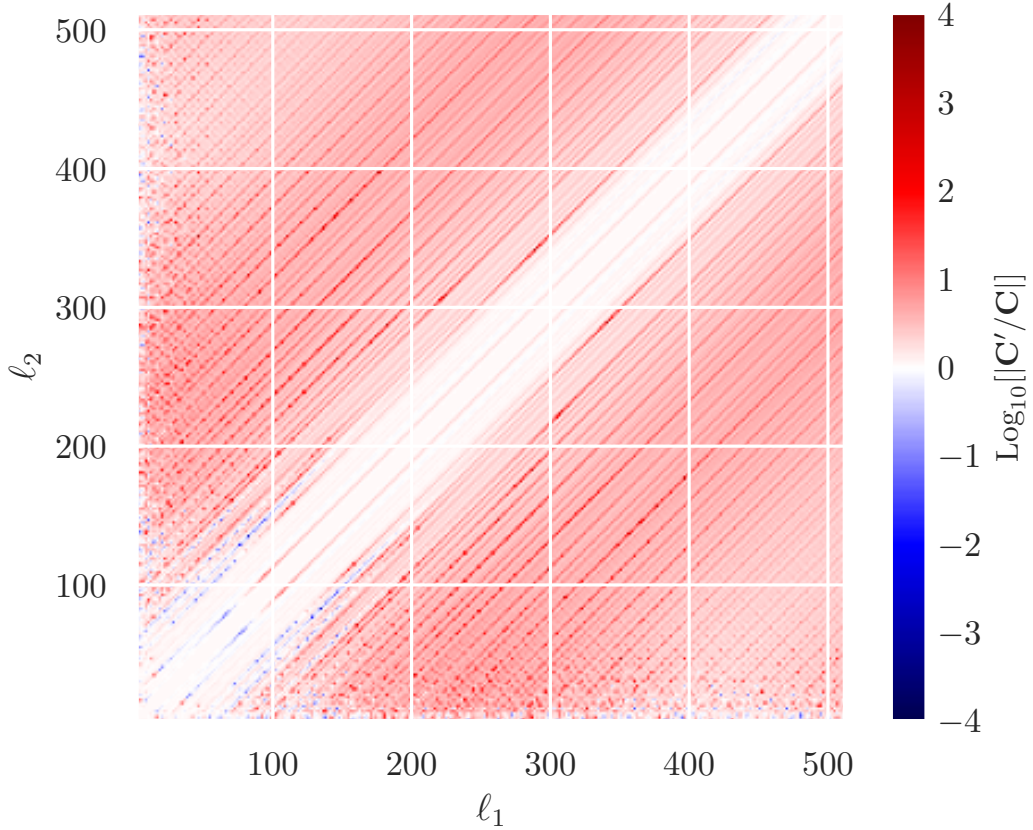


Figure 5.11: Ratio of the analytic Pseudo- $C_\ell$  covariance matrix for the  $C_\ell^{EE}$  power spectrum for the cases with ( $\mathbf{C}'$ ) and without stars ( $\mathbf{C}$ ) applied to the main mask. Note that we only plot the covariance matrix for even- $\ell$  values only (due to the very small values for the odd- $\ell$  case and so their ratios are dominated by numerical noise).

This new covariance matrix can then be propagated into parameter contours to see if these increased long-range correlations (which fiducially have very small values) have any meaningful effect on cosmological parameter constraints. This is shown in Figure 5.12. Here, we see that there are negligible differences on the parameter contours between the two cases for our QML estimator, however there is a slight broadening in the contours for the Pseudo- $C_\ell$  estimator which is consistent with the loss of sky area to the star mask. This shows that the Pseudo- $C_\ell$  estimator is more sensitive to the addition of a star mask than the QML estimator, further highlighting the benefits of the QML method.

### 5.4.5 Non-Gaussian maps

Throughout our paper, we have been applying our estimator to Gaussian realisations of the cosmic shear field. However, as it has been shown that the convergence field  $\kappa$  is more accurately described by a log-normal distribution [262, 263], an investigation of how our estimators perform when applied to these non-Gaussian maps was undertaken. This is because as the QML estimator assumes that the underlying power spectrum coefficients follow a Gaussian distribution, any non-Gaussianities present in the shear field could induce non-optimality into the recovered power spectra which would increase errors.

The `Flask` software package was used to generate log-normal maps [13]. The ‘shift parameter’ that corresponds to the minimum value of the convergence field required by



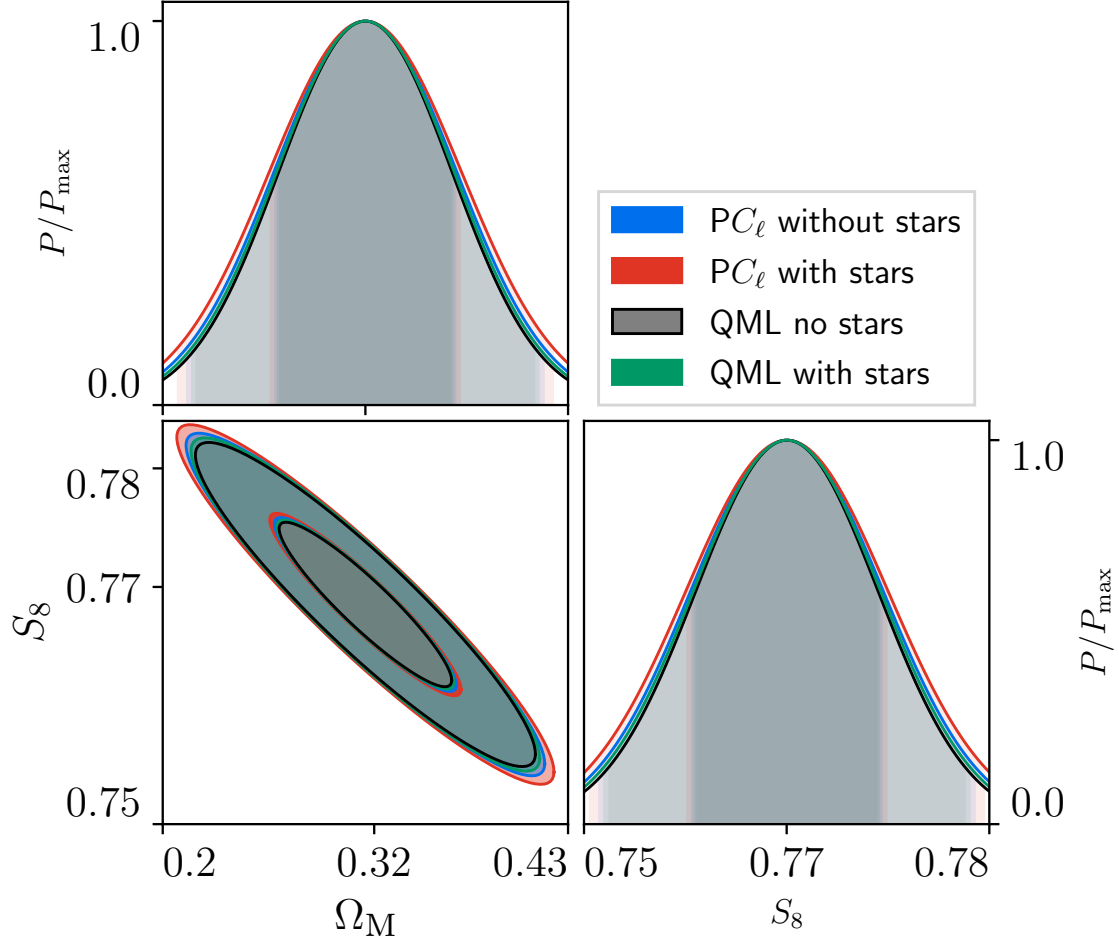


Figure 5.12: Fisher parameter constraints comparison between QML and Pseudo- $C_\ell$ , where both estimators have a maximum multipole of  $\ell_{\text{MAX}} = 512$ , for the cases with and without the star mask applied to both estimators. Here we see that the Pseudo- $C_\ell$  estimator is more sensitive to the inclusion of the star mask through the relative increase in parameter contours when compared to the QML contours.

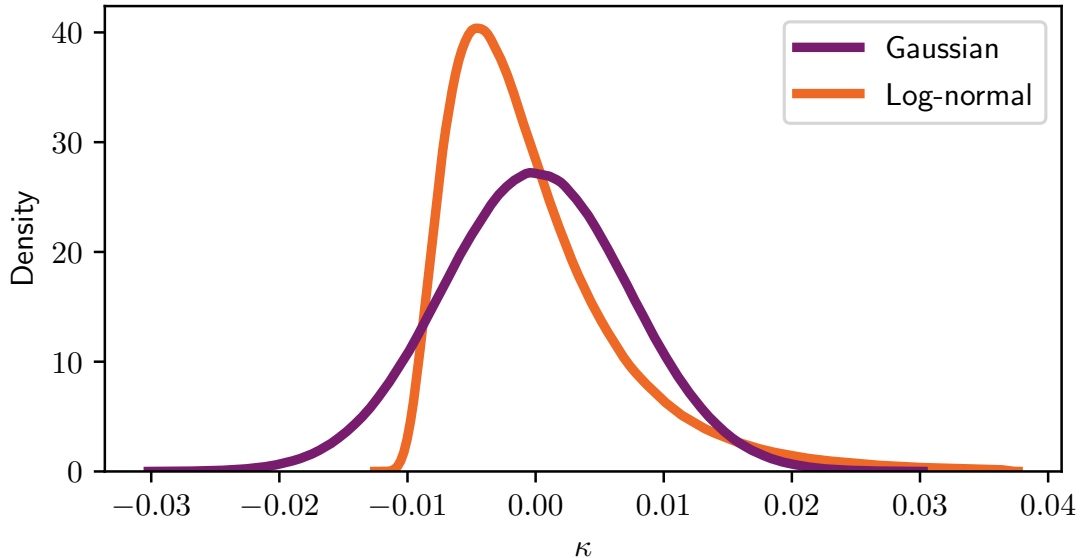


Figure 5.13: Histogram showing the field values of a Gaussian and log-normal realisation of the convergence field  $\kappa$  for the same underlying power spectrum

`Flask` was set to 0.01214, following [261]. The log-normal maps were generated at a resolution of  $N_{\text{side}} = 1024$  and then downgraded to a resolution of  $N_{\text{side}} = 256$  as required to be processed through our estimators. A histogram showing the distribution of  $\kappa$  values for a Gaussian and log-normal realisation is shown in Figure 5.13. This log-normal convergence field is then propagated to a slightly modified shear field, which we can apply the estimators to.

Since the covariance of the QML estimator is no longer given by the inverse Fisher matrix, we have to obtain estimates for the QML errors from an ensemble of numerical realisations. The results of applying the QML and Pseudo- $C_\ell$  estimators to an ensemble of 2 500 Gaussian and log-normal realisations is shown in Figure 5.14. Here, we see that the ratio of the power spectrum errors for the two distributions are virtually identical which demonstrates that the relative behaviour of our estimators remains unchanged even when applied to maps that the underlying likelihood does not fully describe. Since the largest differences between the estimators for our setup occur on the largest scales which is where the effects of the non-Gaussianity is weak, this is not surprising.

## 5.5 Conclusions

We have presented a new implementation of the optimal quadratic maximum likelihood estimator that is the most efficient publicly available code of its type. Using our new estimator, we have compared the statistical properties of the expected power spectrum for forthcoming Stage-IV weak lensing surveys, using realistic survey conditions, between our QML implementation and an existing Pseudo- $C_\ell$  code. We found that the sub-optimality of the Pseudo- $C_\ell$  estimator resulted in marginally increased statistical errors for the  $E$ -mode power spectra propagating to increased parameter contours when using Fisher forecasting. In addition, we found a significant increase in the precision for the  $B$ -mode power spectra when applying our QML estimator over the Pseudo- $C_\ell$  method, which raises the hopes of being able to further constrain new  $B$ -mode physics using forthcoming surveys. Our results show that the application of QML methods to cosmic shear data provides a

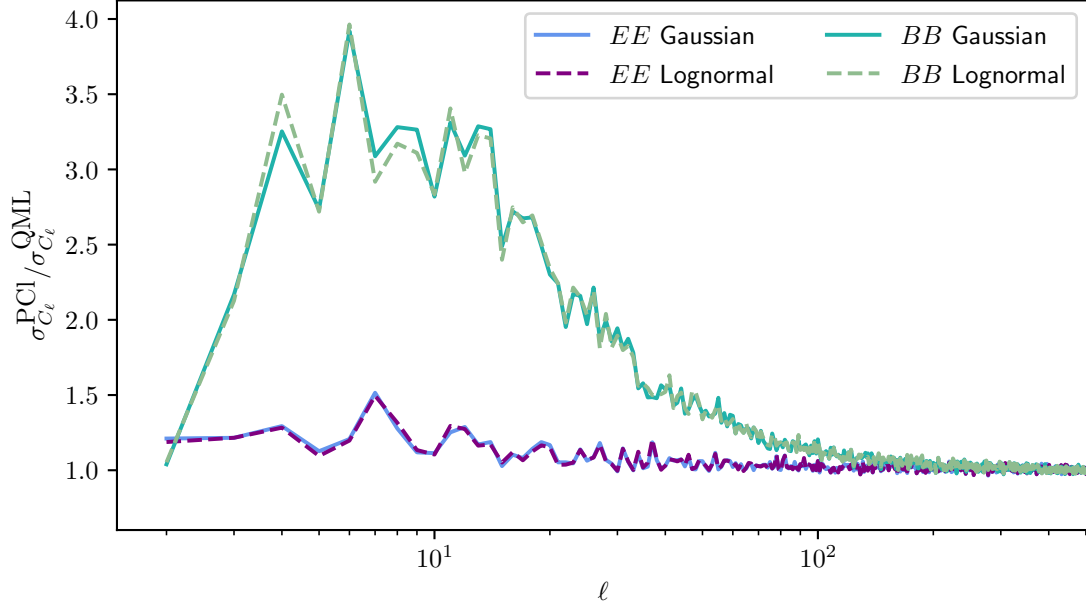


Figure 5.14: Ratio of the power spectrum errors for the Pseudo- $C_\ell$  method with respect to the QML estimator applied to both Gaussian and log-normal realisations. Here, we see that the results are indistinguishable between the two distributions.

useful cross-check to existing methods, and could have many interesting applications for the constraints of new  $B$ -mode physics.


Our new estimator could be extended in numerous ways, for example the QML method can be easily applied to spin-0 fields such as photometric galaxy clustering. Since our estimator yield the best improvements on the largest physical scales, scales at which primordial non-Gaussianity has the largest effects on the observed signal, the use of our new estimator could enable tighter constraints on primordial non-Gaussianity. In addition, photometric galaxy clustering data can be combined with cosmic shear to form a combined  $3 \times 2$ -point investigation which our estimator could be applied to. We leave these applications of our estimator to future work. We also note that our estimator could also be applied to thermal Sunyaev-Zeldovich data, which is a powerful probe of cosmology at relatively low multipoles ( $\ell \lesssim 10^3$ ) [264, 265]. This overlaps with the multipole region where QML provides the best improvements over the Pseudo- $C_\ell$  estimator, and so could provide sufficiently tighter constraints when applied to these data-sets.

Since QML methods deal with data at the pixel-level, they are well suited for dealing with contaminants and effects that can only be described accurately in terms of pixels in the maps. One such problem is the effect of spatially varying noise over survey area, which could arise from different seeing conditions encountered as a telescope surveys the sky or the properties of the detector evolving as data is taken or even from the slight varying of diffuse foreground light levels which are aimed to be minimised for any cosmic shear survey but may still nevertheless contaminate some pointings. These pixel-level effects can easily be incorporated into the QML estimator through an appropriate modification of the noise matrix  $\mathbf{N}$ , whereas the Pseudo- $C_\ell$  method utilises Fourier transforms and these pixel-level effects get diffused over a wide  $\ell$  range and thus become harder to model. This could further reduce the optimality of the Pseudo- $C_\ell$  estimator. We leave a dedicated investigation of how such effects affect the two estimators to future work.

To conclude, we have shown that the Pseudo- $C_\ell$  estimator is close to optimal on small scales for a simplified *Euclid*-like weak lensing survey. Despite this, the QML estimator is

better suited for a variety of applications, including  $E/B$ -mode separation, complex noise patterns, and complicated survey geometries. With systematics expected to dominate the error budget of upcoming surveys it is increasingly important to demonstrate the consistency of results derived from different analysis pipelines - the fast, publicly available implementation of the QML estimator that we have presented in this work represents a significant step forward in this regard.

## Data availability

All data presented in this work has been generated by the authors. The code to do so can be found on our GitHub repository located at <https://github.com/AlexMaraio/WeakLensingQML> .

## Acknowledgements

AM would like to thank all members of Lensing Coffee at the IfA for many useful conversations and invaluable support. AH thanks Uroš Seljak for useful discussion. AH and AT are supported by a Science and Technology Facilities Council (STFC) Consolidated Grant. For the purpose of open access, the author has applied a Creative Commons Attribution (CC BY) licence to any Author Accepted Manuscript version arising from this submission.

## Appendices

### 5.A Demonstration of unbiased estimators

The core feature of any power spectrum estimator is that the mean of the recovered spectrum matches the expected values for a known input spectrum. Here, we demonstrate that our new QML implementation correctly recovers the mean of our input spectrum and that it is also consistent with the Pseudo- $C_\ell$  mean. Hence, any differences in their variances will not be due to a difference in scaling between the two estimators. Figures 5.15 and 5.17 show the average  $EE$ - and  $BB$ -spectra for an ensemble of five thousand random realisations of the same input spectra, with the ratios of the average recovered spectrum to the input spectrum shown in Figures 5.16 and 5.18. Here, we see that both estimators accurately recover the input values over the entire  $\ell$  range and thus our new QML estimator is unbiased and the differences in variance between it and the Pseudo- $C_\ell$  estimator is intrinsic to the method. However, we note that Figures 5.16 and 5.18 show that the average values produced for the QML estimator are significantly noisier than those for the Pseudo- $C_\ell$  estimator. This is a direct result of the use of a numerical estimate of the Fisher matrix instead of its exact analytic calculation. Through Figures 5.5 and 5.19, we have shown that our numerical estimation method recovers the analytic calculation of the Fisher matrix on average, with the level of noise determined by the number of maps that have been averaged over (see Equation 5.28). Hence, the accuracy of the multipole estimates can be increased by simply computing the Fisher matrix with an increased number of maps.

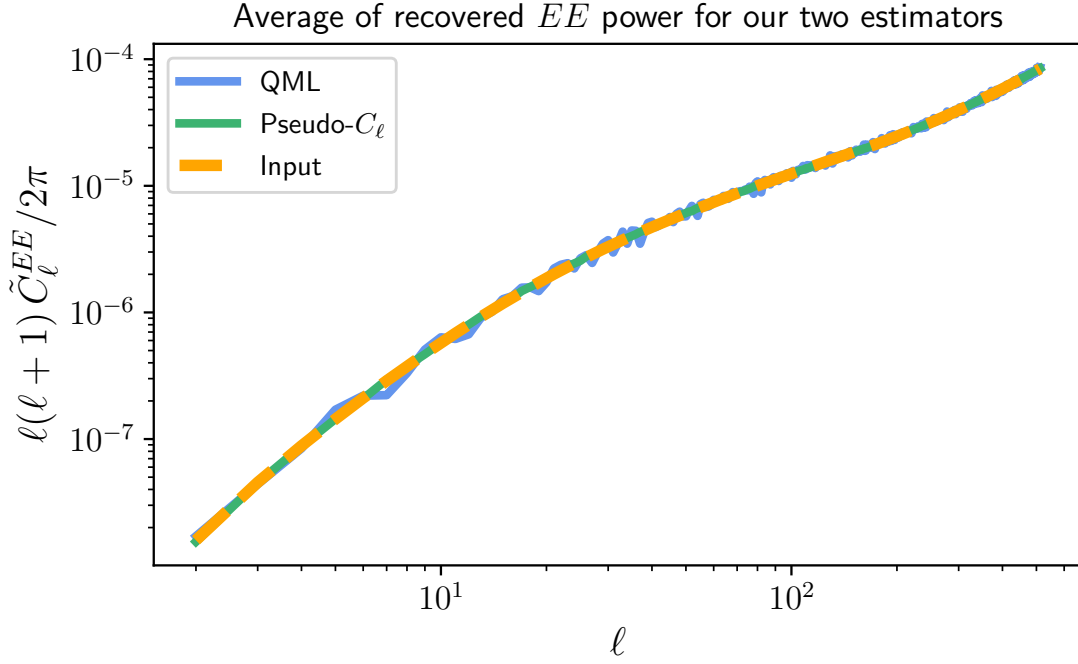


Figure 5.15: Comparison of the average  $C_\ell^{EE}$  spectrum values for the QML and Pseudo- $C_\ell$  estimators recovered from an ensemble of five thousand random realisations and the fiducial input spectrum.

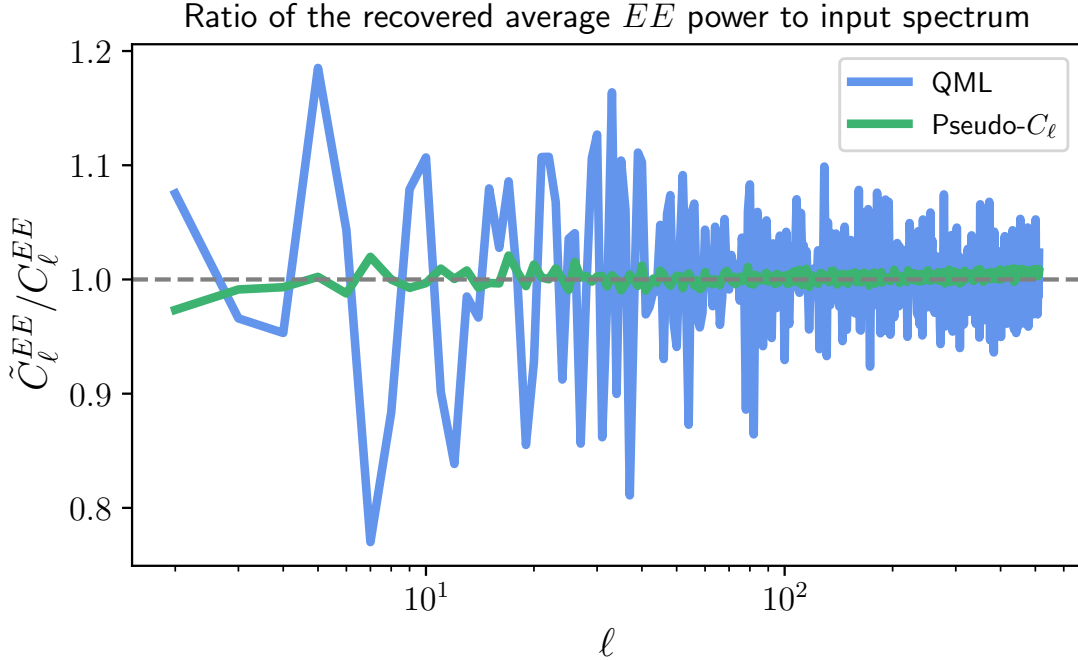


Figure 5.16: Ratio of the average  $C_\ell^{EE}$  spectrum values for the QML and Pseudo- $C_\ell$  estimators to the fiducial input spectrum. This shows that both estimators correctly recover the input spectrum on average as both estimator's averages exhibit roughly random scatter around the  $y = 1$  line (dashed grey line), and thus both estimators are unbiased estimators of the power spectrum.

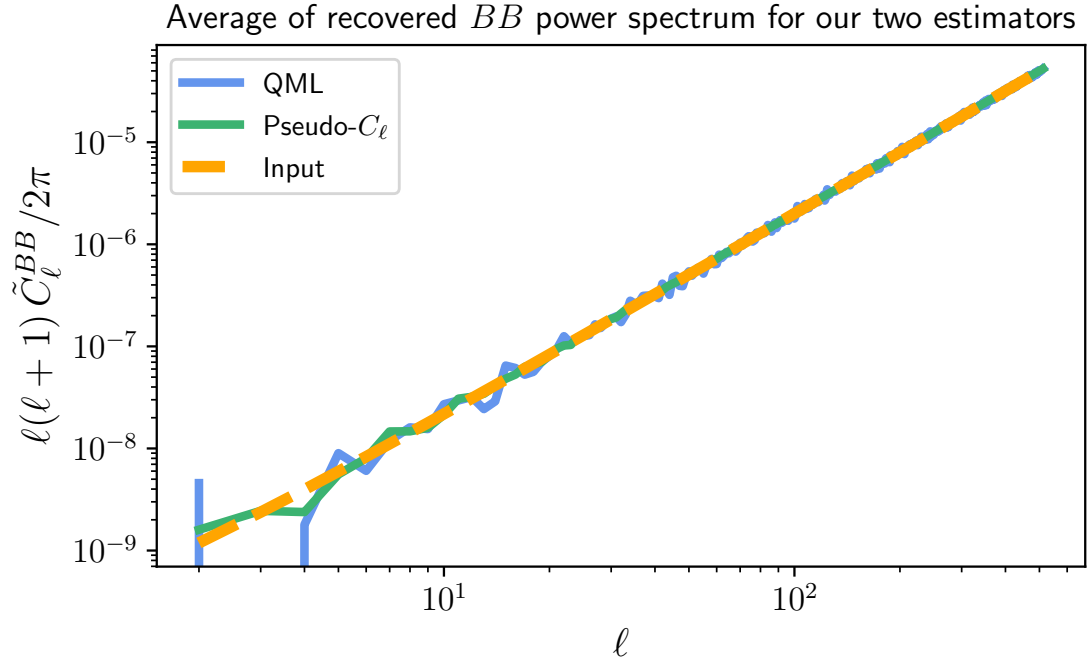


Figure 5.17: Similar plot to Figure 5.15, but now for the  $BB$ -spectrum.

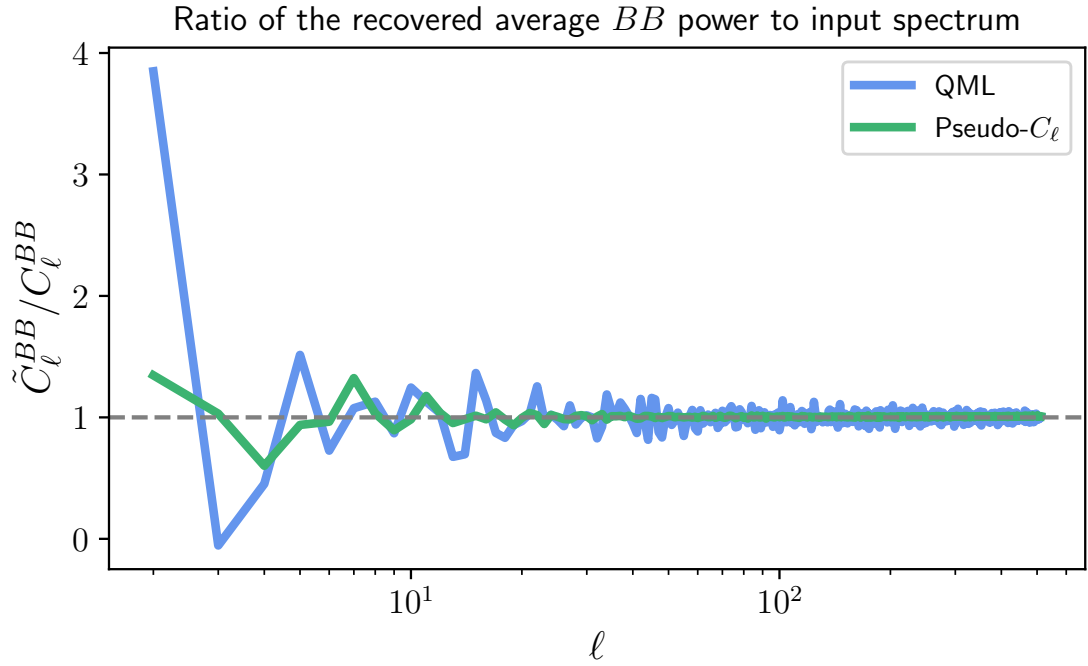


Figure 5.18: Similar plot to Figure 5.16, but again now for the  $BB$ -spectrum

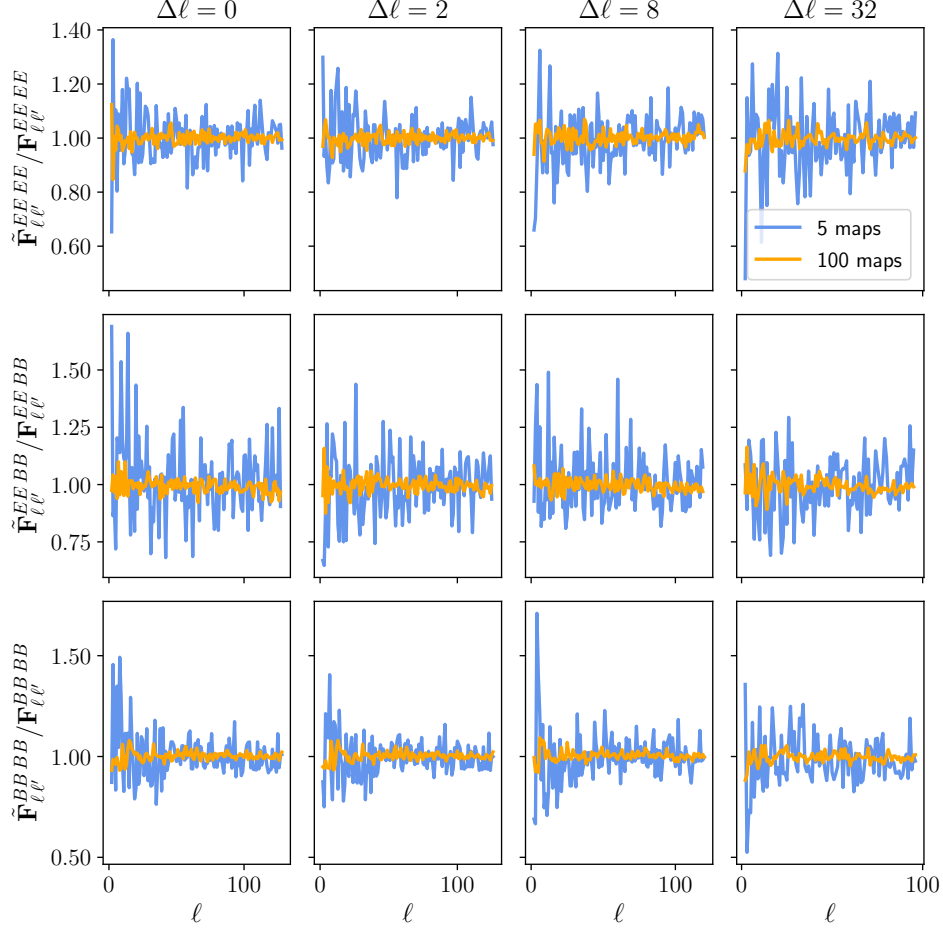


Figure 5.19: Ratio of our numerically-derived  $C_\ell$ -Fisher matrix to the analytic result for a map resolution of  $N_{\text{side}} = 64$ , presented for the cases where we average over five and one hundred maps. Here, we plot the  $EE-EE$ ,  $EE-BB$ , and  $BB-BB$  components separately, with varying off-sets from the diagonal in the different columns. We see good agreement between our estimator and existing results for all combination of spectra and off-sets, and so deduce that our numerical estimate is consistent with the analytic result.

## 5.B Ratio of numeric to analytic Fisher

Figure 5.19 shows the ratio of our numerically computed  $C_\ell$  Fisher matrix to that computed using analytic methods for a number of different off-set values from the diagonal. Here, we see that all curves simply exhibit random scatter around unity which shows that our numerical estimates of the Fisher matrix is an unbiased estimate of the true values. The residual noise in the Fisher matrix gives rise to negligible differences in parameter confidence contours.



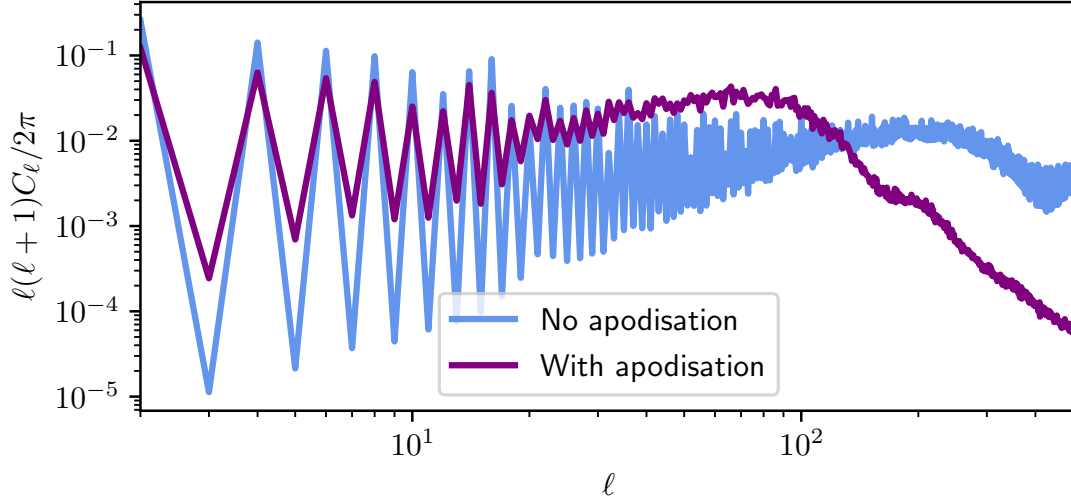


Figure 5.20: Power spectrum of our mask, with stars included, for cases with and without apodisation applied.

## 5.C Sensitivity to apodisation

Previously, we have discussed how apodisation of the mask is not required for QML methods whereas there are certain advantages to doing so for the Pseudo- $C_\ell$  method. This is because apodisation reduces the effects of sharp edges that may be present in the mask. To investigate the effects of apodisation, we have applied a  $2^\circ$  apodisation using the  $\mathcal{C}^2$  scheme as described in [17] to our mask, including stars. We note that for this apodisation scale and scheme, the sky area reduces from  $f_{\text{sky}} = 33\%$  to  $f_{\text{sky}} = 22\%$ . Figure 5.20 shows the power spectrum of our mask with and without apodisation applied. Here, we see that the effect of apodisation is to vastly reduce the small-scale power of the mask. The effect of this suppression of small-scale power results in the reduction in long-range correlations in the covariance matrix, as can be shown from Equation 5.35, and thus the computation and inversion of the mixing matrix should be more accurate when apodisation is applied. The ratio of the analytic Pseudo- $C_\ell$  covariance matrix for the  $C_\ell^{EE}$  spectrum for the cases of with and without apodisation is shown in Figure 5.21. This shows that for values along and close to the diagonal, the loss of sky area causes significant increases in the variances in the power spectrum. For mode-pairs that are highly separated we see a notable decrease in their covariances, which once again can be seen from Equation 5.35.

Figure 5.22 shows the ratio of the errors for the Pseudo- $C_\ell$  (the square-root of the diagonal of the covariance matrix) with respect to our QML estimator for the case of with and without apodisation. Here, we see that the effect of apodisation is to increase the errors of the Pseudo- $C_\ell$  method - which is a direct result in the loss of sky area that apodisation produces.

The covariance matrix for the case where we have applied apodisation can then be propagated into parameter constraints, which is shown in Figure 5.23. Here, we see that the direct loss of sky area associated with apodisation results in broadened parameter contours which is not offset by the decrease in long-range correlations that apodisation suppresses in the covariance matrix.

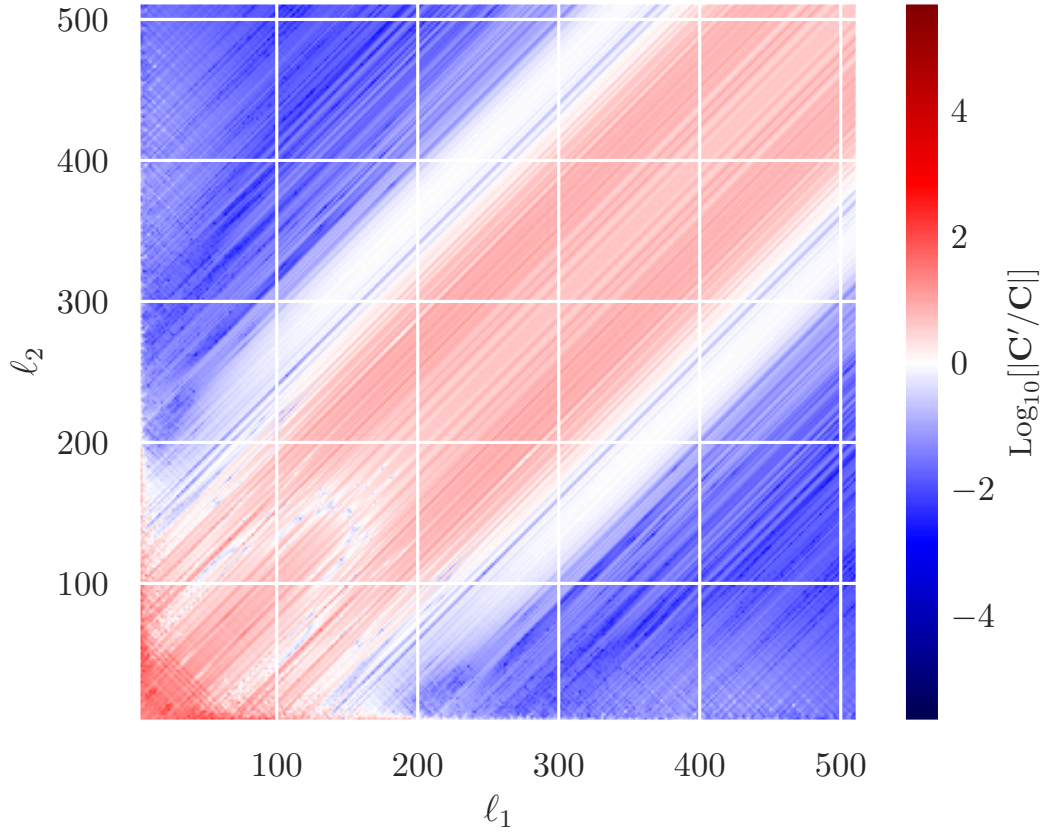


Figure 5.21: Ratio of the analytic Pseudo- $C_\ell$  covariance matrix for the  $C_\ell^{EE}$  power spectrum for the cases with ( $C'$ ) and without ( $C$ ) mask apodisation applied.

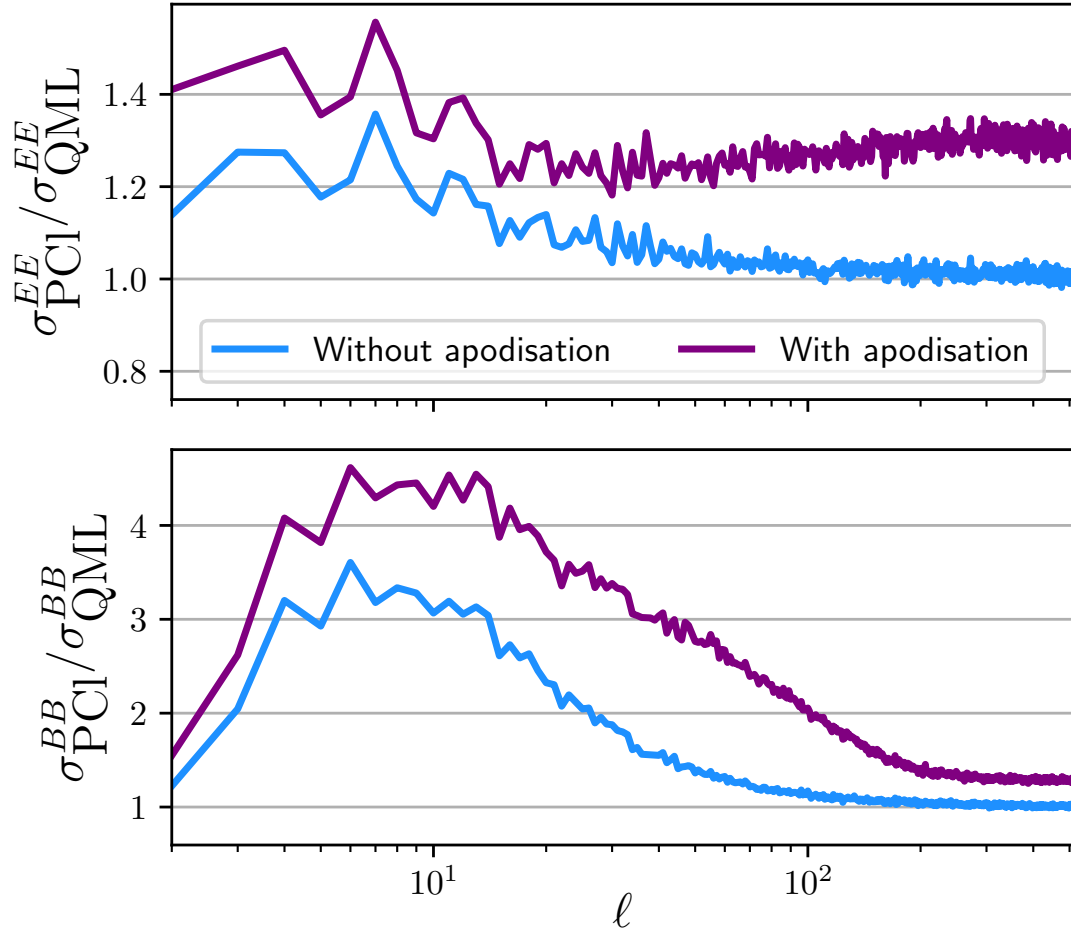


Figure 5.22: Ratio of  $C_\ell$  errors of the Pseudo-Cl method with respect to our QML estimator for the cases with and without apodisation.

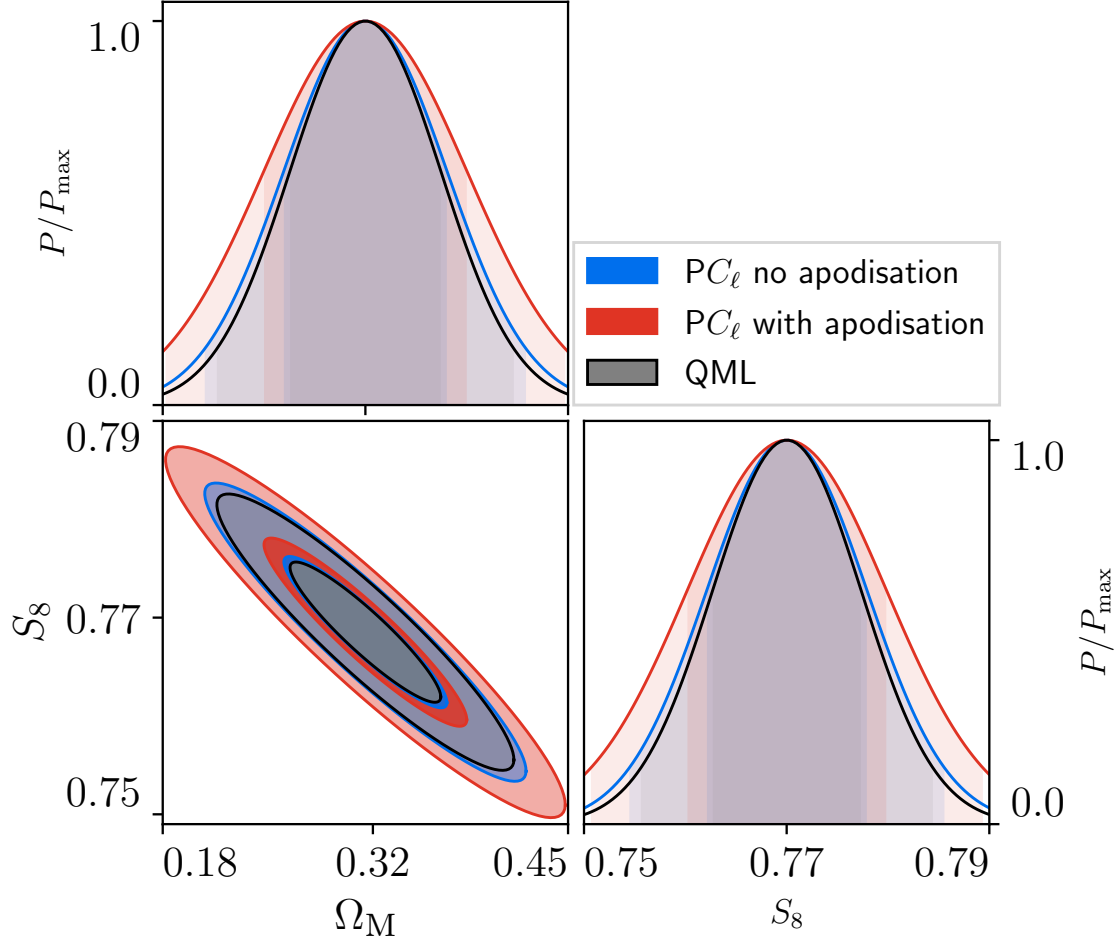


Figure 5.23: Fisher parameter constraints comparison between QML and Pseudo- $C_\ell$  where both estimators have a maximum multipole of  $\ell_{\max} = 512$  and for the case where apodisation has been applied for the Pseudo- $C_\ell$  method. We see a large broadening for the Pseudo- $C_\ell$  contour with apodisation applied, which is consistent with the loss of sky area that apodisation results in.

*I foresee all sorts of unforeseen problems  
Such as?  
If I could foresee them, they wouldn't be unforeseen*  
—Yes, Prime Minister

# 6

## Mitigating baryon feedback bias in cosmic shear through a theoretical error covariance in the matter power spectrum

---

This chapter was published in *Monthly Notices of the Royal Astronomical Society* as Maraio, Hall, and Taylor (2025) [2].

**Outline.** Forthcoming cosmic shear surveys will make precise measurements of the matter density field down to very small scales, scales which are dominated by baryon feedback. The modelling of baryon feedback is crucial to ensure unbiased cosmological parameter constraints; the most efficient approach is to use analytic models, but these are limited by how well they can capture the physics of baryon feedback. We investigate the fitting and residual errors of various baryon feedback models to a suite of hydrodynamic simulations, and propagate these to cosmological parameter constraints for cosmic shear. We present an alternative formalism to binary scale-cuts through the use of a theoretical error covariance, which is a well-motivated alternative using errors in the power spectrum modelling itself. We depart from previous works by modelling baryonic feedback errors directly in the matter power spectrum, which is the natural basis to do so and thus preserves information in the lensing kernels. When including angular multipoles up to  $\ell_{\text{MAX}} = 5000$ , and assuming *Euclid*-like survey properties, we find that even multi-parameter models of baryon feedback can introduce significant levels of bias. In contrast, our theoretical error reduces the bias in  $\Omega_{\text{M}}$  and  $S_8$  to acceptable levels, with only a modest increase in parameter variances. The theoretical error approach bypasses the need to directly determine the per-bin  $\ell_{\text{MAX}}$  values, as it naturally suppresses the biasing small-scale information. We also present a detailed study of how flexible HMCode-2020, a widely-used non-linear and baryonic feedback model, is at fitting a range of hydrodynamical simulations.

## 6.1 Introduction

Cosmic shear is the coherent distortion in the apparent shapes of galaxies due to the matter distribution of the large-scale structure of the universe [32, 33, 206]. These distortions are sensitive to the total matter inhomogeneities along the line-of-sight, and thus are a powerful probe of the non-luminous dark matter, which ordinarily cannot be directly observed using telescopes. Cosmic shear is also sensitive to the detailed physics of baryons, particularly on small scales, within the Universe (see Section 3.8). By making accurate measurements, along with robust theoretical modelling, cosmic shear is able to provide detailed knowledge about the physics and geometry of the Universe.

Cosmic shear surveys have already placed tight constraints on the fundamental physics and properties of our Universe, especially on the growth of structure parameter  $S_8$ , defined as  $S_8 \equiv \sigma_8 \sqrt{\Omega_M/0.3}$ . The results from existing surveys have been well-studied, with data coming from the Kilo-Degree Survey (KiDS-1000) [209, 214, 266], the Dark Energy Survey (DES-Y3) [210, 267–269], and Hyper Suprime-Cam (HSC-Y3) [167, 270].

Over the next decade, an unprecedented amount of high-quality cosmic shear data will be released. This will come from the recently launched *Euclid* space telescope [158, 164], the Legacy Survey of Space and Time (LSST) at the *Rubin* observatory [207], and the *Roman* space telescope [208]. Since the quality and quantity of cosmic shear data that is expected to be produced is so vast, the accuracy of the theoretical modelling is required to be as equally precise.

While the majority of the matter in the Universe is dark matter, which only interacts gravitationally, the baryons in the Universe, while appearing to be lighter in total mass, have an equally large affect on the dynamics of the Universe – particularly on small scales. Baryons are responsible for the heating and cooling of gas, the creation and demise of stars, and play an important part in the feedback from active galactic nuclei (AGN) and supernovae, both of which can have a considerable impact on the matter power spectrum over a wide range of scales (see Figure 3.12 showing suppressions upwards of 20 % around angular scales of  $\ell \sim 1000$ , scales which have already been well-measured by current Stage-III surveys and will be measured with increased precision using Stage-IV surveys) [123].

The modelling of baryon feedback and its effects on cosmic shear cosmology has been discussed extensively in the literature, with very many different methods and implementations proposed to mitigate its effects. These include Schneider & Teyssier (2015) [271], Giri & Schneider (2021) [272], Aricò et al. (2021) [273], Huang et al. (2019) [274], Salcido et al. (2023) [275] and Mead et al. (2020) [106], among many others. Cosmic shear is a measurement in angular-space due to the necessity of using coarse photometric redshift estimates, and so this makes the measurements of cosmic shear sensitive to high- $k$  wavenumbers throughout any  $\ell$  values in the angular power spectrum. It is at high  $k$  where feedback effects become relevant.

A popular approach to mitigating baryonic effects in cosmic shear analyses is to introduce scale-cuts into the data-vector. Here, physically smaller scale elements in the data vector beyond a cut-off, either in real-space  $\theta_{\min}$  or in Fourier-space  $\ell_{\max}$ , are completely discarded even if high signal-to-noise observations have been taken. These scale-cuts are often dependent on the redshift of the source galaxies, as for further away redshift bins the same physical scale is given by smaller  $\theta$  or larger  $\ell$ . One issue that arises with such scale-cuts is that it by definition is a *hard cut* on the data. For example, if it was chosen that  $\ell_{\max} = 2000$ , then  $\ell = 2000$  would be included in an analysis whereas the  $\ell = 2001$  mode would be excluded<sup>1</sup>, even though these modes will be highly coupled and have very similar theoretical uncertainties. The use of these binary scale cuts have been discussed heavily in previous cosmic shear results, most recently in the Dark Energy Survey’s Year

---

<sup>1</sup>I’m sorry Dave, I’m afraid I can’t let you include that mode in an analysis — HAL 9000.

3 results (real-space) [267, 276], the Kilo-Degree Survey fourth data release (KiDS-1000, in real-space) [266], and Hyper Suprime-Cam’s Year 3 results (harmonic-space) [167].

Since the use and location of a hard scale cut could be considered somewhat unphysical, in the sense that we have two consecutive data points one with little error and one with infinite error, we investigate and present results for an alternative: the use of a theoretical error covariance which acts as a soft scale cut that is informed by our inability to correctly model baryonic feedback down to arbitrarily small scales. This has been explored in the literature previously, with the theory being originally presented in Baldauf et al. (2016) [277], expanded upon in Sprenger et al. (2018) [278], and applied to mock cosmic shear analyses in Moreira et al. [279], among others [280]. Baryonic feedback effects directly impact the matter power spectrum, which is then integrated over to produce effects in the lensing angular power spectrum. Thus, when we model our theoretical uncertainties coming from baryonic feedback, it is most natural to do so in the matter power spectrum and propagate these uncertainties to the angular power spectrum. Moreira et al. (2021) [279] investigated theoretical uncertainties with respect to the *angular* power spectrum, and so we are revisiting this formalism but extending it to the underlying matter power spectrum. Since baryonic feedback contaminates only the matter power spectrum, not the lensing kernels associated with cosmic shear, isolating the errors associated with the matter power spectrum then propagating these to the angular power spectrum is a sensible alternative approach. The theoretical uncertainties approach is similar to analytic marginalisation of small-scale physics, which also results in an additional term to the covariance matrix [281].

This Chapter is structured as follows: in Section 6.2 we outline the need for analytic baryon feedback models and the use of hydrodynamical simulations, Section 6.3 discusses our methodology for constructing our theoretical error covariance, in Section 6.4 we present our results for cosmological parameter constraints using a selection of baryon feedback models, and Section 6.5 summarises our findings.

## 6.2 Modelling baryonic feedback in the matter power spectrum

Accurate evaluations of the non-linear dark-matter-only matter power spectrum is of extreme importance to any cosmic shear analysis [283]. There are numerous ways to accurately evaluate this. For example, many models descend from the original halo model presented in the early 2000s [102, 284–286]: the HALOFIT model presented in Ref. [103], and HMCode models that originate with HMCode-2015 [104], then HMCode-2016 [105], and most recently HMCode-2020 [106]. All these models serve to provide accurate predictions for the non-linear dark-matter-only matter power spectrum as a function of cosmological parameters.

We now wish to go one step further and include the effects of baryonic feedback physics on the matter power spectrum into our numerical models. We are motivated to develop numerical descriptions of baryon feedback because it allows for easy comparison between theoretical models and observational data, thus allowing the data to place constraints on parameters of the model, or even in model selection. Many of these parameter constraints or model selection analyses using Stage-IV cosmic shear survey data will come from Markov chain Monte Carlo (MCMC) analyses [287]. These MCMC analyses depend heavily on the evaluation speed for each sample, since very many samples are needed for accurate results ( $\sim 10^5$ - $10^6$  samples required). Thus, the speed of simple numerical models of baryonic feedback are desirable to avoid excessive run-times. While analytic tools are much sought-after, their limited accuracy in matching a wide-range of baryon feedback physics limits



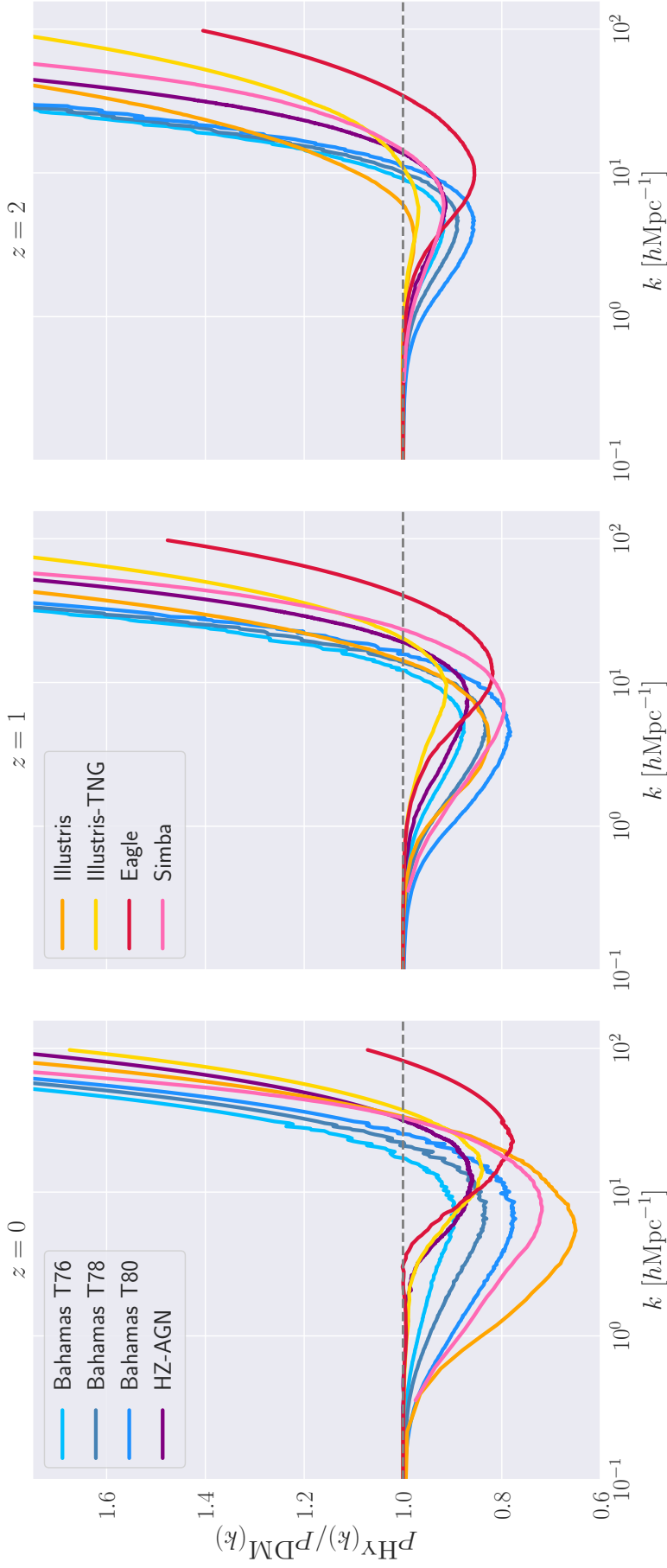


Figure 6.1: Ratios of the matter power spectrum with baryonic feedback in to their dark-matter-only counterparts at redshifts 0, 1, and 2, for various hydrodynamical simulations, as given in Table 6.1. Here, ‘BAHAMAS TXY’ corresponds to the same underlying BAHAMAS hydro-sim, just run at different  $\Delta T_{\text{heat}}$  values, which corresponds to the amplitude of AGN feedback within their simulation [282]. Note that SIMBA was run on a smaller box-size with respect to the other simulations (as shown in Table 6.1), and thus we do not have access to data below a certain  $k$  for SIMBA, which is much larger than the smallest  $k$  modes available for the other hydro-sims. All data here (plus data for intermediate redshifts) has been taken from existing public repositories, see the [data availability](#) section for more information.

their use in current cosmological surveys as to not bias parameter constraints.

The best tests of baryon physics come from fully hydrodynamical cosmological simulations (hydro-sims). These simulations aim to capture the physics of dark matter clustering and galaxy formation and evolution using extremely large volumes, with a box side length of  $L \gtrsim 100 \text{ Mpc}/h$  (in comoving units), and across a wide range of redshifts. In addition, hydrodynamical simulations aim to implement modelling of astrophysical processes which are significantly more complex than gravitational attraction, and may include star formation, stellar feedback, chemical evolution of the interstellar medium, active galactic nuclei (AGN) growth and feedback, among others [123]. For a recent review of hydro-sims, see Refs. [288] and [289].

The development and extraction of results from hydro-sims are an incredibly active area of research with very many groups developing their own implementations of hydrodynamical effects within simulations. Recent works include the FLAMINGO simulation [290], MILLENNIUMTNG [291], with past works including SIMBA [292], ILLUSTRIS [293], ILLUSTRISTNG [294], HORIZON-AGN [295], BAHAMAS [282], Eagle [296], and COSMO-OWLS [297] simulations.

These simulations mainly differ in their implementations of sub-grid physics. Hydro-sims require the use of sub-grid models since the the scales of many important physical processes that make up baryonic feedback (such as gas cooling, star formation and stellar feedback, supermassive black hole formation and evolution, and AGN feedback), occur on scales smaller than their ordinary particle mesh grid [289]. Hence, to model these physical processes, hydro-sims need to infer their existence in between nodes of the simulation, hence the name of sub-grid models. For example, the scales over which AGN inject energy into the interstellar medium occurs on scales which cannot be numerically resolved – and thus hydro-sims must approximate their macroscopic effects thorough sub-grid models [289]. AGN feedback can be divided into two modes, each with their own sub-grid implementation: a quasar mode which is associated with the electromagnetic radiation emitted from the accreted matter, and a radio mode which is formed from the highly collimated jets of relativistic matter. Since AGN activity impact a wide range of scales, matching the sub-grid nature of the AGN themselves to the macroscopic impact on nearby nodes of the hydro-sim is a challenging problem. Furthermore, supernovae explosions inject huge quantities of energy into their surrounding interstellar medium, which is far smaller than the simulated grid size. Thus, a sub-grid model for supernovae feedback must be implemented, which can inject its energy and momentum either thermally or kinematically [288]. There are suggestions that these sub-grid physics differences are connected to the gas fraction in galaxy groups and clusters [298].

Hydrodynamical simulations are extremely computationally expensive due to the need for large volumes, to reduce cosmic variance and capture clustering on cosmological scales, and the need to model small-scale behaviour, which directly impacts the larger-scale clustering. Thus, these simulations need sufficient resolution else the baryonic feedback physics which we wish to capture will simply be washed out on larger scales and also sufficient volume. This presents a challenging dynamic range problem, hence the very many different simulations that implement these range of physics.

To isolate the effect of baryonic physics on the matter power spectrum when compared to the dark-matter-only non-linear power spectrum, we use the baryon response function,  $R(k, z)$ , defined as

$$R(k, z) \equiv \frac{P^{\text{Hy}}(k, z)}{P^{\text{DM}}(k, z)}, \quad (6.1)$$

which isolates the effects of baryon physics from the general non-linear spectrum, and is especially useful for reducing the effects of cosmic variance on the power spectrum

when using hydro-simulations. This ratio is approximately insensitive to the cosmological parameters that  $P^{\text{Hy}}(k)$  and  $P^{\text{DM}}(k)$  were generated using, provided that they are the same cosmology [299, 300]. This makes the baryon response function especially useful when trying to compare predictions between different hydro-sims run at different cosmologies. Since every hydro-sim has a different implementation of their astrophysical processes, the range of curves for  $R(k, z)$  can be extremely broad. Figure 6.1 plots this ratio for a variety of different hydro-sims for three redshifts. This shows the general behaviour of  $R(k, z)$  that has been well explored previously [123]: there is a dip in expected power on non-linear scales ( $1 h\text{Mpc}^{-1} \lesssim k \lesssim 10 h\text{Mpc}^{-1}$  at  $z = 0$ ) due to baryon feedback processes, such as AGN, jets, and supernovae, expelling matter reducing clustering, while the dramatic increase on highly non-linear scales ( $k \gtrsim 10 h\text{Mpc}^{-1}$ ) is due to additional clustering from the ability of baryons to undergo radiative cooling, increasing small-scale clustering, and from star formation within the simulations [301]. Also shown in Figure 6.1 is the level of scatter in the prediction of  $R(k, z)$  for different hydro-sims, with the depth and location of the suppression and location of the upturn highly simulation dependant with very little common consensus between these simulations. Ref. [299] has shown that much of this scatter in the predictions for the suppression in the simulations can be explained by how the amplitude of the suppression is strongly correlated with the mean baryon fraction in haloes of mass  $\sim 10^{14} M_{\odot}$  [298].

It should be noted that Figure 6.1 shows that baryonic feedback is also highly redshift dependent, both in the amplitude and scale-dependence of the suppression, on a per-hydro-sim basis (with some general scatter in this redshift scaling too). We see that the largest suppression of power comes from redshift zero, with suppression gradually decreasing with increasing redshift. While it is true that the star formation rate within galaxies and the accretion rate of matter into the supermassive black holes, and thus the AGN luminosity, peaks around redshift  $\sim 2 - 4$  [302], this does not necessarily mean that the suppression in the matter power spectrum should peak at this redshift. This is because gravitational clustering is a time-evolutionary process, and so the suppression at redshift 2 can only *grow* with respect to the dark-matter-only model over the next ten billion years to redshift zero.

Due to the large scatter in the predictions of the hydro-sims, we take an agnostic approach to their results: we assume that each of these simulations are equally trustworthy, and thus any of these predictions for their  $R(k, z)$  must be equally reliable. We must also assume that the true description of our Universe lies somewhere in this ensemble in order to correctly match observational data. Hence, any baryon physics model must be able to recreate all of these curves in order for us to sufficiently trust that it could potentially capture the real physics of our Universe. This level of scatter in the hydro-sims has lead to the development of many baryonic physics models, especially those which aim to match the simulations through neural-network emulator methods, such as the BACCO emulator presented in Ref. [273]. BACCO claims accuracy 1-2% for scales  $1 h\text{Mpc}^{-1} < k < 5 h\text{Mpc}^{-1}$  and redshifts  $0 < z < 1.5$ , and again finds that the most important parameter that controls baryon feedback physics is the gas fraction per halo mass. Furthermore, BCEMU [272] implements the ‘baryonification model’ prescription [303] which claims percent-level accuracy for scales below  $k \sim 10 h\text{Mpc}^{-1}$  at redshifts  $z < 2$ .

We are motivated to find correct descriptions of baryon feedback physics due to their large impact on results obtained from cosmic shear surveys. Future Stage-IV cosmic shear surveys hope to probe extremely small scales, up to a maximum multipole of  $\ell_{\text{MAX}} \sim 5000$  [158], corresponding to an approximate physical scale of around 1.2 Mpc, 4.1 Mpc, and 6.5 Mpc at redshifts 0.25, 1, and 2, respectively. These small angular scales probe the highly non-linear regime in the matter power spectrum, as shown in Figure 6.2. Here, we plot the cumulative sum of the derivate of the angular power spectrum coefficients  $C_{\ell}$  at certain  $\ell$  values as a function of  $k$ . This shows the relative contribution for each

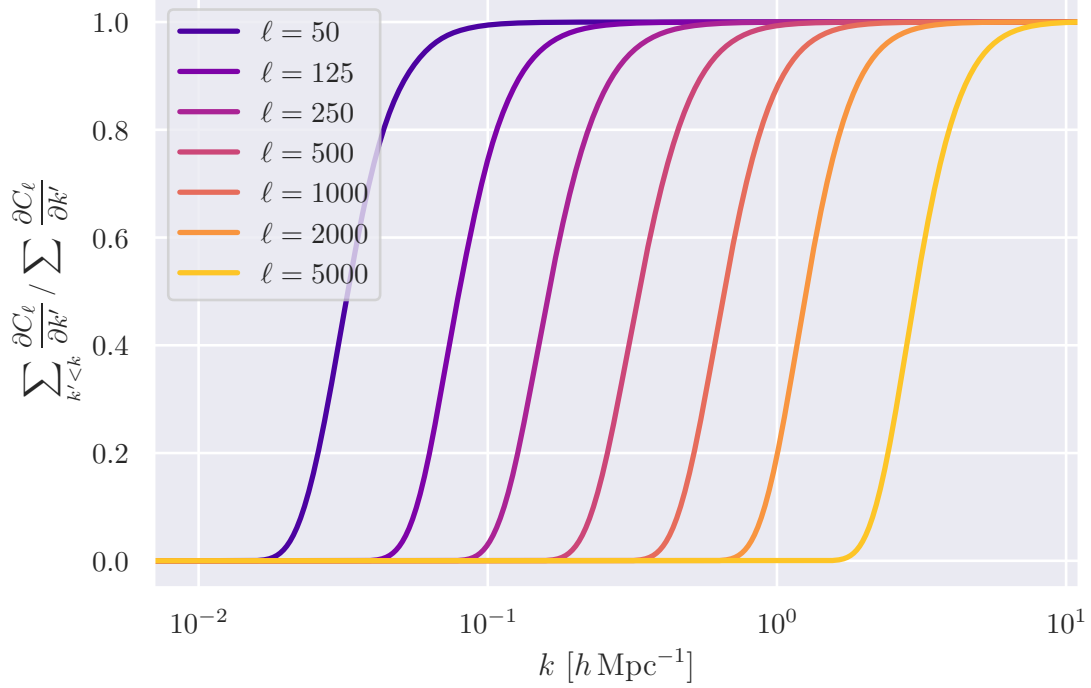


Figure 6.2: Cumulative sum of the derivate of the cosmic shear power angular power spectrum coefficients  $C_\ell$ , at certain  $\ell$  modes, with respect to the wavenumber  $k$  in the Limber integral (Equation 6.4). The sum of the derivatives for each multipole is normalised to unity for easy comparison between different modes. This includes the contributions from the lensing kernels and the matter power spectrum. Derivatives were taken for a Gaussian source redshift distribution located at  $\bar{z} = 0.33$  and width  $\sigma_z = 0.15$ .

$k$  mode to each  $C_\ell$  value. Hence, we find that if we hope to probe angular scales up to  $\ell = 5000$ , then we need to have a strong understanding of the matter power spectrum up to scales  $k \sim 10 h\text{Mpc}^{-1}$  – including the details of baryonic physics. If these scales are not correctly modelled, then this could induce catastrophic biases in a cosmic shear analysis [274, 304], particularly for the constraints on dark energy [305]. The alternative is to reduce the maximum multipole  $\ell_{\text{MAX}}$  in our analyses, though this discards potentially useful cosmological information.

This motivates us to test the accuracy of baryonic feedback models up to these small scales, and assess how different treatments of baryonic physics impact constraints obtained from forthcoming cosmic shear surveys.

### 6.2.1 Theoretical error formalism

Since we do not have models of baryonic physics that completely match our complete set of hydrodynamical simulations, there will always be some residual error for any given model of baryon feedback physics as a function of scale and redshift. Rather than treating our models as a perfectly known quantity and limiting our scales of interest, we can directly incorporate these known errors through the use of the ‘theoretical uncertainty’ formalism first presented in Ref. [277]. We now have a theoretical error data-vector  $\vec{\epsilon}$ , which quantifies the difference between the true, underlying physical model and what our approximative methods calculate, which is bound by an envelope  $\vec{E}$ . This theoretical error has its associated covariance matrix,  $\mathbf{C}^{\text{E}}$ , which can be written as a function of the

amplitude of the error,  $\vec{E}$ , and a correlation matrix  $\boldsymbol{\rho}$  as

$$\mathbf{C}^{\text{E}} = \vec{E} \boldsymbol{\rho} \vec{E}^{\text{T}}. \quad (6.2)$$

In the Gaussian approximation, we can simply model the inclusion of the theoretical error on the likelihood as simply the addition of our theoretical error covariance,  $\mathbf{C}^{\text{E}}$ , to our existing data covariance matrix (which includes the contributions from cosmic variance),  $\mathbf{C}^{\text{D}}$ , to give

$$\mathbf{C}^{\text{TOT}} = \mathbf{C}^{\text{D}} + \mathbf{C}^{\text{E}}. \quad (6.3)$$

The theoretical error formalism can be, in principle, applied to any effect that changes summary statistics that is not yet perfectly modelled. This approach of marginalising over the errors in the model was first applied to baryonic physics effects for cosmic shear surveys in Ref. [279], where they modelled the errors and correlations directly in  $\ell$ -space. They constructed several versions of the error envelope function  $E(\ell)$ , all featuring the similar term of the error ratio of best-fit  $C_\ell$  values to the values generated from hydro-sims. They also assumed a Gaussian-like function in  $(\ell - \ell')^2$  for their correlation matrix, with a characteristic correlation length  $L$  determining the widths of the correlation matrix.

Since baryonic effects directly change the matter power spectrum, which is then propagated to cosmic shear summary statistics, we are motivated to investigate the theoretical errors in  $k$ -space for the matter power spectrum and then propagate those to  $\ell$ -space. There is no theoretical error associated with the lensing kernels, so by isolating the theoretical uncertainties to the matter power spectrum only, we might hope to preserve information from geometry this way. The task now becomes one to find an appropriate theoretical error envelope function  $\vec{E}$  and correlation matrix  $\boldsymbol{\rho}$  in  $k$ -space.

## 6.3 Methodology

### 6.3.1 Modelling forthcoming cosmic shear surveys

We use the standard prescription for the cosmic shear power spectrum [32, 33, 206] where the power spectrum is, for tomographic redshift bins labelled by  $a$  and  $b$ , is given as

$$C_\ell^{ab} = \frac{9}{4} \frac{\Omega_{\text{M}}^2 H_0^4}{c^4} \int_0^{\chi_{\text{max}}} d\chi \frac{g_a(\chi) g_b(\chi)}{a^2(\chi)} P\left(k = \frac{\ell}{\chi}, z = z(\chi)\right), \quad (6.4)$$

where  $a(\chi)$  is the scale factor,  $P$  is the non-linear matter power spectrum, and  $g(\chi)$  is the lensing kernel given as

$$g_a(\chi) = \int_\chi^{\chi_h} d\chi' n_a(\chi') \frac{f_K(\chi' - \chi)}{f_K(\chi')}, \quad (6.5)$$

where  $n(\chi)$  is the probability density of source galaxies as a function of comoving distance. To evaluate the non-linear matter power spectrum with baryonic feedback, we used HMCode-2020 with  $T_{\text{AGN}} = 7.8$ .

Since every galaxy has an intrinsic ellipticity, this introduces a shape noise term into the power spectrum with a flat value  $N_\ell$  given as

$$N_\ell^{ab} = \frac{\sigma_\epsilon^2}{\bar{n}} \delta^{ab}, \quad (6.6)$$

where  $\sigma_\epsilon$  is the standard deviation of the intrinsic galaxy ellipticity dispersion per component,  $\bar{n}$  is the expected number of observed galaxies per steradian, and  $\delta^{ab}$  is the Kronecker- $\delta$  symbol. We assume *Euclid*-like values where it is expected that 30 galaxies per square

arcminute will be observed, but we divide these into five photometric redshift bins, giving  $\bar{n} = 6 \text{ gals/arcmin}^2$  [158]. We take  $\sigma_\epsilon = 0.21$ .

We use five Gaussian redshift bins with means located at  $\bar{z} = \{0.33, 0.66, 1.0, 1.33, 1.66\}$  all with standard deviation of  $\sigma_z = 0.15$ . This gives us 15 unique power spectrum combinations and 120 unique covariance matrix blocks.

We model the Gaussian covariance matrix as the four-point function [157], given by

$$\text{Cov}[C_\ell^{ab}, C_{\ell'}^{cd}] = \frac{C_\ell^{ac} C_\ell^{bd} + C_\ell^{ad} C_\ell^{bc}}{(2\ell + 1) f_{\text{sky}}} \delta_{\ell\ell'}, \quad (6.7)$$

where  $f_{\text{sky}}$  is the fraction of sky observed by the cosmic shear survey. We take a *Euclid*-like value of  $f_{\text{sky}} = 0.35$ .

To reduce the dimensionality of our power spectrum and covariance matrices, we bin the power spectrum. We use linear binning of five bins up to  $\ell = 100$ , and then use logarithmic binning with twenty bins from  $\ell = 100$  to  $\ell = 5000$ . We use an  $\ell$ -mode weight of  $\ell(\ell + 1)$  when binning.

### 6.3.2 Constructing our $k$ -space theoretical covariance

As outlined in Section 6.2.1, the theoretical error formalism requires us to quantify an error envelope function  $\vec{E}$  and a correlation matrix  $\rho$ , and since our uncertainties from baryonic physics are best specified in  $k$ -space, we will first construct our  $k$ -space covariance matrix. We will first discuss the construction of our envelope function  $\vec{E}$ .

There is no absolute choice for the functional form of  $\vec{E}$ . [279] investigated many choices for the form of  $\vec{E}$ , with the ‘mirror’ envelope being a good fit to the data. Here, we follow their method and take the maximum deviation for each  $k$ -mode and redshift across a suite of hydrodynamical simulations to the best-fitting values of a baryon feedback model (see Section 6.3.6). This gives the maximum relative difference in the baryonic response function (Equation 6.1) as

$$\Delta R(k, z) = \max_{k, z} \left| \frac{R^{\text{HYDRO}}(k, z)}{R^{\text{MODEL}}(k, z)} - 1 \right|. \quad (6.8)$$

We then turn this into an amplitude by multiplying by a fiducial dark-matter-only power spectrum,

$$E(k, z) = P^{\text{DM}}(k, z) \Delta R(k, z). \quad (6.9)$$

where  $P^{\text{DM}}(k, z)$  was evaluated using the HMCode-2020 DM-only model.

With our amplitude function specified, we now wish to construct our  $k$ -space correlation matrix. Here, we are considering the correlations between two pairs of points  $(k_1, z_1)$  and  $(k_2, z_2)$ . We follow previous works that have employed the theoretical uncertainties approach (for example Refs. [277–279, 306]) by choosing a factorisable Gaussian correlation matrix of the form

$$\rho[(k_1, z_1), (k_2, z_2)] = \exp \left[ -\frac{\log(k_1/k_2)^2}{\sigma_{\log k}^2} \right] \exp \left[ -\frac{(z_1 - z_2)^2}{\sigma_z^2} \right], \quad (6.10)$$

where  $\sigma_{\log k}$  and  $\sigma_z$  are the characteristic correlation scales in  $\log k$ - and redshift-space, respectively. In our fiducial analyses, we used values of  $\sigma_{\log k} = 0.25$  and  $\sigma_z = 0.25$ . These values were motivated from Figure 6.1 where we see that the baryonic response function  $R(k, z)$  is correlated on scales of approximately a quarter of a decade in  $\log k$  space with approximately the same coupling in redshift-space. We discuss the effects of changing  $\sigma_{\log k}$  and  $\sigma_z$  in Section 6.4.4.



We are motivated to use factorisable Gaussians since we know that baryon feedback has a relatively local effect on the matter power spectrum, that is neighbouring wavenumbers and redshifts behave similarly and thus should have highly correlated covariances, whereas vastly different wavenumbers and redshifts have very different evolutionary physics, and thus should be less correlated. Furthermore, we are motivated to use the logarithmic differences in  $k$ -space since our wavenumbers span many orders of magnitude (see Figure 6.1), and thus an ordinary difference might not properly reflect this.

Combining our envelope function and correlation matrix, we find that our complete  $k$ - and redshift-space covariance matrix is given by

$$\begin{aligned} \text{Cov}[(k_1, z_1), (k_2, z_2)] = & P^{\text{DM}}(k_1, z_1) \Delta R(k_1, z_1) P^{\text{DM}}(k_2, z_2) \Delta R(k_2, z_2) \times \\ & \exp \left[ -\frac{\log(k_1/k_2)^2}{\sigma_{\log k}^2} \right] \times \exp \left[ -\frac{(z_1 - z_2)^2}{\sigma_z^2} \right]. \quad (6.11) \end{aligned}$$

We note that by working directly with errors in the matter power spectrum, which is the underlying quantity that we have limited knowledge in modelling (not the angular power spectrum values), this should capture the full phenomenology of the errors in baryonic feedback effects on the matter power spectrum. This contrasts with the work of [279] which also aims to mitigate baryonic physics effects through the use of a theoretical uncertainty, though they quantify their theoretical uncertainty through the differences in the angular power spectrum values.

### 6.3.3 Propagating covariances to $\ell$ -space

With our  $k$ - and redshift-space covariance matrix specified, we can now propagate this into an  $\ell$ -space covariance matrix, which can then be added to the data covariance to give our overall covariance matrix.

Equation 6.4 gave the cosmic shear power spectrum as the Limber integral of the matter power spectrum weighted by the geometrical factors. Hence, if we now want to propagate our uncertainties in the  $P(k)$  into an additional covariance matrix for the  $C_\ell$  values, we can integrate this again, which yields

$$\begin{aligned} \text{Cov}[C_{\ell_1}^{ab}, C_{\ell_2}^{cd}] = & \left[ \frac{9 \Omega_{\text{M}}^2 H_0^4}{4 c^4} \right]^2 \times \\ & \int_0^{\chi_{\text{max}}} \int_0^{\chi_{\text{max}}} d\chi_1 d\chi_2 \frac{g_a(\chi_1) g_b(\chi_1)}{a^2(\chi_1)} \frac{g_c(\chi_2) g_d(\chi_2)}{a^2(\chi_2)} \text{Cov}[(k_1, z_1), (k_2, z_2)], \quad (6.12) \end{aligned}$$

where  $k_1 = \frac{\ell_1}{\chi_1}$  and  $k_2 = \frac{\ell_2}{\chi_2}$ . We are motivated to use Limber's approximation here to simplify the double integral since the low  $\ell$  region in which the approximation is imprecise will have a negligible contribution to the total covariance.

### 6.3.4 Numerical evaluation of the matter power spectrum with baryon feedback

Our construction of the  $(k, z)$ -space covariance matrix can be applied to any model of baryon feedback, with models ranging from purely analytical methods using the Zel'dovich approximation [130], to semi-analytic models (e.g. HMCode [106]), to purely numerical emulation (e.g. BACCO [273] and BCCMU [303]).

We have chosen HMCode-2020 as our model of choice for the matter power spectrum and baryonic feedback response since they claim that their dark-matter-only spectrum has

RMS errors of less than 5 per-cent, and that their baryonic feedback response is accurate to within the 1 per-cent level for redshifts  $z < 1$  and scales ( $k < 20 h\text{Mpc}^{-1}$ ), over a range of cosmologies [106]. Thus, HMCode-2020 is a natural choice for computing the matter power spectrum for use in cosmic shear analyses, which is confirmed by its use in recent major cosmic shear results such as the joint KiDS-1000–DES-Y3 analysis [204].

HMCode-2020 comes in two distinct flavours for modelling baryon physics:

- A full six-parameter description with free-parameters of the halo concentration,  $B$ , the stellar mass fraction in haloes,  $f_*$ , and the halo mass break scale,  $M_b$ , along their redshift evolution counterparts. The redshift evolution for each physical parameter  $X$  is given by the fixed form of  $X(z) = X_0 \times 10^{z X_z}$ .
- A one-parameter version where the feedback temperature  $T_{\text{AGN}}$  encapsulates the combined baryon physics of the full model. The one-parameter model was constructed by fitting a linear relationship to the six-parameter version using the BAHAMAS simulations. Since the one-parameter model was specifically constructed to the BAHAMAS simulations, there is no guarantee of its accuracy to other hydrodynamical simulators or even the baryon physics of our own Universe.
- We also test a three-parameter version, which is analogous to the six-parameter model but with fixed redshift evolution. This is a useful test as there arises significant degeneracies between the amplitude and redshift evolution of each parameter, and thus by fixing its evolution we can test if this extra degree of freedom is necessary.

While a more general description of baryon feedback physics should have more freedom to better match different physical models, it comes at the cost of additional nuisance parameters which needs to be included and marginalised over in any analysis. This could slow down the convergence of analysis pipelines, and in the case of very many parameter models, unnecessarily decreasing constraints on the core cosmological parameters due to the need to excessively marginalise over these baryonic nuisance parameters. Hence, while we are focusing on the inclusion of theoretical uncertainties into our analysis pipeline, we also look at how going from a one- to three- to six-parameter baryonic feedback model changes our results.

### 6.3.5 Chosen hydrodynamical simulations

We make use of the ‘power spectrum library’ presented in Ref. [299]<sup>2</sup> and from the CAMELS Project [307]<sup>3</sup> to build up a suite of six hydrodynamical simulations (with three flavours of the Bahamas simulations) as shown in Table 6.1. This gives us a wide range of baryon feedback models against which we can benchmark our analytic models to.

### 6.3.6 Fitting HMCode to hydrodynamical simulations

Armed with our three baryon feedback models and a suite of hydrodynamical simulations, we can now go about performing a best-fit analysis of our models to the hydro-sims in order to quantify each model’s maximum deviation as a function of wavenumber and redshift (Equation 6.8). To do so, we performed a maximum likelihood fit where we simultaneously fitted across redshifts  $z \leq 2$  with flat weighting in redshifts, and wavenumbers over the range  $0.01 h\text{Mpc}^{-1} \leq k \leq 20 h\text{Mpc}^{-1}$  with a  $k^2$  weighting on each wavenumber to roughly approximate the cosmic variance contribution. We are free to choose an arbitrary  $k$ -mode weighting since our envelope function is arbitrary, and so there is no correct choice for

<sup>2</sup><https://powerlib.strw.leidenuniv.nl>

<sup>3</sup><https://camels.readthedocs.io/>



Table 6.1: The six hydrodynamical simulations used in this work to benchmark and compare models of baryon feedback physics to.

Hydro-sim	Box-size (Mpc)	Number of particles	Baryonic mass resolution [ $M_\odot$ ]	Cosmology	Reference
Bahamas	400/ $h$	$2 \times 1024^3$	$7.66 \times 10^8 h^{-1}$	WMAP 9	[282]
Horizon-AGN	100/ $h$	$1024^3$	$8.3 \times 10^7$	WMAP 7	[295]
Illustris	106.5	$1820^3$	$1.6 \times 10^6$	WMAP 7	[293]
Illustris-TNG 100	75/ $h$	$2 \times 1820^3$	$9.44 \times 10^5 h^{-1}$	Planck 2015	[294]
Eagle	100	$1504^3$	$1.81 \times 10^6$	Planck 2013	[296]
Simba	25/ $h$	$1024^3$	$2.85 \times 10^5$	Planck 2013	[292]

either a  $k$ - or  $z$ -mode weight here. We experimented with flat, and a pure cosmic variance weight of  $k^3$ , and settled on our  $k^2$  weighting as somewhere in between. Note that, since we use equal spacing in  $\log(k)$ , we find  $\Delta \log k = [\Delta k]/k$  when summing over  $k$ . This gives our loss function for each model and hydro-sim as

$$\mathcal{L} = \sum_{k,z} k^2 \left( R^{\text{HYDRO}}(k, z) - R^{\text{HMCODE}}(k, z) \right)^2. \quad (6.13)$$

The HMCode power spectra were generated at the same cosmology at which the hydro-sims were run at, with the minimisation routine just varying the astrophysical baryonic parameters. The Minuit optimiser, a robust optimiser as part of the CosmoSiS<sup>4</sup> analysis framework [19], was used to maximise the fit for the baryonic parameters. Since we there is freedom in the form of the weight function for each  $(k, z)$ -mode, different choices for the analytic form of  $\mathcal{L}$  effectively adds little to that freedom.

### 6.3.7 Fitting the $C_\ell$ values

To obtain estimates for the biases in cosmological parameters due to baryon feedback, many MCMC analyses were run. We used a custom CosmoSiS pipeline using the PolyChord nested sampler [194, 195] with parameters `LivePoints` = 1000, `num_repeats` = 60, `boost_posteriors` = 10, and `tolerance` = 0.001 for all analyses. We sampled only over  $\Omega_c$  and  $A_s$  for our cosmological parameters, giving results in terms of  $\Omega_m$ ,  $\sigma_8$ , and  $S_8$ , since cosmic shear surveys are most sensitive to these cosmological parameters. Thus, any induced bias will be greatest in these parameters. In addition, we also sample over our one, three, and six baryonic feedback parameters, depending on the model, with wide priors, as shown in Table 6.2, on these nuisance parameters.

We ran analyses with just the ordinary Gaussian covariance matrix for our cosmic shear fields (Equation 6.7), and with the additional theoretical error covariances (Equation 6.12) added to the Gaussian covariance (Equation 6.3).

A Gaussian likelihood was used, which has been shown to be a good approximation to the full Wishart distribution on the cut-sky [184, 261] under the assumption of Gaussian-only terms in the covariance matrix, which we are employing.

We generate the input cosmic shear  $C_\ell$  values for each hydro-sim by taking each hydro-sim’s baryon response function  $R$  and multiplying it by HMCode’s dark-matter only matter power spectrum at the hydro-sim’s cosmology, giving

$$P^{\text{HY}}(k, z) = R(k, z) \times P^{\text{HMCODE-DM}}(k, z). \quad (6.14)$$

Thus, we are isolating the effects of baryon feedback in the  $C_\ell$  values, and not studying other effects, for example the details of the non-linear matter power spectrum.

<sup>4</sup><https://cosmosis.readthedocs.io/>

Table 6.2: Uniform priors used for the HMCode baryonic feedback models.  $T_{\text{AGN}}$  is used only in the one-parameter models, with the three-parameter model sampling over just the individual amplitude parameters ( $X_0$ ), and the six-parameter model including the redshift dependence too ( $X_z$ ). See Figure 2.11 for the affect of these astrophysical parameters on the matter power spectrum, its description for a full explanation of their physical interpretation, and Figure 3.12 for their affect on the cosmic shear angular power spectrum. We give a brief reprise of their description here:  $B$  is the halo concentration parameter which accounts for gas being expelled from halo centres through AGN activity,  $f_*$  representing the contribution of stellar objects at the centre of haloes, and  $M_b$  changing the value of the characteristic mass that haloes are susceptible to gas loss from AGN activity [106].

Parameter	Uniform prior
$T_{\text{AGN}}$	[4.0, 12.0]
$B_0$	[0.25, 7.0]
$B_z$	[-0.5, 0.5]
$f_{*,0}$	[0.0, 5.0]
$f_{*,z}$	[-5.0, 5.0]
$M_{b,0}$	[5.0, 20.0]
$M_{b,z}$	[-2.5, 2.5]

## 6.4 Results

### 6.4.1 Results of fitting HMCode to hydro-sims

The first task was to fit our three HMCode baryon physics models to the suite of hydro-sims. Figure 6.3 shows the goodness of fit statistic for each hydro-sim for our 1-, 3-, and 6-parameter model. We see that the 1-parameter model generally provides a poor fit to our hydro-sims due to its inability to match the general baryon feedback models. When we extend the generality to 3- and 6-parameters, the goodness of fit increases which matches our intuition that a more general model with higher degrees of freedom should do a better job at matching arbitrary data sets. It should be noted that the HMCode 1-parameter model was specifically designed to closely match the BAHAMAS simulations, and so it is no surprise that it has a better fit to BAHAMAS than other simulations.

While our goodness of fit values provide a valuable insight into how well our three models fit the simulation data overall, we can look at the ratios for the HMCode predictions to the hydro-sims results to see how our fit changes with scales. Figure 6.4 plots the ratio of the best-fit HMCode model to the hydro-sims baryonic response function for our three  $n$ -parameter models as a function of scale at redshift  $z = 0$ . We see that the more general three- and six-parameter models are better able to match the hydro-sims than the one-parameter model, which is to be expected from more general models, and is shown by a reduced amplitude in the relative differences. We also see the extreme nature of the ILLUSTRIS simulation, where the six-parameter model can only poorly match its feedback. This may question the validity of the HMCode-2020 feedback model since the more extreme nature of the feedback as found in ILLUSTRIS as been shown to more accurately match the feedback present in our Universe using Sunyaev-Zeldovich measurements [308] and strongly disfavours simulations with lower feedback amplitudes [309]. We leave the task of reconstructing these fits with other, perhaps more general, models of baryonic feedback that can fit larger-amplitude simulations to future work.

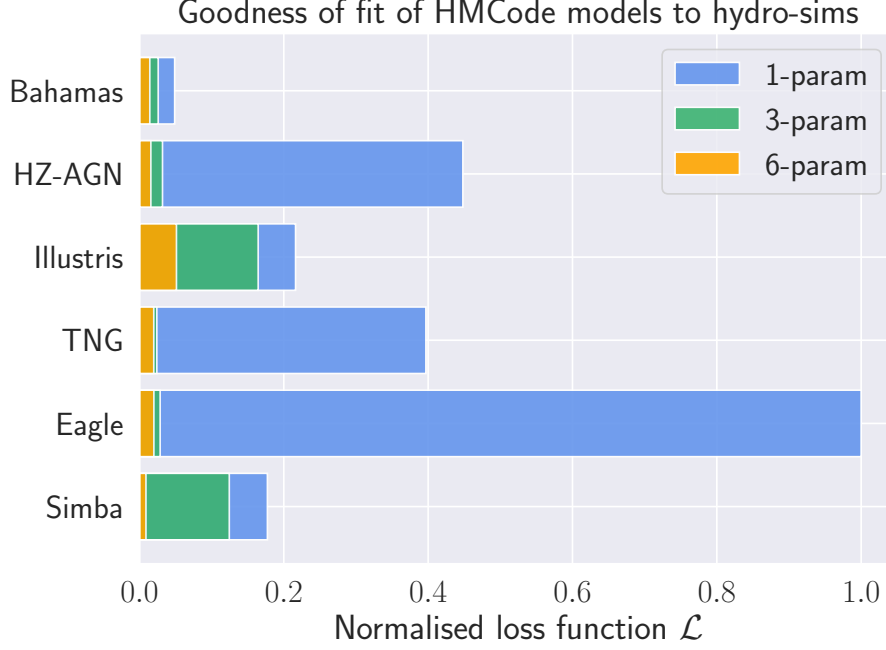


Figure 6.3: Goodness of fit statistics for the HMCode 1-, 3-, and 6-parameter models for our suite of hydro-simulations. We plot the reduced loss function  $\mathcal{L}$  values (Equation 6.13 divided by the total number of data-points across our redshift and wavenumber ranges) since each hydro-sim has a different number of redshift bins and wavenumbers that the power spectra were evaluated at, normalised to the one-parameter model for the Eagle hydro-sim. Here, we see the inflexibility of the 1-parameter model results in significant deviations across all simulations (except BAHAMAS which it was constructed to fit well), which indicates a poor fit to the data. Extending the model to 3- and then 6-parameters further increases the goodness of fit to simulations, since we open up additional degrees of freedom within the model. We note that the feedback within ILLUSTRIS is quite extreme, and thus produces a degraded fit even with the six-parameter model.

## 6.4.2 Constructing the envelope

Now that we know how well each of our feedback models match our suite of hydro-sims, we can combine these to form our ‘envelope function’  $\Delta R(k, z)$  introduced in Equation 6.8.  $\Delta R$  encodes the maximum deviation of each baryon feedback model to all hydro-sims as a function of wavenumber and redshift. This acts as a standard deviation to our theoretical error as each baryon feedback model has an inherent uncertainty and we have quantified this with the envelope of the residual discrepancies between the hydro-sims and the best-fitting  $R(k, z)$  for each simulation.

We plot  $\Delta R(k, z)$  in Figure 6.5, which shows our envelope function as a function of wavenumber  $k$  for select redshift values. We see that, in general, the errors increase with  $k$  which corroborates our understanding that our theoretical models do worse at the smaller scales we probe. We also see that higher redshifts tend to produce a better fit across all of the models which can be understood through Figure 6.1: we see that at higher redshifts, the suppression due to baryons is reduced, smoothing our response function  $R$ , and also moving the suppression to smaller wavenumbers. This acts to allow our baryonic feedback models to better match the hydro-sims, though our errors do increase to very large values on at high  $k$  at high redshifts.

We note that the six parameter model has a distinctive double-hump feature, which is a direct result of the poor fit to ILLUSTRIS on scales  $10^{-1}h\text{Mpc}^{-1} < k < 1h\text{Mpc}^{-1}$ ,

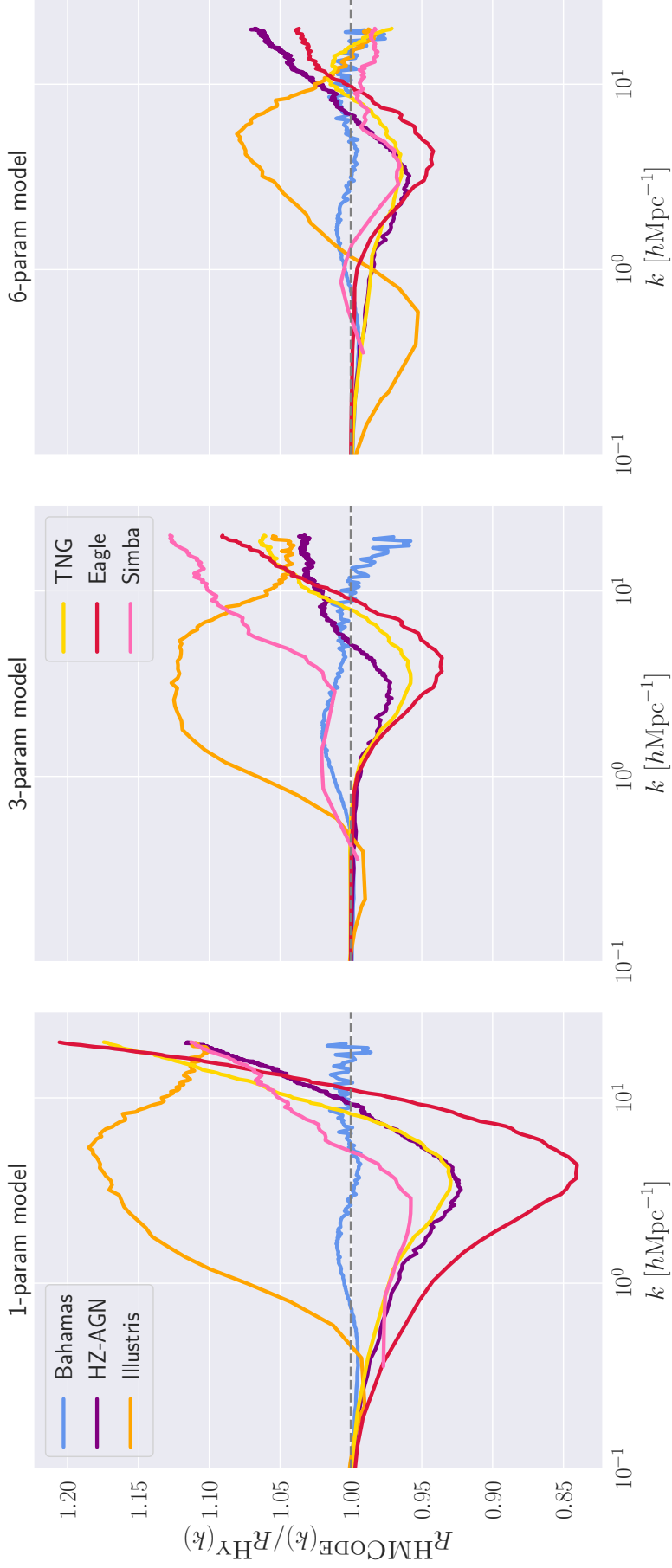


Figure 6.4: Ratios of the best-fitting HMCode one-, three-, and six-parameter models to the underlying hydro-sims baryonic response function  $R$  at redshift  $z = 0$ . We see that HMCode tends to fit the data better, as given by the smaller amplitude, as we increase the generality of the model, which is to be expected. Note that we fitted across all redshifts of each of the hydro-sims for  $z \leq 2$ , where here we are just plotting the  $z = 0$  slice. Similar curves are found at higher redshifts.

as shown in Figure 6.4. One could remove ILLUSTRIS when constructing the maximum deviation envelope, and such this double-hump would no longer appear.

### 6.4.3 Constructing the $\ell$ -space theoretical uncertainty covariance matrix

Our numerical envelope in  $(k, z)$ -space can then be doubly integrated (Equation 6.12) to give us our  $\ell$ -space covariance matrix. Figure 6.6 plots the ratio of the block diagonals of the covariance matrix with our additional theoretical error to that without theoretical error. We see that for  $\ell$  modes below  $\ell \simeq 200$  there is no effect of our theoretical error covariance, since these  $\ell$  modes are unaffected by baryon feedback physics. Above this, we see that our theoretical error covariance acts to increase the total covariance, thus suppressing  $\ell$  modes here and down-weighting them in our likelihood analyses. We note that this is strongly dependent on the combination of spectra considered, with low redshift bins having a smaller error than those at high redshift (which is a direct consequence of our baryon feedback modelling being less accurate at high redshift). We see that, because we are considering the covariances of the auto-spectra only, that the ratios tend to unity at high- $\ell$  which is due to the inclusion of shape noise (which dominates the auto-spectra for large  $\ell$  modes) in the overall covariance matrix.

We plot the total theoretical uncertainty matrix,  $\mathbf{C}^E$  in Figure 6.7. Here, we see that the amplitude of the full matrix reflects what is shown in the diagonals only of Figure 6.6, that the amplitude of the theoretical uncertainties generally grow as we consider further away redshift bin combinations (going from bottom-left to top-right). We also see that while each sub-block of the full matrix peaks along its diagonal, it has significant support with comparable values for many off-diagonal entries, which acts to boost the effects of the theoretical uncertainties over what the diagonal values can provide.

### 6.4.4 Parameter constraints and biases

Using our three different baryon feedback models, we can run our MCMC pipeline to estimate the biases in our cosmological parameters, the total matter density  $\Omega_M$  and the lensing amplitude  $S_8$ , with and without our additional theoretical error. We take each hydrodynamical simulations' baryon feedback response function as the ground truth input values into our cosmic shear pipeline (Equation 6.14). We run our analyses for each baryon feedback model against each hydro-sim, with and without the additional theoretical error to determine the biases on the cosmological parameters due to the effects of baryon feedback.

#### Binary scale-cuts

We first look at the value of the biases in  $\Omega_M$  and  $S_8$  as a function of maximum multipole when using a traditional binary scale-cuts approach. Figure 6.8 plots the  $\Omega_M$ ,  $\sigma_8$ , and  $S_8$  offset contours for the Simba hydro-sim when analysed using the one-parameter model for a range of maximum  $\ell$ -modes allowed in the analysis. We see that only the  $\ell_{\text{MAX}} = 500$  analysis produces results that are consistent with the input parameters to within  $1\sigma$ , with even the  $\ell_{\text{MAX}} = 1000$  analysis producing biased results. Each subsequent analysis where we increase the maximum  $\ell$ -mode serves to both increase the raw bias in the cosmological parameters (since the high  $\ell$ -modes capture more of the impact from baryon feedback) and reduce the area of the contours (since we are now including the more constraining higher  $\ell$ -modes), which vastly increases the relative bias in the cosmological parameters.

Hence, if we were to introduce a binary scale-cut for our data that keeps the  $\Delta\Omega_M - \Delta S_8$  to be consistent within  $1\sigma$ , a cut slightly larger than  $\ell_{\text{MAX}} = 500$  might be made

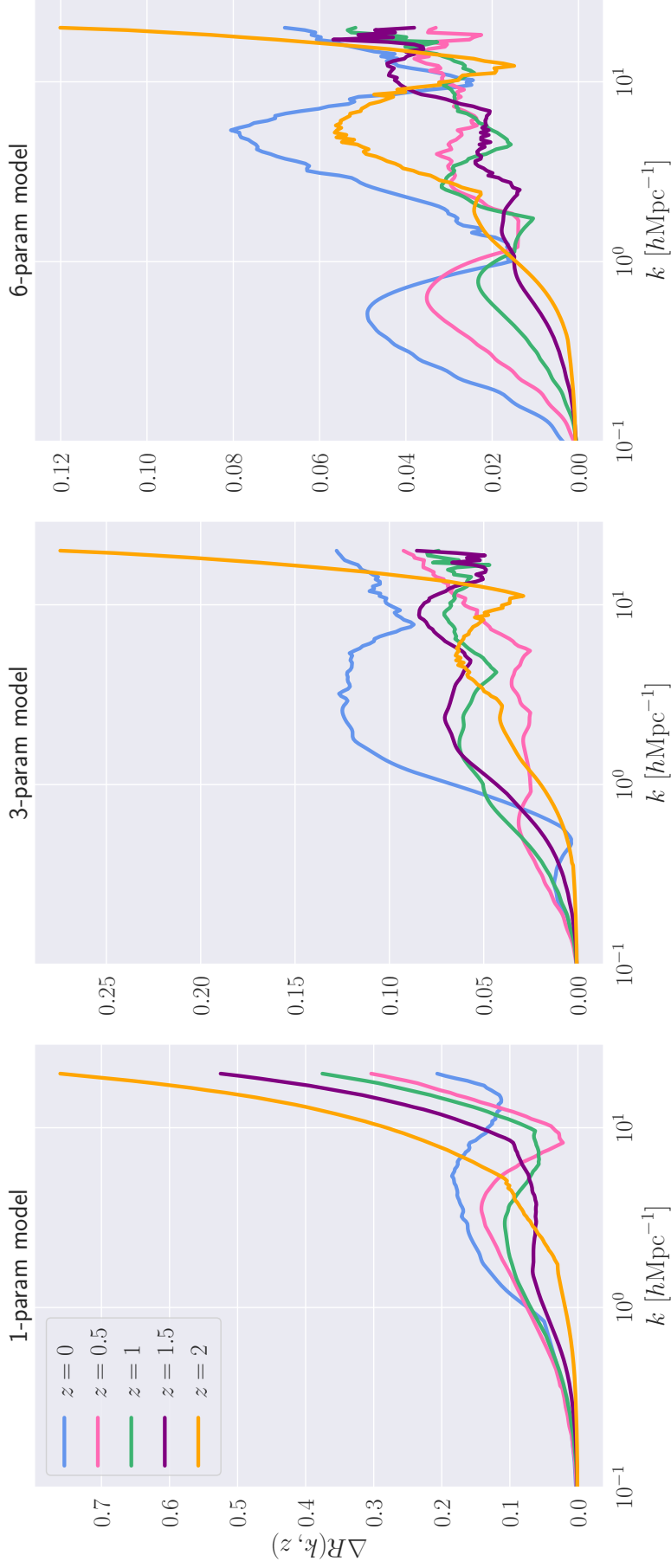


Figure 6.5: Our envelope function  $\Delta R(k, z)$  encoding the maximum deviation of our three **HMC**Code models to the hydro-sims as a function of wavenumber  $k$  plotted for select redshifts. We see that the amplitude of our envelope decreases as we go from one- to three- to six-parameters (as noted by the decreasing values in each of the panel’s individual  $y$ -axes), and so we assign less theoretical uncertainties to those models that better match the data. The apparent noisy behaviour of these curves is due to numerical noise in the hydro-sims, but also from our choice of envelope function, which uses the absolute value of the error ratio.

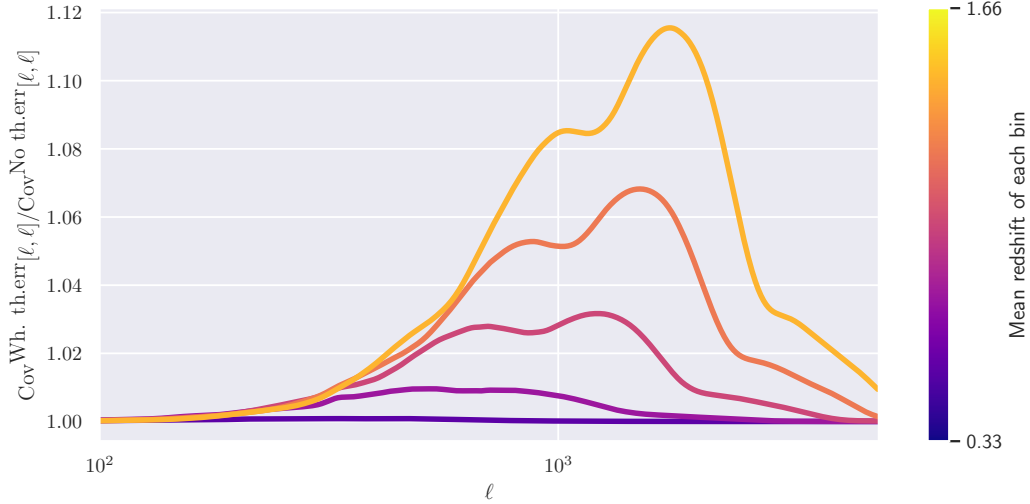


Figure 6.6: Ratio of the diagonals of auto-spectra elements of our  $C_\ell$  covariance matrix with our additional theoretical error to that without theoretical error. Here, we see that the amplitude of the additional theoretical error strongly depends on the redshift bins of the auto-spectra considered, with higher redshift bins containing more theoretical error than closer bins. We note that there is significant support on the off-diagonals for our theoretical covariance, and thus the total covariance with theoretical error is much larger than just the ratios showed here.

for our idealised Stage-IV like cosmic shear survey. However, to avoid making these analysis decisions ourselves, which have little physical motivation behind them and apply simultaneously to all hydro-sims in our ensemble, we can turn to our theoretical error modelling instead of making binary scale-cuts.

### Including a theoretical error covariance

Tables 6.3 and 6.4 summarises our results for the biases in  $\Omega_M$  and  $S_8$ , respectively. Here, we present the amplitude of the bias, that is the difference in the mean of our MCMC chains to the fiducial value, and the relative bias, which is the difference divided by the reported standard deviation from the MCMC chains for each parameter, with and without the effects of our additional theoretical error. The baryonic feedback parameters for each model are marginalised over when we present results for  $\Omega_M$ ,  $\sigma_8$  and  $S_8$ .

### One-parameter model

In general, the one-parameter model without additional theoretical error produces a significant biases in the recovered parameters, with at least a  $3\sigma$  offset in either  $\Omega_M$  or  $S_8$  for all hydro-sims excluding BAHAMAS (recall that the one-parameter model was constructed by fitting to BAHAMAS data only). The results of the very significant biases in the remaining five hydro-sims shows that the one-parameter model of baryon feedback for a *Euclid*-like survey up to  $\ell_{\text{MAX}} = 5000$  is completely impractical if we wish to recover unbiased results from the analyses of cosmic shear data.

When we introduce our additional theoretical error into the analysis, we see that biases in both cosmological parameters fall dramatically across all hydro-sims for our one-parameter model. We see a reduction in both the raw offset values, and a significant decrease in the relative bias in terms of each parameter’s standard deviation. This demonstrates our theoretical uncertainties modelling is correctly identifying the scales in which baryonic feedback are not correctly modelled by the one-parameter model, down-weighting



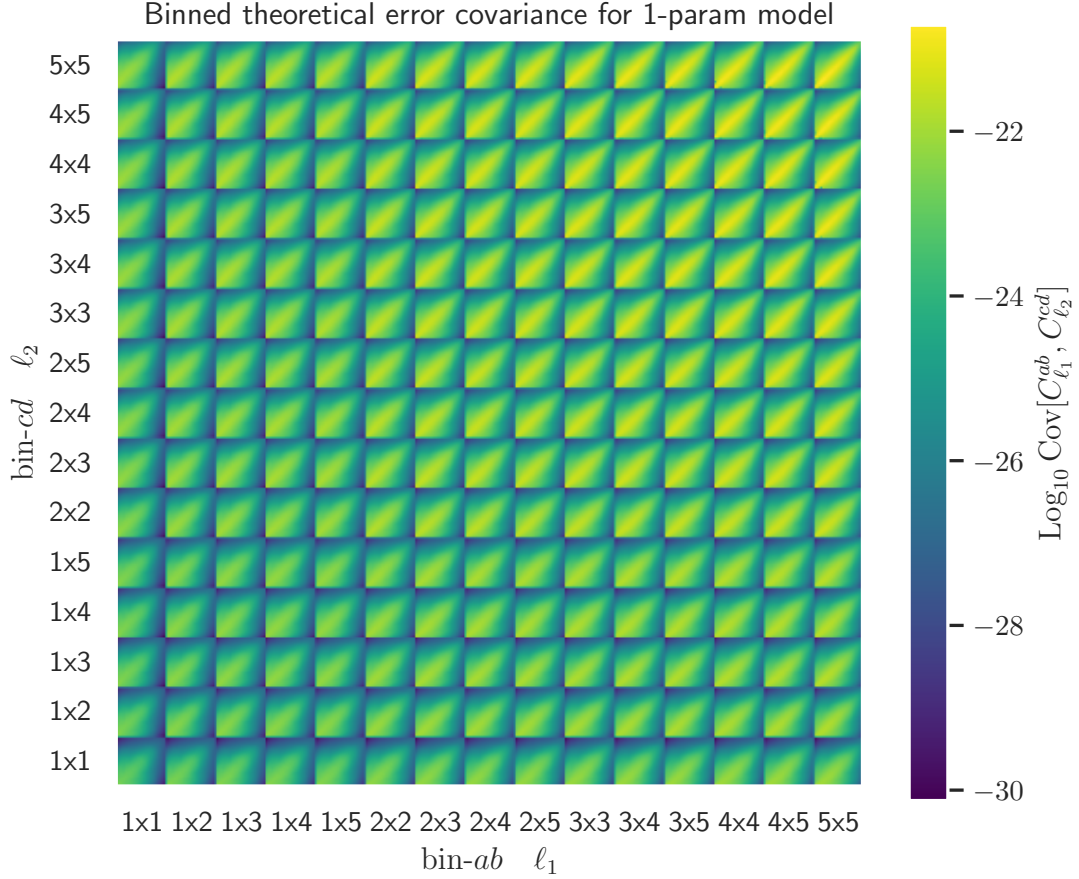


Figure 6.7: Plot of the binned theoretical error matrix  $\mathbf{C}^E$  for the one-parameter model across all fifteen redshift bin combinations and twenty five binned band-powers. Here, we see that the amplitude of our theoretical error matrix generally grows as we consider higher redshift bins (e.g. the  $5 \times 5 \times 5 \times 5$  sub-block is significantly brighter, and thus of larger magnitude, than the  $1 \times 1 \times 1 \times 1$  sub-block). We also see that for each sub-block, the theoretical error is greatest along the  $\ell_1 = \ell_2$  diagonal, though there is significant support along the off-diagonal terms, which serves to increase the overall effect of our theoretical uncertainty modelling.

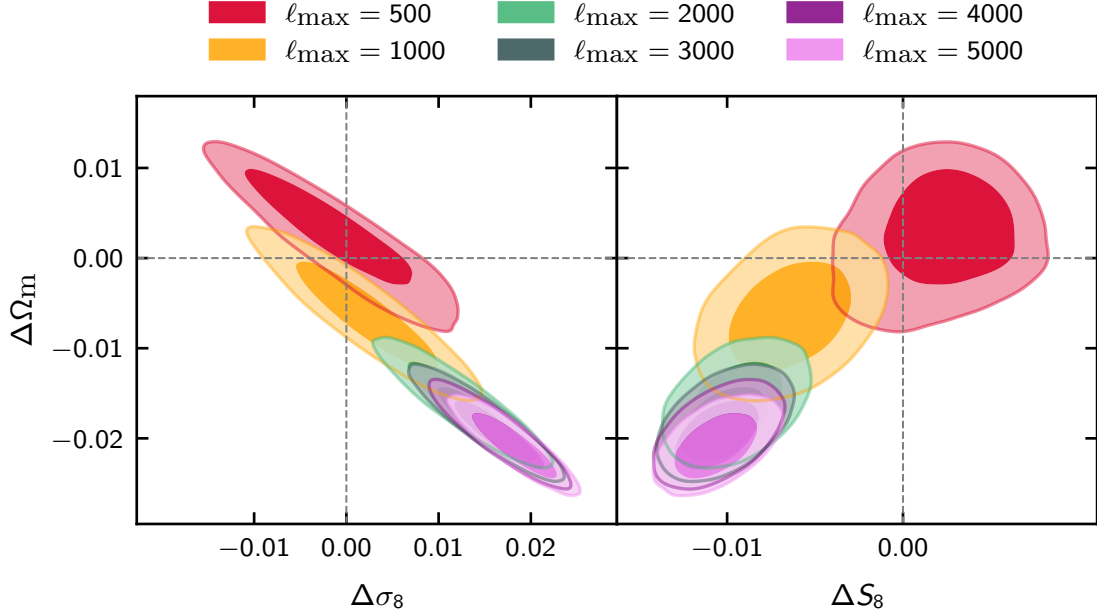


Figure 6.8: 2D  $\Omega_M$ - $\sigma_8$  and  $\Omega_M$ - $S_8$  offset contours for the one-parameter baryon feedback model for the SIMBA hydro-sim for a range of maximum  $\ell$ -modes considered in the analysis, without the inclusion of our additional theoretical uncertainty covariance. As we increase  $\ell_{\text{MAX}}$ , we are increasing the number of modes that are contaminated by baryon feedback, and thus bias our cosmological parameters away from the fiducial value. It is interesting to note that even for the  $\ell_{\text{MAX}} = 1000$  analysis, which is a considerably conservative scale-cut even for Stage-III surveys (e.g. HSC-Y3 [167]), our results are biased by more than  $2\sigma$  in all cosmological parameters for our Stage-IV-like survey when using SIMBA as the ground-truth. This motivates the development and inclusion of a theoretical uncertainty covariance as to retain the maximum information possible from the smallest scales, without incurring the significant biases seen in this Figure.

them in our analyses, and thus resulting in significantly less biased cosmological parameter constraints. However, we still see significant ( $>1\sigma$ ) biases in many hydro-sims even when using theoretical error. This is due to the one-parameter model being inadequate when considering a *Euclid*-like weak lensing survey.

### Three- and six-parameter models

As expected, the more general three- and six-parameter models result in smaller absolute biases, which reflects their ability to better match more general baryon feedback scenarios, but at the cost of decreased precision due to the need to marginalise over more parameters. Hence, we see that the relative biases show a strong decrease when going to our many-parameter versions, which is an effect of decreased absolute bias and increased uncertainties.

Figure 6.9 plots the 2D  $\Omega_M$ - $\sigma_8$  and  $\Omega_M$ - $S_8$  offset contours for our three baryon feedback models with and without our theoretical error added for the Simba hydro-sim. This highlights the degeneracies that exist between these parameters, finding the usual ‘lensing banana’ that is the natural degeneracy between  $\Omega_M$  and  $\sigma_8$ . These contours gradually move to the origin as we increase the number of parameters in the baryon feedback model, and increase in size as we are marginalising over more parameters.

Figure 6.10 plots the 2D  $\Omega_M$ - $\sigma_8$  offset contours for the one-parameter model for our suite of hydro-sims for the case of with and without our theoretical error. We see that

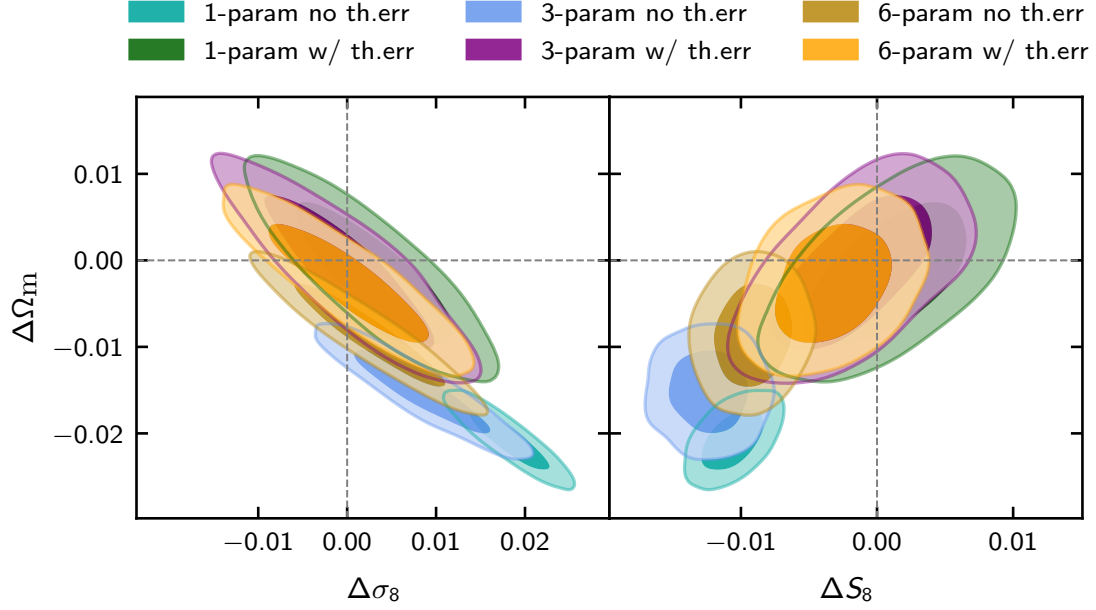


Figure 6.9: 2D  $\Omega_M$ - $\sigma_8$  and  $\Omega_M$ - $S_8$  offset contours for the three baryon feedback models with and without our theoretical error for the SIMBA hydro-sim. We can clearly see that the one-parameter model without theoretical error (light grey contour) produces a tight constraint on our cosmological parameters that is extremely far from the correct value. When we add our theoretical error to the data covariance (dark green contour), we find that the one-parameter model *is* able to recover the correct values, with an appropriate increase in the size of the contour. We see that the three- and six-parameter models, while more flexible, are unable to correctly recover unbiased results without the addition of our theoretical uncertainties.

without the theoretical error the recovered contours are highly constraining, which is a result of marginalising over a single baryon feedback parameter only, with a large degree of scatter between the hydro-sims. It is interesting to note that this scatter appears to be roughly along the degeneracy direction, though it appears random which quadrant each hydro-sim falls into.

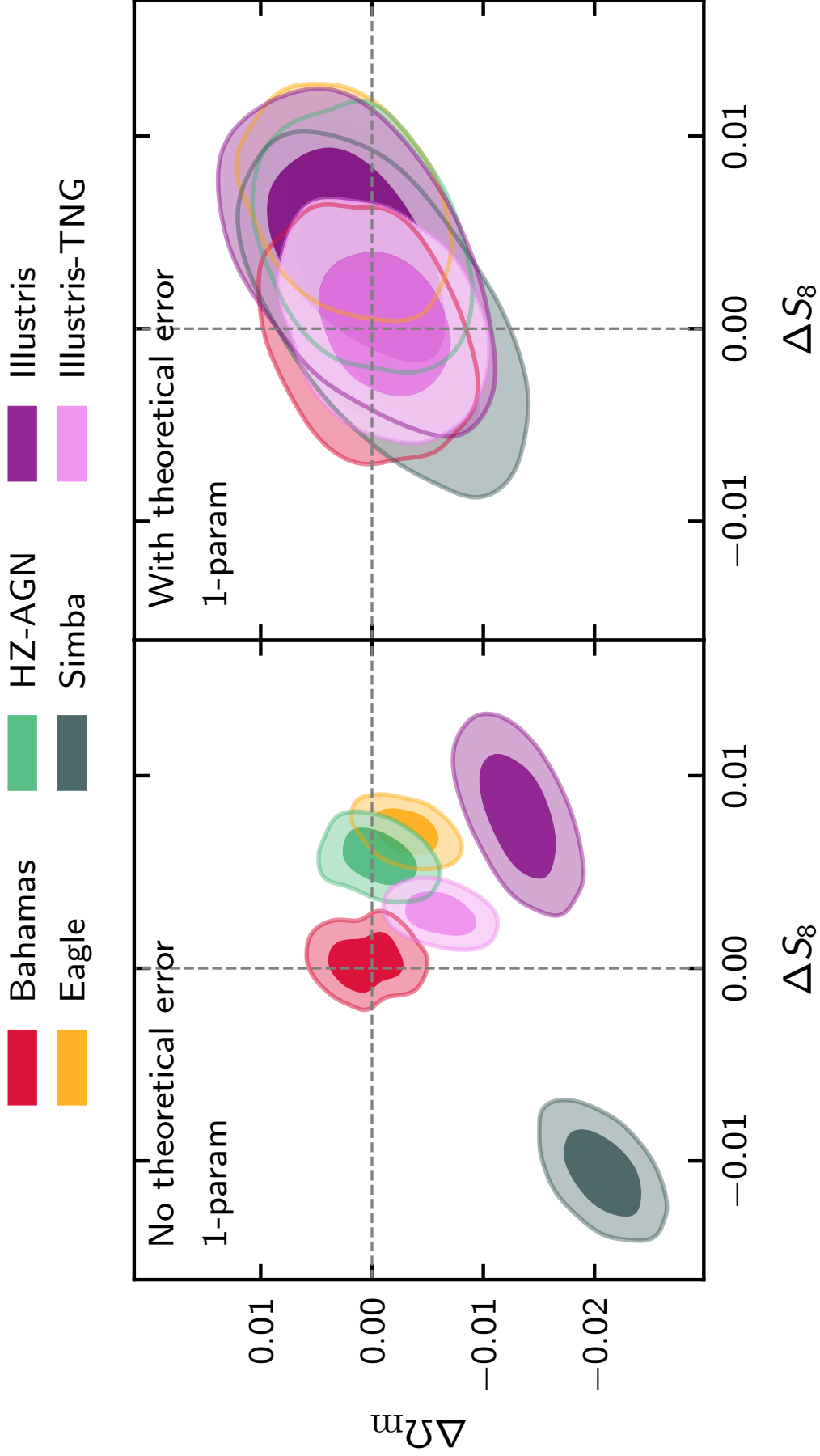


Figure 6.10: 2D  $\Omega_M$ - $S_8$  offset contours for the one-parameter baryon feedback model without and with the addition of our theoretical error for all our range of hydro-sims considered. We can see that without theoretical error, the one-parameter model produces a large degree of scatter for all hydro-sims, with only BAHAMAS being consistent with the input cosmology. With the introduction of theoretical error, we see that the contours increase and all except EAGLE become unbiased at the  $2\sigma$  level.

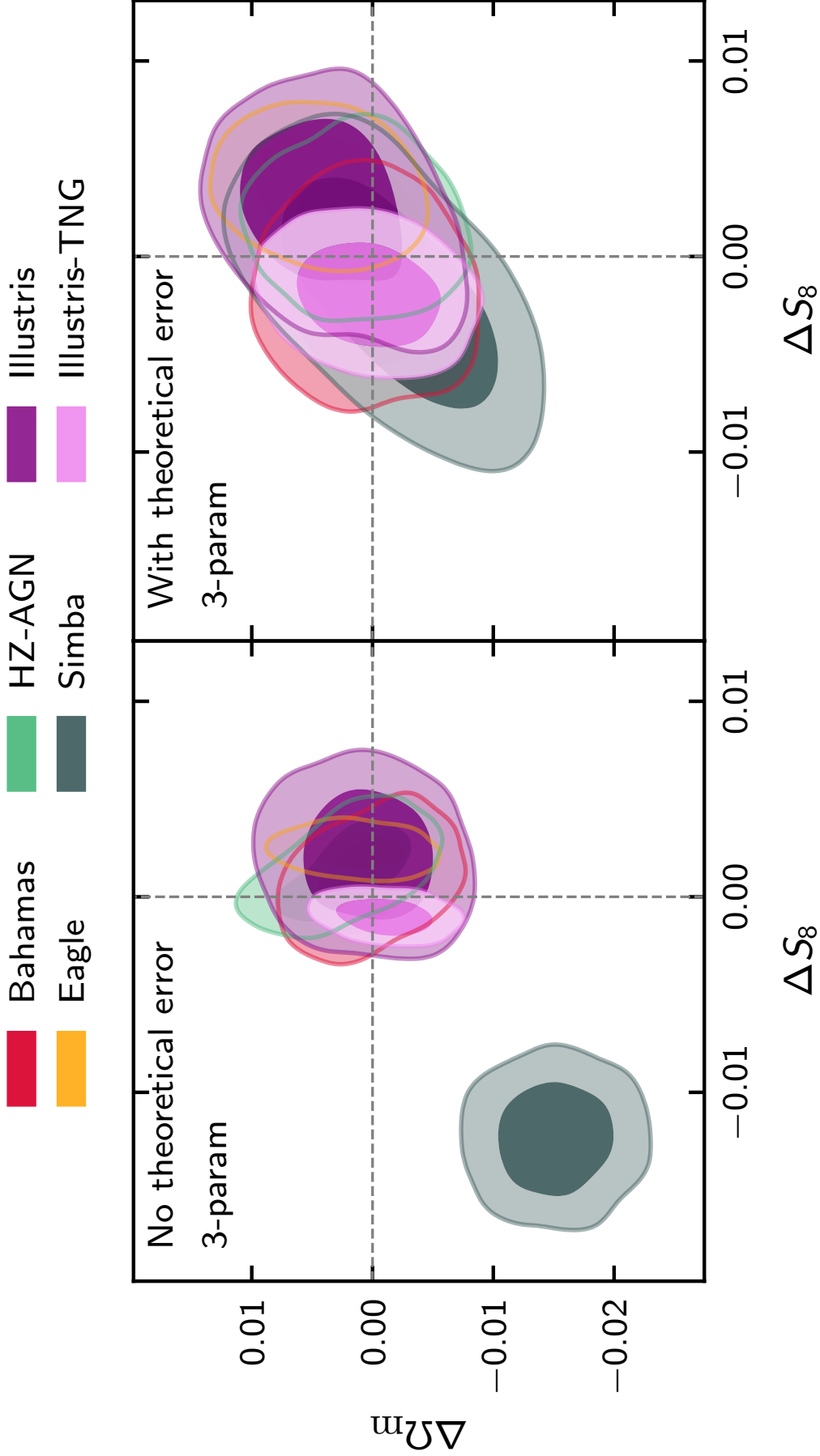


Figure 6.11: 2D  $\Omega_M$ - $S_8$  offset contours for the three-parameter baryon feedback model without and with the addition of our theoretical error for our range of hydro-sims considered. When compared to the less flexible one-parameter model, we see that the three parameter model without additional theoretical error is better able to recover the input cosmology for a wider range of simulations, though EAGLE, ILLUSTRIS-TNG, and SIMBA remain biased to at least the  $2\sigma$  level. We note the general increase in the contour's area going from the one- to three-parameter model which is associated with marginalising over more baryon feedback parameters. We see that with theoretical error, all contours are unbiased at the  $2\sigma$  level.

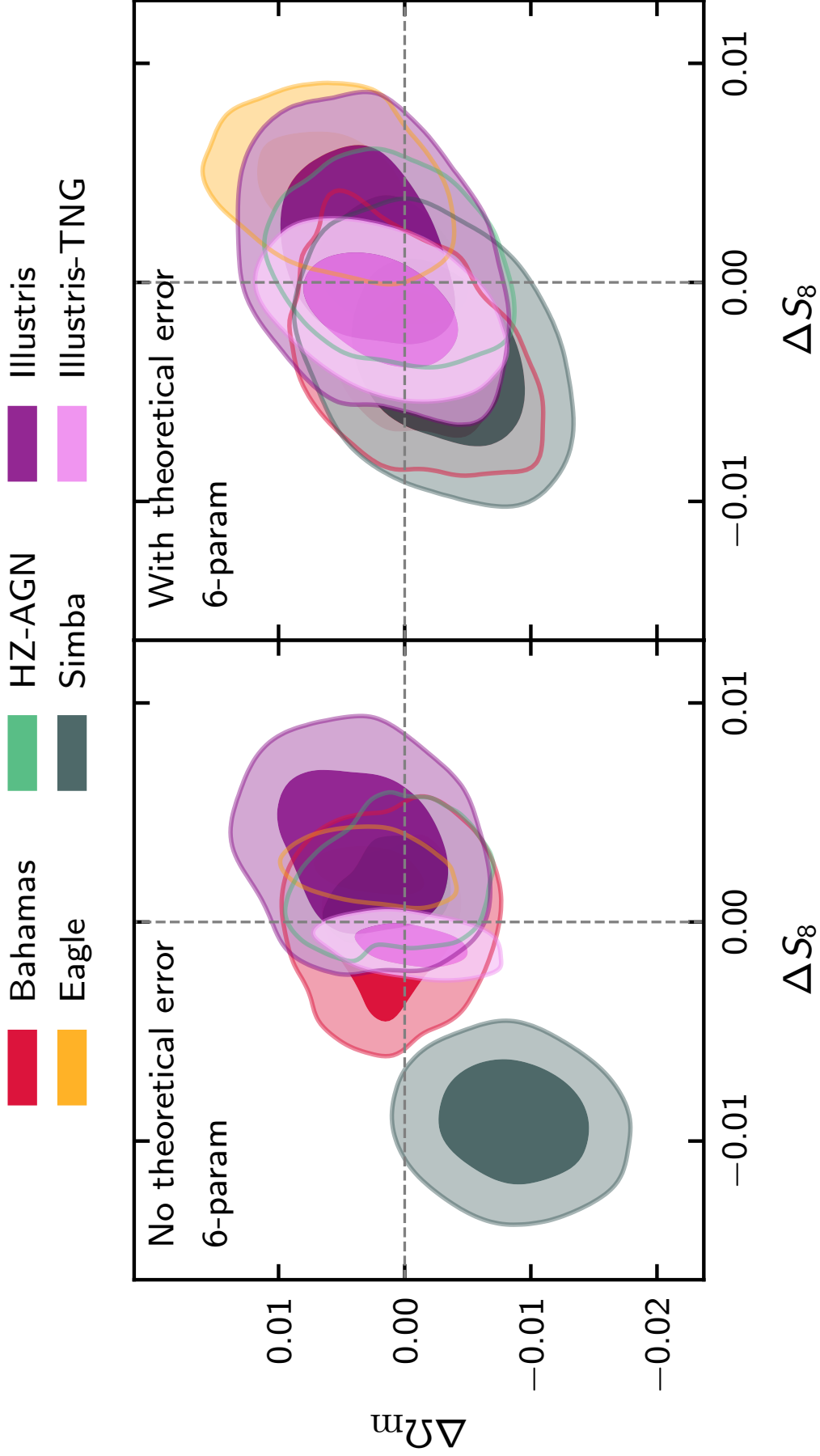


Figure 6.12: 2D  $\Omega_m$ - $S_8$  offset contours for the six-parameter baryon feedback model without and with the addition of our theoretical error for our range of hydro-sims considered. Again, we see an extension of the general trend in the contours without additional theoretical error: an increase in the contours with them moving towards the origin. We see that even with a six-parameter model, it is not sufficient to recover unbiased constraints from the SIMBA simulation.

Table 6.3: Table summarising our results for the bias in  $\Omega_M$  as found from our MCMC analyses using our suite of six hydro-sims and three baryon feedback models, without and with our additional theoretical error modelling added to the covariance matrix when going to  $\ell_{\text{MAX}} = 5000$ . We see that without theoretical error, the one-parameter model generally produces significant biases ( $> 3\sigma$ ) from the true value, with only BAHAMAS giving small biases in  $\Omega_M$  and  $S_8$ . These biases reduce to less than  $1\sigma$  with the inclusion of our theoretical error in the one-parameter model, highlighting the effectiveness of our theoretical error modelling. We see that the three- and six-parameter result in less bias in  $\Omega_M$ , though some hydro-sims still give large biases for the six-parameter model (i.e. SIMBA and EAGLE). The inclusion of our theoretical error covariance into the three- and six-parameter models further reduces the bias.

Hydro-sim and model	$100\Delta\Omega_M$	No th. err.	$\Delta\Omega_M/\sigma_{\Omega_M}$	No th. err.	$100\Delta\Omega_M$	With th. err.	$\Delta\Omega_M/\sigma_{\Omega_M}$	With th. err.
BAHAMAS 1-param		0.057		0.258		0.038		0.098
BAHAMAS 3-param		0.012		0.038		0.049		0.127
BAHAMAS 6-param		0.100		0.276		-0.085		-0.206
EAGLE 1-param		-0.306		-1.535		0.224		0.587
EAGLE 3-param		0.149		0.520		0.433		1.186
EAGLE 6-param		0.274		0.962		0.573		1.459
HORIZON-AGN 1-param		-0.057		-0.255		0.079		0.199
HORIZON-AGN 3-param		0.224		0.631		0.123		0.331
HORIZON-AGN 6-param		0.109		0.325		0.105		0.269
ILLUSTRIS 1-param		-1.317		-5.690		0.128		0.249
ILLUSTRIS 3-param		0.048		0.127		0.373		0.828
ILLUSTRIS 6-param		0.328		0.761		0.295		0.652
SIMBA 1-param		-2.071		-8.828		-0.158		-0.293
SIMBA 3-param		-1.513		-4.723		-0.155		-0.276
SIMBA 6-param		-0.858		-2.206		-0.257		-0.567
ILLUSTRIS-TNG 1-param		-0.613		-2.885		-0.107		-0.277
ILLUSTRIS-TNG 3-param		-0.110		-0.424		0.035		0.091
ILLUSTRIS-TNG 6-param		-0.055		-0.185		0.181		0.453



Table 6.4: Table similar to Table 6.3 but now for the bias in  $S_8$  as found from our MCMC analyses. We see that without theoretical error, the one-parameter model results in at least a  $3\sigma$  bias from the true value for all hydro-sims except BAHAMAS, which reduces when going to a multi-parameter model. Our theoretical error is able to significantly reduce the bias in the one-parameter model, though we see a multi-parameter model is essential to ensure unbiased constraints across all hydro-sims.

Hydro-sim and model	$100\Delta S_8$	No th. err.	$\Delta S_8/\sigma_{S_8}$	No th. err.	$100\Delta S_8$	With th. err.	$\Delta S_8/\sigma_{S_8}$	With th. err.
BAHAMAS 1-param		0.038		0.386		-0.028		-0.101
BAHAMAS 3-param		0.083		0.492		-0.210		-0.819
BAHAMAS 6-param		0.010		0.042		-0.360		-1.468
EAGLE 1-param		0.709		8.802		0.660		2.579
EAGLE 3-param		0.240		3.742		0.360		2.039
EAGLE 6-param		0.240		3.207		0.441		2.443
HORIZON-AGN 1-param		0.574		6.002		0.464		1.616
HORIZON-AGN 3-param		0.137		0.865		0.158		0.759
HORIZON-AGN 6-param		0.165		1.070		0.089		0.448
ILLUSTRIS 1-param		0.796		3.710		0.377		1.024
ILLUSTRIS 3-param		0.208		0.950		0.253		0.867
ILLUSTRIS 6-param		0.325		1.289		0.135		0.435
SIMBA 1-param		-1.059		-7.096		0.081		0.207
SIMBA 3-param		-1.235		-6.469		-0.180		-0.480
SIMBA 6-param		-0.916		-4.903		-0.328		-1.156
ILLUSTRIS-TNG 1-param		0.281		3.701		0.033		0.130
ILLUSTRIS-TNG 3-param		-0.100		-1.602		-0.193		-1.083
ILLUSTRIS-TNG 6-param		-0.106		-1.628		-0.122		-0.715

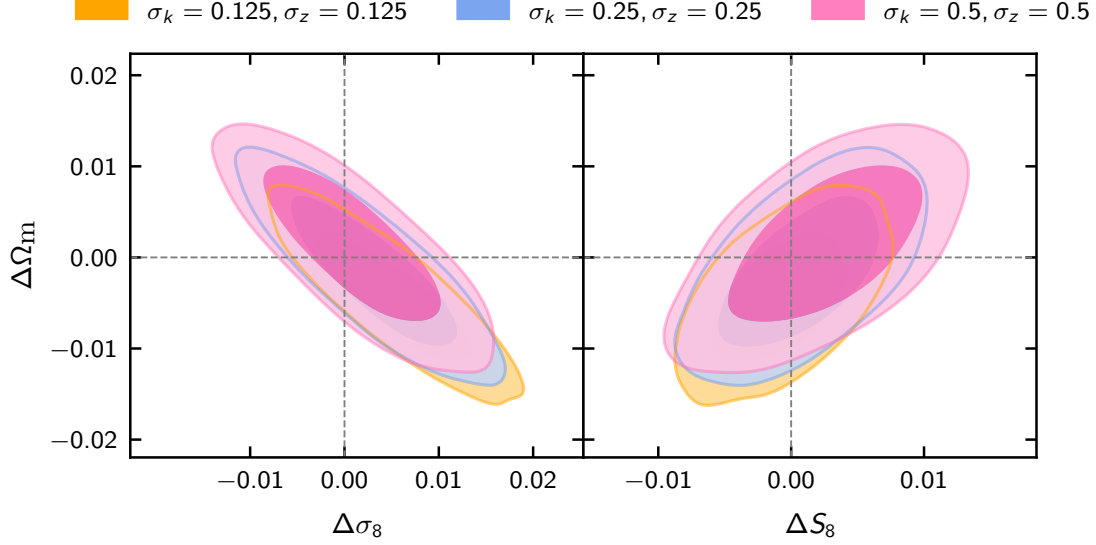


Figure 6.13: 2D  $\Omega_M$ - $\sigma_8$  and  $\Omega_M$ - $S_8$  contours for the Simba hydro-sim using the one-parameter model with theoretical error where we are changing the values of  $\sigma_k$  and  $\sigma_z$ . Here, we see that as we increase their values, the effects of the theoretical error covariance become larger - increasing the size and decreasing the biases in the contours.

### Dependency on $\sigma_k$ and $\sigma_z$

In our propagated covariance matrix (Equation 6.11) we introduced two coupling scales,  $\sigma_k$  and  $\sigma_z$ , which were both set at 0.25 in our fiducial analyses. Here, we investigate the effects of changing their values, and the effects it has on parameter constraints. We note that in our fiducial analyses, the baryon feedback physics of the SIMBA simulation is strong enough that even the six-parameter model of baryon feedback produces significantly biased cosmological parameter constraints (Figure 6.12). Thus, SIMBA is a good testing ground to see how the contours react to the changing of these values.

In general, as  $\sigma_k$  and  $\sigma_z$  increase we are increasing the number of wavenumber and redshift modes that contribute to a given  $(\ell_1, \ell_2)$  pair, respectively. This increases the size of our  $\ell$ -space theoretical error covariance, further suppressing the high- $\ell$  modes that are contaminated by baryonic feedback. However, in the limit that  $\sigma_k$  and  $\sigma_z$  tend to infinity, then both Gaussian terms tend to unity and the double integral becomes factorisable in  $(k, k')$ -space and thus is equivalent to some rank-1 update of the form  $\vec{x}\vec{x}^T$ , where  $\vec{x}$  is some vector in  $\ell$ -space. Since this is a rank-1 addition to our data covariance matrix, this is equivalent to marginalisation over a single parameter. However, since we know that single parameter models for baryonic feedback do not correctly model the wide range of behaviour of baryonic feedback effects seen in the hydro-sims, it would be incorrect to take this limit for the values of  $\sigma_k$  and  $\sigma_z$ .

The regime in which our theoretical error covariance reduces to a rank-1 matrix will be determined by the maximum  $k$ -space difference between different  $\ell$ -modes. For example, Figure 6.2 shows that there is an approximate two decade difference in  $\log k$  between our smallest and largest  $\ell$ -mode. Thus, if one were to choose a value for  $\sigma_k$  that easily encompassed these values within one standard deviation, then we would expect our theoretical error covariance to collapse to the rank-1 limit. Since our values chosen for  $\sigma_k$  are much less than two decades, we expect that our values to not fall within this limit.

In Figure 6.13, we plot the 2D contours for three different combinations of  $\sigma_k$  and  $\sigma_z$ . Larger values of these parameters allow for longer-scale correlations in wavenumber and redshift, and thus produce a larger amplitude for the theoretical error covariance matrix.

Figure 6.13 shows that these larger values suppress high- $\ell$  modes more than for smaller values, which is seen by the larger contours and a reduction in the bias from baryon feedback. While on the range of values that we tested larger values increase the effectiveness of the theoretical error covariance, larger values also increase the correlation length between different wavenumbers and redshifts in the covariance matrix which decreases the adaptability of our theoretical error covariance to match more general models of baryon feedback physics. In the limit that these values go to infinity, we would be saying that all wavenumbers and redshifts are 100% correlated, which is unphysical since we know that baryonic effects in the power spectrum are quite local at high  $k$ . Equally, in the limit that these values go to zero, we would be maximally destroying information through the covariance matrix by assuming that each wavenumber and redshift has an independent error which are uncorrelated between similar modes. Ultimately, there is less than a  $1\sigma$  shift in contours plotted in Figure 6.13, and so our implementation of the theoretical error approach is broadly insensitive to the values of  $\sigma_k$  and  $\sigma_z$ .

We investigate the effects of changing these coupling parameters in our three- and six-parameter models in Appendix 6.A, which shows a similar trend to the one-parameter model in that larger values produce increased contours with less baryonic bias in them.

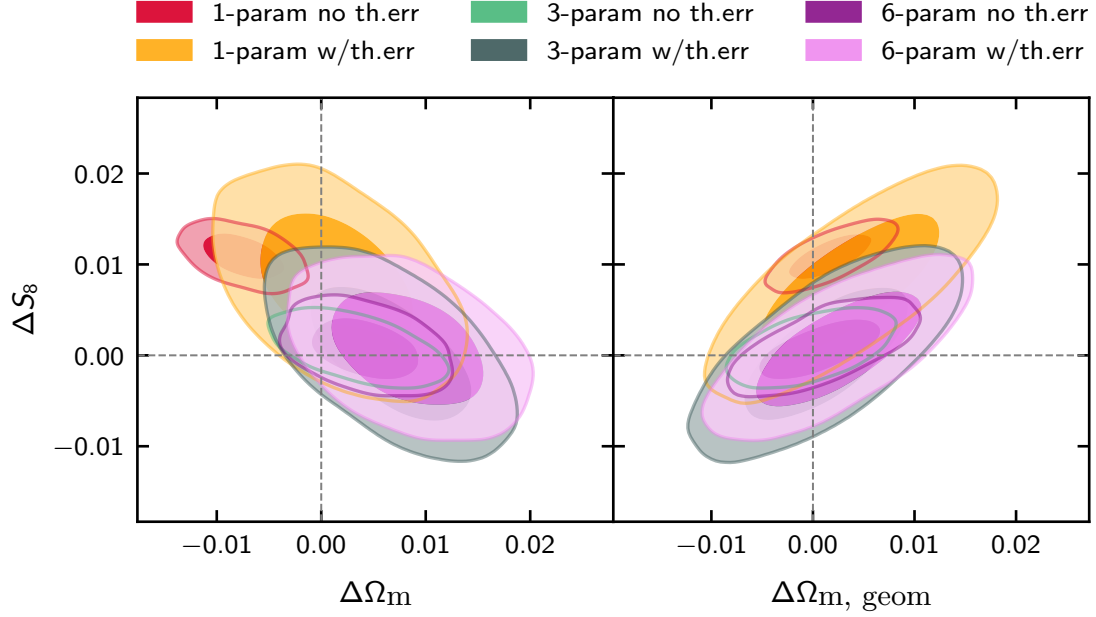


Figure 6.14: 2D  $\Omega_M$ - $S_8$  and  $\Omega_{M \text{ geom}}$ - $S_8$  contours for different baryon feedback models without and with the addition of our theoretical error with the EAGLE hydro-sim. We see that without theoretical error, the one-parameter model produces results that are biased in  $S_8$  and  $\Omega_M$ , but can identify that the information from the lensing kernels is not affected by baryonic feedback, and thus produces unbiased estimates for  $\Omega_{M \text{ geom}}$ .

### Growth-structure split

The information in the cosmic shear power spectrum (Equation 6.4) comes from two pieces: the geometrical factors of the lensing kernels, and in the matter power spectrum, both depending on the matter density  $\Omega_M$ . It can be advantageous to decouple this matter density in two: a factor that describes the geometry of the Universe through the computation of the comoving distances in the lensing kernel,  $\Omega_{M \text{ geom}}$ , and the growth of structure in the universe that is used in the computation of the matter power spectrum,  $\Omega_M$  [310]. This growth-structure split of the matter density has been applied to existing cosmic shear data-sets, including the Dark Energy Survey [311, 312] and the Kilo-Degree Survey [313].

We are motivated to apply this growth-structure split to our approach of modelling the theoretical uncertainties at the matter power spectrum level. By quantifying the errors directly in  $P(k)$ , and then propagating to the angular power spectrum, we are hopefully preserving information in the lensing kernels. Our lensing kernels have no theoretical uncertainties associated with them, and so we hope to preserve information about  $\Omega_{M \text{ geom}}$  even with our scale cuts present.

Thus, we can repeat a sub-set of our MCMC analyses to investigate how the inclusion of our theoretical error changes the constraints on  $\Omega_M$  and  $\Omega_{M \text{ geom}}$ . This is presented in Figure 6.14. Here, we see that without our theoretical uncertainties, the inflexible one-parameter model leads to a bias in  $\Omega_M$  but remains unbiased in the geometrical term  $\Omega_{M \text{ geom}}$ . This tells us that while our data-vector may still be contaminated with baryonic feedback from the matter power spectrum, information from the lensing kernels can still be extracted from cosmic shear data. When we introduce our theoretical error terms to the covariance matrix, we down-weight baryonic contaminated modes, and so become consistent in  $\Omega_M$  and  $\Omega_{M \text{ geom}}$  at the cost of increased contour sizes.

## 6.5 Discussion and conclusions

We have presented results for parameter constraints using various hydrodynamical simulations as ground truths analysed with three different baryon feedback models, with and without an additional theoretical error covariance. We have seen that constraints on cosmological parameters are significantly biased for a forthcoming Stage-IV like cosmic shear survey using as low as a maximum  $\ell$ -mode of  $\ell_{\text{MAX}} = 1000$  when analysing the hydrodynamical simulation’s data using a single parameter for baryon feedback. This is consistent with previous results in the literature, for example in Ref. [314] finding a harmonic-space scale cut of  $\ell_{\text{MAX}} \sim 500$  was needed for the case of DES-Y3 mock data against a model without baryonic feedback in.

Hence, we are motivated to more accurately model the errors associated in the matter power spectrum arising from baryon feedback over the more traditional binary scale-cuts approach, resulting in our theoretical error covariance. This theoretical error was then applied to our model of baryon feedback across our suite of hydrodynamical simulations, finding that our parameters biases decreased with smaller absolute and relative off-sets when going to the same maximum multipole in our analysis.

We note that some hydro-sims still yield a significant ( $> 1\sigma$ ) bias in cosmological parameters when using our theoretical error covariance for the single-parameter model, which indicates that such a basic model will be unsuitable for application to Stage-IV cosmic shear survey data. While the multi-parameter models tended to do better in producing unbiased results, our theoretical error covariance was still needed to ensure that all hydro-sim results were unbiased when going to  $\ell_{\text{MAX}} = 5000$ .

The theoretical error formalism is a general method for quantifying the known errors of a method to realisations of the data. This method can be applied to a wide-range of modelling problems within cosmology and astrophysics, where we have applied it to baryonic feedback within the matter power spectrum. To that end, the theoretical error is not a fixed quantity. If next generation hydrodynamical simulations release that feature, for example, improved subgrid models of physical processes that we know we are currently lacking [289], then it would make sense to replace the older simulations in our suite with these new releases. This would alter our error envelope function, improving or reducing our degree of trust in our numerical baryonic feedback models. Alternatively, as new baryonic feedback models are developed which are more accurate to the hydro-sims, the need for a theoretical error covariance becomes diminished. Though these new models will have to come from advancements in the analytic or semi-analytic modelling of baryonic feedback itself as numerical run-times from the convergence of MCMC chains would be significantly affected if we were to use more-general models that contain many more free-parameters than the six used here.

With multi-parameter models of baryonic feedback, the effectiveness of external priors (that is, information on baryonic feedback not from cosmic shear alone) become increasingly powerful. In recent years, observational constraints on baryonic feedback have come from the thermal Sunyaev-Zeldovich effect in CMB observations [315], and diffuse x-ray backgrounds [316]. With ever increasing precision data taken on our Universe across the entire electromagnetic spectrum, the power of external priors and cross-correlation with Stage-IV cosmic shear surveys for baryonic feedback physics constraints will be immense.

The Holy Grail of baryonic feedback models will, of course, be a model that can fit all hydro-sims with no free parameters.<sup>5</sup> However, while we are making progress towards this

---

<sup>5</sup>This is not a requirement on the baryonic feedback models, per se, but on the requirements on the ensemble of hydrodynamical simulations to converge to a single prediction for the evolution of  $P^{\text{Hy}}(k, z)$ . With no scatter in the hydro-sims, deriving a fitting formulae for baryonic feedback physics becomes trivial.

goal, for example BACCO [273], a theoretical error covariance is highly valuable until then. We expect the formalism that we have presented and validated here will be of significant value to forthcoming Stage-IV weak lensing surveys.

## Acknowledgements

We acknowledge HPC resources from the IRIS computing consortium. AH acknowledges support from a Royal Society University Research Fellowship. For the purpose of open access, the author has applied a Creative Commons Attribution (CC BY) licence to any Author Accepted Manuscript version arising from this submission.

## Data availability

The hydrodynamical simulation data used in this article were taken from the ‘power spectrum library’ [299]<sup>6</sup> and from the CAMELS Project [307]<sup>7</sup>, which include the BAHAMAS [282], HORIZON-AGN [295], ILLUSTRIS [293], ILLUSTRIS-TNG [294], EAGLE [296], and SIMBA [292] simulations. We thank their authors for making their data publicly available. No new data was generated in support of this research.

## Appendices

### 6.A Dependency of the covariance on the coupling parameters

In Section 6.4.4 we looked at the one-parameter model and its dependency on the coupling parameters  $\sigma_k$  and  $\sigma_z$ . Here, we present a comparison between all three baryon feedback models and investigate their dependency on the coupling parameters. Figure 6.15 uses SIMBA as the ground-truth, which features quite significant baryonic feedback, and Figure 6.16 using ILLUSTRIS-TNG, which has less extreme feedback. When using SIMBA as the ground-truth, we see a that there is a strong link between the coupling parameter’s values and the cosmological parameter biases for the one-parameter model, whereas the more general three- and six-parameter models are approximately insensitive to  $\sigma_k$  and  $\sigma_z$  due to their ability to better fit the data (thus have less significant theoretical uncertainties associated with these models). We also see that, when using ILLUSTRIS-TNG as the ground-truth, since all three feedback models can adequately fit the data, increasing  $\sigma_k$  and  $\sigma_z$  serves to slightly broaden the contours only, with no significant effect on the parameter means.

---

<sup>6</sup><https://powerlib.strw.leidenuniv.nl>

<sup>7</sup><https://camels.readthedocs.io/>

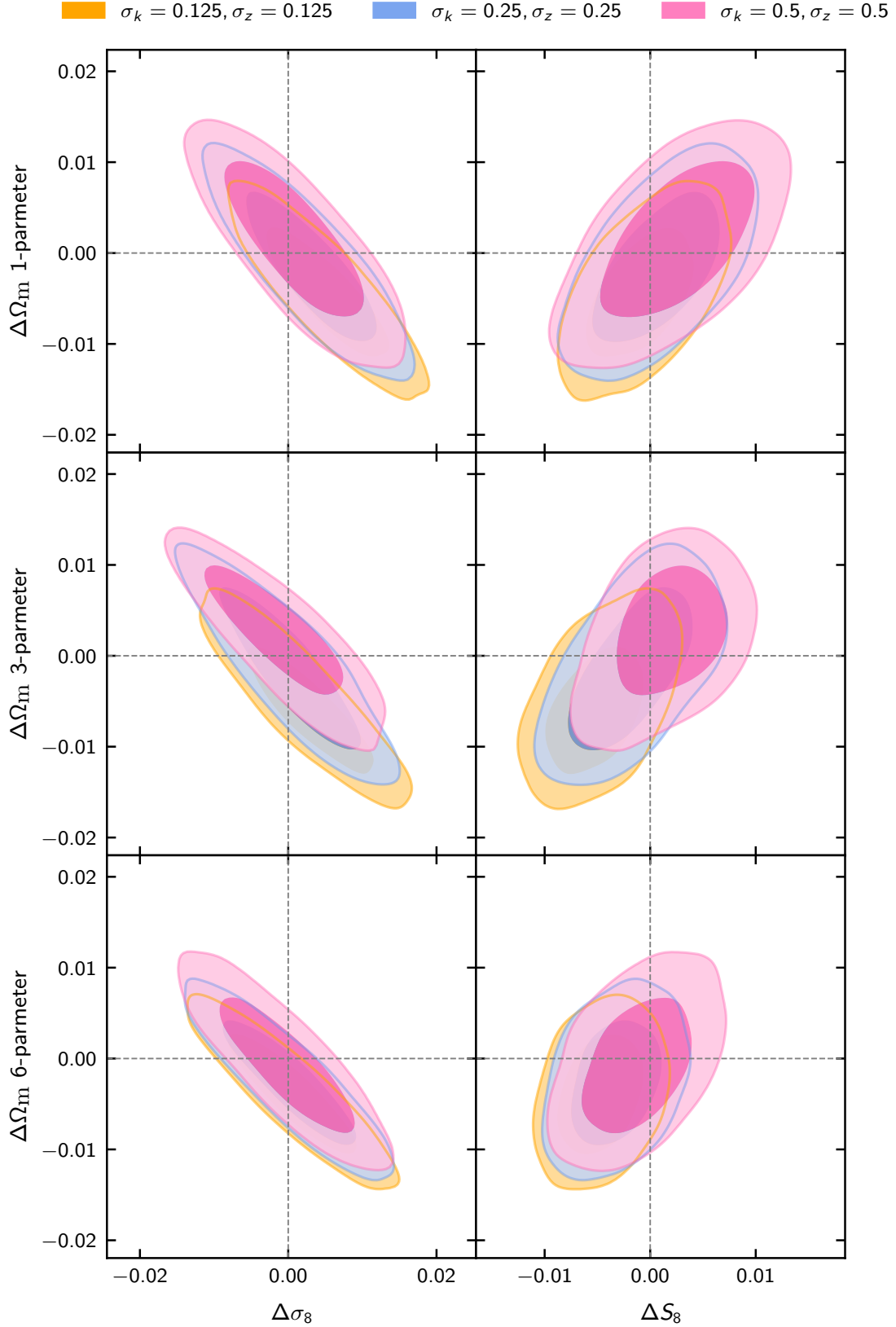


Figure 6.15:  $\Omega_{\text{M}}\text{-}\sigma_8$  and  $\Omega_{\text{M}}\text{-}S_8$  contours for the SIMBA hydro-sim using the one-, three-, and six-parameter models (descending rows) with theoretical error for different values of  $\sigma_k$  and  $\sigma_z$  (different coloured contours). We see that increasing these values produces a stronger effect for the theoretical covariance, increasing the suppression of small-scale modes and thus reducing the bias from baryonic feedback.



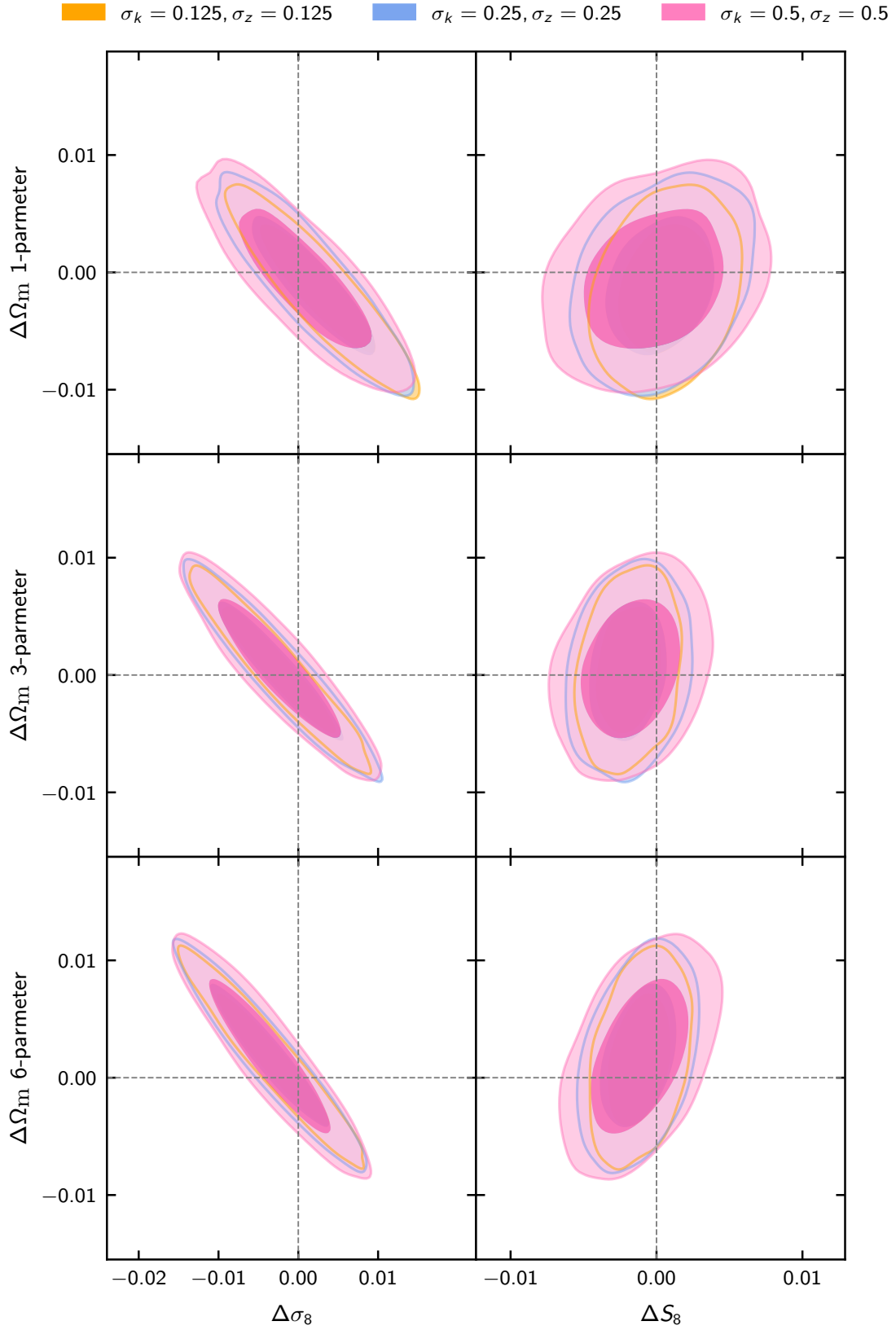


Figure 6.16: Similar plot to Figure 6.15, but for the ILLUSTRIS-TNG hydro-sim instead of SIMBA. Since ILLUSTRIS-TNG can be well fitted by each of our HMCode models with theoretical error, the effect of changing  $\sigma_k$  and  $\sigma_z$  is just to increase or decrease the size of the contours, without effecting the bias in these parameters.

Quest?  
I'm already on a quest!

—Shrek

Hold on, I'm not done,  
One more time, with feeling!

—Bon Jovi

7

# Mitigating baryon feedback bias in cosmic shear through development of new techniques to optimise binary cuts

---

**Outline.** In this chapter, I present an overview of existing methods for the derivation of binary scale cuts that mitigate baryonic feedback bias in a Stage-III survey. I then show how if we applied these methods to Stage-IV-like mock data, then headline constraints on  $S_8$  would be no better than those from existing surveys. Using this as motivation, I go on to extend existing methods by explicitly incorporating baryonic feedback models, and show how we can extract much more information while keeping bias at acceptable levels. While specialised to baryonic feedback in cosmic shear only, the methods presented here are easily applicable to  $3 \times 2$ pt analyses, and to the mitigation of other effects, such as intrinsic alignments and non-linear galaxy clustering.

## 7.1 Introduction & motivation

In this thesis, we have already seen how the modelling of baryonic physics in the matter power spectrum is a hugely complex task, both in terms of numerical implementations in hydrodynamical simulations and analytical descriptions in our Boltzmann code solvers. These baryonic physical processes have no pure analytical expressions, and thus we are forced to rely on semi-analytical and numerical methods. As with any method, we aim to benchmark these methods to the available data to quantify their accuracy and errors over the physical domain that these models are used in. Since we are concerned with baryonic feedback, our data comes from numerical hydrodynamical simulations which aim to capture ‘the Universe in a box’. This led to the use of the theoretical uncertainties approach, which was successfully used to mitigate baryonic feedback in Chapter 6 of this thesis.

Our application of the theoretical uncertainties approach was limited to the cosmic shear angular power spectrum,  $C_\ell^{ab}$ . However, there exist other estimators for cosmic shear they have been used in existing analyses, namely the two-point angular correlation

functions ( $\xi_{\pm}^{ab}$ ), band powers ( $\mathcal{B}_n^{ab}$ ), and COSEBIs ( $E_n^{ab}$ ). The theoretical expectation value of these new observables are simply integrals of the underlying angular power spectrum with different weighting functions, though they do measure different fundamental properties of the cosmic shear maps and thus are distinct observables from the angular power spectrum. Hence, one could propagate our  $C_{\ell}$  theoretical uncertainty matrix into these bases, just as we propagated our  $k$ -space covariance into  $\ell$ -space. However, these further integrations could be a problem of considerable numerical complexity. Therefore, the investigation of baryonic feedback biases for these additional observables would still require the use of binary cuts, and so they maintain a place within our cosmic shear analysis toolkits.

Furthermore, our investigation of the theoretical uncertainty covariance only looked at the cosmic shear spectrum. This is just one prong of the three-headed beast that is the ‘ $3 \times 2$ pt’ analyses, which include galaxy clustering and galaxy-galaxy lensing. The  $3 \times 2$ pt data-vector will be the foundation of cosmological analyses using Stage-IV galaxy surveys, since it provides maximal constraining power. Thus, while the theoretical uncertainties approach has been applied to mitigate non-linear galaxy bias in the  $2 \times 2$ pt data-vector (which lacks the pure shear-shear signal) separately [317], it may not be trivial to combine these approaches in one consistent package.

Additionally, there exists the Bernardeau-Nishimichi-Taruya (BNT) transformation [318], which aims to isolate the redshift information from each source galaxy bin through the use of a linear mixing matrix. This isolation in redshift-space forms a much tighter  $k \Leftrightarrow \ell$  relation in the matter power spectrum, and thus if one were to apply a  $k_{\text{max}}$  to an analysis of a given model, then this would result in more appropriate  $\ell_{\text{MAX}}$  values than in the ordinary Limber approximation [164]. It has been proposed to use the BNT transform in all *Euclid* weak lensing cosmological analyses, and it forms part of the core *Euclid* CLOE code [164].

Perhaps the strongest reason to investigate binary scale cuts is that they have been used widely in existing Stage-III survey analyses [223, 226, 232, 269, 314, 319], and thus form the baseline default choice for Stage-IV surveys.

Hence, we are suitably motivated to investigate the properties of binary scale cuts for future, Stage-IV cosmic shear surveys. The enhanced statistical precision that the forthcoming surveys have require us to investigate the properties of all statistical methods that will be used on the next-generation of data, which include the application and derivation of scale cuts. We will again focus on the impact of baryonic feedback as the source of our biases that we will be mitigating through scale cuts, though our methods are extendable to any source of bias that varies as a function of scale.

## 7.2 The Dark Energy Survey’s scale cuts approach

We are motivated to look at existing Stage-III approaches to scale cuts to inform us about our approach to the future Stage-IV surveys. The approach that DES took to mitigate the effects of baryonic physics is detailed in Ref [269]. Here, they quantify baryonic effects in the cosmic shear observables ( $\xi_{\pm}(\vartheta)$  for DES) through the use of the  $\chi^2$  statistic. First, they generate a synthetic data-vector without any baryonic feedback  $\xi_{\pm, \text{base}}^{ab}$  and then one with baryonic ‘contamination’,  $\xi_{\pm, \text{baryon}}^{ab}$ . To generate this contaminated data-vector, they take the OWLS hydrodynamical simulation’s matter power spectrum, since that represents an extreme scenario of AGN feedback. It is important to note that these data-vectors are fixed quantities, and do not change as a function of scale-cuts.

To determine the scale cuts from these two data-vectors, they construct a  $\chi^2$  difference between them, where they only focus on a specific combination of spectra,  $ab$ . This gives

the per-bin  $\chi^2$  criterion as

$$\left(\xi_{\pm, \text{baryon}}^{ab} - \xi_{\pm, \text{base}}^{ab}\right) \mathbf{C}_{abab}^{-1} \left(\xi_{\pm, \text{baryon}}^{ab} - \xi_{\pm, \text{base}}^{ab}\right)^{\text{T}} \leq \frac{\chi_{\text{crit}}^2}{N}, \quad (7.1)$$

where  $\chi_{\text{crit}}^2$  is the targeted  $\chi^2$  value that is split between  $N$  spectra, and  $\mathbf{C}_{abab}^{-1}$  is the sub-block corresponding to the spectra  $ab$  of the inverse covariance matrix and has shape  $N[\vartheta_{\pm}^{ab}] \times N[\vartheta_{\pm}^{ab}]$  where  $N[\vartheta_{\pm}^{ab}]$  is the number of angular modes in bin combination  $ab$  for either the  $\xi_+$  or  $\xi_-$  function. Note that in the DES-Y3 approach, they treat  $\xi_+$  and  $\xi_-$  as *separate* spectra. Thus, they find different values for  $\vartheta_{\text{min}}$  for  $\xi_+^{ab}$  and  $\xi_-^{ab}$  for the same bin combination  $ab$ . Hence, while they may have four tomographic bins, which would give ten unique combinations for the angular power spectrum, they have  $N = 20$  since there is an additional factor of two coming from the two shear correlation functions. They describe an ‘iterative procedure’ was used to obtain the value of  $\chi_{\text{crit}}^2 < 0.5$  [269]. The values of  $\vartheta_{\text{min}}^{ab}$  would then be adjusted to fit the criteria above, taking the minimum value that would satisfy it.

While this is certainly a way to optimise your scale cuts such that it mitigates baryonic feedback in a data-vector, it suffers from several key issues:

- The  $\chi^2$  statistic is in data-space. While this tells us how statistically significant the difference between the two data-vectors are, it does not tell us anything about how these differences in the data-vectors affect our cosmological inference from these data-vectors. Naturally, a larger  $\chi^2$  would correlate with larger differences in cosmological parameters, but this depends on the parameter’s response to the observables — which is different for each observable. Hence, a determination of the relation between  $\chi_{\text{crit}}^2$  and the level of bias induced for each combination of observables considered needs to be computed for each survey and is not necessarily easily comparable between different surveys and data releases.
- Equation 7.1 works bin-by-bin, in that while it still contains some information from other bins through the inverse covariance matrix, it only looks at the scale cuts on a bin-by-bin basis. Thus, it does not include contributions from the cross-correlations of the spectra in the inverse covariance matrix that would otherwise contribute to the  $\chi^2$  (and thus final likelihood). Let us demonstrate with a simple  $2 \times 2$  example. Consider a data-vector of length two: a mean vector  $\vec{\mu} = (\mu_A, \mu_B)$  and a realisation vector  $\vec{d} = (d_A, d_B)$  giving the vector  $\vec{\delta} \equiv \vec{d} - \vec{\mu} = (A, B)$ . It has an associated covariance matrix  $\mathbf{C}$  given by  $\mathbf{C} = \begin{pmatrix} C_{AA} & C_{AB} \\ C_{AB} & C_{BB} \end{pmatrix}$  and inverse covariance matrix<sup>1</sup>  $\mathbf{C}^{-1} = \begin{pmatrix} D_{AA} & D_{AB} \\ D_{AB} & D_{BB} \end{pmatrix}$ . The full  $\chi^2$  of this is given by

$$\chi^2 = \vec{\delta} \mathbf{C}^{-1} \vec{\delta}^{\text{T}} \quad (7.2)$$

$$= (A, B) \begin{pmatrix} D_{AA} & D_{AB} \\ D_{AB} & D_{BB} \end{pmatrix} \begin{pmatrix} A \\ B \end{pmatrix} \quad (7.3)$$

$$= A^2 D_{AA} + 2AB D_{AB} + B^2 D_{BB}, \quad (7.4)$$

which clearly has contributions from the cross-correlations in the (inverse) covariance matrix. If we were to repeat this exercise, but instead isolating the  $A$  and  $B$  components separately and computing a ‘total’  $\chi^2$  from them, we find

$$\chi_A^2 = A^2 D_{AA} \quad (7.5)$$

$$\chi_B^2 = B^2 D_{BB} \quad (7.6)$$

$$\therefore \chi_{\text{sum}}^2 = \chi_A^2 + \chi_B^2 = A^2 D_{AA} + B^2 D_{BB} \neq \chi^2. \quad (7.7)$$

<sup>1</sup>I’ve used  $D$  to label the elements of the inverse covariance matrix as to not confuse between the elements of the non-inverted covariance matrix. Thus  $D_{AB} \equiv (\mathbf{C}^{-1})_{AB}$ .

Thus, the sum of our individual  $\chi^2$  is not necessarily the same as the total  $\chi^2$  computed when including the cross-correlations.

Since these cross-correlations carry cosmological information, and are included when computing the likelihood for cosmological inference, it is important to keep them when determining the scale cuts to be used in any analysis. Thus, a holistic approach where we include the entire covariance matrix should be used when determining any scale cuts.

- ☉ The DES approach aims to mitigate against *any and all* baryonic feedback. This is because they take their base data-vector to have no baryonic feedback in at all. While this approach may have certainly worked in the lower-precision Stage-III era, it's not particularly suitable to apply to the forthcoming Stage-IV era experiments. This is because baryonic feedback affects a large range of scales, and thus mitigating against all effects throws away significant amounts of data. Additionally, we have models of baryonic feedback, some of which are extremely accurate down to small scales and high redshifts, so it's not a case of having no appropriate models at all. Thus, if we were to apply even a basic model of baryonic feedback physics then we would find that the scale cuts allow the inclusion of smaller scales, thus increasing the constraining power of our data-vector. This does, however, require that we marginalise over any new baryonic feedback parameters included in our models. It is hoped that the increase in precision coming from the inclusion of much more constraining angular modes mitigates against any information lost from marginalisation.

Do note that while DES used  $\xi_{\pm}$  as their summary statistics, we are using the power spectrum  $C_{\ell}$  values instead. Thus, when investigating our scale cuts, we are interested in the maximum multipole to include in our analyses,  $\ell_{\text{MAX}}$ , which is equivalent to their quest for  $\vartheta_{\text{min}}$ .

### 7.3 Detailed look at the per-bin $\chi^2$

As explained above, the scale cuts used in the DES-Y3 analysis were derived from optimising Equation 7.1, which worked bin-by-bin. We then showed in Equation 7.7 that these individual  $\chi^2$  values do not necessarily reflect the total  $\chi^2$  of the entire data-vector. We can now investigate the properties of how going bin-by-bin is reflected in the  $\chi^2$  values.

To set up our two fiducial data-vectors, we computed our base baryon-free set of  $C_{\ell}$  values using the `mead2020` model as included in CAMB as part of the Core Cosmological Library (CCL). For our baryon-contaminated data-vector, the `mead2020_feedback` one-parameter model was used with  $T_{\text{AGN}} = 8.0$ . To be broadly equivalent to the DES-Y3 setup, four Gaussian photometric redshift bins were created, with means  $\bar{z} = \{0.4, 0.8, 1.2, 1.6\}$  with widths  $\sigma_z = 0.2$ . With four bins, we get ten different unique spectra:  $1 \times 1$ ,  $1 \times 2$ ,  $1 \times 3$ ,  $1 \times 4$ ,  $2 \times 2$ ,  $2 \times 3$ ,  $2 \times 4$ ,  $3 \times 3$ ,  $3 \times 4$ ,  $4 \times 4$ . Thus, we have ten different  $\chi^2$  curves to investigate as a function of  $\ell_{\text{MAX}}$ .

First, let us look at how including baryonic feedback in our  $C_{\ell}$  data vector changes their values. This is shown in Figure 7.1. Here, we see that the  $C_{\ell}$  values are the same on the very largest scales, however as soon as we cross about  $\ell \gtrsim 20$ , then the AGN and supernovae activity within our baryonic feedback model starts suppressing the  $C_{\ell}$  values. This suppression grows as we go to smaller and smaller scales, eventually reaching about a 20% decrement. We also note that this suppression profile is bin-dependent, with the lowest redshift bins deviating from the base data-vector at a much lower  $\ell$  value than the higher redshift bins. Thus, naïvely, one may assume that the lower redshift bins would have a larger  $\chi^2$  difference between the base data-vector and our baryon contaminated

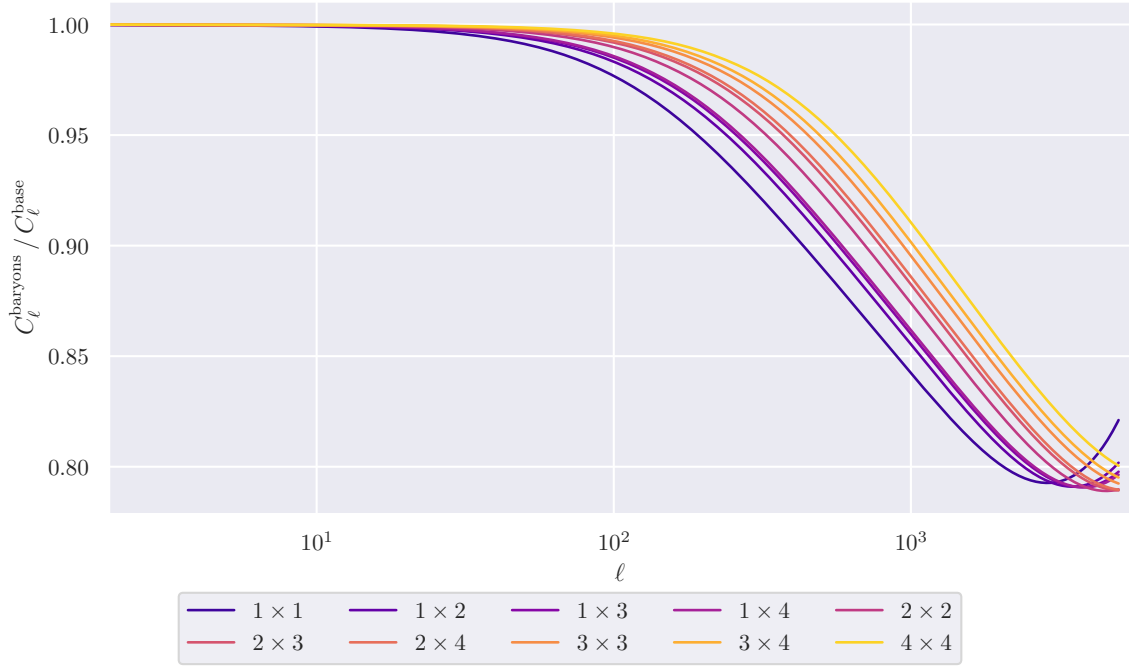


Figure 7.1: Ratio of our  $C_\ell$  data-vectors with baryonic feedback to that of no baryonic feedback. We can see that AGN and supernovae activity causes a large suppression in the power spectrum that effects a large range of  $\ell$  values. We also see that baryonic physics causes the suppression to move to larger  $\ell$  values for higher redshift bins.

data-vector based on the above plot. However, it is important to note that due to the larger cosmic shear signal from higher redshift bins, the overall signal-to-noise of these high redshift bins is much larger than the lower redshift bins. Hence, when we look at our  $\chi^2$  differences per-bin, we find that the higher redshift bin differences are more statistically significant.

Figure 7.2 plots the  $\chi^2$  differences obtained using the left-hand side of Equation 7.1 for each spectra (that is the angular power spectrum for each unique auto- and cross-correlation combination of our four bins), as a function of maximum multipole. Here, we see that the larger signal-to-noise of the higher redshift bins causes the  $\chi^2$  differences to be much larger than for the lower redshift bins. This results in a much lower  $\ell_{\text{MAX}}$  for the higher redshift bins, which is exactly what was found by the Dark Energy Survey when producing their scale cuts.<sup>2</sup> It is also important to note that we plot the  $\chi^2$  values of the entire data-vector as a function of  $\ell_{\text{MAX}}$  in the dot-dashed blue line. This shows that the overall  $\chi^2$  is not simply the sum of the individual  $\chi^2$  values, and that it has a slightly different behaviour to that of the individual spectra.

We also note that the  $\chi^2$  values in Figure 7.2 are quite large, since we are applying Stage-IV survey specifications to our fiducial data-vectors. Thus, if we were to apply the DES-Y3 cut of  $\chi^2_{\text{crit}} = 0.5$ , split equally between the ten bin pairs, then this would result in extraordinarily aggressive scale cuts.

<sup>2</sup>Though, of course, DES worked in correlation functions so they found a larger  $\vartheta_{\text{min}}$  for the higher redshift bins.

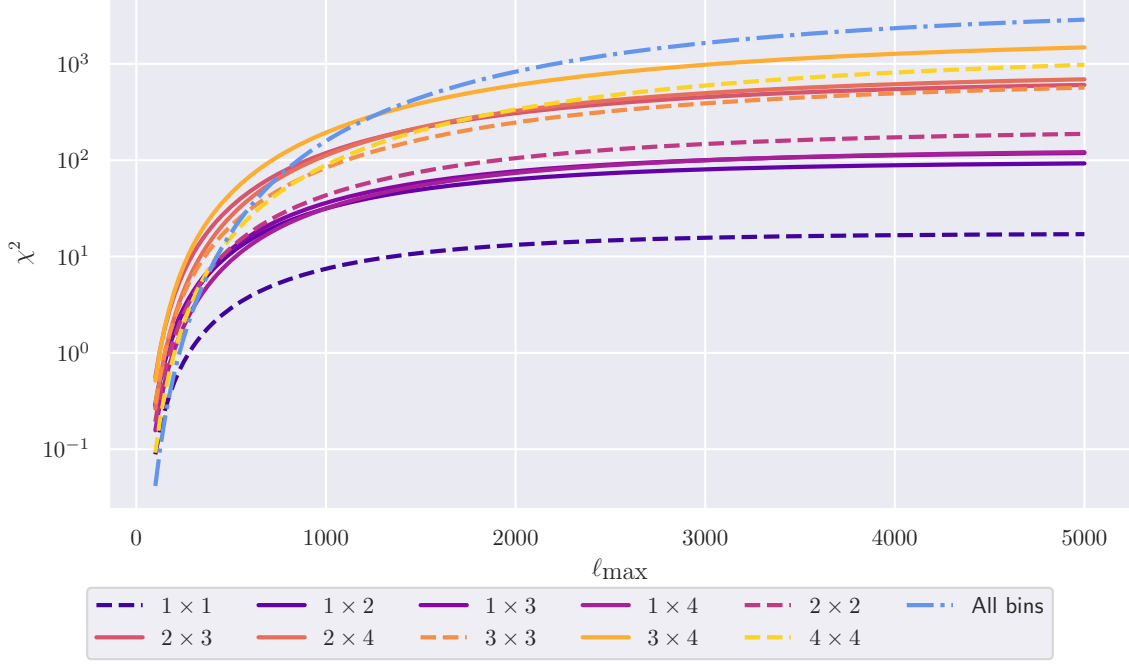


Figure 7.2: Plot of the different  $\chi^2$  values as a function of  $\ell_{\text{MAX}}$  for each of our ten different spectra, in solid and dashed curves, along with the total  $\chi^2$  for the entire data-vector in the dot-dashed blue curve. We plot the auto-spectra with dashed lines to make it immediately obvious that, due to the inclusion of shape noise in the auto-spectra only, these curves have a lower  $\chi^2$  compared to their cross-spectra counterparts.

## 7.4 Insufficiencies of the DES-Y3 approach in the Stage-III era

While the DES-Y3 approach to scale cuts may appear to be a sensible approach to mitigate baryonic feedback in Stage-III data, we can show that their scale cuts did not effectively remove contamination from their data-vectors. Since their  $\chi^2$  analysis aimed to reduce baryonic feedback in their data-vectors to ‘acceptable levels’, which was defined as a shift in the parameter’s mean of no greater than  $0.3\sigma$  [269], if we were to analyse these data-vectors using a model with and without baryonic feedback we should find the same results for cosmological parameters.

To this end, we have performed a re-analysis of the joint DES-Y3 and KiDS-1000 cosmic shear analysis [320], which presents the tightest constraints using cosmic shear Stage-III data yet. Hence, this is a good testing ground to see of changing baryonic feedback models and its effects  $S_8$  and  $\Omega_M$  values inferred from the data.

Results were obtained using the DES-Y3+KiDS-1000 example pipeline as provided with COSMOSIS, which was altered to use either a ‘zero-parameter’ model, which is the `mead2020` model without baryonic feedback, and the one- and three-parameter `mead2020_feedback` models. It should be noted that the one-parameter model was used in their fiducial analysis, though they also investigated neglecting baryonic feedback though a dark-matter-only matter power spectrum. The `PolyChord` sampler was used, matching the joint analysis, with the same precision settings too. In addition to the astrophysical baryonic feedback parameters already mentioned, our analysis matched that presented in Ref. [320] by sampling over six cosmological parameters ( $\Omega_B h^2$ ,  $\Omega_C h^2$ ,  $h$ ,  $n_s$ ,  $S_8$ ,  $\Sigma m_\nu$ ), four intrinsic alignment, and thirteen redshift calibration nuisance parameters.



Figure 7.3 presents the triangle plot for the distribution of  $\Omega_{\text{M}}$ ,  $\sigma_8$  and  $S_8$  for our re-analysis of the DES-Y3+KiDS-1000 data-vector, along with the results from *Planck* 2018 for comparison. Table 7.1 also shows the one-dimensional marginalised means and  $1\sigma$  errors for the three cosmological parameters. We see that while the peaks in the one-dimensional distributions are extremely close between all three baryonic feedback models, there is a significant tail out to larger  $\sigma_8$  and  $S_8$  values in the one- and three-parameter models when compared to the dark-matter only analysis. We expect that the inclusion of one and three additional nuisance parameters would act to slightly broaden the marginalised contours of our cosmological parameters, but in an overall scaling of the  $1\sigma$  errors. However, what we see is that there is a clear one-sided broadening to the parameter’s distributions in favour of larger  $\sigma_8$  and  $S_8$  values. Hence, we can say that the one- and three-parameter models are extracting additional information from the data-vector that the dark-matter-only model cannot, and thus their scale cuts were not totally sensitive to all baryonic feedback.

To reiterate, the scale cuts used in Ref. [320] for the DES-Y3 data-vector were derived using the DES-Y3 methodology previously described (Equation 7.1, and presented in Ref. [269]). For the KiDS-1000 part of the data-vector, they mitigate baryonic feedback by raising the minimum angular scale in the COSEBI integral from  $\vartheta_{\text{min}} = 0.5$  arcmin to  $\vartheta_{\text{min}} = 2.0$  arcmin and the use of the one-parameter baryonic feedback model. The KiDS team do not explicitly do a DES-like per-bin  $\chi^2$  analysis to determine per-bin biases, though it should be noted that DES-Y3 contributes a significant part of the overall signal-to-noise of the joint analysis.

This extension of  $S_8$  out to larger values when changing the baryonic feedback model was also seen in Ref. [321], which jointly analysed DES-Y3, KiDS-1000, and HSC-Y1 data using the *Baccoemu* baryonification emulator [273, 280, 322–324], and taking the existing data-vectors down to significantly smaller scales (an  $\ell_{\text{MAX}}$  of 4500). *Baccoemu* features seven free parameters in its baryonic feedback model, and so should be even more flexible than our three-parameter model. It should be noted that Ref. [321] found an anomalously low value of  $\Omega_{\text{M}}$  of  $\Omega_{\text{M}} = 0.212^{+0.017}_{-0.032}$ , which is in tension to *Planck* at the  $\sim 3\sigma$  level, and lower than each of the survey’s own individual analyses<sup>3</sup>. Therefore, we are currently in a situation where analysing existing data-sets with different numerical algorithms (the baryonic feedback models) and analysis choices (the chosen scale cuts) yield different results for the key cosmic shear observables ( $\Omega_{\text{M}}$  and  $S_8$ ), which are in tension with *Planck* at some level or another. If we are to use the Stage-III surveys as a springboard into the Stage-IV era, then we should quantify and acknowledge these shortcomings before applying the same inadequate methods to much more precise data in an actual cosmological analysis.

## 7.5 Insufficiencies of the DES-Y3 approach in the Stage-IV era

We have seen that the offsets between baryonic feedback models is relatively small for the DES-Y3 +KiDS-1000 data vector when using the DES-Y3 approach to determining scale cuts from baryonic physics, though non-zero. While this automatically suggests that these

<sup>3</sup>Naturally, it may cause alarms that in trying to solve the  $\sim 2\sigma$  tension in  $S_8$  one has caused a  $\sim 3\sigma$  tension in  $\Omega_{\text{M}}$  which was previously not under any tensions. Ref. [321] do not find their results particularly alarming, since there could be many systematic or astrophysical effects, such as intrinsic alignments, which show up at such large multipoles using existing Stage-III survey data. Cosmic shear analyses using Stage-IV data, which were designed to probe these small-scales with as little systematic effects possible, on these small-scales will be the key to unravelling the  $S_8$  (and this  $\Omega_{\text{M}}$ ) tension.

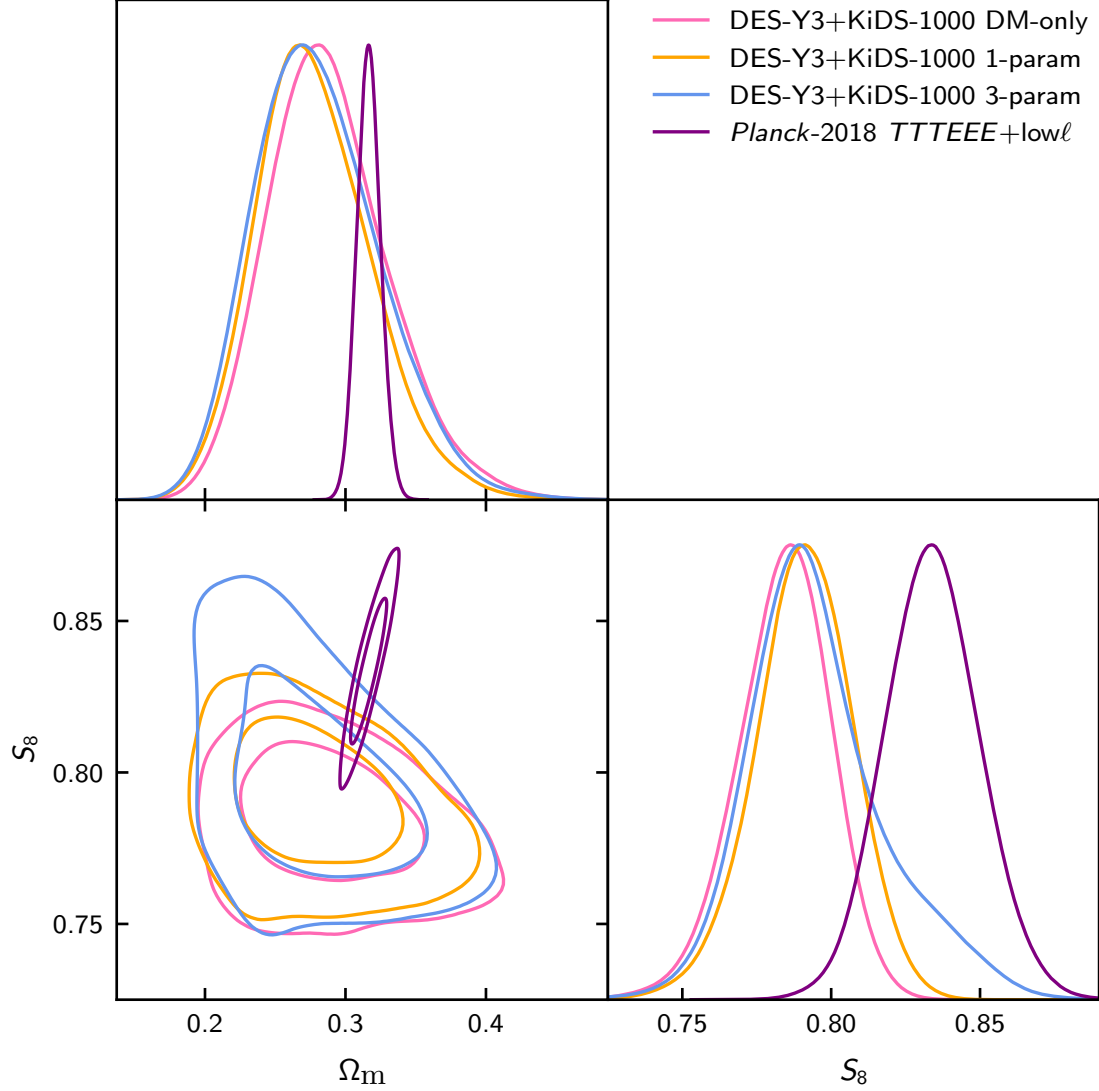


Figure 7.3: Triangle plot highlighting the distribution of the key cosmic shear statistics,  $\Omega_m$ ,  $\sigma_8$ , and  $S_8$ , for the DES-Y3+KiDS-1000 data-vector using three different models of baryonic feedback, with the *Planck* 2018 results present for comparison [325]. We see that the changing of the baryonic feedback model does have an impact on the distribution of the cosmological parameters, particularly for  $S_8$  – the most well constrained parameter using cosmic shear. We see that is a significant tail out to large  $S_8$  values when considering the three-parameter model, that isn’t present in either the zero- or one-parameter models. The exact values for the mean and  $1\sigma$  errors one-dimensional marginalised values are presented in Table 7.1.

Table 7.1: Results for the mean and  $1\sigma$  errors for the DES-Y3+KiDS-1000 analysis using three different models of baryonic feedback, along with results from *Planck* 2018 ‘TT,TE,EE+lowE’ [325] analysis for comparison. These values are in excellent agreement with the values presented in Ref. [320] for the DM-only and one-parameter models. We note that the mean of the  $S_8$  distributions systematically increases as we go from DM-only, to one- and then three-parameter models. Though these values are still within a  $1\sigma$  uncertainty of each other, the mean of  $S_8$  distributions shifts by larger than the stated  $0.3\sigma$  tolerance.

Survey & modelling	$S_8$	$\sigma_8$	$\Omega_M$
DES+KiDS DM-only	$0.784^{+0.016}_{-0.014}$	$0.807 \pm 0.065$	$0.288^{+0.036}_{-0.048}$
DES+KiDS 1-param	$0.791^{+0.017}_{-0.015}$	$0.828 \pm 0.068$	$0.278^{+0.035}_{-0.045}$
DES+KiDS 3-param	$0.797^{+0.017}_{-0.026}$	$0.830^{+0.067}_{-0.088}$	$0.281^{+0.037}_{-0.051}$
<i>Planck</i>	$0.834 \pm 0.016$	$0.8120 \pm 0.0073$	$0.3166 \pm 0.0084$

approaches might be insufficient for Stage-IV surveys, we can perform an investigation into just how insufficient these methods might be with future data-sets.

## 7.5.1 Stage-IV cosmic shear surveys

To properly understand if the DES-Y3 approach of determining scale cuts through Equation 7.1 is sufficient in the Stage-IV era, we can generate sets of scale cuts using an adapted version of this method and see how they compare between Stage-III and Stage-IV surveys. For comparison, we will use three mock surveys: DES-Y1-like, DES-Y3-like, and a *Euclid*-DR3-like (the final data release from the planned six-year survey) surveys. The properties of the cosmic shear surveys can be summarised into their total observed galaxy density,  $\bar{n}_{\text{gal}}$ , and their sky fraction observed,  $f_{\text{sky}}$ . The values for our three mock surveys are specified in Table 7.2. Of course, there are many more differences between Stage-III and Stage-IV surveys beyond these two summary statistics, such as the accuracy of the shear measurements, precision on the photometric redshift estimates of each galaxy, number of tomographic redshift bins used in an analysis, and the maximum redshift at which source galaxies have been observed to (changing the  $n(z)$  distributions). However, as  $\bar{n}_{\text{gal}}$  and  $f_{\text{sky}}$  directly feed into the data-space covariance matrix, changing their values have a direct effect on the impact of baryonic feedback in cosmic shear surveys. Thus, by just changing these two values, we can test the reaction of our scale cuts to different survey specifications.

Through having increased resolution detectors and higher sensitivity down to fainter magnitude detectors, Stage-IV surveys will observe many more galaxies than their Stage-III predecessors, thus increasing  $\bar{n}_{\text{gal}}$ . By being able to average many more galaxies ellipticities in each pixel, this decreases the contributions of shape noise in the power spectrum, thereby increasing the size of the signal-dominated region in  $\ell$ -space and allowing more information to be extracted from the power spectra.

By surveying more of the sky to produce a larger  $f_{\text{sky}}$ , more pairs of pixels can be included for each  $\ell$  mode. This decreases the  $\ell$ -space covariance matrix for every  $\ell$  mode. Thus, surveys with larger  $\bar{n}_{\text{gal}}$  and  $f_{\text{sky}}$  are able to meaningfully probe higher  $\ell$  modes and extract more information from every available  $\ell$  mode, thus are highly sensitive to baryonic physics.

Table 7.2 highlights just how large the increase in precision in the data that forthcoming

Table 7.2: Assumed survey specifications used in our analyses. We have condensed the properties of a Stage-III and Stage-IV survey into their total observed galaxy density,  $\bar{n}_{\text{gal}}$ , and the observed sky fraction,  $f_{\text{sky}}$ . All three surveys assume  $\sigma_{\epsilon} = 0.26$ .

Survey	Total $\bar{n}_{\text{gal}}$	Survey area [deg <sup>2</sup> ]	$f_{\text{sky}}$
DES-Year1	6	1,321	3.2%
DES-Year3	6	5,000	12.1%
<i>Euclid</i> -DR3	30	14,500	35.0%

Stage-IV surveys will have over existing Stage-III results. With a nearly order of magnitude increase in the galaxy density and a trebling of the sky area, Stage-IV surveys will both probe to higher  $\ell$  modes, and have them more tightly constrained than Stage-III. Hence, with this dramatic increase in the precision on the data, existing methods to mitigate baryonic feedback physics may not be sufficient, which is what we will explore now.

To simplify our analyses to a ‘proof-of-concept’ rather than a more rigorous detailed analysis, we restrict ourselves to three tomographic bins for both our Stage-III and Stage-IV mock surveys. This restricts the number of power spectra to six, and thus we only need to derive six scale cuts using our methods.

## 7.5.2 Extending the DES-Y3 approach to power spectra

The Dark Energy Survey chose to use the correlation functions ( $\xi_{\pm}^{ab}(\vartheta)$ ) as their cosmic shear summary statistic, which is a perfectly valid choice. However, it can be considered slightly more natural to work in the power spectrum ( $C_{\ell}^{ab}$ ), and thus we can formulate an equivalent equation to Equation 7.1 but now working in  $\ell$ -space. For a single bin<sup>4</sup> combination  $ab$ , this gives the  $\chi^2$  criterion as

$$\left(C_{\ell, \text{baryon}}^{ab} - C_{\ell, \text{base}}^{ab}\right) \mathbf{C}_{abab}^{-1} \left(C_{\ell, \text{baryon}}^{ab} - C_{\ell, \text{base}}^{ab}\right)^{\text{T}} \leq \frac{\chi_{\text{crit}}^2}{N}. \quad (7.8)$$

For our  $\ell$ -space covariance matrix, we assume the standard Gaussian form of

$$\text{Cov} \left[ C_{\ell}^{ab}, C_{\ell'}^{cd} \right] = \frac{\delta_{\ell\ell'}}{(2\ell+1) f_{\text{sky}}} \left( C_{\ell}^{ac} C_{\ell}^{bd} + C_{\ell}^{ad} C_{\ell}^{bc} \right), \quad (7.9)$$

where we can now directly see how a larger value of  $f_{\text{sky}}$  reduces the covariance between  $\ell$ -modes. Note that the  $C_{\ell}$  values in Equation 7.9 refer to the *total* power spectrum, that of the cosmological signal plus noise,

$$C_{\ell}^{ab} = C_{\ell, \text{signal}}^{ab} + N_{\ell}^{ab}. \quad (7.10)$$

Here,  $N_{\ell}^{ab}$  is the noise power spectrum in bin  $ab$  and is given by

$$N_{\ell}^{ab} = \frac{\sigma_{\epsilon}^2}{\bar{n}} \delta_{ab}, \quad (7.11)$$

where  $\bar{n}$  is the average surface galaxy density of that bin, and the Kronecker- $\delta$  ensures that only auto-spectra contain shape noise. Thus, observing more galaxies which, in turn, increases  $\bar{n}$  and decreases the amplitude of the noise spectra. We use  $\chi_{\text{crit}}^2 = 1.5$  which gives a per-bin value of  $\chi_{\text{crit}}^2 = 0.25$  in all analyses. This was chosen through an iterative scheme where a range of  $\chi_{\text{crit}}^2$  values were trialled and the resulting scale cuts and parameter contours were compared against each other. Note that this is a factor of three

<sup>4</sup>Give me a bin, Vasili. One bin only, please — Captain Ramius.

larger than the value of  $\chi_{\text{crit}}^2 = 0.5$  as used in the DES-Y3 analysis, which is a result of us using simplified survey configurations and a simplified covariance matrix.

Note that we also use the same value of  $\chi_{\text{crit}}^2$  for all surveys in our analyses, since we have assumed that the mapping between  $\chi^2$  and parameter biases are independent on the survey specification. For a realistic analysis, it may be more appropriate to determine the value of  $\chi_{\text{crit}}^2$  which lead to acceptable levels of bias on a per-survey basis. It would be worth investigating how survey specifications change the  $\chi^2$  to parameter biases mapping, especially since a survey such as *Euclid* will go from a DR1, to DR2, and finally a DR3 analysis and so the allowable  $\chi_{\text{crit}}^2$  value may well change between data releases.

### 7.5.3 Scale cuts

With our  $\chi^2$  criterion in  $\ell$ -space constructed, we can apply it for our mock DES-Y1, DES-Y3, and *Euclid*-DR3 surveys and explore how the scale-cuts behave for our surveys. To do so, we need to generate sets of  $C_{\ell,\text{base}}^{ab}$  and  $C_{\ell,\text{baryon}}^{ab}$ . For the base data-vector, this is simple as we can use the dark-matter-only *mead2020* model as part of HMCODE-2020. For the baryon contaminated data-vector, DES-Y3 used the Overwhelmingly Large Simulations (OWLS) [123, 326] which, they claim, features an ‘extreme’ implementation of baryonic feedback compared to other hydrodynamical simulations in the literature. However, since its release in 2011, there have been numerous other releases of hydrodynamical simulations which claim that they feature more realistic implementations of baryonic feedback<sup>5</sup>. For our baryonic contaminated data-vectors, we use an ensemble of five hydro-sims: BAHAMAS, HORIZON-AGN, ILLUSTRIS, ILLUSTRIS-TNG, and EAGLE. Thus, when we compute Equation 7.8, we average over our five hydro-sims to compute an average  $\chi^2$  value which can be compared against our critical value  $\chi_{\text{crit}}^2$ .

We are motivated to average over an ensemble of hydrodynamical simulations, which brings added numerical complexity and increased run-times, since each hydro-sim has its own baryonic feedback profile (see Figure 6.1) and so have different errors for each  $\ell$ -mode and redshift bin pair. Hence, one hydro-sim could produce large errors on intermediate  $\ell$  modes, while fitting the high- $\ell$  region successfully while another hydro-sim features the opposite. Thus, if we are to adequately derive scale cuts which successfully mitigate baryonic feedback, then we wish to include information from all available hydro-sims. Note that we average here instead of taking the maximum since the average is more numerically stable when repeatedly fitting our models to the data. We again take an agnostic approach to the hydro-sims and provide each simulation with an equal weight in the average.

The results for our six bin-dependent scale cuts using the  $\chi^2$  method mitigating against all baryonic feedback for our three mock surveys are presented in Table 7.3. Here, we see that the higher signal-to-noise of the higher redshift bins act to decrease the allowable  $\ell_{\text{MAX}}$  for the given  $\chi_{\text{crit}}^2$  value. We also see that, due to the inclusion of shape noise in the auto-spectra only, these auto-spectra generally have higher allowable  $\ell_{\text{MAX}}$  values over their comparable cross-spectra. We also see the dramatic impact that the larger  $\bar{n}_{\text{gal}}$  and  $f_{\text{sky}}$  values of our *Euclid*-DR3-like survey has on our derived scale cuts. Not even being able to reach an  $\ell_{\text{MAX}}$  of one hundred for various bins before the impact of baryon feedback becomes significant shows that extremely aggressive scale cuts are needed if we were to eliminate all baryonic feedback from our Stage-IV data-vectors.

<sup>5</sup>Generally, the matter power spectrum is of little importance to the benchmarking (and thus determination of what ‘realistic’ means) since thus far there has been little constraint on the shape and amplitude of baryonic feedback in the matter power spectrum (hopefully Stage-IV surveys will change this!). Hence, the use of other physical observables which are much better constrained have driven the development of the hydro-sims which aim to match these observables to ever increasing accuracy. Examples include the galaxy stellar mass function, the hot gas fraction within haloes, and the star formation rate [135, 309].

Table 7.3: Results for our scale cuts (that is the maximum possible  $\ell$  multipole that satisfies the criterion) using the DES-Y3 ( $\chi^2$ , no baryons) approach for our three mock surveys. We clearly see the increase in sky areas serves to decrease the allowable  $\ell_{\text{MAX}}$  from DES-Y1 to DES-Y3, and then the dramatic decrease the  $\ell_{\text{MAX}}$ ’s our *Euclid*-like survey. This also clearly shows the decrease in the  $\ell_{\text{MAX}}$  as we go to higher redshift bins, and the impact of shape noise on the auto-spectra. An  $\ell_{\text{MAX}}$  of 50 was the lower bound of the optimisation.

Bin	DES-Y1	DES-Y3	<i>Euclid</i> -DR3
$1 \times 1$	5000	870	226
$1 \times 2$	898	408	80
$1 \times 3$	888	440	124
$2 \times 2$	851	390	91
$2 \times 3$	506	183	73
$3 \times 3$	695	319	122

### 7.5.4 Illustration of data-loss from aggressive scale-cuts

To illustrate how much cosmological information is lost from the extremely aggressive scale cuts for our *Euclid*-DR3-like survey, presented in Table 7.3, we can perform a simple Monte Carlo Markov chain (MCMC) analysis. Using a fiducial noise-free uncontaminated data-vector, we can obtain cosmological parameter contours from our DES-Y3-like and *Euclid*-DR3-like surveys using both no cuts (all scales down to  $\ell_{\text{MAX}} = 5000$  for all bins), and the  $\chi^2$  cuts from Table 7.3. This is shown in Figure 7.4, plotting the two-dimensional contours for  $\Omega_{\text{M}}\text{-}\sigma_8$  and  $\Omega_{\text{M}}\text{-}S_8$ .

Here, we see that our scale cuts dramatically reduce the amount of cosmological information from our data-vectors, as shown by the increased size of the contours with respect to the no-cut curves. It is interesting to see that the one-dimensional distribution of  $S_8$  when we impose the  $\chi^2$ -derived scale cuts is extremely similar between our DES-Y3 and *Euclid*-like surveys. This suggests that, since  $S_8$  is the most well constrained parameter and is essentially the amplitude of the lensing signal [177], the  $\chi^2$  cuts are indirectly placing limits on  $S_8$ . Hence, if we are to use Stage-IV surveys to probe the  $S_8$  tension, then we need to come up with alternate scale cut strategies to optimise our  $S_8$  distributions.

### 7.5.5 Verifying the scale cuts

Table 7.3 presents the sets of scale cuts for our three mock surveys that aimed to eliminate any baryonic contamination from the data-vectors. But how can we be sure that these scale cuts effectively eliminate baryonic feedback? To do so, we can use one of our hydrodynamical simulations’ data-vector that features a large amplitude of baryonic feedback, and repeat the same exercise of Figure 7.4 where we aim to recover cosmological parameter contours from our now contaminated data-vector. Since we are using a dark-matter-only matter power spectrum in our analysis, we *expect* that our results will be biased away from the ground truth unless we have adequately mitigated against baryonic physics through our scale cuts. Hence, this is a good test of the method.

Figure 7.5 presents the two-dimensional  $\Omega_{\text{M}}\text{-}\sigma_8$  and  $\Omega_{\text{M}}\text{-}S_8$  contours using the same scale cuts and methods as Figure 7.4, but now using the EAGLE hydrodynamical simulation as the ground truth. Here, we see that when we apply our scale cuts, even using a dark-matter-only matter power spectrum we correctly recover the ground truth cosmological parameters. This shows that our  $\chi^2$  cuts did effectively remove enough scales to not be impacted by baryonic physics in this situation. For comparison, we plot contours for our DES-Y3 and *Euclid*-DR3 surveys without scale cuts, both of which we expect biases in

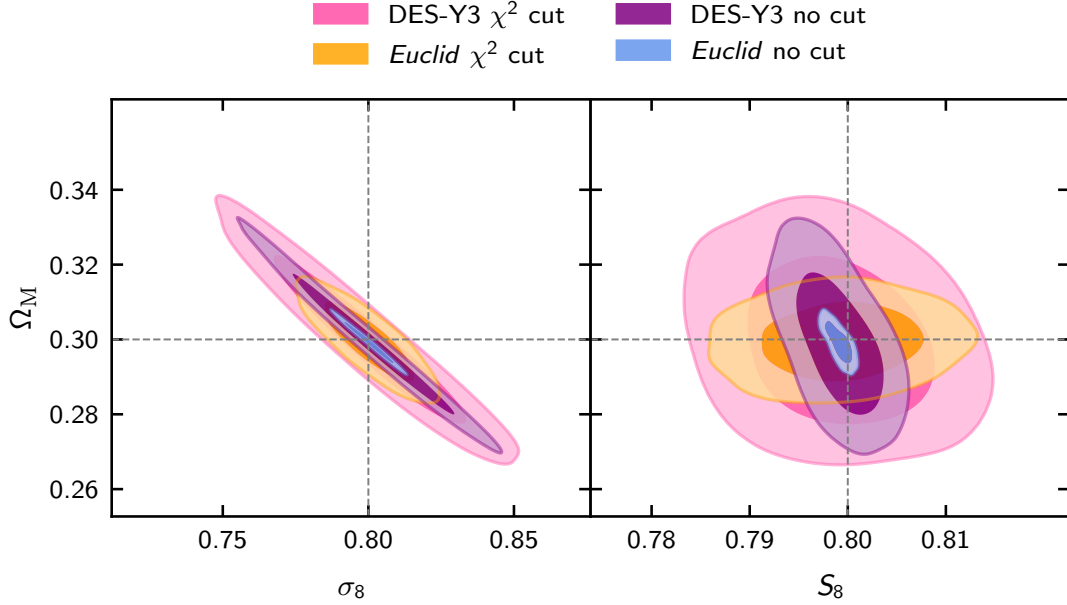


Figure 7.4: Two-dimensional  $\Omega_M$ - $\sigma_8$  and  $\Omega_M$ - $S_8$  contours for our DES-Y3-like and *Euclid*-DR3-like surveys using the  $\chi^2$  derived scale cuts (pink and orange) and no scale cuts (taking a maximum multipole of  $\ell_{\text{MAX}} = 5000$  for all bins, in purple and blue) for comparison. *Left panel:* For our DES-Y3 survey, we see imposing scale cuts derived from the  $\chi^2$  method does not significantly effect the one-dimensional parameter constraints on either  $\Omega_M$  or  $\sigma_8$ . However, it drastically reduces the width of the  $\Omega_M$ - $\sigma_8$  degeneracy, which is probed by  $S_8$ . For our *Euclid*-DR3-like survey, even with aggressively small scale cuts, we still see improvements in  $\Omega_M$  and  $\sigma_8$  over the DES-Y3 results. *Right panel:* Plotting  $S_8$ , which characterises the width of the  $\Omega_M$ - $\sigma_8$  degeneracy, we now see that when we impose the  $\chi^2$  criterion for the scale cuts, this acts to optimise the  $S_8$  distribution regardless of survey specifications. Hence, even with dramatically improved quality of data from future Stage-IV surveys, our  $S_8$  constraints would be no better off than our existing Stage-III results when imposing no baryonic feedback in the data-vector. Since a key goal of Stage-IV experiments is to probe the  $S_8$  tension, having an  $S_8$  distribution no tighter than DES-Y3 would be a disappointing outcome.



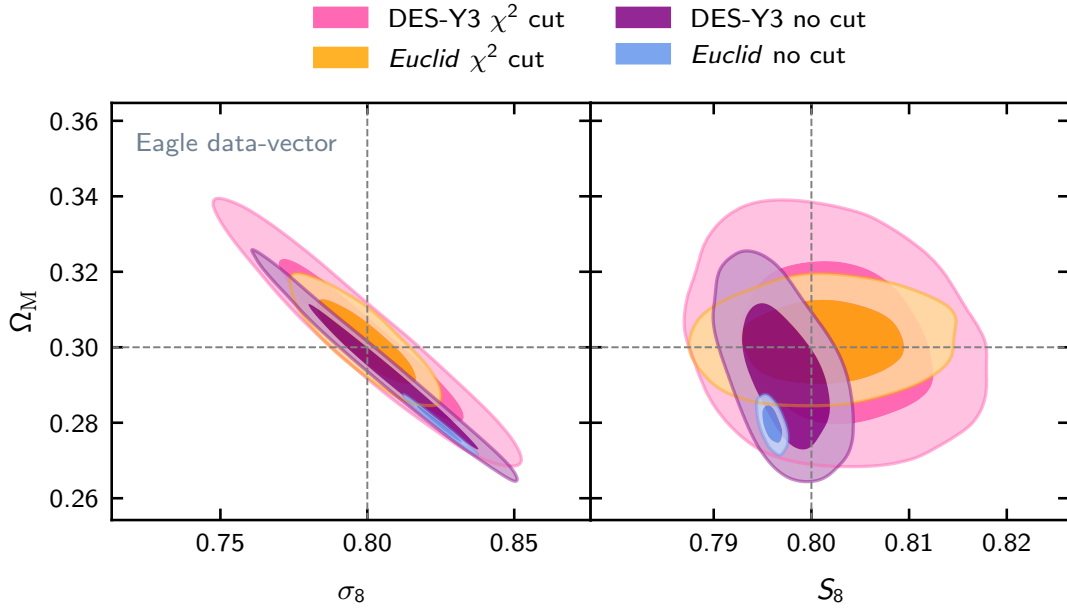


Figure 7.5: Two-dimensional  $\Omega_{\text{M}}\text{-}\sigma_8$  and  $\Omega_{\text{M}}\text{-}S_8$  contours for our DES-Y3-like and *Euclid*-DR3-like surveys using  $\chi^2$ -derived and no scale cuts, using the EAGLE hydro-sim featuring baryonic feedback as the ground truth, and recovered using a dark-matter-only model. We see that without scale cuts, our two surveys are highly biased, which is to be expected when a dark-matter-only model is used. When we impose our scale cuts to eliminate baryonic feedback from our data-vector, we find that our contours are centred correctly, albeit with extremely compromised precision on  $\Omega_{\text{M}}$ ,  $\sigma_8$ , and  $S_8$ .

due to our dark-matter-only modelling. We see that the DES-Y3 results are biased at the level of around  $1\sigma$ , whereas the results for our *Euclid*-like survey are extremely biased at  $>5\sigma$ .

Hence, the balancing act becomes one of trying to preserve as much information as possible to extract as much cosmological information from the data vectors as possible without becoming susceptible to biases from baryonic physics.

### 7.5.6 Comparing to a $k$ -space cut

It is interesting to note that Table 7.3 shows that as we increase the mean redshift of each spectra, the allowable  $\ell_{\text{MAX}}$  decreases. This is in contrast to other previous analyses for cosmic shear scale cuts which were motivated by a cut in wavenumber-space ( $k$ -cuts), for example the DES-Y1 approach [314].

$k$ -cuts are often motivated by the desire to eliminate physical scales that feature baryonic feedback in the matter power spectrum from our cosmic shear summary statistics. When looking at the Limber integral for the  $C_\ell$  values using the matter power spectrum, of

$$C_\ell^{ab} = \frac{9\Omega_M^2 H_0^4}{4} \int_0^{\chi_h} d\chi \frac{g_a(\chi) g_b(\chi)}{a^2(\chi)} P_\delta \left( k = \frac{\ell}{\chi}, z = z(\chi) \right), \quad (7.12)$$

we see that for fixed wavenumber  $k$ , larger comoving distances (as is the case for higher redshift bins) produces larger angular multipole values. Thus, if one chooses a naïve scale cut in  $k$ -space only, then one would find that for fixed  $k_{\text{MAX}}$  higher redshift bins give larger allowable multipoles  $\ell_{\text{MAX}}$  – which is opposite of the results from using the  $\chi^2$  method. While it is true that for fixed a  $\ell$  mode, the corresponding wavenumber values are smaller for higher redshift bins (shown in Figure 7.6), which would indicate that baryonic physics plays a smaller role in the  $C_\ell$  values, the dramatic increase in signal-to-noise of these higher redshifts bins places tighter constraints on the allowable errors than for low redshift bins.

## 7.6 Extending the $\chi^2$ method

It is clear that if we were to continue to apply the DES-Y3 approach of reducing impact of baryonic feedback on our data-vectors to acceptable levels, then headline constraints from forthcoming Stage-IV surveys would only be marginally better than existing Stage-III surveys – despite the overwhelmingly large increase in the precision on the data. Hence, we must come up with alternative methods, or adaptations of existing methods, if we are to truly unleash the constraining power of Stage-IV surveys. The major limitation with the DES-Y3 approach is that we compare the hydrodynamical simulations with dark-matter-only models. This naturally results in harsh scale cuts from the poor modelling. While modelling baryonic feedback is inherently a difficult process, we do have many existing models in the literature – each with their own error profiles. Thus, we can extend the DES-Y3 approach by now taking the difference between the hydro-sims and the results from baryonic feedback models. By taking the same approach of computing the average  $\chi^2$  to our ensemble of hydro-sims, we can now derive sets of physically motivated binary scale cuts for each baryonic feedback model for each mock survey.

### 7.6.1 Fitting baryonic feedback models to hydro-sims

Now that we are using models of baryonic feedback, our  $\chi^2$  criterion becomes

$$\left( C_{\ell, \text{baryon}}^{ab} - C_{\ell, \text{model}}^{ab} \right) \mathbf{C}_{abab}^{-1} \left( C_{\ell, \text{baryon}}^{ab} - C_{\ell, \text{model}}^{ab} \right)^T \leq \frac{\chi_{\text{crit}}^2}{N}, \quad (7.13)$$

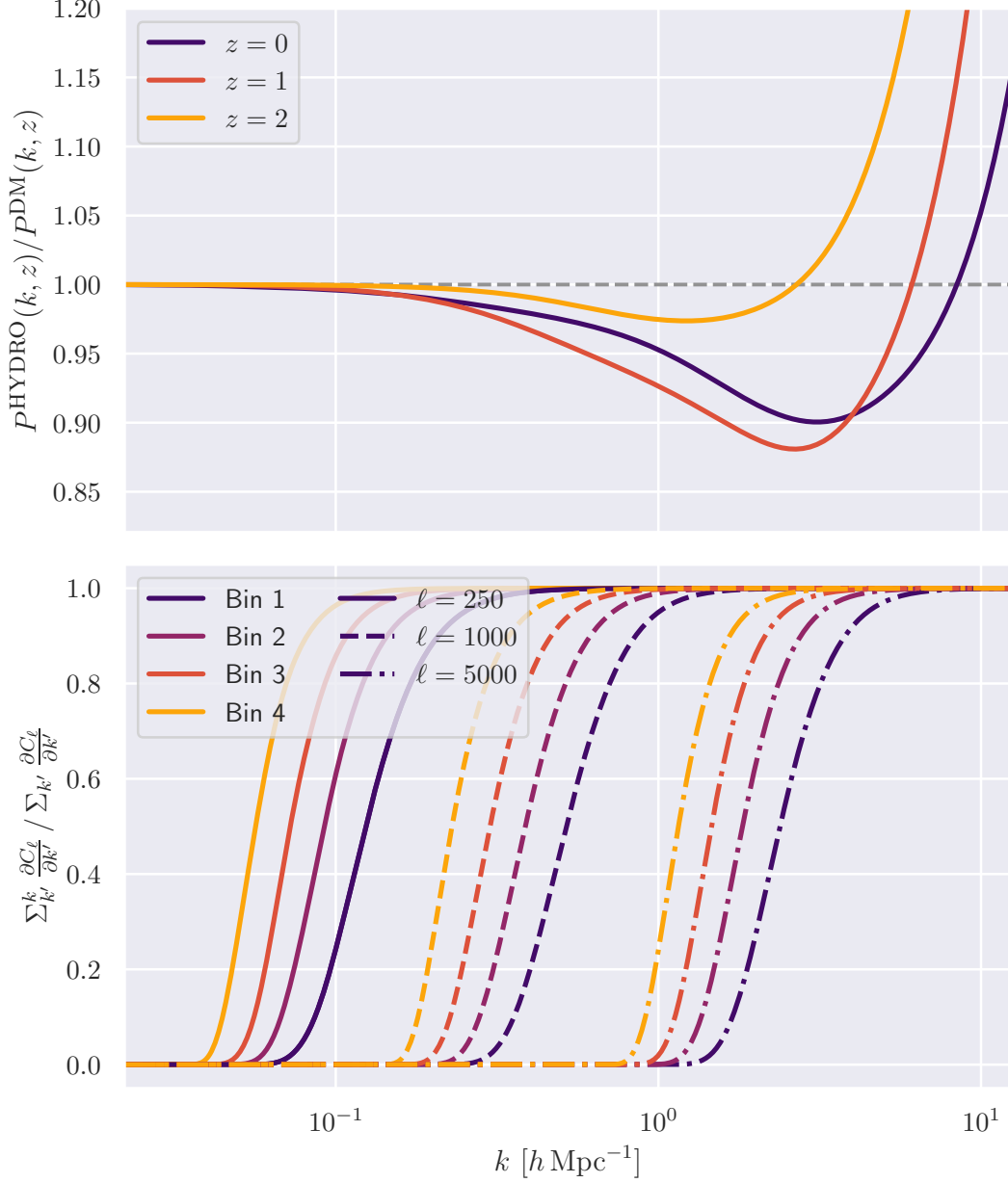


Figure 7.6: *Top panel*: Ratio of the matter power spectrum with baryonic feedback in to the dark-matter-only power spectrum as a function of wavenumber  $k$  for three fixed redshifts  $z = 0, 1, 2$ . We see that baryonic feedback is highly redshift dependent, and so a simple redshift-independent cut in  $k$ -space is insufficient to accurately model it. *Bottom panel*: Normalised cumulative sum of the derivative of the  $C_\ell$  values with respect to  $k$  for four different Gaussian redshift bins with centres  $\bar{z} = \{0.33, 0.66, 1.00, 1.50\}$  and for three fixed  $\ell$  values. We see that for fixed  $\ell$ , the higher redshift bins have contributions from smaller  $k$  values, which would indicate that these bins have less contributions from baryonic feedback, however the top panel shows that baryonic feedback is highly redshift dependent and so this relation isn't as simple.

where  $C_{\ell, \text{model}}^{ab}$  are the  $C_\ell$  values using a particular model. The question now becomes how to find these model  $C_\ell$  values for a given hydro-sim, which gives us the error in these values to be used in our  $\chi^2$  criterion. To do so, we used a maximum-likelihood optimiser to find the best-fitting  $C_\ell$  values for a given model. The baryonic parameters, along with cosmological parameters  $A_s$  and  $\Omega_c$ , were varied by the optimiser to find the best-fit values.

Since we are now fitting our models to the hydro-sims, it is important to note that these fits become  $\ell_{\text{MAX}}$  dependent. This is because, for an insufficient model of baryonic feedback, the optimiser has to sacrifice accuracy at lower multipoles when trying to fit down to higher multipoles (since those have a larger signal-to-noise than larger angular scales) to optimise the maximisation of the global likelihood. This problem is illustrated in Figure 7.7, which plots the ratio of the best-fitting  $C_\ell$  values for our one-parameter and three-parameter models against the ground-truth values for the ILLUSTRIS-TNG hydro-dynamical simulation, for three values of  $\ell_{\text{MAX}}$ . We see that for an  $\ell_{\text{MAX}}$  of 250, there is very little baryonic contamination within our data-vectors, and so achieve greater than percent-level accuracy with our fits for both baryonic feedback models. When we extend down to an  $\ell_{\text{MAX}}$  of 2000 and then 5000, we significantly increase the effects of baryonic contamination within our data-vectors, and so become sensitive to the accuracy of our chosen model of baryonic feedback. In order to optimise the global likelihood, which is weighted towards larger  $\ell$  values from their higher signal-to-noise, the optimiser prefers to alter the values of  $A_s$  and  $\Omega_c$  such that a better fit at high  $\ell$  can be obtained at the expense of low  $\ell$  accuracy. This problem becomes particularly acute for the one-parameter model at an  $\ell_{\text{MAX}}$  of 5000, since the model simply does not fit the data well.

It should be noted that for very high  $\ell$  multipoles, shape noise dominates the covariance matrix and so the contribution to the  $\chi^2$  from these modes is reduced. Hence, the model can have excursions out to very large relative amplitudes without changing the  $\chi^2$  by significant amounts.

We refer the reader back to Sections 2.6.3 and 6.3.4, and Table 6.2 for an introduction, discussion, and reminder about the relevant astrophysical baryonic feedback parameters that feature in the HMCode-2020 model. We also refer back to Table 6.1 presenting the specifications of the hydrodynamical simulations chosen in this work.

It is clear looking at Figure 7.7 that if we were one to go about computing a  $\chi^2$  for an  $\ell_{\text{MAX}}$  of 250 for all three fits, then one would arrive at three very different values. Hence, when we wish to go about obtaining an estimate for  $(C_{\ell, \text{baryon}}^{ab} - C_{\ell, \text{model}}^{ab})$  in our determination of the scale cuts (Equation 7.13) then this itself is an  $\ell_{\text{MAX}}$  dependent quantity. This dependence should be accounted for when optimising the scale cuts using any criterion.

To be explicit, the steps that we used to obtain scale cuts using our modified  $\chi^2$  method were as follows:

- On a grid ranging from  $\ell_{\text{MAX}} = 150$  to  $\ell_{\text{MAX}} = 5000$  with  $\ell = 25$  spacing, fit the one- and three-parameter HMCode to each of the five hydro-sims in our ensemble. We use  $A_s$  and  $\Omega_m$  along with the baryonic parameters as the free-parameters in the fit. For the angular power spectrum and its covariance matrix, we use five linearly-spaced bins from  $\ell = 2$  to  $\ell = 100$ , and then twenty logarithmically-spaced bins from  $\ell = 101$  to  $\ell = \ell_{\text{MAX}}$ . We use Equation 3.96 to determine the  $\ell$ -space covariance matrix, which is used in the optimisation of the Gaussian likelihood.
- With the fits to the hydro-sims obtained, we can go about evaluating the  $\chi^2$  criterion to determine the scale cuts for each bin pair  $ab$ . Since we are only performing a one-dimensional optimisation, the **GridMax** sampler worked well for our use-case.
- For each  $\ell_{\text{MAX}}$  considered by the **GridMax** sampler, we round up to the nearest multiple of 25, which allows us to load in the previously calculated best-fits of each hydro-sim.

Table 7.4: Results for our scale cuts using our ‘modified  $\chi^2$ ’ approach for our two mock surveys and two baryonic feedback models. We again see that the increased precision going from our mock DES-Y3 to mock *Euclid*-DR3 survey lowers the allowable maximum multipole across the bin ranges. We also see that the increased flexibility of the three-parameter model over the one-parameter model reduces errors in the  $C_\ell$  fits, and thus increases the maximum multipole for a given error budget. Though we still see extremely low values of  $\ell_{\text{MAX}}$  in the  $2 \times 3$  bins as a result of using the  $\chi^2$  criterion for our *Euclid*-like survey.

Bin	DES-Y3 1-param	<i>Euclid</i> 1-param	DES-Y3 3-param	<i>Euclid</i> 3-param
$1 \times 1$	5000	5000	5000	5000
$1 \times 2$	2897	923	5000	2897
$1 \times 3$	4497	1501	5000	4497
$2 \times 2$	4798	485	5000	531
$2 \times 3$	3703	200	4892	210
$3 \times 3$	4892	337	5000	489

We then take the *ab* sub-block of the data vector for each hydro-sim and the *abab* sub-block of the inverse covariance matrix calculated for the given  $\ell_{\text{MAX}}$  to compute the  $\chi^2$  for each hydro-sim. We then take the maximum  $\chi^2$  value from the set of hydro-sims, which is then compared against  $\chi_{\text{crit}}^2$  to form our likelihood.

- The **GridMax** sampler then optimises the maximum multipole such that the likelihood, and thus criterion, is maximised.

## 7.6.2 Results for our modified $\chi^2$ method

With our best-fit analysis performed using our two baryon feedback models on our suite of hydrodynamical simulations, we can use our ‘modified  $\chi^2$ ’ criterion to determine scale cuts. These are shown in Table 7.4. We see the general trends that emerged in the no-baryons case continue for the case where baryonic feedback is included in the theoretical models: that the extra constraining power of *Euclid* over DES results in much lower scale cuts across the board, which can be partially mitigated by using a three-parameter model over a single-parameter model.

Therefore, using our set of derived scale cuts, we now want to see what impact these have on the mitigation of baryonic feedback using contaminated data-vectors.

### MCMC results using scale cuts

To obtain estimates of how our cosmic shear analyses react to the scale cuts imposed in Table 7.4, we can repeat our MCMC analyses where we use various hydrodynamical simulations as the input power spectra, and investigate the associated biases in cosmological parameters from them. Figure 7.8 plots the 2D parameter contours using our modified  $\chi^2$  method for the BAHAMAS hydro-sim as the ground truth, with Figure 7.9 using EAGLE as the ground truth.

In these figures, we see that through using a baryonic feedback method and deriving scale cuts using these methods, we arrive at results that allow our *Euclid*-like survey to harness its increased statistical power over our DES-Y3-like survey to better constrain all three cosmological parameters (which was not true for the no-baryons case). This certainly gives some reassurances behind the motivation for Stage-IV surveys! Secondly, Table 7.4 showed that the scale cuts from our three-parameter model allowed the probing

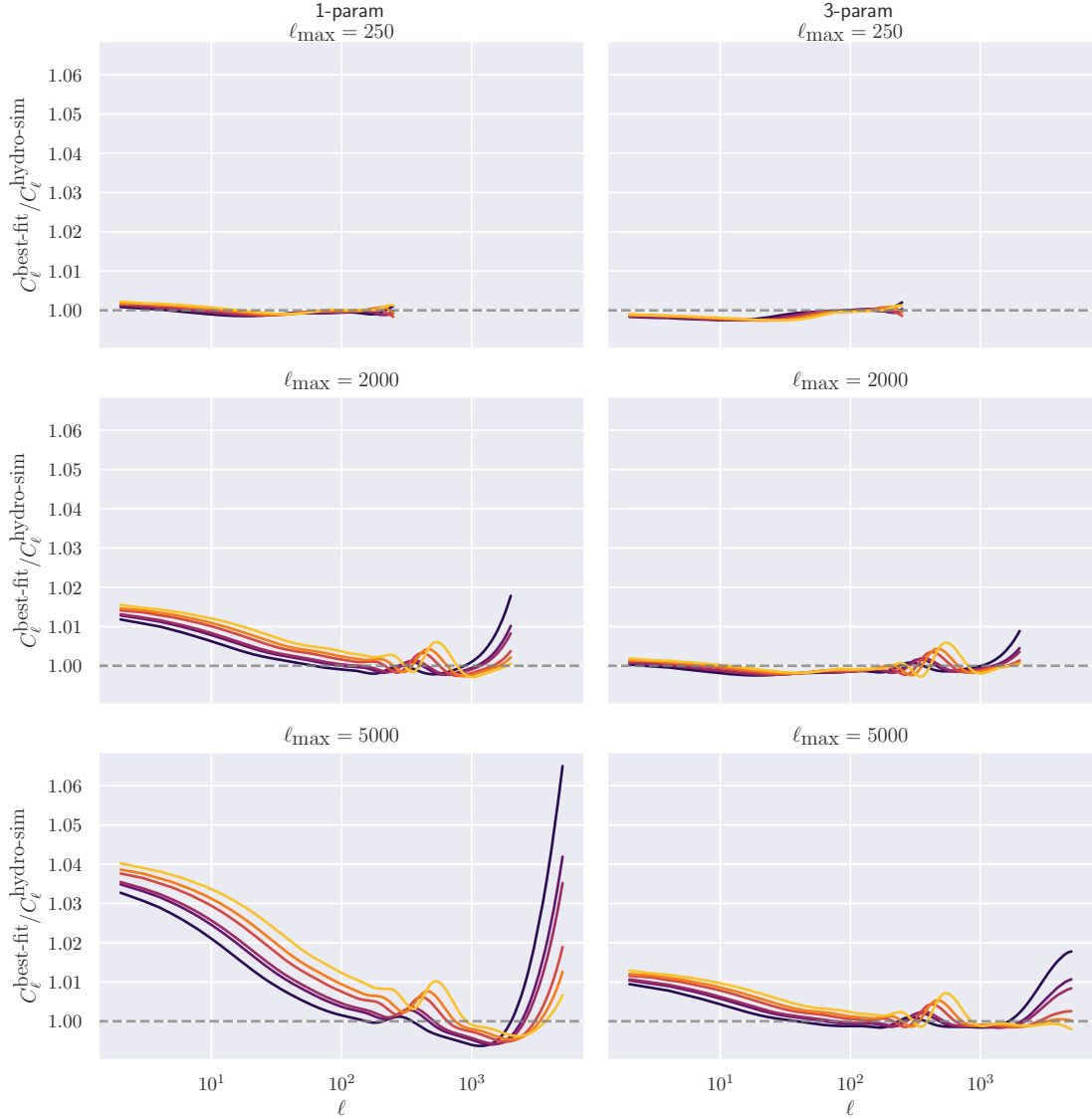


Figure 7.7: Plot of the ratio of the best-fitting  $C_\ell$  values of our one- and three-parameter models to that of the baryonic feedback from the ILLUSTRIS-TNG hydrodynamical simulation. We see that when limiting the fit to an  $\ell_{\text{MAX}}$  of 250, the errors are much less than 1% across the entire  $\ell$  range. However, when we extend the fit down to an  $\ell_{\text{MAX}}$  of 2000 and then 5000, these previously well-fitted values now have significantly larger errors in the fit, since the optimiser is optimising the global likelihood that sacrifices the fit of low  $\ell$  values. The curves are coloured to approximate their redshift, with the lighter yellow curves for higher redshift bins. We see that at high  $\ell$ , where the signal-to-noise is largest, the higher redshift bins tend to have a better fit than for lower redshift bins, owing to the larger signal-to-noise of these higher redshift bins. This also shows how the more flexible three-parameter model produces significantly better fits when baryonic feedback becomes important at  $\ell_{\text{MAX}}$ 's of 2000 and 5000. Thus, when determining  $(\vec{C}_\ell^{\text{truth}} - \vec{C}_\ell^{\text{model}})$ , this is an  $\ell_{\text{MAX}}$  dependent quantify.

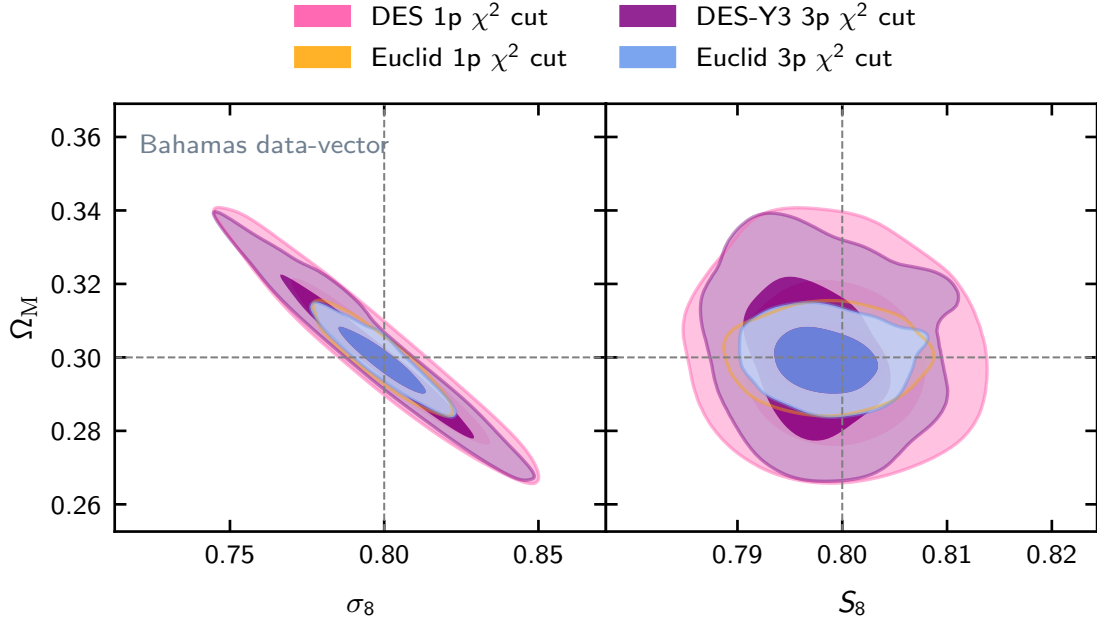


Figure 7.8: Two-dimensional  $\Omega_M$ - $\sigma_8$  and  $\Omega_M$ - $S_8$  contours for our DES-Y3-like and *Euclid*-DR3-like surveys using the  $\chi^2$  with a baryonic feedback model derived scale cuts for the BAHAMAS hydro-sim as input. First, we see that there is no baryonic feedback bias present in any of the analyses presented (though that is to be expected from the BAHAMAS hydro-sim since the one-parameter HMCode model was explicitly trained on BAHAMAS only). Secondly, we see that the increased constraining power of *Euclid* over DES-Y3 can be utilised to further constrain  $S_8$  over what our mock DES-Y3 can achieve. Thirdly, we see that the more relaxed scale cuts from using the three-parameter over the one-parameter model allow us to extract more information from our data vectors (the purple and blue contours being smaller than their pink and yellow counterparts) without inducing biases for the BAHAMAS data-vector.

of higher-order multipoles than those allowed from the one-parameter model. While these new multipoles should bring additional constraining power, this is somewhat mitigated by sampling over two additional nuisance parameters. However, what we see in Figures 7.8 and 7.9 is that there is a net decrease in the parameter’s covariance for both hydro-sims when going from one to three parameters. This provides strong motivation for us to use more general models of baryonic feedback which allow us to probe smaller-scales than simpler models, even if this comes at the expense of additional nuisance parameters that need marginalising over. The extra information from accessing the higher-order multipoles more than compensates for the additional parameters.

## 7.7 Scale cuts in parameter-space

As we have described, the  $\chi^2$  values operate in data-space. Whilst this is a natural choice, especially since it does not require any transformations of our data-vector or its covariance matrix, it may not properly reflect the biases in cosmological constraints that these data-vectors are used to obtain. Thus, we wish to transform these quantities into parameter-space to obtain more physical scale cuts.



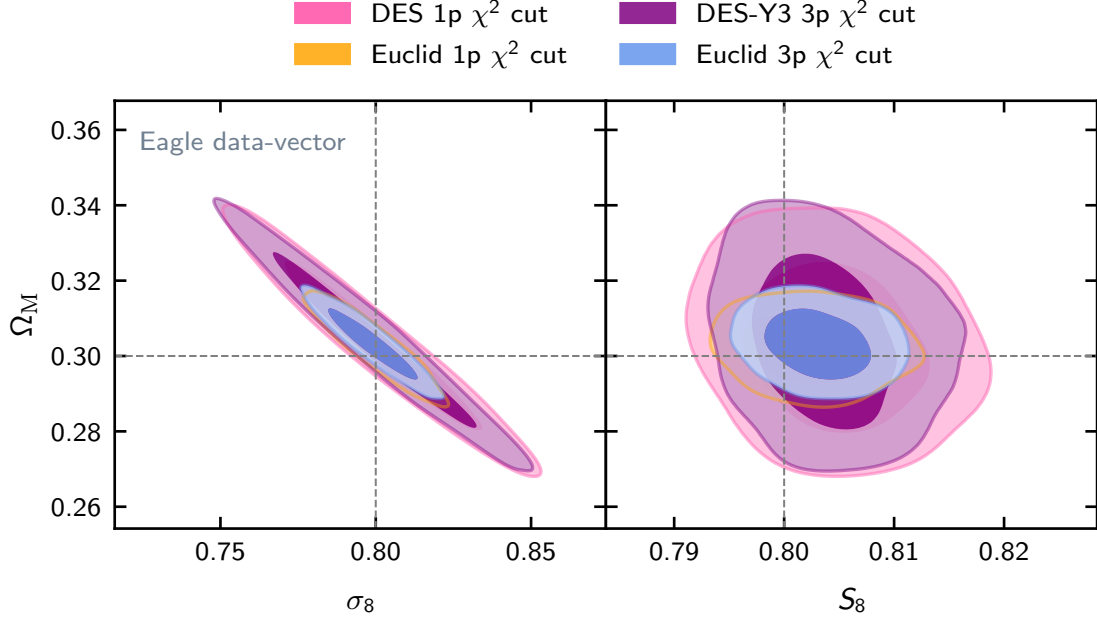


Figure 7.9: Two-dimensional  $\Omega_M$ - $\sigma_8$  and  $\Omega_M$ - $S_8$  contours for our DES-Y3-like and *Euclid*-DR3-like surveys using the  $\chi^2$  with a baryonic feedback model derived scale cuts for the EAGLE hydro-sim as input. As EAGLE features more significant baryonic feedback over BAHAMAS, it provides a good testing ground for our scale cuts methods. What we see is broadly similar to the results for BAHAMAS presented in Figure 7.8: we are now able to take advantage of the additional information in the *Euclid* covariance with smaller parameter constraints for all three cosmological parameters; and that the three-parameter model can still deliver unbiased results with smaller parameter covariances over the one-parameter model. This is because, while the three-parameter model can access higher-order multipoles, the increase in constraining power is somewhat counteracted by the two additional nuisance parameters that need marginalising over to present these cosmological contours.

### 7.7.1 The Fisher matrix and figures of merit & bias

The two quantities that we are interested in are the figure of merit (FoM) and the figure of bias (FoB). Both of these are derived from the Fisher matrix,  $\mathbf{F}_{\alpha\beta}$ , defined as [157]

$$\mathbf{F}_{\alpha\beta} = \frac{\partial \vec{C}_\ell}{\partial \vartheta_\alpha} \mathbf{C}^{-1} \frac{\partial \vec{C}_\ell}{\partial \vartheta_\beta}. \quad (7.14)$$

Thus, the Fisher matrix encodes both the covariance of our underlying data-vector, and the response of our data-vector to the parameters that we are interested in constraining through our analyses. From the Fisher matrix, we can construct the figure of merit, which encodes how well our parameters are constrained, with larger values giving increased constraining power. To calculate the constraining power of two specific parameters  $\alpha$  &  $\beta$ , we need to use the marginalised Fisher matrix  $\tilde{\mathbf{F}}_{\alpha\beta}$ , which is computed by inverting the full Fisher matrix, isolating the rows and columns that correspond to our parameters only, and then re-inverting the matrix. This gives our figure of merit as

$$\text{FoM}_{\alpha\beta} = \sqrt{\det [\tilde{\mathbf{F}}_{\alpha\beta}]}. \quad (7.15)$$

From our Fisher matrix, we can also compute the figure of bias, which encodes how a mis-specification in the data-vector can lead to biases in the cosmological parameters.

Table 7.5: Values of  $\Delta\chi^2 / \text{FoB}^2$  as a function of confidence level and degrees of freedom, taken from Ref. [327]. These can be calculated from the inverse cumulative distribution function of the  $\chi^2$  distribution.

$\sigma$ offset	$p$	$\nu = 1$	$\nu = 2$	$\nu = 4$
$1\sigma$	68.3 %	1.00	2.30	4.72
$2\sigma$	95.4 %	4.00	6.17	9.70
$3\sigma$	99.7 %	9.00	11.8	16.3

The bias on parameter  $\vartheta_\alpha$ ,  $\delta\vartheta_\alpha$ , is given by [198]

$$\delta\vartheta_\alpha = [\mathbf{F}^{-1}]_{\alpha\beta} \left( \vec{C}_\ell^{\text{true}} - \vec{C}_\ell^{\text{model}} \right) \mathbf{C}^{-1} \frac{\partial \vec{C}_\ell}{\partial \vartheta_\beta}, \quad (7.16)$$

where  $\vec{C}_\ell^{\text{true}}$  is the underlying data-vector that we wish to fit our model to, and  $\vec{C}_\ell^{\text{model}}$  is the resulting best-fit data-vector using our model. The figure of bias can then be computed from the combination of individual parameter biases through [199]

$$\text{FoB} = \sqrt{\delta\vec{\vartheta}_\alpha \tilde{\mathbf{F}}_{\alpha\beta} \delta\vec{\vartheta}_\beta}, \quad (7.17)$$

thus providing an overall summary statistic for how an insufficient model leads to biased parameters.

It is important to note that while the figures of merit and bias may appear to have similar properties, they behave significantly different when considering different parametrisations. This is because the figure of merit is unitful. That is, since it is inversely proportional to the area of the 2D contour, a reparametrisation of the form  $\vartheta_\alpha \rightarrow \vartheta_{\alpha'} = 10\vartheta_\alpha$ , would lead to each entry in the Fisher matrix being one hundred times smaller. Thus, a figure of merit with the new parametrisation is ten times smaller ( $\text{FoM}_{\alpha\beta} \rightarrow \text{FoM}_{\alpha'\beta} = \frac{1}{10}\text{FoM}_{\alpha\beta}$ ) than in the old parametrisation. Though, of course, the physical interpretation of either parametrisation would lead to the same conclusions, and so we mostly care about differences in the figure of merit, rather than its absolute value.

Conversely, the figure of bias *is* unitless and so simple reparametrisations do not affect its value. Hence, it is always the absolute values of the FoB that inform us about parameter biases. Since the Fisher matrix, and thus figure of bias, were derived under Gaussian conditions, we can use the results for the multivariate  $\chi^2$  distribution to find critical values of the FoB which give certain levels of  $\sigma$  offsets. Table 7.5 gives these critical values as a function of the  $\sigma$  offset for one, two, and four degrees of freedom models. Hence, if we were to target no greater than a  $1\sigma$  offset for a two-parameter model, then we could accept a figure of bias no greater than  $\sqrt{2.30}$ . This number is then independent of any parametrisations that we might have, and only depends on our desired precision and number of free parameters in our model.

## 7.7.2 Using the figure of bias for scale cuts

With the figure of bias as our statistic of choice, we can now go about trying to use it to obtain a set of scale cuts. Since we have an ensemble of hydro-sims, each with their own baryonic feedback, we want to guard against *any and all* of them with our figure of bias cuts. Thus, when determining the scale-cuts, we optimise against the maximum of the set,

$$\max \left[ \text{FoB}_{\text{sims}}(\vec{\ell}_{\text{max}}) \right] \leq \text{FoB}_{\text{crit}}, \quad (7.18)$$

Table 7.6: Results for scale cuts using the one-dimensional optimisations using the figure of bias as the critical statistic. We see the same general trends that emerged when using the  $\chi^2$  statistic, that the enhanced statistical precision of *Euclid* demands tighter scale cuts to accept the same level of bias as our DES-Y3-like survey, and that the better-fitting three-parameter model yields looser cuts.

Bin	DES-Y3 1-param	<i>Euclid</i> 1-param	DES-Y3 3-param	<i>Euclid</i> 3-param
$1 \times 1$	5000	2859	5000	5000
$1 \times 2$	5000	199	4850	3399
$1 \times 3$	5000	349	4897	2130
$2 \times 2$	4649	226	4850	3399
$2 \times 3$	1663	249	1830	3148
$3 \times 3$	2150	240	4649	1337

where  $\text{FoB}_{\text{crit}}$  is a free-parameter of the method. We chose to set  $\text{FoB}_{\text{crit}} = 0.5$ , since that provided a good compromise between constraining power and biases, and ensured that no bias would ever be larger than one sigma.

## 7.8 Scale cuts using the figure of bias statistic

### 7.8.1 One-dimensional optimisations

Thus far, we have constructed our scale cuts using our ‘no baryons’ and ‘with baryons’  $\chi^2$  methods for a single bin at a time. The advantage of this approach is that there is a unique solution for each bin, and that the problem becomes  $N \times 1\text{D}$  optimisations, rather than a  $1 \times \text{ND}$  problem. Hence, we wish to continue this approach of using one-dimensional optimisations, but using the figure of bias as our critical statistic.

Table 7.6 shows the set of derived scale cuts using the figure of bias as our critical statistic, for our set of six one-dimensional optimisations. Here, we see the same general trends that emerged when using the  $\chi^2$  as the critical statistic. Since we are applying the FoB criterion on each bin pair individually, and some of the bin pairs are not very constraining, we can go to very high  $\ell_{\text{MAX}}$  in these bins without inducing significant bias. For all analyses, we applied a global maximum of  $\ell_{\text{MAX}} = 5000$ , which is the maximum multipole that the cosmic shear signal can be accurately measured down to for any *Euclid* analyses [328].

Using our sets of derived scale cuts, we can now repeat the same MCMC analyses shown in Figures 7.8 and 7.9 to determine what the effects of these scale cuts are on our parameter covariances and biases. This is presented in Figure 7.10, which shows that all sets of scale cuts derived from our figure of bias statistic correctly produce unbiased contours, verifying our use of the figure of bias as our criterion. We also see that for our *Euclid*-like survey, we find smaller parameter contours for the three-parameter model over the one-parameter model. This is due to the three-parameter model being able to access higher-order multipoles without being susceptible to significant biases.

### 7.8.2 Comparison between 1D $\chi^2$ and FoB scale cuts

We are now in a position where we have developed sets of scale cuts that have been derived from two statistics: the  $\chi^2$  using baryonic feedback models, and the figure of bias. We now wish to compare the performance of these sets of scale cuts to see if there are any

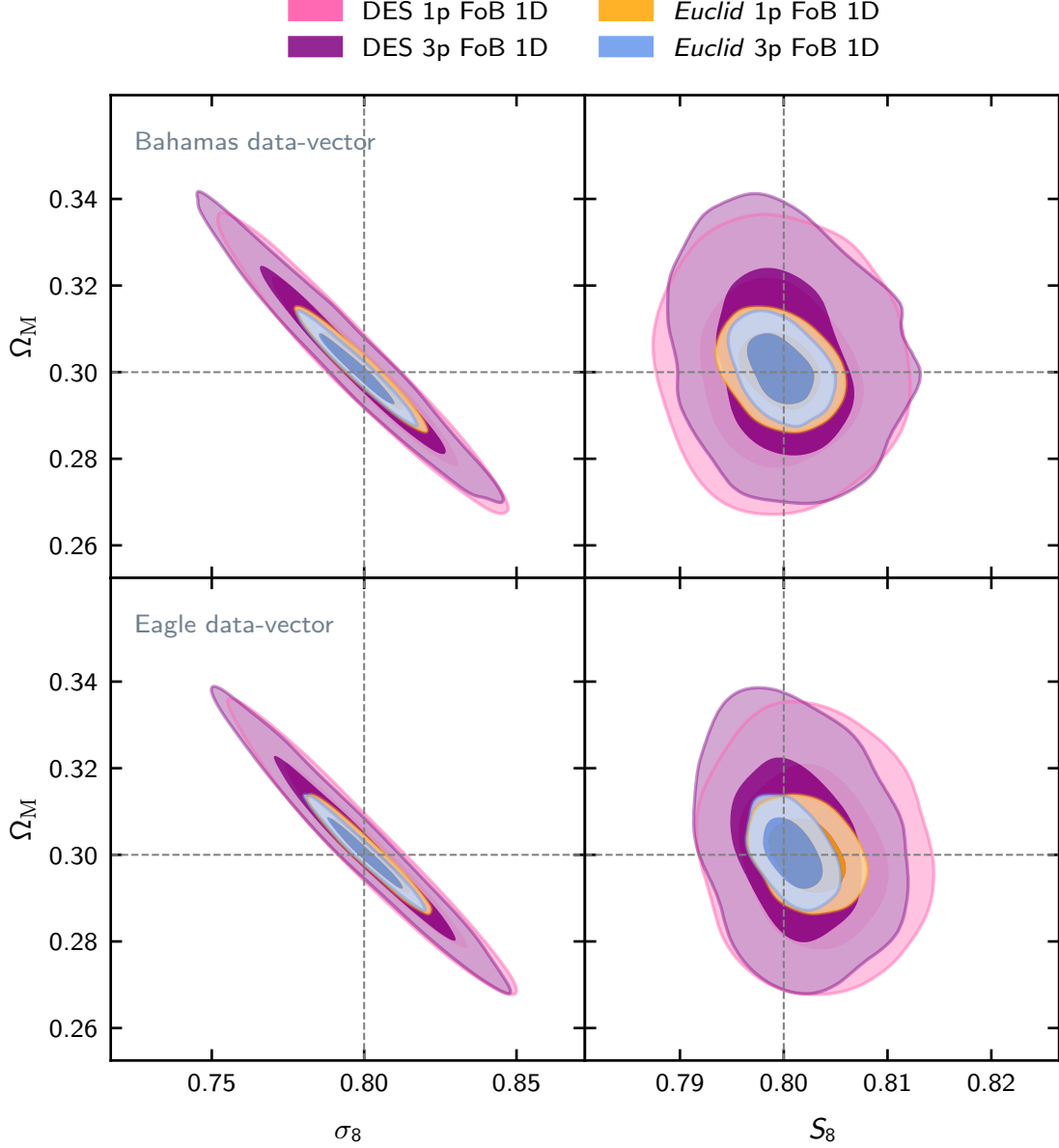


Figure 7.10: Two-dimensional  $\Omega_M$ - $\sigma_8$  and  $\Omega_M$ - $S_8$  contours for our DES-Y3-like and *Euclid*-DR3-like surveys using the figure of bias as our critical statistic with one-dimensional optimisations for the BAHAMAS and EAGLE hydro-sims as input data-vectors. We see that all FoB-derived scale cuts yield unbiased results for our three cosmological parameters, which is verification that the figure of bias can indeed be used to construct scale cuts which correctly mitigate baryonic feedback. We also see that, for our *Euclid*-like survey, the use of the three-parameter model leads to smaller contours over the one-parameter model, since it is able to access higher-order multipoles without biasing our results.

differences in the results of these methods, which could tell us if using either data- or parameter-space lead to more optimal cuts.

Figure 7.11 plots the parameter contours derived from using the  $\chi^2$  and figure of bias statistics for our *Euclid*-like survey. Here, we see that the contours derived from the figure of bias criterion are systematically tighter than their  $\chi^2$  counterparts. This suggests that the figure of bias is correctly identifying and excluding the modes that actually lead to biases in the cosmological parameters, not just the raw differences in the data-vectors that the  $\chi^2$  is computed from. This provides significant verification that the figure of bias can be used for the optimal computation of scale cuts for Stage-IV cosmic shear surveys.

### 7.8.3 Six-dimensional optimisation

Thus far, we have only been doing scale cut optimisation on a bin-by-bin basis. This matches what has been done in the literature previously, and considerably reduces the numerical complexity of our algorithms to determine the scale cuts. However, we know that the scale cuts used in any analysis are not totally independent, since valuable information comes from the cross-correlations between the different spectra. Hence, when we optimise against either a  $\chi^2$  or FoB criterion, then one should account for these cross-correlations in the optimisations. Thus, the optimisation algorithm vary all of the scale cuts together, and so for three tomographic bins, we have six scale cuts to optimise.

We use the one-dimensional optimisations as starting positions for the six-dimensional optimisation. This is because, while we are now including the effects of cross-correlations, if each bin satisfies the FoB criterion itself, then it is hoped that the overall figure of bias will be close to the desired value. This means that the optimisation algorithm hopefully converges much faster now that we are starting it from an informed position, rather than them to random or non-sensible values.

With our starting position given by our one-dimensional optimisations using the figure of bias as our critical statistic, we can move up to exploring the full six-dimensional parameter space and optimising them together. However, as has been found from experimenting with the optimisation algorithm, the six-dimensional figure of bias likelihood surface is far from simple, and so traditional optimisation methods often failed to correctly converge. Hence, a different optimisation technique was employed, which was the **GridMax** sampler as part of COSMOSIS. This optimises the likelihood by probing each dimension individually, while keeping all over variables fixed. This aims to ‘spiral in’ to an optimal solution, and was found to work much better for our complex likelihood surface than other optimisers (such as **Minuit** and **maxlike** as provided with COSMOSIS).

One subtlety to using the **GridMax** sampler is the order in which it probes each dimension in. Since it keeps all other variables fixed as it probes along each axis, the response of the likelihood to the current dimension strongly depends on the other scale cut values. To investigate this effect, numerous chains of the **GridMax** sampler were run, with different orderings of the optimisation. For example, one chain was run with the fiducial ordering of  $(1 \times 1, 1 \times 2, 1 \times 3, 2 \times 2, 2 \times 3, 3 \times 3)$ , whereas another with its inverse ordering  $(3 \times 3, 2 \times 3, 2 \times 2, 1 \times 3, 1 \times 2, 1 \times 1)$ . Both chains give the same figure of bias, but very different results for each bin’s scale cuts.

Tables 7.7 and 7.8 feature ten different sets of scale cuts that were the result of running the **GridMax** sampler in different order of the bin combinations. Even though the value for the figure of bias is the same for each chain (or at least close to be within a small numerical tolerance), the value for the figure of merit and  $\chi^2$  vary quite significantly between each of the runs. We see that there is a loose connection between higher allowable multipoles in the  $2 \times 3$  and  $3 \times 3$  spectra and increased constraining power, via the figure of merit. This suggests that the ‘bias budget’ should be used up in the most constraining spectra, which

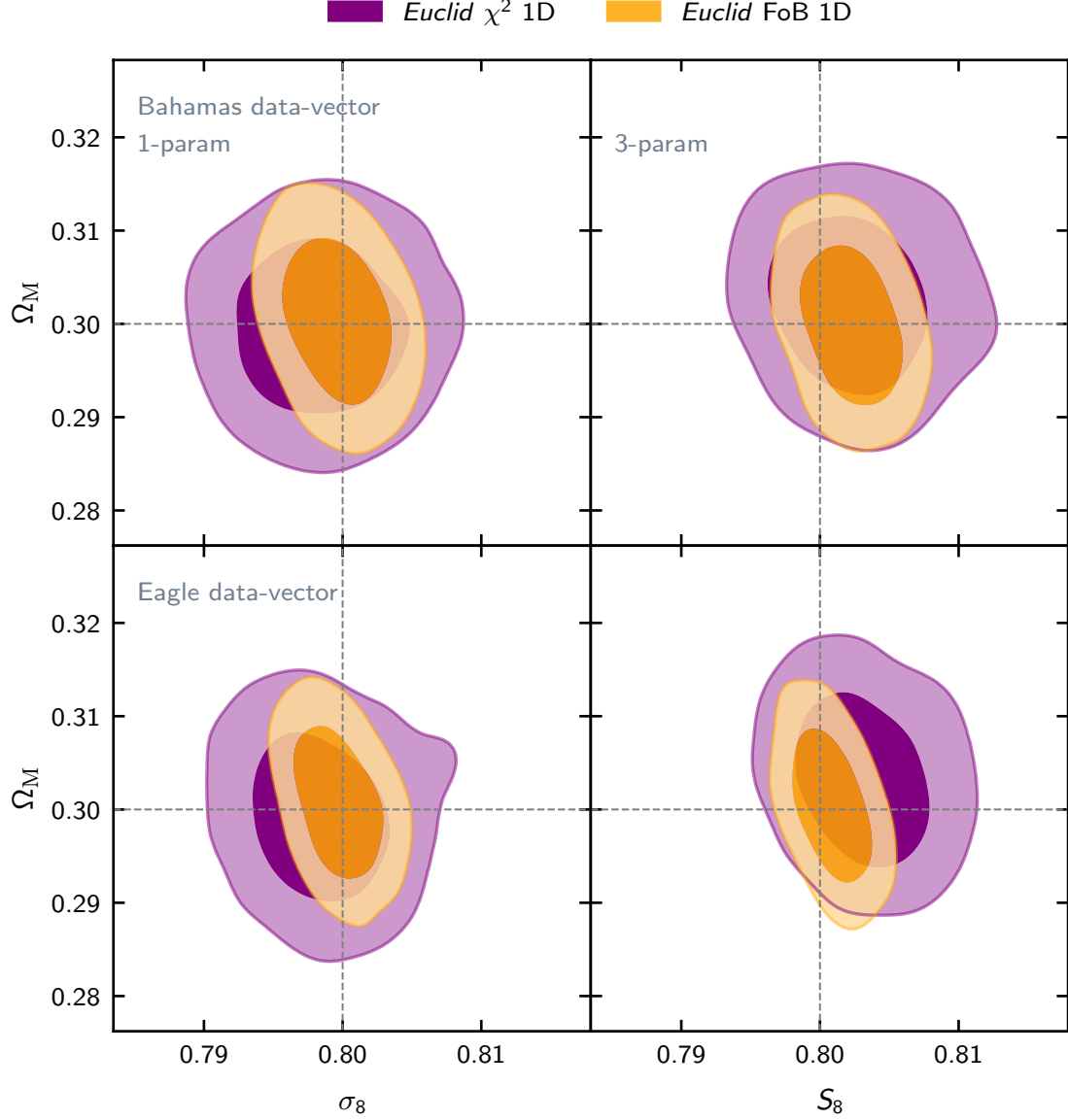


Figure 7.11: Two-dimensional  $\Omega_M$ - $\sigma_8$  and  $\Omega_M$ - $S_8$  contours for our *Euclid*-DR3-like survey comparing the results obtained using both the  $\chi^2$  (purple) and figure of bias (orange) derived scale cuts. The rows of the plot denote the BAHAMAS and EAGLE hydro-sims as input, with the columns plotting the one- and three-parameter models, respectively. We see systematically smaller contours for the figure of bias derived cuts, which suggests that this statistic is more optimal than optimising using the raw data-space  $\chi^2$  values. Here, ‘1D’ refers to use optimising each bin combination individually, and not optimising the global  $\chi^2$  or FoB for all bin combinations simultaneously.

Table 7.7: Scale cuts (that is the maximum possible  $\ell$  multipole) for the one-parameter model obtained using our 6-dimensional optimisation approach using the figure of bias as the critical statistic. We note that there is not a single unique solution which satisfies our criterion, but instead a whole family of solutions. We see that, in general, the optimisation routine has chosen to set one bin’s  $\ell_{\text{MAX}}$  to be quite low (of the order a few hundred), with the remaining five bins having a much larger maximum multipole, with some approaching our hard maximum of 5000. We have sorted the results by their figure of merit for  $(S_8, \Omega_M)$ . We see that the most constraining set of scale cuts, that is the set with the largest FoM, is one in which the smallest  $\ell_{\text{MAX}}$  is still in the thousands. This suggests that the most-optimal set of cuts are where the  $\ell_{\text{MAX}}$  values are all about the same order, and not having an over order of magnitude difference between smallest and largest multipoles.

$1 \times 1$	$1 \times 2$	$1 \times 3$	$2 \times 2$	$2 \times 3$	$3 \times 3$	$\chi^2$	FoM
5000	1681	2957	5000	4744	405	3.74	59000
2859	4234	5000	150	5000	1426	3.69	67300
4301	4489	673	606	4946	2575	4.10	68700
1936	3978	5000	5000	5000	1426	4.44	69300
915	4059	5000	5000	5000	1574	4.35	69900
4489	5000	5000	3723	1426	3468	4.51	69900
4744	5000	5000	5000	5000	1439	4.02	70100
3978	5000	5000	3723	5000	2447	4.54	73000
277	5000	5000	5000	4489	3213	4.29	73400
2192	5000	5000	3723	5000	4489	4.41	74800

then necessitates tighter cuts in the less constraining lower redshift spectra. However, it is clear that by using just the figure of bias, no optimisation routine can give unique solutions, so either additional terms in the likelihood could be included (such as a small weight to the  $\chi^2$  or figure of merit), or another optimisation method is needed to be found.

There are many different choices of scale cuts which keep the overall bias due to mis-modelled baryon feedback within acceptable levels. These differ in the tightness of the resulting constraints on cosmological parameters, and on the overall goodness of fit of the best-fit model.

## 7.9 Discussion and conclusions

In this chapter, we have presented several alternative methods for the derivation of binary scale cuts for cosmic shear surveys. We found that if we were to use DES-Y3-inspired methods where we mitigated against baryonic feedback using a dark-matter-only fiducial model, then the headline constraints on  $S_8$  from a *Euclid*-like survey will be no better than those existing in the literature today.

This provided excellent motivation into investigating alternative approaches, the first of which was the ‘modified  $\chi^2$ ’ method, which modified the  $\chi^2$  through the inclusion of a baryonic feedback model into our fiducial model. This added the complication of fitting baryonic feedback models to the hydro-sims, where now these fits are dependent on the maximum multipole included in the fit. With this challenge overcome, new sets of scale cuts were obtained for our DES-Y3-like and *Euclid*-like surveys. These showed that higher-order multipoles could be included in an analysis without inducing statistically significant bias, which is expected from going from a dark-matter-only model to one including baryonic feedback. These scale cuts were then benchmarked against various hydrodynamical simulations, finding that they do indeed guard against baryonic feedback bias.



Table 7.8: Scale cuts (that is the maximum possible  $\ell$  multipole) for the three-parameter model obtained using our 6-dimensional optimisation approach using the figure of bias as the critical statistic. We note that there is not a single unique solution which satisfies our criterion, but instead a whole family of solutions.

$1 \times 1$	$1 \times 2$	$1 \times 3$	$2 \times 2$	$2 \times 3$	$3 \times 3$	$\chi^2$	FoM
4234	1224	432	3481	512	1171	1.25	33100
741	1305	432	3508	3468	1681	1.39	36400
2192	1251	660	3213	2957	2702	1.57	39200
2575	1412	888	3468	660	3723	1.45	39600
2931	1650	485	3428	888	3871	1.59	39900
2192	1802	2447	2702	3213	2259	1.55	40300
2957	1681	1426	3428	3656	2286	1.40	40300
915	1426	2702	1171	2957	4234	1.52	40400
5000	1936	4489	3468	3468	2339	1.62	42400
5000	4072	4744	4919	3817	2393	2.17	43400

Since we measure parameter biases in, well, parameter space (duh!), it makes sense that our scale cuts could be constructed in this basis too. This provided the motivation for constructing our set of scale cuts that optimised against the value of the figure of bias rather than the  $\chi^2$ . This required the computation of the derivative of the data-vector with respect to our cosmological and astrophysical parameters. With these computed, sets of scale cuts could be derived from the figure of bias criterion. These were found to mitigate baryonic feedback, and result in smaller contours than their  $\chi^2$  counterparts. This indicates that by constructing scale cuts in parameter-space, we are more able to isolate scales which contaminate our cosmological parameters with less reduction in the constraining power over the  $\chi^2$ .

We also extended this method to look at optimising our scale cuts together, in a single six-dimensional optimisation. This was significantly computationally challenging, since the likelihood surface of the scale cuts was far from trivial or well-behaved. This required the use of a non-standard optimiser, the **GridMax** sampler. We then found that there are no unique solutions to our figure of bias criterion, where different chains that were optimised in different orders have the same FoB but different individual scale-cuts and FoM values. This highlights the challenges for deriving sets of scale cuts for future weak lensing surveys that feature very many tomographic redshift bins.

These results presented here are entirely new results in the field, the degeneracy and non-uniqueness of scale cuts has not yet been thoroughly explored in the literature. Furthermore, surveys tend to adopt just one approach to scale cuts without much scrutiny of alternative approaches or statistics, or do not use scale cuts at all. I have shown that using different methods and statistics can lead to the derivation of different sets of scale cuts, with interesting effects on the derived cosmological parameter constraints.

### 7.9.1 Outlook

While we have focused on mitigating the effects of baryonic feedback physics on our cosmic shear summary statistics, the methods presented here using either the  $\chi^2$  or figure of bias statistics provide an excellent basis for extending to other systematic effects which introduce scale-dependent bias into observables. This includes the properties of the non-linear matter power spectrum, the effect of intrinsic alignments, and non-linear bias in galaxy clustering. Each of these physical phenomena and their effects on forthcoming

weak lensing galaxy surveys needs to be quantified and mitigated against to ensure that final results are unbiased. The methods that we have presented for determining binary cuts can easily be extended to include contributions from all of these effects, or even ‘unknown unknown’ effects that may be unravelled with increased precision data.

It is also clear that this work is highly idealised scenario for any cosmic shear survey: sampling over only two cosmological parameters and neglecting all over systematic effects apart from baryonic feedback. We also used only three redshift bins for our analyses, a far cry from the expected thirteen bins that the full *Euclid* analysis could use [329]. This gives us only six spectra to compute the scale cuts from, not ninety-one! This will make the determination of the scale cuts used in their analyses though a rigorous and robust method more important than ever. Hence, a more thorough approach to determining the baryonic biases using the full complexities of a Stage-IV cosmic shear survey is needed before any scale cuts can be accurately determined for that survey.

This was a triumph,  
I'm making a note here: 'huge success'  
—GLaDOS

# 8

## Conclusions

---

**Outline.** In this chapter, I conclude the results featured in my thesis, aim to place these results within the wider cosmological context, and offer some thoughts for the future. Hooray, the thesis is nearly over!

### 8.1 Our place in the Universe

Throughout my thesis, we have seen the great power that forthcoming weak lensing galaxy surveys will have on our ability to measure, constrain, and provide physical insight into our Universe. But as Spider-Man once warned us, ‘With great power comes great responsibility (not to fuck it up!)’. As I write, *Euclid* is sat at  $L_2$  and taking data that is just marvellous (I mean, just look at Figure 4.5!). The technical teams have done a tremendous job to build such a fabulous instrument, and so the onus is very much on us theorists and data analysts to interpret, analyse, and extract the most amount of information possible from the data. This is far from a straightforward process, I have focused on two key areas of research: minimising the errors associated with power spectrum estimation, and mitigating baryonic feedback bias that is induced in our cosmic shear observables in a way that still leaves us with the most amount of information possible from the raw data. It is hoped that the development of these accurate and precise statistical methods will shed light on some of our greatest cosmological mysteries.

While the success of Einstein’s general relativity, the  $\Lambda$ CDM model, and the hot Big Bang model all combine to form the truly marvellous modern cosmological model, see, for example, the brightness of Type Ia supernovae over a large range of redshifts in Figure 2.12, the black-body spectrum of the CMB in Figure 2.13, the temperature anisotropies of the CMB in Figure 2.15, the peak in the clustering of galaxies around the BAO scale in Figure 2.16, and the deflection of light from the gravitational field of the Sun in Figure 3.1, we don’t really know what *actually* makes up 95 % of our Universe! While we may give attractive names to the mysterious components of our Universe, ‘dark matter’ and ‘dark energy’, we have yet to narrow down the exact physical characteristics of these phenomena since their discovery in the 1970’s [36] and 1990’s [37, 38], respectively.

Though we have extremely strong observational evidence of the gravitational interaction of our dark fields — that is dark matter is some cold, collisionless matter that

interacts only through the gravitational field [330], and dark energy is a fundamental property of space-time that acts as a repulsive gravitational force, if dark energy is the cosmological constant  $\Lambda$  — we don’t have satisfying theoretical models of these physical phenomena. Many well-motivated theories to explain dark matter have emerged in the literature, ranging from weakly-interacting massive particles (WIMPs) to primordial black holes, have been suggested to explain the existence of dark matter [331]. The theoretical motivation behind dark energy is no better; if one computes the vacuum energy density using quantum field theory, then you arrive at an answer that is about 120 orders of magnitude larger than the upper limit on the value of  $\Lambda$  from our cosmological observations. This has been dubbed ‘probably the worst theoretical prediction in the history of physics!’ [47].

It’s ironic that the most familiar component of our Universe, that of ordinary baryonic matter that you and I are made of, is almost always too complex to model on cosmological scales and so we need to develop methods to mitigate their mischievous effects on our observables (Chapters 6 and 7). It would certainly be easier to perform a cosmic shear survey in a universe without baryons since we wouldn’t have to marginalise over their properties, though we wouldn’t be there to observe it — nor would there be any light from distant galaxies to measure cosmic shear with, save for the faint cosmic microwave background afterglow from the Big Bang.

*Euclid* will soon be joined by its NASA cousin the *Roman* space telescope [332], and ground-based cousin the *Legacy Survey of Space and Time* (LSST) at the *Rubin* observatory [165], and has already joined its older cousin the ground-based *Dark Energy Spectroscopic Instrument* (DESI) [333]. These make up the four great Stage-IV galaxy survey observatories and will undoubtedly make measurements that make unveiling the mysterious properties of dark matter and dark energy a distinct probability over the next decade. A measurement of  $w_0 \neq -1$  or  $w_a \neq 0$  would be as significant as the measurements that proved  $\Omega_\Lambda > 0$  and the existence of dark energy in the first place!<sup>1</sup>

Thus, while we may not know the detailed physical properties of 95 % of our Universe, and the 5 % that we can explain is too hard to accurately model, it certainly won’t stop us cosmologists from trying to observe our Universe to exquisite precision in the hopes of finally understanding it all. Our new surveys could well be the ‘*Start of Something New*’ for cosmology.

## 8.2 Summary of work and results

The core theme of my thesis has been to develop statistical methods that allow for the extraction of the most amount of information possible from cosmic shear survey data. First, the development of a new implementation of the quadratic maximum likelihood estimator allows us to measure the cosmic shear power spectrum with significantly reduced error bars when compared to the standard Pseudo- $C_\ell$  method. We see that by using QML methods, we are able to reduce the errors on the largest angular scales in the  $E$ -modes by around 20 %, which is equivalent to an increase in the sky area of around 40 %. Given that *Euclid* is already at the limit of what an all-sky weak lensing galaxy survey can achieve, an effective increase of 40 % in the survey area by using an alternative analysis method is not to be passed over! Combine this with the over order of magnitude decrease in the error

---

<sup>1</sup>DESI’s data release one has already shown slight preference for  $w_0 > -1$  and  $w_a < 0$  at a minimum of the  $2.5\sigma$  level [55]. While exciting, these results are the *first* hints at a departure from the  $\Lambda$ CDM model, and so additional, more constraining data from future DESI releases and other Stage-IV surveys is needed before we can truly say that dark energy cannot be described by the cosmological constant. Let’s not forget that the BICEP2 collaboration announced a  $7.0\sigma$  detection of non-zero inflationary  $B$ -modes [334], before *Planck* found that their signal was entirely consistent with the emissions from cosmic dust [335].

bars for the  $B$ -modes, we conclude that analysing future cosmic shear survey data with QML methods would be a worthwhile endeavour that may just help unearth something surprising about our Universe.

The monumental decrease in runtime and RAM usage of my new method over existing QML methods (Figure 5.4), which permits the execution of the QML estimator to far higher multiples than was previously possible, will allow the application of QML methods to more physical problems and far larger data-sets than existing methods could cope with. It would not be out of the realm of possibility to think that such methods, which measure the  $B$ -modes to far greater precision than Pseudo- $C_\ell$  methods, could be instrumental in forming a non-zero detection of  $B$ -modes in either the cosmic shear signal or in the cosmic microwave background polarisation.

An accurate determination of the observationally-measured cosmic shear power spectrum is useless without equally accurate and precise theoretical modelling of the power spectrum, taking into account all of the cosmological and astrophysical effects that contribute to cosmic shear. I have investigated one of the largest sources of said astrophysical effects, which is the impact of baryonic feedback that exists on small-scales within our Universe on cosmic shear. I have shown that using an incorrect, or non-suitable, analytic description of baryonic feedback can induce significant bias in the deduced cosmological parameters from a Stage-IV survey (Figures 6.8 and 6.10). Using this as motivation, I extended the existing theoretical uncertainties approach to quantify the errors associated with three different implementations of the HMCODE-2020 baryonic feedback model. I based my analysis though fitting the baryonic feedback response function of our three analytic models compared to the predictions for an ensemble of six hydrodynamical simulations, which is the natural basis to perform such comparison as it is the underlying physical quantity, and is a new result in the field. From this, I then propagated this into an additional term in the covariance matrix for the angular power spectrum.

Using this additional theoretical error covariance, I showed how using even a basic prescription of baryonic feedback applied to a hydrodynamical simulation featuring extreme baryonic feedback allows the recovered cosmological parameters to be consistent with their true values (Figures 6.10, 6.11, and 6.12). This paves the way for using alternative methods to traditional binary scale cuts which still mitigate baryonic feedback contamination, while attempting to keep as much information content as possible.

Having said that, binary scale cuts have featured extensively in previous Stage-III surveys, and so are prime candidates to be used in the analyses of our Stage-IV surveys. Thus, Chapter 7 was dedicated to investigating the properties of existing binary cuts methods on Stage-IV surveys, finding that if we apply existing methods in the literature to the new data, then our cosmological constraints will be no better than existing results. This drove the development and analysis of alternative methods to derive sets of binary cuts, where we are now explicitly including the properties of baryonic feedback models into the analysis. I compared the use of two statistics, the  $\chi^2$  and figure of bias, to derive sets of scale cuts for our next generation of surveys, finding that there are no unique solutions to this problem.

## 8.3 Future work

Throughout the development of my new implementation of the QML method in Chapter 5, I focused solely on the cosmic shear signal coming from a single redshift bin. Thus, a natural extension to my work is to investigate the properties of the performance of the QML method with respect to the Pseudo- $C_\ell$  method for the case where we include galaxy-galaxy lensing and galaxy position-position information, forming the  $3 \times 2$ pt data-vector which Stage-IV surveys can take full advantage of. The additional information, present

from both the new cosmological probes and cross-correlations with the increased number of redshift bins, could uncover new properties of the QML estimator when compared to the Pseudo- $C_\ell$  method.

The next generation of CMB experiments, the Simons Observatory and CMB-S4, aim to measure the polarisation of the microwave background to unprecedented accuracy. Since the polarisation of the CMB is a spin-2 field and thus completely analogous to our cosmic shear field, the application of my QML method to CMB polarisation would be rather straightforward. Furthermore, since one of the main science goals of these next generation CMB experiments is to place stringent limits on the detection of  $B$ -mode polarisation. If the dramatic decrease in the  $B$ -mode error bars found in my cosmic shear analysis were to propagate over to the CMB, then these QML methods would form an essential role in the detection of  $B$ -modes.

Throughout the development of my implementation of the theoretical uncertainties method to the matter power spectrum, the use of our ensemble of hydrodynamical simulations has underpinned my entire numerical pipeline. Just as we are experiencing a rapid growth in the quality of observations, the hydrodynamical simulation community has continued to make great advancements with new simulations that feature larger volumes, increased baryonic particle mass resolution, total particle counts, and increased accuracy of sub-grid physics. Simulations such as FLAMINGO [290], CAMELS [307, 336] and FLARES [337] have all arisen as the latest state-of-the-art hydro-sims. Hence, a straightforward extension of Chapter 6 would be to include these new simulations in our ensemble, perhaps replacing some of the older simulations such as BAHAMAS and ILLUSTRIS, and seeing how the theoretical error envelope and our HMCode baryonic feedback models react to these new inclusions.

For simplicity, the application of my theoretical error covariance was limited to analyses where we sampled only over the two main cosmological parameters for cosmic shear,  $\Omega_M$  and  $\sigma_8$ , and using five redshift bins. This was done to speed up the convergence of the MCMC chains, and to get estimates for the worst-case scenario for a *Euclid*-like survey. However, the full analysis of *Euclid* data is expected to include sampling over seven cosmological parameters, using thirteen tomographic redshift bins which necessitates the inclusion of well over thirty nuisance parameters for the photometric sample alone [164]. This takes the number of spectra from fifteen in my analysis to a whopping ninety one! Thus, an important result would be to first quantify the level of bias associated with using inadequate methods of baryonic feedback when using hydro-sims as the ground truth, and then investigate the mitigation of these biases through either the inclusion of the theoretical error covariance, or application of binary cuts methods.

At present, the current preliminary forecasts for the final *Euclid* survey data have used the one-parameter model of HMCode-2020 with 32 logarithmic-spaced bins ranging from  $\ell \subseteq [10, 5000]$ . Based on work presented in this thesis, these are certainly *optimistic* targets, though I have no doubt that thorough and extensive validation tests will be performed by the supremely talented *Euclidean*s that I have had the pleasure to work with in my PhD to verify these analysis choices.

## 8.4 Outlook to the future

The future of the cosmological dark sectors have never looked as bright as they have at the time of writing this thesis. The rise of the four great Stage-IV galaxy survey observatories, future CMB experiments, the James Webb Space Telescope [338], the *Athena* X-ray telescope [339], and the *LISA* space-based gravitational wave observatory [340] will all probe our Universe across the entire electromagnetic and gravitational wave spectrum with immense precision.

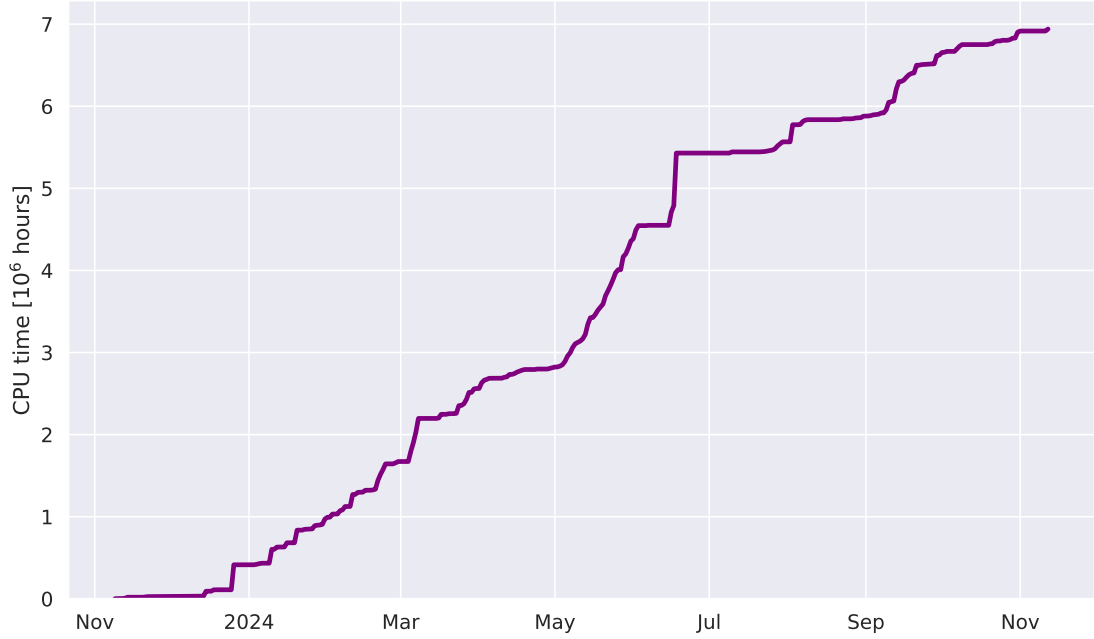


Figure 8.1: Cumulative CPU hours used on the *Euclid*:UK high-performance computing cluster during the last year of my PhD. It shows that in a single year of just one cosmology PhD, my analysis methods required nearly  $7 \times 10^6$  CPU hours.

While each probe will undoubtedly uncover great physical insights into our Universe, just like the Avengers (or perhaps more fittingly, the *Guardians of the Galaxy*) their combined power is far greater than the sum of their parts. For example, while we have treated baryonic feedback as a nuisance astrophysical effect that needs to be marginalised over in our weak lensing cosmological analyses, the physics of baryonic feedback can be directly probed through the kinematic Sunyaev-Zel’dovich (kSZ) effect in observations of the CMB [127, 308], and gas fractions in galaxy clusters from X-ray observations [298, 341]. The development of these external data-sets will allow us to place tight constraints on the physics of baryonic feedback that is independent of our cosmic shear observations and so provide valuable additional insights into both the development of analytic baryonic feedback models, and the development of the hydrodynamical simulations. For example, Ref. [187] found that observations of the kSZ effect strongly disfavoured the more modern ILLUSTRIS-TNG hydrodynamical simulation, instead favouring the more extreme feedback as featured in the original ILLUSTRIS simulation. Thus, by using and combining different cosmological probes, we can gather huge quantities of data that tests the fundamental properties of our Universe.

While the availability and exploitation of such precision data is sure to get any cosmologist buzzing, it is important to recognise that we cannot just blindly increase the size of our data-sets without restriction. To demonstrate this, Figure 8.1 shows the cumulative computing time in CPU hours<sup>2</sup> that I used in the last year of my PhD to perform the analyses presented in Chapters 6 and 7. This shows an impressive total of nearly  $7 \times 10^6$  CPU hours, just shy of 800 CPU years. This computing usage has consumed an approximate 36 000 kWh of energy which, using the UK’s electricity average carbon intensity of  $150 \text{ gCO}_2 \text{ kWh}^{-1}$  in 2024 [342], gives carbon dioxide emissions of around 5400 kgCO<sub>2</sub>, or about ten transatlantic flights from London to New York [343]. It should be noted that the UK’s electricity carbon intensity has fallen dramatically over the last decade, as it

<sup>2</sup>A CPU hour is defined as one thread of a processor working for a wall-clock time of an hour. For example, a 64 core job running for two hours would use 128 CPU hours.



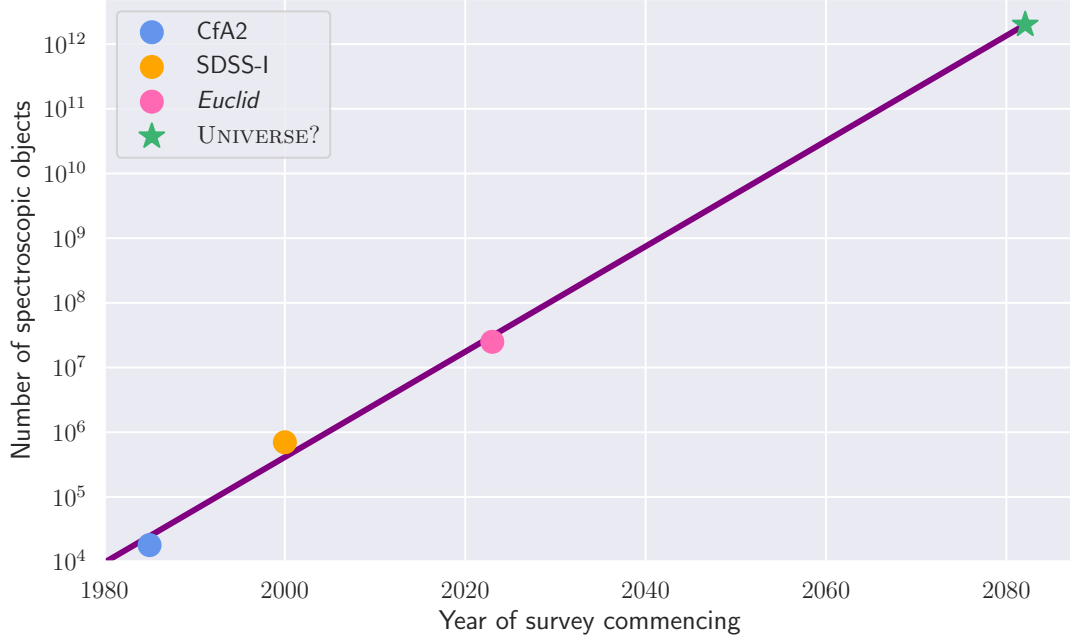


Figure 8.2: Evolution of the number of galaxies in selected spectroscopic surveys as a function of their year of inauguration, ranging from the Center for Astrophysics survey 2 (CfA2) [345], to the Sloan Digital Sky Survey (SDSS-I) [346], and finally to the *Euclid* spectroscopic survey [164]. If we fit a power-law to these three data-points, and then extend to include all galaxies in the observable Universe, of  $2 \times 10^{12}$ , then the UNIVERSE survey could become reality around 2080. I hope to live to see that survey!

averaged  $500 \text{ gCO}_2 \text{ kWh}^{-1}$  in 2012, and hopefully will continue to further fall. Sourcing clean, renewable energy to power our supercomputers is essential if we want the next generations of astronomers and cosmologists to enjoy the same planet that we currently inhabit. Or we could abandon Python and switch to FORTRAN and C++ [344].

To end on a slightly whimsical note, which is about par for my thesis, we can investigate what it would take for us to complete *the* galaxy survey — that is observing *all two trillion galaxies* in our observable Universe [347] spectroscopically. Using some optimistic assumptions, a 280 metre telescope operating at the second Lagrange point,  $L_2$ , could perform a spectroscopic analysis of every galaxy in the observable Universe over a ten-year survey [348]. Of course, massive technological advances would be required to build and launch such a massive telescope into space, but, just like dark energy, one should never discount the accelerated growth of human ingenuity!

This survey may well be closer than we know it. Figure 8.2 plots the growth of the number of galaxies in spectroscopic surveys over time, and so conclude that this mythical survey could become reality around 2080. To get ahead of the curve, I decree that this galaxy survey to end all surveys shall be known as UNIVERSE: UNiversal Investigation of the Vast Extragalactic Regions of Space-time Evolution<sup>3</sup>. All I know is that you could get some seriously tight contours on  $\Omega_M$  and  $\sigma_8$  by using every galaxy in the Universe, but I certainly wouldn't want to be the one running the MCMC to analyse the data – it could well take a universal age to compute!

<sup>3</sup>Created with the brainstorming help of ChatGPT [349].

*My power spectra has doubled since we last met, Count*

—Anakin Skywalker

*Good, twice the matter, double the shear*

—Count Dooku



## Power spectrum of a simple mask

**Outline.** Appendix detailing the derivation for the power spectra of simple masks that vary in either the  $\vartheta$  or  $\phi$  directions, which have been used in my thesis.

### A.1 Simple mask in the $\vartheta$ plane

Much of the first science project (Chapter 5) was spent investigating the properties of masks and how they impact the statistics of fields that are recovered by deconvolving a mask. In the Pseudo- $C_\ell$  method, this deconvolution is sensitive to the power spectrum of the mask. Thus, if we are to understand the mixing matrix well, then we can investigate the analytic properties of the power spectrum of a mask first.

We start out with a simple binary mask that only varies in the  $\vartheta$  plane. For example, Figure A.1 shows a mask that only allows data through in a region between  $\vartheta = \pi/3$  and  $\vartheta = 2\pi/3$ , with no  $\phi$  dependence. To find its power spectrum, we first need to evaluate its spherical harmonic transform into its corresponding  $a_{\ell m}$  values. Recalling Equation 2.108 for the definition of the  $a_{\ell m}$  values for a function on the sphere, we have

$$a_{\ell m} = \int d\Omega(\hat{n}) f(\vartheta, \phi) Y_{\ell m}^*(\vartheta, \phi). \quad (\text{A.1})$$

If our mask is only a function of  $\vartheta$ , then we can write our mask simply as

$$f(\vartheta, \phi) = f(\vartheta). \quad (\text{A.2})$$

The definition of the spherical harmonics,  $Y_{\ell m}$ , are given as

$$Y_{\ell m}(\vartheta, \phi) = \sqrt{\frac{(2\ell+1)}{4\pi} \frac{(\ell-m)!}{(\ell+m)!}} P_{\ell m}(\cos \vartheta) e^{im\phi}, \quad (\text{A.3})$$

where  $P_{\ell m}(x)$  are the associated Legendre polynomials. Recalling the differential element on the sphere can be written as  $d\Omega = \sin \vartheta d\vartheta d\phi$ , we find we can split the  $a_{\ell m}$  integral into

$$a_{\ell m} = \sqrt{\frac{(2\ell+1)}{4\pi} \frac{(\ell-m)!}{(\ell+m)!}} \int_0^\pi d\vartheta \sin \vartheta f(\vartheta) P_{\ell m}(\cos \vartheta) \int_0^{2\pi} d\phi e^{-im\phi}. \quad (\text{A.4})$$

Binary mask only allowing data through the centre

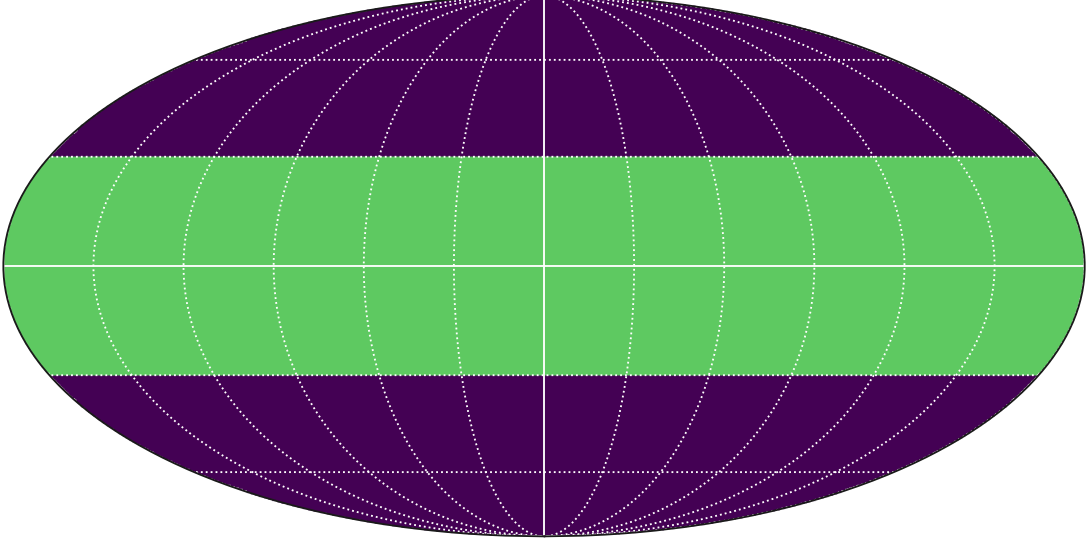


Figure A.1: Simple binary mask that only allows data through within the central angular region  $\frac{\pi}{3} \leq \vartheta \leq \frac{2\pi}{3}$ , shown in green, with the purple region masking out data.

The  $\phi$  integral can be done immediately, yielding a Kronecker- $\delta$  since it is only non-zero when  $m$  is zero, giving

$$\int_0^{2\pi} d\phi e^{-im\phi} = 2\pi\delta_m. \quad (\text{A.5})$$

Since this forces the  $m$  to be zero to give non-zero  $a_{\ell m}$  values, we can substitute in  $m = 0$  into our integral of Equation A.4, we find the  $a_{\ell m}$  values can be written as

$$a_{\ell m} = \delta_m \sqrt{\pi(2\ell + 1)} \int_0^\pi d\vartheta \sin \vartheta f(\vartheta) P_\ell(\cos \vartheta), \quad (\text{A.6})$$

where  $P_\ell(\cos \vartheta)$  are the regular Legendre polynomials. Using our definition of our masking function  $f(\vartheta)$  that it is only non-zero within a certain range of  $\vartheta$  values of  $[A, B]$ , we find our integral becomes

$$a_{\ell m} = \delta_m \sqrt{\pi(2\ell + 1)} \int_A^B d\vartheta \sin \vartheta P_\ell(\cos \vartheta). \quad (\text{A.7})$$

This is now an integral of known Legendre polynomials, which has the standard result of

$$\int_A^B d\vartheta \sin \vartheta P_\ell(\cos \vartheta) = \frac{-P_{\ell-1}(\cos A) + P_{\ell+1}(\cos A) + P_{\ell-1}(\cos B) - P_{\ell+1}(\cos B)}{2\ell + 1}. \quad (\text{A.8})$$

This gives the  $a_{\ell m}$  values of our mask as

$$a_{\ell m} = \delta_m \sqrt{\frac{\pi}{2\ell + 1}} [-P_{\ell-1}(\cos A) + P_{\ell+1}(\cos A) + P_{\ell-1}(\cos B) - P_{\ell+1}(\cos B)]. \quad (\text{A.9})$$

This, transforming these  $a_{\ell m}$  values into our power spectrum coefficients,  $C_\ell$ , we find that the mask's power spectrum to be given by

$$C_\ell = \frac{\pi}{(2\ell + 1)^2} [-P_{\ell-1}(\cos A) + P_{\ell+1}(\cos A) + P_{\ell-1}(\cos B) - P_{\ell+1}(\cos B)]^2. \quad (\text{A.10})$$

If we now assume that our mask is symmetric around  $\vartheta = \pi/2$ , then we can use the parity of the Legendre polynomials [350], of

$$P_\ell(-x) = (-1)^\ell P_\ell(x), \quad (\text{A.11})$$

we can write the power spectrum as

$$C_\ell = \frac{\pi}{(2\ell+1)^2} \left[ \left\{ -1 + (-1)^{\ell-1} \right\} P_{\ell-1}(\cos A) + \left\{ 1 - (-1)^{\ell-1} \right\} P_{\ell+1}(\cos A) \right]^2. \quad (\text{A.12})$$

Thus we see that for odd  $\ell$  values, the two terms in curly brackets cancel out and are left with zero for the  $C_\ell$  values. This simplifies our power spectrum for even  $\ell$  as

$$C_\ell = \frac{4\pi}{(2\ell+1)^2} [P_{\ell+1}(\cos A) - P_{\ell-1}(\cos A)]^2. \quad (\text{A.13})$$

### Limit in large $\ell$

We can further simplify our equation for the power spectrum of our simple mask by taking the limit  $\ell \gg 1$ . Since most of our cosmological information in the power spectrum comes from high- $\ell$  modes, we are motivated to understand the behaviour of the mask's power spectrum in this limit. Since our power spectrum is a function of Legendre polynomials, we can take the large- $\ell$  asymptotic limit of them, finding

$$P_\ell(\cos \vartheta) \simeq \frac{2}{\sqrt{2\pi\ell \sin \vartheta}} \cos \left( \left[ \ell + \frac{1}{2} \right] \vartheta - \frac{\pi}{4} \right), \quad (\text{A.14})$$

which is correct up to order  $\mathcal{O}(\ell^{-3/2})$  corrections. Applying this limit, we find our mask's power spectrum, for even  $\ell$ , to be given by

$$C_\ell = \frac{4\pi}{(2\ell+1)^2} \left[ \frac{2}{\sqrt{\sqrt{3}\pi(\ell+1)}} \cos \left( \frac{\pi\ell}{3} \right) - \frac{2}{\sqrt{\sqrt{3}\pi(\ell-1)}} \cos \left( \frac{\pi\ell-2\pi}{3} \right) \right]^2 \quad (\text{A.15})$$

Where we have used  $\sin \pi/3 = \sin 2\pi/3 = \sqrt{3}/2$ . The cosine terms will cause some oscillations in the  $C_\ell$  values that depend on their  $\ell$  value, however as they are bounded between  $[-1, +1]$ , we can simply label their values as  $\alpha$  and  $\beta$ , as they will only contribute to  $\mathcal{O}(1)$  corrections, and no impact the  $\ell$  scaling of the  $C_\ell$  values. Therefore, this gives us

$$C_\ell = \frac{\pi}{(2\ell+1)^2} \left[ \frac{2}{\sqrt{\sqrt{3}\pi(\ell-1)}} \alpha + \frac{2}{\sqrt{\sqrt{3}\pi(\ell+1)}} \beta \right]^2 \quad (\text{A.16})$$

If we take  $\ell \gg 1$ , we find the  $C_\ell$  values as approximately

$$C_\ell \simeq \frac{\pi}{4\ell^2} \left[ \frac{2}{\sqrt{\sqrt{3}\pi\ell}} (\alpha + \beta) \right]^2, \quad (\text{A.17})$$

$$C_\ell \propto \frac{1}{\ell^3}. \quad (\text{A.18})$$

Thus we find that the  $C_\ell$  values go as  $1/\ell^3$ , and thus when we plot  $\ell(\ell+1)C_\ell$  we find their values scale as  $1/\ell$ .

Additionally, we note that for our simple mask, the cosine terms in Equation A.15 scale as  $\ell\pi/3$ , and thus repeat with a period of  $\ell \rightarrow \ell' = \ell + 6$ . Hence, when we plot the  $C_\ell$  values of our mask, we can plot them starting at  $\ell = 2$ ,  $\ell = 4$ , and  $\ell = 6$ , and take each starting point up in multiples of six. This cancels out the effects of the oscillations by plotting them separately, and thus we are able to discern the overall  $1/\ell$  scaling behaviour more clearly.

We plot the power spectrum of our simple mask in Figure A.2

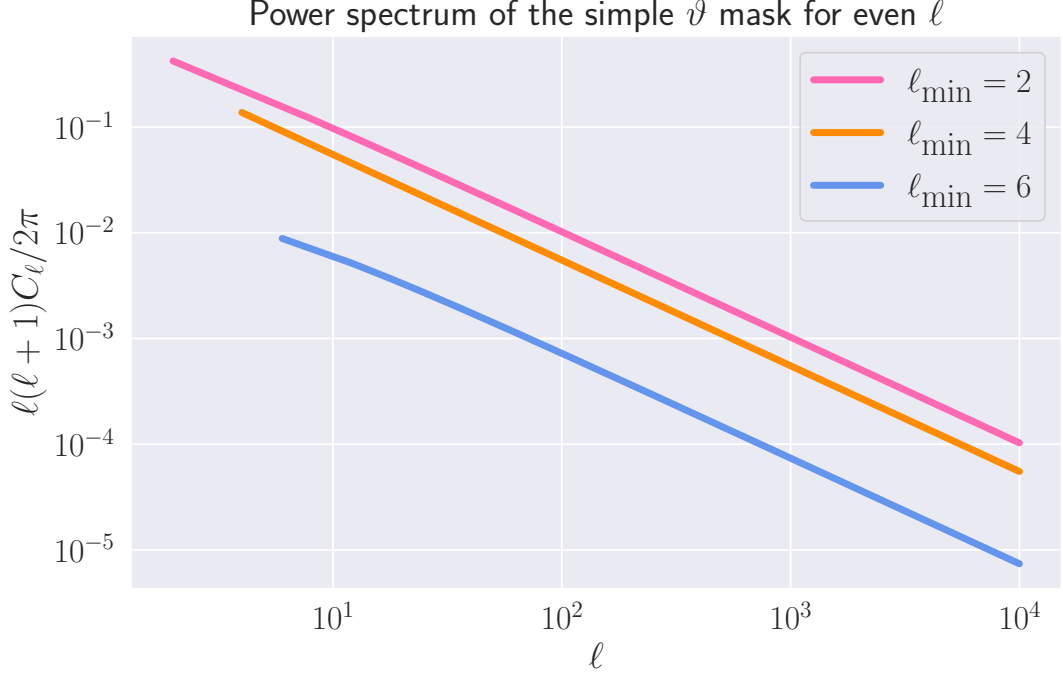


Figure A.2: The power spectrum of our simple binary mask shown in Figure A.1 and computed in Equation A.13. We start from our three starting  $\ell$  positions as demonstrated in Equation A.15, increasing in steps of six. We note the clear  $1/\ell$  behaviour which is shown in Equation A.18. These  $C_\ell$  values computed theoretically are in perfect agreement to their numerical counterpart computed using `healpy`.

## A.2 The convolution of power from masking

When we derived the properties of the Pseudo- $C_\ell$  estimator in Section 5.2.4, the power spectrum of the mask was key to understanding the mixing matrix, which quantifies how different modes on the unmasked-sky couple together when we apply a mask. We can now demonstrate this mode-coupling visually, by investigating how different masks convolve the power spectrum in slightly different ways.

Using a fiducial power spectrum where we have power only for a single multipole, say  $\ell = 50$ , we can generate a map using this input spectrum, apply the mask, and then compute its masked spectrum. By using only a single active multipole in the original spectrum, this is completely analogous to taking a one-dimensional slice of the mixing matrix  $\mathbf{M}_{\ell\ell'}$  at constant  $\ell'$  [218].

Figure A.3 plots the recovered spectra using two masks: a simple mask featuring two cuts in the galactic and ecliptic plane (approximating the necessary cuts to block the Milky Way and our Solar System, respectively); and a final-mission *Euclid*-like space-based survey, which includes masking out of discrete objects such as the Magellanic Clouds and bright stars. We see that the additional objects in our *Euclid*-like mask induce additional coupling for odd- $\ell$  increments over our simple mask, though is still dominated by even- $\ell$  contributions.

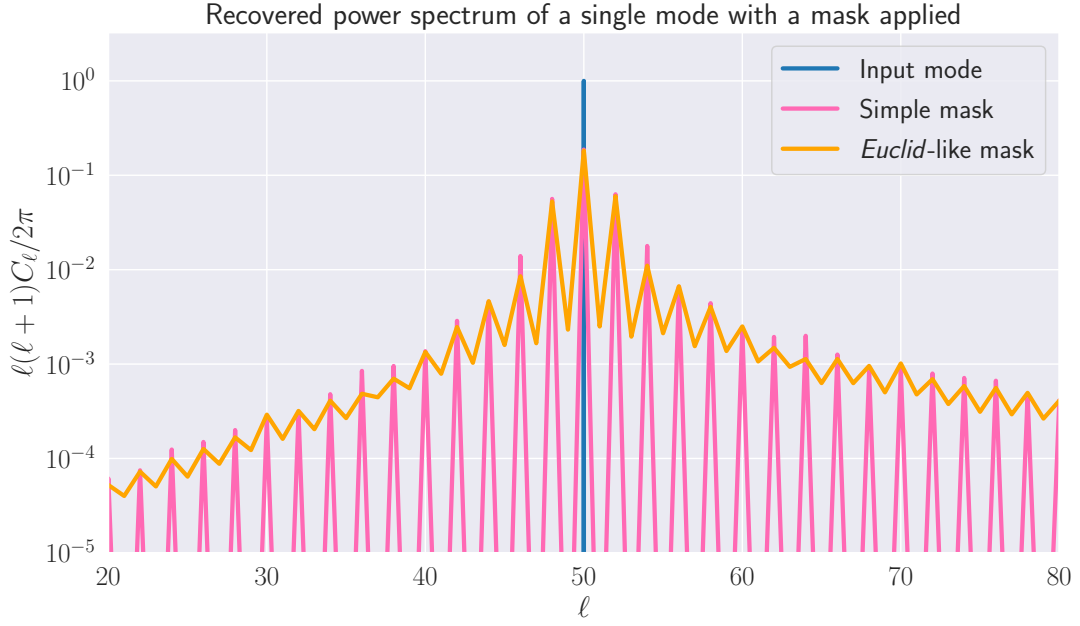


Figure A.3: One-dimensional slices of the Pseudo- $C_\ell$  mixing matrix  $\mathbf{M}_{\ell\ell'}$ , with  $\ell' = 50$ . We see strong support for even  $\ell$  increments, which stem from how both mask's have approximate  $\vartheta$  symmetry, and so their power spectra are suppressed for odd  $\ell$  multipoles. The additional features in the *Euclid*-like mask serve to increase the coupling for odd  $\ell$  intervals over our simple mask. We note that the convolved power produces an asymmetric masked spectrum, with an increased tail out to larger  $\ell$  values. Hence, when one deconvolves the mixing matrix, higher-order multipoles should be computed and included in the inversion, and then cut down post-inversion.

*The neutrinos have mutated,  
and they're heating up the planet!*

—2012

*Oh, I can spend the rest of my life  
having this conversation. Now, please,  
please try to understand before one of us dies.*

—Fawlty Towers



# Dark energy, massive neutrinos, and their impact on cosmology

---

**Outline.** Appendix highlighting the impact of the ‘dark sector’, that is dark energy and massive neutrinos, on the growth of structure within our Universe, their impact on cosmic shear, and how we can observe these physical phenomena.

## B.1 Dark energy

The driving force behind this thesis has been to maximise the information content from weak lensing galaxy surveys, such that we can obtain as much constraining power on the physics and contents of our Universe as possible. Of particular importance has been to constrain the properties of dark energy, which is some cosmological fluid with a negative equation of state such that it provides the accelerated expansion that has been observed in the late-time Universe. The simplest explanation of dark energy is that it is the effect of the cosmological constant  $\Lambda$  that can be included in the Einstein equations (Equation 2.1), and thus  $\Lambda$  is some fundamental property of spacetime which does not evolve with time nor is positional dependant. While we are free to include  $\Lambda$  in the Einstein equations, which gives us the accelerated expansion as observed in the late-time Universe, including  $\Lambda$  as the source of dark energy is not entirely theoretically satisfying since many unanswered questions arise from its inclusion, such as why does  $\Lambda$  has the value that it has, and does it link in anyway to the hypothesised inflationary epoch in the very early Universe?

Hence, there have been huge efforts in cosmology over the past two decades since the first detections of the accelerated expansion to narrow down the properties of dark energy, and to provide well-motivated theoretical explanations for its existence. The primary goal of these observational searches have been to determine if there is any time evolution in the value of  $\Lambda$ , and thus it wouldn’t be a true cosmological constant. This motivates the reparametrisation of the dark energy equation of state ( $w_\Lambda$ ) into the time-dependant form of [53, 54, 351]

$$w_\Lambda(a) = w_0 + w_a \times (1 - a), \quad (\text{B.1})$$

where  $w_0$  is the value today and  $w_a$  encodes the scale factor dependence.

In keeping with the rest of this thesis, we shall denote  $\Lambda$  to mean any dark energy fluid, even if it is not a true cosmological constant.



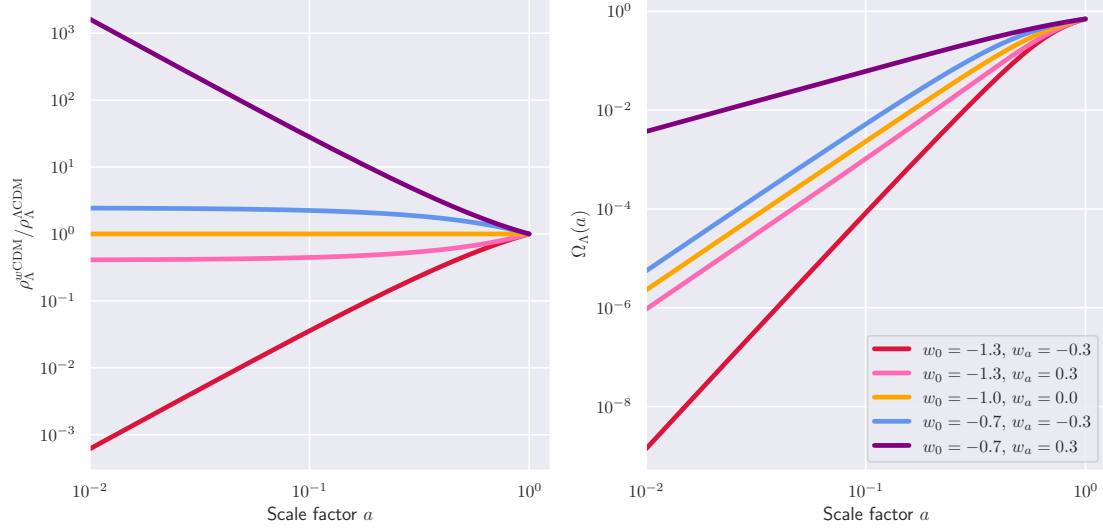


Figure B.1: The physical density of time-evolving dark energy models relative to that of a cosmological constant (left panel) and dark energy density parameters (right panel) for five combinations of  $w_0$  and  $w_a$  values, where the orange curve corresponds to the cosmological constant  $\Lambda$ . We see that more positive values for the equation of state give higher dark energy densities over the Universe’s evolution, and more negative values giving smaller dark energy densities. We see that the densities for the pink and blue curves track the cosmological constant at earlier times, since their equation of states tend to that of the cosmological constant,  $w_\Lambda \rightarrow -1$  as  $a \rightarrow 0$ , only differing in the late-time Universe ( $a \rightarrow 1$ ). The purple and red curves do not have such asymptotic trends of their equation of state, and thus exhibit large deviances in their densities in the early Universe. Note that we require all models to have the same dark energy density today.

Figure B.1 plots the relative physical density and density parameter of dark energy for five different evolutions of the equation of state. Here, we see that more positive values for the equation of state’s evolution gives larger dark energy densities in the past. In particular, for models whose equations of state do not tend to  $-1$  as  $a \rightarrow 0$  give large deviances from the prediction of the cosmological constant  $\Lambda$ . Hence, any cosmological observations that probe the evolution of the dark energy or total energy densities over cosmic time (such as through the evolution of the Hubble rate,  $H(z)$ ) will be sensitive to the values of  $w_0$  and  $w_a$ . Though, as Figure B.1 shows, the varying of  $w_0$  and  $w_a$  values only slightly modifies the dark energy density, particularly out to redshift  $z \sim 2$  (which is the limit that most cosmological surveys are sensitive out to) and for the case that  $w_\Lambda \rightarrow -1$  as  $a \rightarrow 0$ . Hence, high-quality precision measurements are needed over a wide range of redshifts to place meaningful constraints on  $w_0$  and  $w_a$ .

With this in mind, cosmological surveys over the last two decades have been designed from the ground up to place tight constraints on  $w_0$  and  $w_a$ . These have primarily arisen from the mid-2000s Dark Energy Task Force [205] which discussed and recommended the best approaches for placing tight constraints on  $w_0$  and  $w_a$ . As we will see, dark energy both modifies the distance-redshift relation through a modification of the background dynamics of the Universe, and the suppression in the growth of structure thanks to the additional expansion. Since weak lensing is sensitive to both effects, it is a prime candidate to measure the evolution of dark energy, as we shall see in this Appendix.

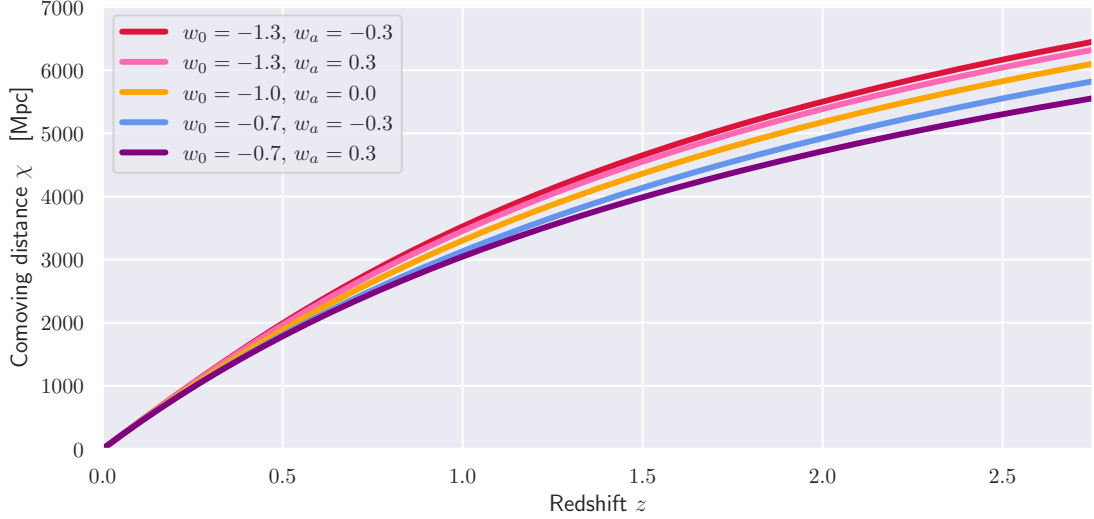


Figure B.2: The distance-redshift relation for five different combination of  $(w_0, w_a)$  values, where the orange curve represents that of the cosmological constant  $\Lambda$ . We see that for more positive values of the equation of state (such as the blue and purple curves), which represents an increase in the historic dark energy density over the evolution of the universe, yield a smaller comoving distance for a given redshift when compared to the cosmological constant, and a larger distance for more negative equations of state (pink and red curves). Constraining the distance-redshift relation to higher redshifts, where the difference between dark energy models is greatest, will help in determining the values of  $w_0$  and  $w_a$  of our Universe.

### B.1.1 The distance-redshift relation

One of the major impacts of dark energy is that it affects the cosmological distance-redshift relation. After all, it was through the use of this relation that the existence of dark energy was discovered! Hence, any observable that uses this relation will also be sensitive to the amount and evolutionary history of the dark energy fluid. For example, if distant galaxies are receding away from us at a greater rate, then a given redshift will actually correspond to a closer comoving distance (via Hubble's law) compared to smaller receding rates. Therefore, dark energy has a crucial role in the cosmological distance-redshift relation and so it is worth investigating how evolving dark energy models modify this relation.

In a universe that features evolving dark energy, such that its equation of state follows Equation B.1, then the distance-redshift relation is given by [352]

$$\chi(z) = \frac{1}{H_0} \int_0^z dz' \left[ \Omega_M(1+z')^3 + \Omega_\Lambda(1+z')^{3(1+w_0+w_a)} e^{-3w_a \frac{z'}{1+z'}} \right]^{-\frac{1}{2}}. \quad (\text{B.2})$$

Hence, we can see that for any universe where  $w_0 \neq -1$  and  $w_a \neq 0$ , there is a redshift dependence to the dark energy density, and so constraining the distance-redshift relation will allow us to directly probe these parameters.

Figure B.2 plots the distance-redshift relation for five different combinations of  $w_0$  and  $w_a$ , where the orange curve corresponds to the cosmological constant  $\Lambda$ . We see that for universes where  $w > -1$ , which corresponds to a greater dark energy density in the universe's past, a given redshift is actually closer to us. If we use the low-redshift approximation of Hubble's law ( $z = H_0 d$ ), then if we have increased accelerated expansion from dark energy (a higher  $H_0$ ) then a source must be closer (smaller distance  $d$ ) for a given redshift  $z$ , and vice-versa. This distance-redshift relation is utilised extensively in

weak lensing, specifically in the lensing kernels and the redshift to evaluate the matter power spectrum at, and so the impact of the changing distance-redshift relation on weak lensing will be investigated next.

### B.1.2 Dark energy in weak lensing

Since this thesis has focused on weak lensing, and specifically the power spectrum of weak lensing as our observable of interest, it is natural to enquire how evolving dark energy models change our observables — and thus if cosmic shear can discern between models of dark energy. First, let us recall the definition of the cosmic shear angular power spectrum (Equation 3.68), which was the Limber integral of the matter power spectrum  $P(k, z)$  weighted by the lensing kernels  $g_a(\chi)$ , and given as

$$C_\ell^{ab} = \frac{9\Omega_M^2 H_0^4}{4} \int_0^{\chi_{\text{MAX}}} d\chi \frac{g_a(\chi) g_b(\chi)}{a^2(\chi)} P\left(k = \frac{\ell}{f_k(\chi)}, z = z(\chi)\right). \quad (\text{B.3})$$

Hence, information about the physics and properties of our Universe come from the combination of these two functions. Dark energy impacts both, since it alters the background dynamics and growth of structure in the Universe, and so information about dark energy in the angular power spectrum will come from the interplay between these two functions. We shall see how evolving dark energy impacts these functions next...

### B.1.3 The lensing kernel

The lensing kernel informs us about the efficiency of the intervening large-scale structure of the Universe at producing lensing distributions in the images of background galaxies. For a given perturbation in the distribution of matter, it produces the maximum distortion in the shapes of galaxies when it is half-way between the source and observer. Mathematically, they are written as an integral over the comoving distance as (Equation 3.44)

$$g(\chi) = \int_\chi^{\chi_{\text{MAX}}} d\chi' n(\chi') \frac{f_k(\chi' - \chi)}{f_k(\chi')}, \quad (\text{B.4})$$

where  $n(\chi)$  is the number density of source galaxies that were imaged. Normally, we assign the position of galaxies that are required in Equation B.4 through their photometric redshift  $z$ , since this is the direct observable. Thus, we require the use of the distance-redshift relation to transform their observed redshifts to comoving coordinate  $\chi$ . This is done through the relationship  $n(\chi)d\chi = n(z)dz$ , hence  $n(\chi) = n(z)\frac{dz}{d\chi}$ . Since this derivative is linked to the expansion history of the Universe through Equation B.2, the  $z$ - $\chi$  mapping is sensitive to the amount and properties of dark energy, and thus our lensing kernels are sensitive to this too.

Figure B.3 plots the lensing kernel as a function of comoving distance  $\chi$  and redshift  $z$  for five different combinations of  $w_0$  and  $w_a$  values. Since we measure the source galaxy positions through their redshift, the lensing kernels do not shift in redshift-space since the redshift observations are anchored observables and irrespective of  $w_0$  and  $w_a$  values. However, we still see that the amplitude of the lensing kernels decrease in redshift-space for models with increased historic dark energy density, since the photons from distant galaxies travel less physical distance and so decreased opportunities to encounter lensing distortions. When we look at the lensing kernels in comoving distance-space, then we see the direct effects of dark energy changing the distance-redshift relation. As now curves with an increased historic dark energy density correspond to a decreased comoving distance for fixed redshift, and so the lensing kernels loose support at much smaller comoving distances.

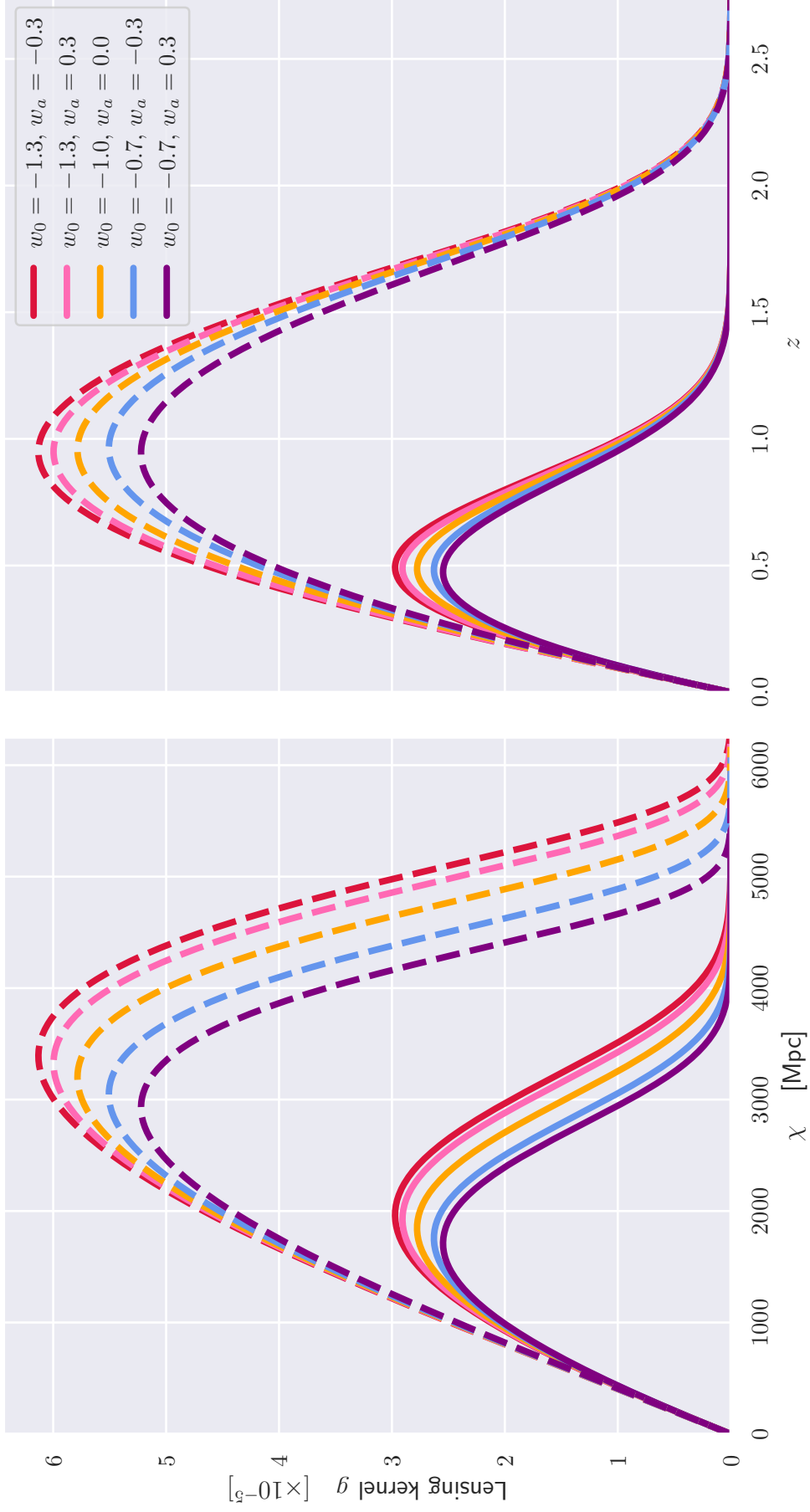


Figure B.3: Lensing kernels as a function of comoving distance  $\chi$  (left panel) and redshift (right panel) for five combinations of  $(w_0, w_a)$  values — where the orange curve corresponds to that of the cosmological constant  $\Lambda$ , and for two different Gaussian redshift bins centred at  $\bar{z} = 1$  (solid curves) and  $\bar{z} = 2$  (dashed curves). We see that changing  $w_0$  and  $w_a$  has a direct impact on the shape and amplitude of the lensing kernels, though their response in distance- and redshift-space is slightly different, as discussed in the text.

### B.1.4 The matter power spectrum

The second key ingredient to the cosmic shear angular power spectrum is the matter power spectrum, which is evaluated over a range of scales and redshifts. Since dark energy serves to accelerate the expansion of the Universe, it makes sense that an increased dark energy density hinders the ordinary gravitational attraction of matter, and thus the growth of structure is suppressed. This decreases the amplitude of the matter power spectrum, and thus decreases the amplitude of our lensing power spectrum. Just as we have done so for the distance-redshift relation and the lensing kernels, we would like to produce predictions for the matter power spectrum for a variety of dark energy evolutions and see the impact it has on the power spectrum. However, one subtlety here is the choice of amplitude normalisation, we can either use the amplitude of the primordial perturbations  $A_s$  (which is more suitable for early-Universe measurements, such as the CMB), or directly normalise the matter power spectrum through  $\sigma_8$  (which is more suitable for late-Universe measurements, such as galaxy clustering and weak lensing). By anchoring the amplitude of the perturbations to either the early or late Universe, the evolution behaviour of the matter power spectrum ratios with redshift changes quite significantly.

Figure B.4 plots the ratio of the matter power spectrum for four models of evolving dark energy to that of the cosmological constant at three redshifts, using either fixed  $A_s$  values (top panel) or fixed  $\sigma_8$  values (bottom panel). The choice of normalisation dramatically changes the evolution of the matter power spectrum with redshift:

- **Fixed  $A_s$ .** With the amplitude of the primordial perturbations fixed, the amplitude of the perturbations that we see in the late-time Universe are a direct result of the evolution of the initial conditions (Section 2.3). Hence, the growth of structure is subject to the background dynamics of the universe. In a universe with an increased dark energy density, the growth of structure is suppressed since the additional dark energy serves to increase the expansion rate, reducing the effect of gravitational collapse. This is why in Figure B.4, the blue and purple curves (which represent an increased historic dark energy density) feature suppression in their matter power spectra with respect to that of the cosmological constant, and that this suppression grows as structures evolve to the present time ( $z = 0$ ). In contrast, the pink and red curves (which represent a decreased historic dark energy density) feature an increase in their matter power spectra, and this increase grows as we evolve to redshift zero.
- **Fixed  $\sigma_8$ .** By fixing  $\sigma_8$  we are fixing the amplitude of the linear matter power spectrum at redshift zero. This is why all four dynamical dark energy models converge at unity around  $k \sim 10^{-2} h\text{Mpc}^{-1}$ . If we are fixing the amplitude today and are in a universe where the perturbations evolve slower than for the cosmological constant (as is the case for increased dark energy), then the amplitude of the perturbations must have been larger in the past, since they evolve more slowly. Hence, we now see that the blue and purple curves predict an excess in power on all scales at higher redshifts, which is in constant to when we fixed  $A_s$ . The reverse effect happens for models with decreased dark energy density (pink and red curves), as now the perturbations can evolve quicker and thus have a smaller amplitude at higher redshifts.

Since the choice of normalisation can have quite a dramatic effect on the evolution of the matter power spectrum (whether we evolve forwards, using  $A_s$ , or backwards, using  $\sigma_8$ ) we should be extremely careful in comparing results for  $A_s$  and  $\sigma_8$  in models of time-evolving dark energy.

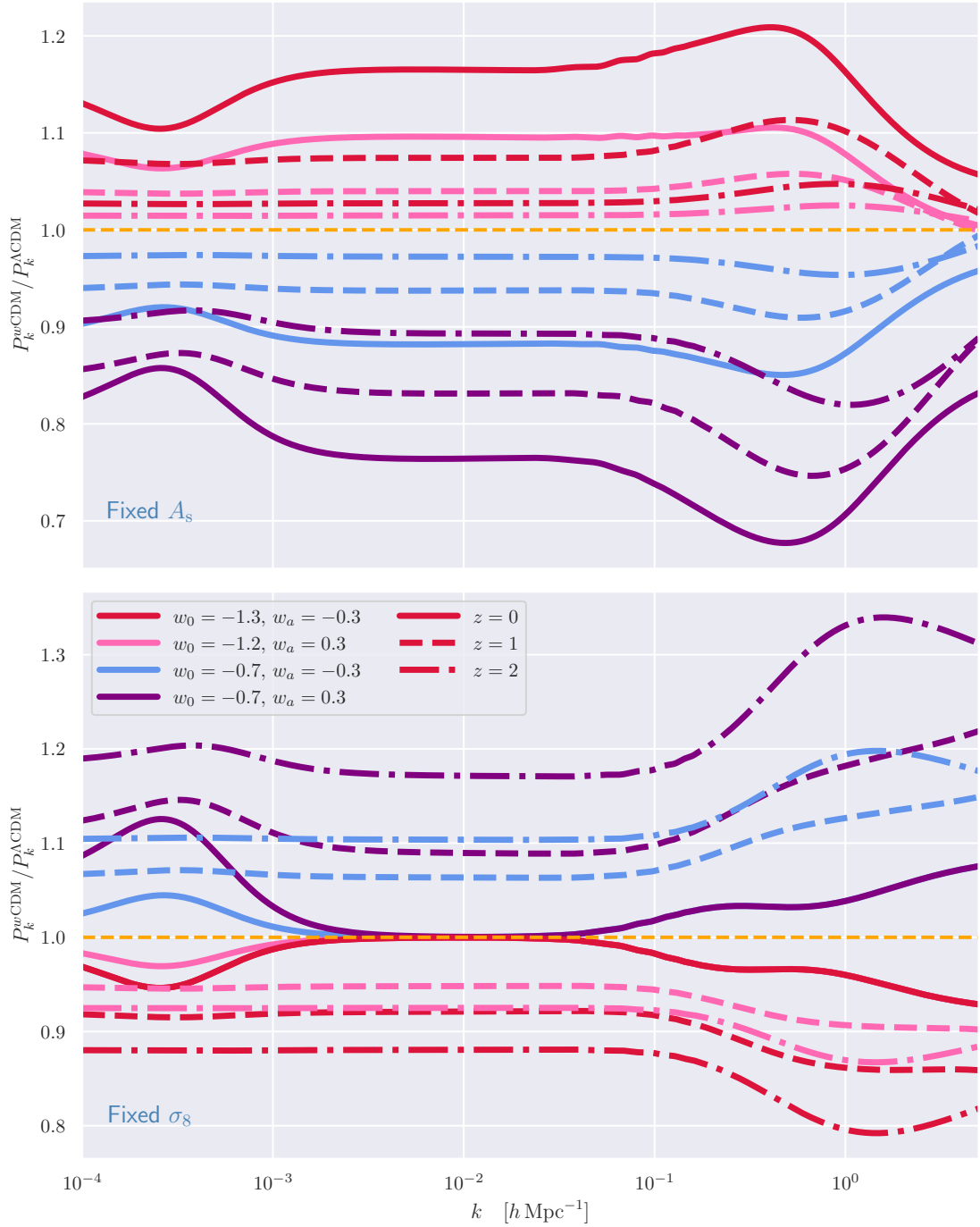


Figure B.4: Ratio of the matter power spectrum for four models of time-evolving dark energy densities to the matter power spectrum for the cosmological constant, where we have fixed  $A_s$  in the upper panel and  $\sigma_8$  in the lower panel, and for three redshifts. Here, we see the difference between anchoring the amplitude of the density perturbations in either the early ( $A_s$ ) or late ( $\sigma_8$ ) universe. For the case of anchoring  $A_s$ , we see that the differences in the  $P(k)$  grow with redshift, whereas anchoring  $\sigma_8$  we are fixing the amplitude at  $z = 0$  on linear scales where the background dynamics predict large deviances at higher redshifts. Hence, when using models of time-evolving dark energy we should be careful which amplitude we fix.

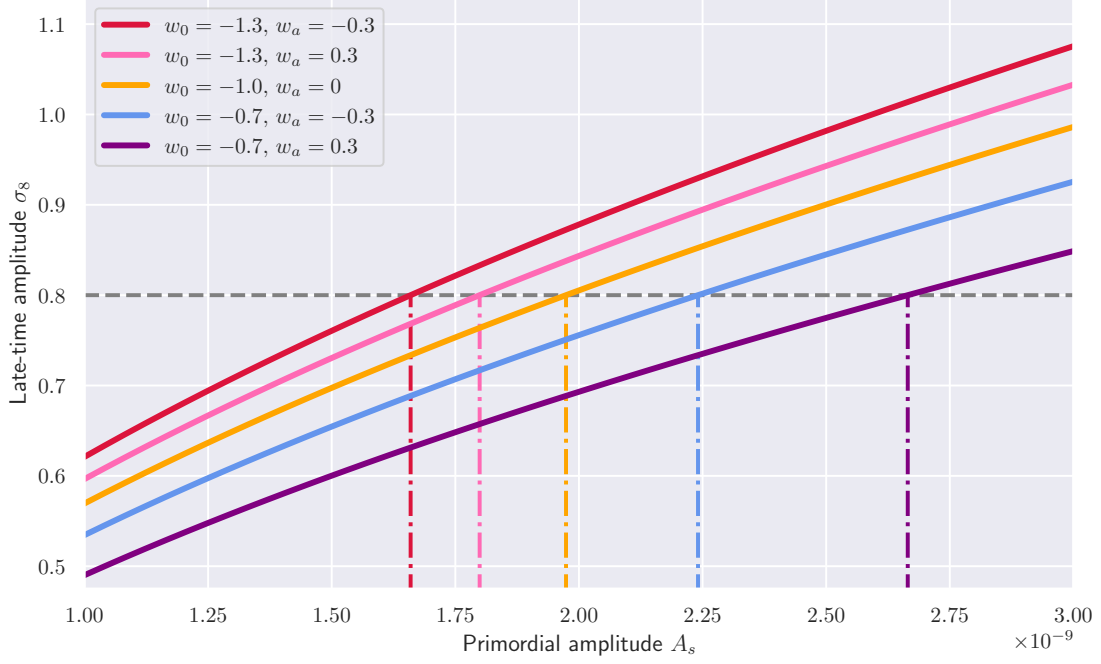


Figure B.5: The relationship between the late-time amplitude  $\sigma_8$  to the primordial amplitude  $A_s$  for five different dark energy evolutionary models, where the orange curve corresponds to the cosmological constant. While we see that each curve follows the basic trend, that  $\sigma_8 \propto \sqrt{A_s}$ , the normalisation is sensitive to the dark energy dynamics. Models which feature a larger dark energy densities require a larger primordial amplitude  $A_s$  for a given value of  $\sigma_8$  observed today, as shown in the dot-dashed lines. Hence, constraining  $A_s$  and  $\sigma_8$  individually would allow us to constrain the time-evolution of dark energy.

### B.1.5 The $A_s$ – $\sigma_8$ relation

For an otherwise fixed cosmology, there exists a one-to-one mapping between  $A_s$  and  $\sigma_8$ , given by  $A_s \propto \sigma_8^2$ . While this general relationship is still true for any universe with a time-evolving dark energy field, the exact constant of proportionality changes when compared to the cosmological constant model of dark energy. Figure B.5 plots this relationship between the primordial and late-time amplitudes for our five models of dynamical dark energy. We see that for a fixed value of  $\sigma_8$  that is observed today, models that feature a decreased historic dark energy (such as the pink and red curves) require a lower value of the primordial amplitude when compared to that of the cosmological constant. This shows that the growth of structure is much more efficient in these models which feature decreased dark energy densities.

To demonstrate this further, we can plot the evolution of the the late-time matter perturbation amplitude  $\sigma_8$  as a function of redshift, i.e.  $\sigma_8(z)$ , where we independently fix either  $A_s$  or  $\sigma_8$ . This is shown in Figure B.6 where we see that when  $A_s$  is fixed, the different background dynamics of the dark energy models lead to suppressed or enhanced clustering strength compared to that of the cosmological constant and so give different values for  $\sigma_8$  at  $z = 0$ . However, when we fix the value of  $\sigma_8$  at  $z = 0$ , we require different primordial amplitudes since the structure formation efficiency has been altered. Since cosmic shear is sensitive to the growth of structure over the Universe’s evolution, it should be able to discern models of evolving dark energy and their  $w_0$  and  $w_a$  parameters.



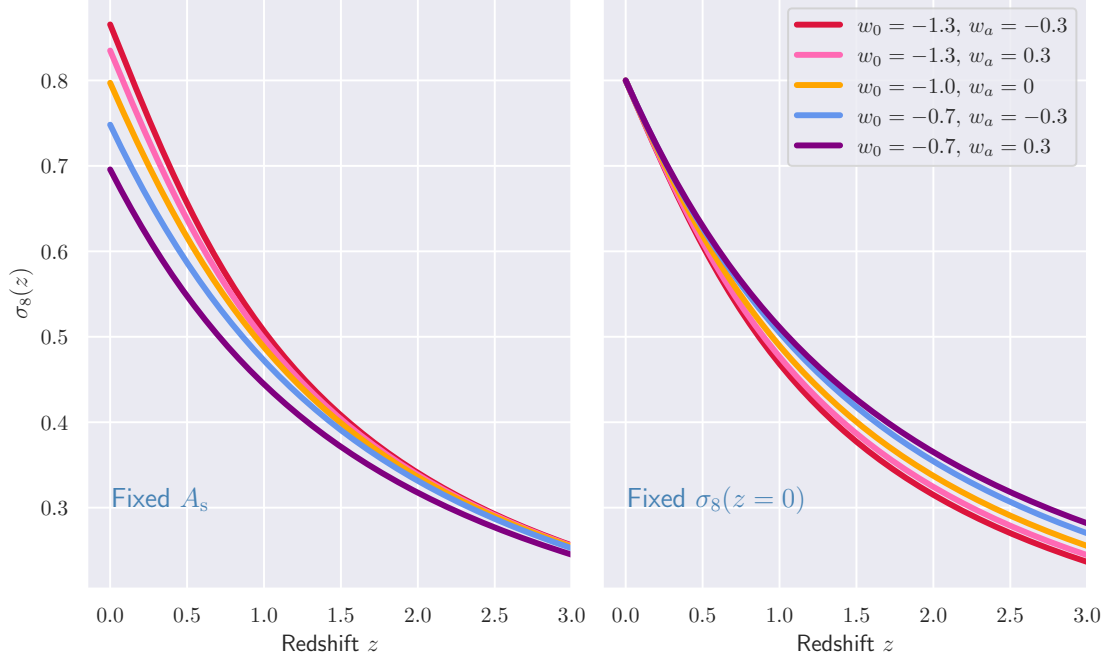


Figure B.6: The evolution in the late-time matter perturbation parameter  $\sigma_8$  as a function of redshift for five different dark energy evolutionary models, where we have either fixed the value of the primordial perturbation amplitude (left panel) or the value of  $\sigma_8$  observed today (right panel).

### B.1.6 Cosmic shear angular power spectrum

Now that we know that dark energy effects both the weak lensing kernels and the matter power spectrum, we can quantify the effects of dynamical dark energy models on the cosmic shear angular power spectrum. Since we found that by choosing to fix either  $A_s$  or  $\sigma_8$  had a dramatic effect on the evolution of the matter power spectrum, we can predict that this choice will also have an impact on the cosmic shear power spectrum too. Hence, we can fix them individually and see how the  $C_\ell$  values react in models of dynamical dark energy.

Figure B.7 plots the ratios of the cosmic shear angular power spectrum for four models of dynamical dark energy to that of the cosmological constant for two Gaussian redshift bins. For the case where we fix  $A_s$ , we see an almost scale-invariant enhancement or suppression in the angular power spectrum for models with a decreased or increased historic dark energy density, respectively. This arises due to the lensing kernels and matter power spectrum both scaling the same way with variable dark energy density using fixed  $A_s$ . However, when we change to fixing  $\sigma_8$  instead, we see that the ratios become much more  $\ell$ -dependant and that the amplitude of the enhancement or suppression becomes much smaller. This is because now the lensing kernels and matter power spectrum act in opposite directions to the effects of evolving dark energy, and so give rise to the curves seen. We also see that the ratios also diverge with increasing redshift (the centre of bin  $a$  is closer than that of bin  $b$ ), which make sense given that dark energy is a late-time effect, and so lower redshift sources will be more susceptible to variable dark energy than higher redshift sources. Note that time-evolving dark energy also affects the redshift that the matter power spectrum is evaluated over in the  $C_\ell$  Limber integral, since it is evaluated at  $z = z(\chi)$  — thus dependent on the distance-redshift relation — which further alters the  $C_\ell$  values and their distribution across redshift bins.



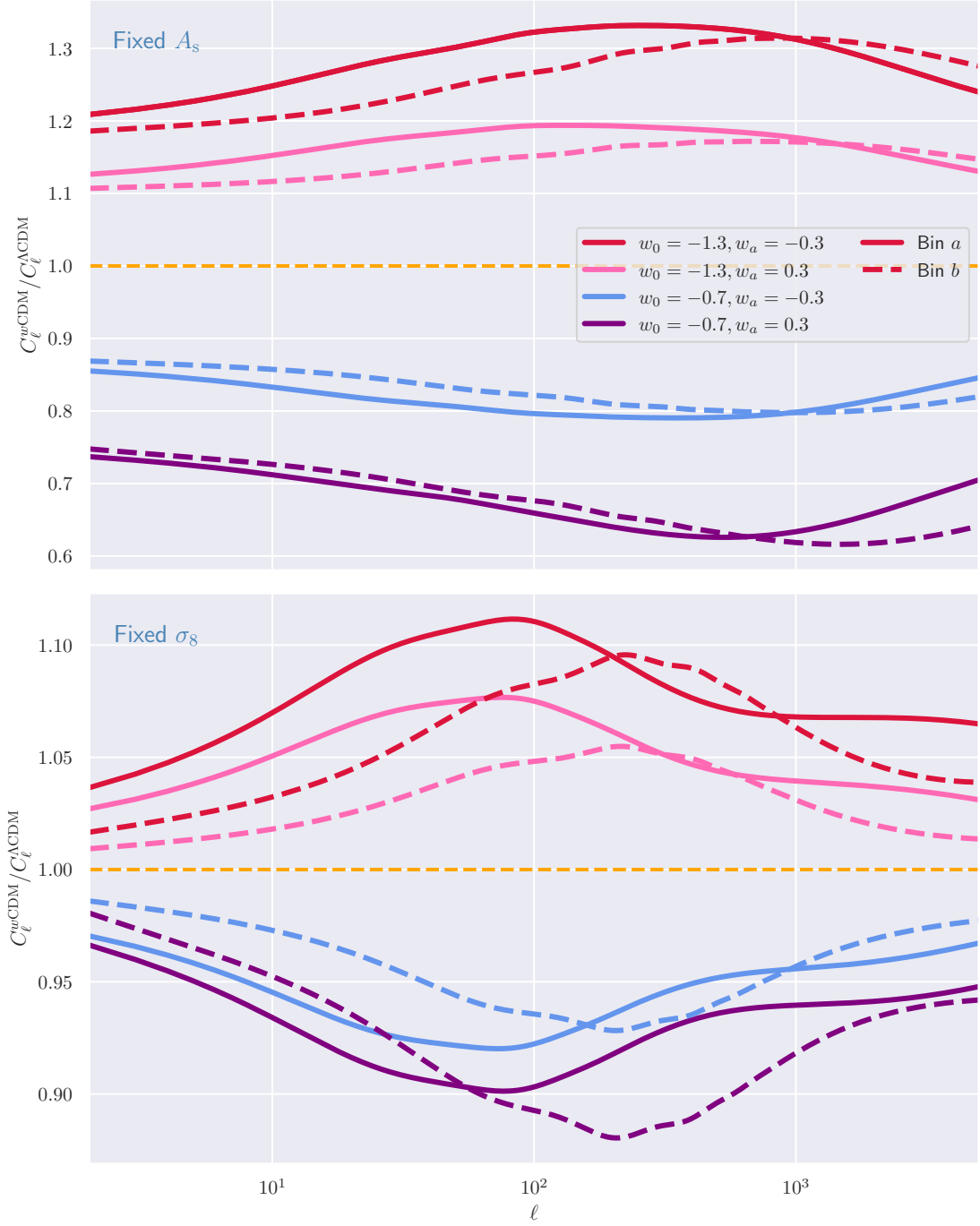


Figure B.7: Ratio of the cosmic shear angular power spectrum for four models of time-evolving dark energy to that of the cosmological constant, where we have fixed  $A_s$  in the upper panel and  $\sigma_8$  in the lower panel, and for two Gaussian redshift bins centred at  $\bar{z} = 0.5$  (solid curves) and  $\bar{z} = 2.0$  (dashed curves). When fixing  $A_s$ , we see almost scale-invariant growth or suppression in the angular power spectrum for models with decreased or increased dark energy densities, respectively. This is a result of how the lensing kernels and matter power spectrum both scale together with the dark energy density when fixing  $A_s$ . However, when we fix  $\sigma_8$ , the lensing kernels and matter power spectrum react to changing dark energy densities in opposite ways. Hence, we see an increased  $\ell$ -dependence to the ratios and that the size of the ratios decreased when compared to the fixed  $A_s$  ratios, since the two contributions somewhat cancel each other out.

## B.2 Neutrinos

In addition to placing tight constraints on the evolution of dark energy, forthcoming Stage-IV cosmic shear surveys are prime candidates to place tight constraints on the properties of neutrino, through their impact on cosmological observables. Neutrinos, whose name were dubbed by Enrico Fermi meaning *little neutral one* in humorous and grammatically incorrect Italian [353], are neutral leptonic elementary particles that interact via the weak nuclear and gravitational forces. The Standard Model of particle physics predicts that neutrinos come in three flavours: the electron neutrino, the muon neutrino, and the tauon neutrino — in analogy to the charged leptonic particles — and this has been experimentally confirmed by accelerator experiments [354].

Neutrino oscillation experiments are sensitive to the squared mass differences in the individual neutrino masses, that is  $\Delta m_{ab}^2 = m_a^2 - m_b^2$ , and have shown that at least two of the neutrino flavours are massive [65]. Cosmological observations are sensitive to the total neutrino mass,  $\Sigma m_\nu$ , and so provide an excellent compliment to the oscillation experiments in constraining the neutrino masses. Cosmology is also sensitive to the effective number of neutrinos,  $N_{\text{eff}}$ , which is given by  $N_{\text{eff}} = 3.044$  for the Standard Model [355].

Massive neutrinos impact cosmology in two distinct ways since their small, but non-zero, mass means that they act as relativistic particles in the early universe, and then transition to being non-relativistic in the later universe — the only such particles to undergo such transition [55]. When neutrinos are relativistic in the early universe, they free-stream over large distances. This suppresses the gravitational clustering of matter, and thus causes a suppression in the matter power spectrum on small scales. The amplitude of suppression is given by approximately  $P^{\Sigma m_\nu}(k)/P^{0m_\nu}(k) = 1 - 8f_\nu$ , where  $f_\nu = \Omega_{\nu,0}/\Omega_{\text{m},0}$  is the neutrino mass fraction [356]. When neutrinos become non-relativistic, they act the same way as baryons and dark matter do, and hence affect the background expansion rate of the universe and slightly alter observables such as the distance-redshift relation. Therefore, cosmology (and in particular the Stage-IV surveys) are prime candidates for measuring neutrino properties [357].

Figure B.8 plots the ratios of the matter power spectrum (top panel) and cosmic shear angular power spectrum (bottom panel) for three cosmologies with different non-zero neutrino masses with respect to that of massless neutrinos. We see the confirmation of the linear approximation, that the matter power spectrum is suppressed on small scales due to neutrino free-streaming, and that the amplitude of suppression scales with the neutrino masses. This suppression in the matter power spectrum then directly feeds into a suppression in the cosmic shear angular power spectrum, though now this is convolved with the effects of neutrino masses in the lensing kernels thanks to the slightly altered background dynamics.

## B.3 Summary

We have seen that the properties of time-evolving dark energy and massive neutrinos both affect the cosmic shear angular power spectrum in their own ways, with particular impact on small angular scales. Hence, an accurate and precise determination of the experimental power spectrum from observations, coupled with robust theoretical modelling of physical phenomena such as baryonic feedback and the determination of associated scale-cuts will ensure that the constraints on evolving dark energy and neutrinos are unbiased and precise as possible. Both of which have been discussed heavily in this thesis, and showing how the application of techniques developed here can be used to maximise information from weak lensing analyses.

*Tara procrastinators!*

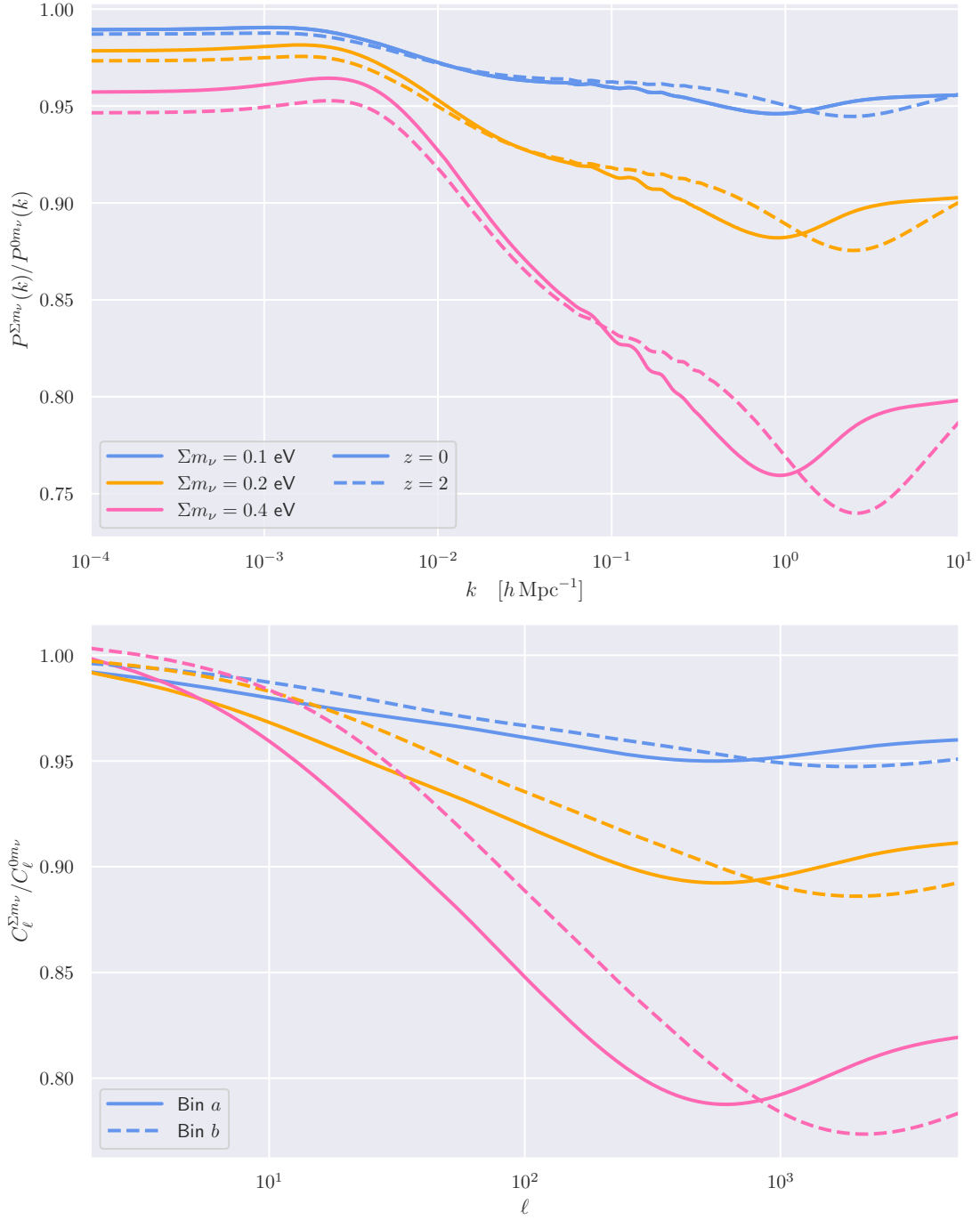


Figure B.8: Ratio of the matter power spectrum (top panel) and cosmic shear angular power spectrum (bottom panel) for three models of non-zero neutrino masses with respect to that of zero neutrino masses, for two redshifts (in the  $P(k)$ ) and for two Gaussian redshift bins centred at  $\bar{z} = 0.5$  (solid curves) and  $\bar{z} = 2.0$  (dashed curves) for the  $C_\ell$  values. We see that increasing the neutrino masses directly increases the suppression in the clustering on small scales. Hence, accurately measuring the cosmic shear angular power spectrum down to small scales will enable tight constraints on the neutrino masses. Ratios computed for an otherwise fixed cosmology for a flat  $\Lambda$ CDM Universe that is compatible with observations.

If I have seen further,  
it is by standing on the shoulders of giants.  
—Isaac Newton

## References

---

- [1] A. Maraio, A. Hall and A. Taylor, *Testing quadratic maximum likelihood estimators for forthcoming Stage-IV weak lensing surveys*, *Mon. Not. Roy. Astron. Soc.* **520** (2023) 4836 [[2207.10412](#)].
- [2] A. Maraio, A. Hall and A. Taylor, *Mitigating baryon feedback bias in cosmic shear through a theoretical error covariance in the matter power spectrum*, *Mon. Not. Roy. Astron. Soc.* **537** (2025) 1749 [[2410.12500](#)].
- [3] C. R. Harris, K. J. Millman, S. J. van der Walt, R. Gommers, P. Virtanen, D. Cournapeau et al., *Array programming with NumPy*, *Nature* **585** (2020) 357 [[2006.10256](#)].
- [4] P. Virtanen, R. Gommers, T. E. Oliphant, M. Haberland, T. Reddy, D. Cournapeau et al., *SciPy 1.0: Fundamental Algorithms for Scientific Computing in Python*, *Nature Methods* **17** (2020) 261 [[1907.10121](#)].
- [5] W. McKinney, *Data Structures for Statistical Computing in Python*, in *Proceedings of the 9th Python in Science Conference*, S. Van der Walt and J. Millman, eds., pp. 56 – 61, 2010, [DOI](#).
- [6] J. D. Hunter, *Matplotlib: A 2D Graphics Environment*, *Computing in Science & Engineering* **9** (2007) 90.
- [7] M. L. Waskom, *seaborn: statistical data visualization*, *Journal of Open Source Software* **6** (2021) 3021.
- [8] A. Lewis and S. Bridle, *Cosmological parameters from CMB and other data: A Monte Carlo approach*, *Phys. Rev. D* **66** (2002) 103511 [[astro-ph/0205436](#)].
- [9] A. Lewis, A. Challinor and A. Lasenby, *Efficient computation of CMB anisotropies in closed FRW models*, *Astrophys. J.* **538** (2000) 473 [[astro-ph/9911177](#)].
- [10] C. Howlett, A. Lewis, A. Hall and A. Challinor, *CMB power spectrum parameter degeneracies in the era of precision cosmology*, *JCAP* **04** (2012) 027 [[1201.3654](#)].
- [11] A. Lewis, *GetDist: a Python package for analysing Monte Carlo samples*, [1910.13970](#).
- [12] LSST DARK ENERGY SCIENCE collaboration, *Core Cosmology Library: Precision Cosmological Predictions for LSST*, *Astrophys. J. Suppl.* **242** (2019) 2 [[1812.05995](#)].

- [13] H. S. Xavier, F. B. Abdalla and B. Joachimi, *Improving lognormal models for cosmological fields*, *Mon. Not. Roy. Astron. Soc.* **459** (2016) 3693 [[1602.08503](#)].
- [14] N. Tessore, A. Loureiro, B. Joachimi, M. von Wietersheim-Kramsta and N. Jeffrey, *GLASS: Generator for Large Scale Structure*, *The Open Journal of Astrophysics* **6** (2023) [[2302.01942](#)].
- [15] K. M. Gorski, E. Hivon, A. J. Banday, B. D. Wandelt, F. K. Hansen, M. Reinecke et al., *HEALPix - A Framework for high resolution discretization, and fast analysis of data distributed on the sphere*, *Astrophys. J.* **622** (2005) 759 [[astro-ph/0409513](#)].
- [16] A. Zonca, L. Singer, D. Lenz, M. Reinecke, C. Rosset, E. Hivon et al., *healpy: equal area pixelization and spherical harmonics transforms for data on the sphere in Python*, *Journal of Open Source Software* **4** (2019) 1298.
- [17] LSST DARK ENERGY SCIENCE collaboration, *A unified pseudo- $C_\ell$  framework*, *Mon. Not. Roy. Astron. Soc.* **484** (2019) 4127 [[1809.09603](#)].
- [18] G. Guennebaud et al., “*Eigen v3*.” <http://eigen.tuxfamily.org>, 2010.
- [19] J. Zuntz, M. Paterno, E. Jennings, D. Rudd, A. Manzotti, S. Dodelson et al., *CosmoSIS: modular cosmological parameter estimation*, *Astron. Comput.* **12** (2015) 45 [[1409.3409](#)].
- [20] I. Newton, *Philosophiæ Naturalis Principia Mathematica*. England, 1687.
- [21] A. Einstein, *The Foundation of the General Theory of Relativity*, *Annalen Phys.* **49** (1916) 769.
- [22] A. Einstein, *Cosmological Considerations in the General Theory of Relativity*, *Sitzungsber. Preuss. Akad. Wiss. Berlin (Math. Phys. )* **1917** (1917) 142.
- [23] C. O’Raifeartaigh, M. O’Keeffe, W. Nahm and S. Mitton, *Einstein’s 1917 static model of the universe: a centennial review*, *Eur. Phys. J. H* **42** (2017) 431 [[1701.07261](#)].
- [24] V. M. Slipher, *Radial velocity observations of spiral nebulae*, *The Observatory* **40** (1917) 304.
- [25] S. Weinberg, *The first three minutes: A modern view of the origin of the Universe*. Basic Books, New York, 1993.
- [26] G. Lemaître, *The expanding universe*, *Mon. Not. Roy. Astron. Soc.* **91** (1931) 490.
- [27] H. S. Leavitt, *1777 variables in the Magellanic Clouds*, *Annals of Harvard College Observatory* **60** (1907) 87.
- [28] H. S. Leavitt and E. C. Pickering, *Periods of 25 Variable Stars in the Small Magellanic Cloud.*, *Harvard College Observatory Circular* **173** (1912) 1.
- [29] E. Hubble, *A relation between distance and radial velocity among extra-galactic nebulae*, *Proc. Natl. Acad. Sci. U.S.A.* **15** (1929) 168.
- [30] G. Lemaître, *A homogeneous universe of constant mass and increasing radius accounting for the radial velocity of extra-galactic nebulae*, *Mon. Not. Roy. Astron. Soc.* **91** (1931) 483.

- [31] F. W. Dyson, A. S. Eddington and C. Davidson, *A determination of the deflection of light by the sun's gravitational field, from observations made at the total eclipse of May 29, 1919*, *Phys. Trans. Roy. Soc. London* **220** (1920) 291.
- [32] M. Bartelmann and P. Schneider, *Weak gravitational lensing*, *Phys. Rept.* **340** (2001) 291 [[astro-ph/9912508](#)].
- [33] M. Kilbinger, *Cosmology with cosmic shear observations: a review*, *Rept. Prog. Phys.* **78** (2015) 086901 [[1411.0115](#)].
- [34] F. Zwicky, *Die Rotverschiebung von extragalaktischen Nebeln*, *Helvetica Physica Acta* **6** (1933) 110.
- [35] F. Zwicky, *Republication of: The redshift of extragalactic nebulae*, *General Relativity and Gravitation* **41** (2009) 207.
- [36] V. C. Rubin, J. Ford, W. K. and N. Thonnard, *Rotational properties of 21 SC galaxies with a large range of luminosities and radii, from NGC 4605 ( $R=4kpc$ ) to UGC 2885 ( $R=122kpc$ )*, *Astrophys. J.* **238** (1980) 471.
- [37] SUPERNOVA COSMOLOGY PROJECT collaboration, *Measurements of  $\Omega$  and  $\Lambda$  from 42 high redshift supernovae*, *Astrophys. J.* **517** (1999) 565 [[astro-ph/9812133](#)].
- [38] SUPERNOVA SEARCH TEAM collaboration, *Observational evidence from supernovae for an accelerating universe and a cosmological constant*, *Astron. J.* **116** (1998) 1009 [[astro-ph/9805201](#)].
- [39] O. Lahav and A. R. Liddle, *The Cosmological Parameters (2021)*, [2201.08666](#).
- [40] PLANCK collaboration, *Planck 2018 results. VI. Cosmological parameters*, *Astron. Astrophys.* **641** (2020) A6 [[1807.06209](#)].
- [41] P. Schneider, J. Ehlers and E. E. Falco, *Gravitational Lenses*, Astronomy and Astrophysics Library. Springer, Berlin, 1992, [DOI](#).
- [42] N. Kaiser and G. Squires, *Mapping the dark matter with weak gravitational lensing*, *Astrophys. J.* **404** (1993) 441.
- [43] N. Kaiser, G. Wilson and G. A. Luppino, *Large scale cosmic shear measurements*, [astro-ph/0003338](#).
- [44] D. J. Bacon, A. R. Refregier and R. S. Ellis, *Detection of weak gravitational lensing by large-scale structure*, *Mon. Not. Roy. Astron. Soc.* **318** (2000) 625 [[astro-ph/0003008](#)].
- [45] L. van Waerbeke et al., *Detection of correlated galaxy ellipticities on CFHT data: First evidence for gravitational lensing by large scale structures*, *Astron. Astrophys.* **358** (2000) 30 [[astro-ph/0002500](#)].
- [46] D. M. Wittman, J. A. Tyson, D. Kirkman, I. Dell'Antonio and G. Bernstein, *Detection of weak gravitational lensing distortions of distant galaxies by cosmic dark matter at large scales*, *Nature* **405** (2000) 143 [[astro-ph/0003014](#)].
- [47] M. P. Hobson, G. P. Efstathiou and A. N. Lasenby, *General relativity: An introduction for physicists*. Cambridge Univ. Pr., Cambridge, 2006, [DOI](#).

- [48] K. Schwarzschild, *On the Gravitational Field of a Mass Point According to Einstein's Theory*, *Sitzungsber. Preuss. Akad. Wiss. Berlin (Math. Phys.)* **1916** (1916) 189 [[physics/9905030](#)].
- [49] J. C. Mather et al., *Measurement of the Cosmic Microwave Background spectrum by the COBE FIRAS instrument*, *Astrophys. J.* **420** (1994) 439.
- [50] PLANCK collaboration, *Planck 2018 results. I. Overview and the cosmological legacy of Planck*, *Astron. Astrophys.* **641** (2020) A1 [[1807.06205](#)].
- [51] D. J. Griffiths, *Introduction to Electrodynamics*. Cambridge University Press, 5 ed., 2023, [DOI](#).
- [52] D. Huterer and M. S. Turner, *Prospects for probing the dark energy via supernova distance measurements*, *Phys. Rev. D* **60** (1999) 081301 [[astro-ph/9808133](#)].
- [53] E. V. Linder, *Exploring the expansion history of the universe*, *Phys. Rev. Lett.* **90** (2003) 091301 [[astro-ph/0208512](#)].
- [54] E. V. Linder, *Cosmic growth history and expansion history*, *Phys. Rev. D* **72** (2005) 043529 [[astro-ph/0507263](#)].
- [55] DESI collaboration, *DESI 2024 VI: Cosmological constraints from the measurements of baryon acoustic oscillations*, *JCAP* **02** (2025) 021 [[2404.03002](#)].
- [56] P. Schneider, *Extragalactic Astronomy and Cosmology: An Introduction*. Springer Berlin, Heidelberg, 2nd ed., 2015, [DOI](#).
- [57] G. Gamow, *The Evolution of the Universe*, *Nature* **162** (1948) 680.
- [58] PARTICLE DATA GROUP collaboration, *Review of particle physics*, *Phys. Rev. D* **110** (2024) 030001.
- [59] R. A. Alpher, H. Bethe and G. Gamow, *The origin of chemical elements*, *Phys. Rev.* **73** (1948) 803.
- [60] R. H. Dicke, P. J. E. Peebles, P. G. Roll and D. T. Wilkinson, *Cosmic black-body radiation*, *Astrophys. J.* **142** (1965) 414.
- [61] A. Liddle, *An Introduction to Modern Cosmology*. Wiley, Chichester, 3rd ed., 2015.
- [62] A. H. Guth, *The Inflationary Universe: A Possible Solution to the Horizon and Flatness Problems*, *Phys. Rev. D* **23** (1981) 347.
- [63] A. D. Linde, *A New Inflationary Universe Scenario: A Possible Solution of the Horizon, Flatness, Homogeneity, Isotropy and Primordial Monopole Problems*, *Phys. Lett.* **108B** (1982) 389.
- [64] K. A. Milton, *Theoretical and experimental status of magnetic monopoles*, *Rept. Prog. Phys.* **69** (2006) 1637 [[hep-ex/0602040](#)].
- [65] PARTICLE DATA GROUP collaboration, *Review of Particle Physics*, *PTEP* **2022** (2022) 083C01.
- [66] A. D. Linde, *Primordial Inflation Without Primordial Monopoles*, *Phys. Lett. B* **132** (1983) 317.
- [67] A. R. Liddle and S. M. Leach, *How long before the end of inflation were observable perturbations produced?*, *Phys. Rev. D* **68** (2003) 103503 [[astro-ph/0305263](#)].



- [68] S. Dodelson and L. Hui, *A Horizon ratio bound for inflationary fluctuations*, *Phys. Rev. Lett.* **91** (2003) 131301 [[astro-ph/0305113](#)].
- [69] B. Ryden, *Introduction to cosmology*. Cambridge University Press, Cambridge, 2nd ed., 2016, [DOI](#).
- [70] K. Marzouk, A. Maraio and D. Seery, *Non-Gaussianity in D3-brane inflation*, *JCAP* **02** (2022) 013 [[2105.03637](#)].
- [71] J. Torrado, C. T. Byrnes, R. J. Hardwick, V. Vennin and D. Wands, *Measuring the duration of inflation with the curvaton*, *Phys. Rev.* **D98** (2018) 063525 [[1712.05364](#)].
- [72] J. A. Peacock, *Cosmological Physics*. Cambridge University Press, 1998.
- [73] Z. Earnshaw, *Measurement of the one lepton final state of  $t\bar{t}Z$  with  $Z \rightarrow \nu\bar{\nu}$  with the ATLAS detector*, PhD thesis, University of Sussex, 2024. [DOI](#).
- [74] L. Kofman, A. D. Linde and A. A. Starobinsky, *Reheating after inflation*, *Phys. Rev. Lett.* **73** (1994) 3195 [[hep-th/9405187](#)].
- [75] D. H. Lyth and A. R. Liddle, *The Primordial Density Perturbation: Cosmology, Inflation and the Origin Of Structure*. Cambridge Univ. Pr., Cambridge, 2009.
- [76] A. R. Liddle and D. H. Lyth, *Cosmological inflation and large scale structure*. Cambridge Univ. Pr., Cambridge, 2000, [DOI](#).
- [77] D. Griffiths, *Introduction to Elementary Particles*. Wiley, 2nd ed., 2008, [DOI](#).
- [78] P. W. Higgs, *Broken Symmetries and the Masses of Gauge Bosons*, *Phys. Rev. Lett.* **13** (1964) 508.
- [79] F. Englert and R. Brout, *Broken Symmetry and the Mass of Gauge Vector Mesons*, *Phys. Rev. Lett.* **13** (1964) 321.
- [80] A. Djouadi and J. I. Illana, *Steven Weinberg and Higgs physics*, *Nucl. Phys. B* **1004** (2024) 116541 [[2401.07838](#)].
- [81] ATLAS collaboration, *Observation of a new particle in the search for the Standard Model Higgs boson with the ATLAS detector at the LHC*, *Phys. Lett.* **B716** (2012) 1 [[1207.7214](#)].
- [82] CMS collaboration, *Observation of a New Boson at a Mass of 125 GeV with the CMS Experiment at the LHC*, *Phys. Lett.* **B716** (2012) 30 [[1207.7235](#)].
- [83] S. Weinberg, *The Quantum theory of fields. Vol. 1: Foundations*. Cambridge Univ. Pr., Cambridge, 2005, [DOI](#).
- [84] S. Dodelson and F. Schmidt, *Modern Cosmology*. Academic Press, Amsterdam, 2nd ed., 2021, [DOI](#).
- [85] C. T. Byrnes, *Lecture notes on non-Gaussianity*, *Astrophys. Space Sci. Proc.* **45** (2016) 135 [[1411.7002](#)].
- [86] D. Wands, *Local non-Gaussianity from inflation*, *Class. Quant. Grav.* **27** (2010) 124002 [[1004.0818](#)].
- [87] D. H. Lyth and Y. Rodriguez, *The Inflationary prediction for primordial non-Gaussianity*, *Phys. Rev. Lett.* **95** (2005) 121302 [[astro-ph/0504045](#)].



- [88] N. Bartolo, E. Komatsu, S. Matarrese and A. Riotto, *Non-Gaussianity from inflation: Theory and observations*, *Phys. Rept.* **402** (2004) 103 [[astro-ph/0406398](#)].
- [89] P. Meszaros, *The behaviour of point masses in an expanding cosmological substratum*, *Astron. Astrophys.* **37** (1974) 225.
- [90] L. Amendola and S. Tsujikawa, *Dark Energy: Theory and Observations*. Cambridge University Press, 1, 2015, [DOI](#).
- [91] B. M. Schaefer, *Formation of the First Black holes: Formation and evolution of the cosmic large-scale structure*, [1807.06269](#).
- [92] J. Prat and D. Bacon, *Weak Gravitational Lensing*, [2501.07938](#).
- [93] I. Tkachev, *Cosmology and Dark Matter*, in *2016 European School of High-Energy Physics*, vol. 5, pp. 259–294, 2017, [[1802.02414](#)], [DOI](#).
- [94] F. Bernardeau, S. Colombi, E. Gaztanaga and R. Scoccimarro, *Large scale structure of the universe and cosmological perturbation theory*, *Phys. Rept.* **367** (2002) 1 [[astro-ph/0112551](#)].
- [95] B. Bahr-Kalus, D. Parkinson and E.-M. Mueller, *Measurement of the matter-radiation equality scale using the extended baryon oscillation spectroscopic survey quasar sample*, *Mon. Not. Roy. Astron. Soc.* **524** (2023) 2463 [[2302.07484](#)].
- [96] P. J. E. Peebles, *The Gravitational-Instability Picture and the Nature of the Distribution of Galaxies*, *Astrophys. J.* **189** (1974) L51.
- [97] P. J. E. Peebles, *The Large-Scale Structure of the Universe*. Princeton University Press, Princeton, 1980, [DOI](#).
- [98] U. Seljak, *Analytic model for galaxy and dark matter clustering*, *Mon. Not. Roy. Astron. Soc.* **318** (2000) 203 [[astro-ph/0001493](#)].
- [99] J. A. Peacock and R. E. Smith, *Halo occupation numbers and galaxy bias*, *Mon. Not. Roy. Astron. Soc.* **318** (2000) 1144 [[astro-ph/0005010](#)].
- [100] C.-P. Ma and J. N. Fry, *Deriving the nonlinear cosmological power spectrum and bispectrum from analytic dark matter halo profiles and mass functions*, *Astrophys. J.* **543** (2000) 503 [[astro-ph/0003343](#)].
- [101] M. Asgari, A. J. Mead and C. Heymans, *The halo model for cosmology: a pedagogical review*, *The Open Journal of Astrophysics* **6** (2023) [[2303.08752](#)].
- [102] VIRGO CONSORTIUM collaboration, *Stable clustering, the halo model and nonlinear cosmological power spectra*, *Mon. Not. Roy. Astron. Soc.* **341** (2003) 1311 [[astro-ph/0207664](#)].
- [103] R. Takahashi, M. Sato, T. Nishimichi, A. Taruya and M. Oguri, *Revising the Halofit Model for the Nonlinear Matter Power Spectrum*, *Astrophys. J.* **761** (2012) 152 [[1208.2701](#)].
- [104] A. Mead, J. Peacock, C. Heymans, S. Joudaki and A. Heavens, *An accurate halo model for fitting non-linear cosmological power spectra and baryonic feedback models*, *Mon. Not. Roy. Astron. Soc.* **454** (2015) 1958 [[1505.07833](#)].

- [105] A. Mead, C. Heymans, L. Lombriser, J. Peacock, O. Steele and H. Winther, *Accurate halo-model matter power spectra with dark energy, massive neutrinos and modified gravitational forces*, *Mon. Not. Roy. Astron. Soc.* **459** (2016) 1468 [[1602.02154](#)].
- [106] A. Mead, S. Brieden, T. Tröster and C. Heymans, *HMcode-2020: Improved modelling of non-linear cosmological power spectra with baryonic feedback*, *Mon. Not. Roy. Astron. Soc.* **502** (2021) 1401 [[2009.01858](#)].
- [107] THE EVENT HORIZON TELESCOPE collaboration, *First Sagittarius A\* Event Horizon Telescope Results. VII. Polarization of the Ring*, *The Astrophysical Journal Letters* **964** (2024) L25.
- [108] THE EVENT HORIZON TELESCOPE collaboration, *First Sagittarius A\* Event Horizon Telescope Results. VIII. Physical Interpretation of the Polarized Ring*, *The Astrophysical Journal Letters* **964** (2024) L26.
- [109] B. Balick and R. L. Brown, *Intense sub-arcsecond structure in the galactic center*, *Astrophys. J.* **194** (1974) 265.
- [110] S. W. Hawking, *A Brief History of Time: From the Big Bang to Black Holes*. Bantam Press, London, 1988.
- [111] C. Bambi, *Astrophysical Black Holes: A Review*, *Proc. of Sci.* **362** (2020) 028 [[1906.03871](#)].
- [112] LIGO SCIENTIFIC, VIRGO collaboration, *Observation of Gravitational Waves from a Binary Black Hole Merger*, *Phys. Rev. Lett.* **116** (2016) 061102 [[1602.03837](#)].
- [113] KAGRA, VIRGO, LIGO SCIENTIFIC collaboration, *GWTC-3: Compact Binary Coalescences Observed by LIGO and Virgo during the Second Part of the Third Observing Run*, *Phys. Rev. X* **13** (2023) 041039 [[2111.03606](#)].
- [114] GRAVITY collaboration, *Polarimetry and astrometry of NIR flares as event horizon scale, dynamical probes for the mass of Sgr A\**, *Astron. Astrophys.* **677** (2023) L10 [[2307.11821](#)].
- [115] EVENT HORIZON TELESCOPE collaboration, *First M87 Event Horizon Telescope Results. VI. The Shadow and Mass of the Central Black Hole*, *Astrophys. J. Lett.* **875** (2019) L6 [[1906.11243](#)].
- [116] X.-B. Wu, F. Wang, X. Fan, W. Yi, W. Zuo, F. Bian et al., *An ultraluminous quasar with a twelve-billion-solar-mass black hole at redshift 6.30*, *Nature* **518** (2015) 512 [[1502.07418](#)].
- [117] EUCLID collaboration, *Euclid Legacy Science prospects*, *PoS ICHEP2022* (2022) 096 [[2211.11709](#)].
- [118] S. E. I. Bosman, J. Álvarez-Márquez, L. Colina, F. Walter, A. Alonso-Herrero, M. J. Ward et al., *A mature quasar at cosmic dawn revealed by JWST rest-frame infrared spectroscopy*, *Nature Astronomy* **8** (2024) 1054 [[2307.14414](#)].
- [119] J. Yang et al., *A SPectroscopic Survey of Biased Halos in the Reionization Era (ASPIRE): A First Look at the Rest-frame Optical Spectra of  $z > 6.5$  Quasars Using JWST*, *Astrophys. J. Lett.* **951** (2023) L5 [[2304.09888](#)].

- [120] P. Padovani et al., *Active galactic nuclei: what's in a name?*, *Astron. Astrophys. Rev.* **25** (2017) 2 [[1707.07134](#)].
- [121] A. D. Gow, P. Clark and D. Rycanowski, *I'm in AGNi: A new standard for AGN pluralisation*, [2403.20302](#).
- [122] R. Levine and N. Y. Gnedin, *Active Galactic Nucleus Outflows and the Matter Power Spectrum*, *The Astrophysical Journal Letters* **649** (2006) L57 [[astro-ph/0604308](#)].
- [123] M. P. van Daalen, J. Schaye, C. M. Booth and C. D. Vecchia, *The effects of galaxy formation on the matter power spectrum: A challenge for precision cosmology*, *Mon. Not. Roy. Astron. Soc.* **415** (2011) 3649 [[1104.1174](#)].
- [124] B. R. McNamara and P. E. J. Nulsen, *Heating Hot Atmospheres with Active Galactic Nuclei*, *Ann. Rev. Astron. Astrophys.* **45** (2007) 117 [[0709.2152](#)].
- [125] A. C. Fabian, *Observational Evidence of AGN Feedback*, *Ann. Rev. Astron. Astrophys.* **50** (2012) 455 [[1204.4114](#)].
- [126] D. J. Croton, V. Springel, S. D. M. White, G. De Lucia, C. S. Frenk, L. Gao et al., *The Many lives of AGN: Cooling flows, black holes and the luminosities and colours of galaxies*, *Mon. Not. Roy. Astron. Soc.* **365** (2006) 11 [[astro-ph/0602065](#)].
- [127] R. A. Sunyaev and I. B. Zeldovich, *Microwave background radiation as a probe of the contemporary structure and history of the universe*, *Annual Review of Astron and Astrophys* **18** (1980) 537.
- [128] A. M. C. Le Brun, I. G. McCarthy and J.-B. Melin, *Testing Sunyaev–Zel’dovich measurements of the hot gas content of dark matter haloes using synthetic skies*, *Mon. Not. Roy. Astron. Soc.* **451** (2015) 3868 [[1501.05666](#)].
- [129] S. Amodeo et al., *Atacama Cosmology Telescope: Modeling the gas thermodynamics in BOSS CMASS galaxies from kinematic and thermal Sunyaev-Zel’dovich measurements*, *Phys. Rev. D* **103** (2021) 063514 [[2009.05558](#)].
- [130] I. Mohammed and U. Seljak, *Analytic model for the matter power spectrum, its covariance matrix, and baryonic effects*, *Mon. Not. Roy. Astron. Soc.* **445** (2014) 3382 [[1407.0060](#)].
- [131] S. Li, A. Frank and E. G. Blackman, *Triggered star formation and its consequences*, *Mon. Not. Roy. Astron. Soc.* **444** (2014) 2884 [[1404.5924](#)].
- [132] C. Gallart, M. Monelli, T. Ruiz-Lara, A. Calamida, S. Cassisi, M. Cignoni et al., *The Star Formation History of Eridanus II: On the Role of Supernova Feedback in the Quenching of Ultrafaint Dwarf Galaxies*, *Astrophys. J.* **909** (2021) 192 [[2101.04464](#)].
- [133] G. Dashyan and Y. Dubois, *Cosmic ray feedback from supernovae in dwarf galaxies*, *Astron. Astrophys.* **638** (2020) A123 [[2003.09900](#)].
- [134] V. Strait, G. Brammer, A. Muzzin, G. Desprez, Y. Asada, R. Abraham et al., *An Extremely Compact, Low-mass Galaxy on its Way to Quiescence at  $z = 5.2$* , *Astrophys. J. Lett.* **949** (2023) L23 [[2303.11349](#)].
- [135] E. Jones, B. Smith, R. Davé, D. Narayanan and Q. Li, *SIMBA-EOR: early galaxy formation in the SIMBA simulation including a new sub-grid interstellar medium model*, *Mon. Not. Roy. Astron. Soc.* **535** (2024) 1293 [[2402.06728](#)].

- [136] J. F. Navarro, C. S. Frenk and S. D. M. White, *A Universal Density Profile from Hierarchical Clustering*, *Astrophys. J.* **490** (1997) 493 [[astro-ph/9611107](#)].
- [137] E. Cappellaro, *Supernovae and their cosmological implications*, *Riv. Nuovo Cim.* **45** (2022) 549.
- [138] F. Y. Zhao, R. G. Strom and S. Y. Jiang, *The Guest Star of AD185 must have been a Supernova*, *Chinese J. Astron. Astrophys.* **6** (2006) 635.
- [139] D. Branch and G. A. Tammann, *Type ia supernovae as standard candles*, *Ann. Rev. Astron. Astrophys.* **30** (1992) 359.
- [140] DES collaboration, *First Cosmology Results Using Type Ia Supernovae From the Dark Energy Survey: Analysis, Systematic Uncertainties, and Validation*, *Astrophys. J.* **874** (2019) 150 [[1811.02377](#)].
- [141] DES collaboration, *First Cosmology Results using Type Ia Supernovae from the Dark Energy Survey: Constraints on Cosmological Parameters*, *Astrophys. J. Lett.* **872** (2019) L30 [[1811.02374](#)].
- [142] M. Hicken, P. Challis, S. Jha, R. P. Kirshner, T. Matheson, M. Modjaz et al., *CfA3: 185 Type Ia Supernova Light Curves from the CfA*, *Astrophys. J.* **700** (2009) 331 [[0901.4787](#)].
- [143] M. Hicken, P. Challis, R. P. Kirshner, A. Rest, C. E. Cramer, W. M. Wood-Vasey et al., *CfA4: Light Curves for 94 Type Ia Supernovae*, *Astrophys. J. S.* **200** (2012) 12 [[1205.4493](#)].
- [144] C. Contreras, M. Hamuy, M. M. Phillips, G. Folatelli, N. B. Suntzeff, S. E. Persson et al., *The Carnegie Supernova Project: First Photometry Data Release of Low-Redshift Type Ia Supernovae*, *Astronomical J.* **139** (2010) 519 [[0910.3330](#)].
- [145] M. D. Stritzinger, M. M. Phillips, L. N. Boldt, C. Burns, A. Campillay, C. Contreras et al., *The Carnegie Supernova Project: Second Photometry Data Release of Low-redshift Type Ia Supernovae*, *Astronomical J.* **142** (2011) 156 [[1108.3108](#)].
- [146] D. J. Fixsen, E. S. Cheng, J. M. Gales, J. C. Mather, R. A. Shafer and E. L. Wright, *The Cosmic Microwave Background Spectrum from the Full COBE FIRAS Data Set*, *Astrophys. J.* **473** (1996) 576 [[astro-ph/9605054](#)].
- [147] A. A. Penzias and R. W. Wilson, *A Measurement of excess antenna temperature at 4080-Mc/s*, *Astrophys. J.* **142** (1965) 419.
- [148] PLANCK collaboration, *Planck 2018 results. IV. Diffuse component separation*, *Astron. Astrophys.* **641** (2020) A4 [[1807.06208](#)].
- [149] SIMONS OBSERVATORY collaboration, *The Simons Observatory: Science goals and forecasts*, *JCAP* **02** (2019) 056 [[1808.07445](#)].
- [150] A. Lee, M. H. Abitbol, S. Adachi, P. Ade, J. Aguirre, Z. Ahmed et al., *The Simons Observatory*, in *Bulletin of the American Astronomical Society*, vol. 51, p. 147, Sept., 2019, [[1907.08284](#)], DOI.
- [151] J. Carlstrom, K. Abazajian, G. Addison, P. Adshead, Z. Ahmed, S. W. Allen et al., *CMB-S4*, in *Bulletin of the American Astronomical Society*, vol. 51, p. 209, Sept., 2019, [[1908.01062](#)], DOI.

- [152] CMB-S4 collaboration, *Snowmass 2021 CMB-S4 White Paper*, [2203.08024](#).
- [153] J. R. Fergusson and E. P. S. Shellard, *Primordial non-Gaussianity and the CMB bispectrum*, *Phys. Rev. D* **76** (2007) 083523 [[astro-ph/0612713](#)].
- [154] DESI collaboration, *First detection of the BAO signal from early DESI data*, *Mon. Not. Roy. Astron. Soc.* **525** (2023) 5406 [[2304.08427](#)].
- [155] P. Coles, *Einstein, Eddington and the 1919 eclipse*, *Nature* **568** (2019) 306.
- [156] I. Smail, R. S. Ellis and M. J. Fitchett, *Gravitational lensing of distant field galaxies by rich clusters: I. - faint galaxy redshift distributions*, *Mon. Not. Roy. Astron. Soc.* **270** (1994) 245 [[astro-ph/9402048](#)].
- [157] EUCLID collaboration, *Euclid preparation: VII. Forecast validation for Euclid cosmological probes*, *Astron. Astrophys.* **642** (2020) A191 [[1910.09273](#)].
- [158] EUCLID collaboration, *Euclid Definition Study Report*, [1110.3193](#).
- [159] E. P. Hubble, *Extragalactic nebulae*, *Astrophys. J.* **64** (1926) 321.
- [160] W. Hu, *Power spectrum tomography with weak lensing*, *Astrophys. J. Lett.* **522** (1999) L21 [[astro-ph/9904153](#)].
- [161] W. M. Baker, S. Tacchella, B. D. Johnson, E. Nelson, K. A. Suess, F. D'Eugenio et al., *A core in a star-forming disc as evidence of inside-out growth in the early Universe*, *Nature Astronomy* **9** (2025) 141 [[2306.02472](#)].
- [162] P. Jakobsen, P. Ferruit, C. Alves de Oliveira, S. Arribas, G. Bagnasco, R. Barho et al., *The Near-Infrared Spectrograph (NIRSpec) on the James Webb Space Telescope. I. Overview of the instrument and its capabilities*, *Astron. Astrophys.* **661** (2022) A80 [[2202.03305](#)].
- [163] M. Bolzonella, J. M. Miralles and R. Pelló, *Photometric redshifts based on standard SED fitting procedures*, *Astron. Astrophys.* **363** (2000) 476 [[astro-ph/0003380](#)].
- [164] EUCLID collaboration, *Euclid. I. Overview of the Euclid mission*, [2405.13491](#).
- [165] LSST collaboration, *LSST: from Science Drivers to Reference Design and Anticipated Data Products*, *Astrophys. J.* **873** (2019) 111 [[0805.2366](#)].
- [166] A. C. Carnall, R. J. McLure, J. S. Dunlop and R. Davé, *Inferring the star formation histories of massive quiescent galaxies with BAGPIPES: evidence for multiple quenching mechanisms*, *Mon. Not. Roy. Astron. Soc.* **480** (2018) 4379 [[1712.04452](#)].
- [167] R. Dalal et al., *Hyper Suprime-Cam Year 3 results: Cosmology from cosmic shear power spectra*, *Phys. Rev. D* **108** (2023) 123519 [[2304.00701](#)].
- [168] EUCLID collaboration, *Euclid preparation. X. The Euclid photometric-redshift challenge*, *Astron. Astrophys.* **644** (2020) A31 [[2009.12112](#)].
- [169] EUCLID collaboration, *Euclid: Calibrating photometric redshifts with spectroscopic cross-correlations*, *Astron. Astrophys.* **670** (2023) A149 [[2208.10503](#)].
- [170] EUCLID collaboration, *Euclid preparation. XVIII. The NISP photometric system*, *Astron. Astrophys.* **662** (2022) A92 [[2203.01650](#)].



- [171] R. Mehrem, *The plane wave expansion, infinite integrals and identities involving spherical bessel functions*, *Appl. Math. Comput.* **217** (2011) 5360 [[0909.0494](#)].
- [172] D. Limber, *The Analysis of Counts of the Extragalactic Nebulae in Terms of a Fluctuating Density Field. II*, *Astrophys. J.* **119** (1954) 655.
- [173] H. S. Grasshorn Gebhardt and D. Jeong, *Fast and accurate computation of projected two-point functions*, *Phys. Rev. D* **97** (2018) 023504 [[1709.02401](#)].
- [174] M. LoVerde and N. Afshordi, *Extended Limber Approximation*, *Phys. Rev. D* **78** (2008) 123506 [[0809.5112](#)].
- [175] H. Helmholtz, *Über integrale der hydrodynamischen gleichungen, welche den wirbelbewegungen entsprechen.*, *Journal für die reine und angewandte Mathematik* **1858** (1858) 25.
- [176] EUCLID collaboration, *Euclid: Optimising tomographic redshift binning for  $3\times 2$ pt power spectrum constraints on dark energy*, [2501.07559](#).
- [177] A. Hall, *Cosmology from weak lensing alone and implications for the Hubble tension*, *Mon. Not. Roy. Astron. Soc.* **505** (2021) 4935 [[2104.12880](#)].
- [178] D. Copeland, A. Taylor and A. Hall, *Towards determining the neutrino mass hierarchy: weak lensing and galaxy clustering forecasts with baryons and intrinsic alignments*, *Mon. Not. Roy. Astron. Soc.* **493** (2020) 1640 [[1905.08754](#)].
- [179] C. Heymans et al., *CFHTLenS tomographic weak lensing cosmological parameter constraints: Mitigating the impact of intrinsic galaxy alignments*, *Mon. Not. Roy. Astron. Soc.* **432** (2013) 2433 [[1303.1808](#)].
- [180] P. Lemos, A. Challinor and G. Efstathiou, *The effect of Limber and flat-sky approximations on galaxy weak lensing*, *JCAP* **05** (2017) 014 [[1704.01054](#)].
- [181] P. Schneider, T. Eifler and E. Krause, *COSEBIs: Extracting the full E-/B-mode information from cosmic shear correlation functions*, *Astron. Astrophys.* **520** (2010) A116 [[1002.2136](#)].
- [182] M. Asgari, P. Schneider and P. Simon, *Cosmic Shear Tomography and Efficient Data Compression using COSEBIs*, *Astron. Astrophys.* **542** (2012) A122 [[1201.2669](#)].
- [183] W. J. Percival and M. L. Brown, *Likelihood methods for the combined analysis of CMB temperature and polarisation power spectra*, *Mon. Not. Roy. Astron. Soc.* **372** (2006) 1104 [[astro-ph/0604547](#)].
- [184] R. E. Upham, M. L. Brown and L. Whittaker, *Sufficiency of a Gaussian power spectrum likelihood for accurate cosmology from upcoming weak lensing surveys*, *Mon. Not. Roy. Astron. Soc.* **503** (2021) 1999 [[2012.06267](#)].
- [185] R. Trotta, *Bayesian Methods in Cosmology*, [1701.01467](#).
- [186] H. Jeffreys, *An Invariant Form for the Prior Probability in Estimation Problems*, *Proceedings of the Royal Society of London Series A* **186** (1946) 453.
- [187] B. Hadzhiyska, K. Wolz, S. Azzoni, D. Alonso, C. García-García, J. Ruiz-Zapatero et al., *Cosmology with 6 parameters in the Stage-IV era: efficient marginalisation over nuisance parameters*, *The Open Journal of Astrophysics* **6** (2023) 23 [[2301.11895](#)].

- [188] A. Heavens, *Statistical techniques in cosmology*, [0906.0664](#).
- [189] J. Skilling, *Nested sampling for general Bayesian computation*, *Bayesian Analysis* **1** (2006) 833 .
- [190] G. Ashton et al., *Nested sampling for physical scientists*, *Nature* **2** (2022) [\[2205.15570\]](#).
- [191] F. Feroz and M. P. Hobson, *Multimodal nested sampling: an efficient and robust alternative to MCMC methods for astronomical data analysis*, *Mon. Not. Roy. Astron. Soc.* **384** (2008) 449 [\[0704.3704\]](#).
- [192] F. Feroz, M. P. Hobson and M. Bridges, *MultiNest: an efficient and robust Bayesian inference tool for cosmology and particle physics*, *Mon. Not. Roy. Astron. Soc.* **398** (2009) 1601 [\[0809.3437\]](#).
- [193] F. Feroz, M. P. Hobson, E. Cameron and A. N. Pettitt, *Importance Nested Sampling and the MultiNest Algorithm*, *Open J. Astrophys.* **2** (2019) 10 [\[1306.2144\]](#).
- [194] W. J. Handley, M. P. Hobson and A. N. Lasenby, *PolyChord: nested sampling for cosmology*, *Mon. Not. Roy. Astron. Soc.* **450** (2015) L61 [\[1502.01856\]](#).
- [195] W. J. Handley, M. P. Hobson and A. N. Lasenby, *PolyChord: next-generation nested sampling*, *Mon. Not. Roy. Astron. Soc.* **453** (2015) 4385 [\[1506.00171\]](#).
- [196] M. Tegmark, *Measuring cosmological parameters with galaxy surveys*, *Phys. Rev. Lett.* **79** (1997) 3806 [\[astro-ph/9706198\]](#).
- [197] M. Tegmark, A. Taylor and A. Heavens, *Karhunen-Loeve eigenvalue problems in cosmology: How should we tackle large data sets?*, *Astrophys. J.* **480** (1997) 22 [\[astro-ph/9603021\]](#).
- [198] A. Amara and A. Refregier, *Systematic Bias in Cosmic Shear: Beyond the Fisher Matrix*, *Mon. Not. Roy. Astron. Soc.* **391** (2008) 228 [\[0710.5171\]](#).
- [199] J. Gordon, B. F. de Aguiar, J. a. Rebouças, G. Brando, F. Falciano, V. Miranda et al., *Modeling nonlinear scales with the comoving Lagrangian acceleration method: Preparing for LSST Y1*, *Phys. Rev. D* **110** (2024) 083529 [\[2404.12344\]](#).
- [200] EUCLID collaboration, *Euclid: Covariance of weak lensing pseudo- $Cl$  estimates - Calculation, comparison to simulations, and dependence on survey geometry*, *Astron. Astrophys.* **660** (2022) A114 [\[2112.07341\]](#).
- [201] EUCLID collaboration, *Euclid preparation - LII. Forecast impact of super-sample covariance on  $3\times 2$ pt analysis with Euclid*, *Astron. Astrophys.* **691** (2024) A318 [\[2310.15731\]](#).
- [202] A. G. Riess et al., *A Comprehensive Measurement of the Local Value of the Hubble Constant with  $1\text{ km s}^{-1}\text{ Mpc}^{-1}$  Uncertainty from the Hubble Space Telescope and the SH0ES Team*, *Astrophys. J. Lett.* **934** (2022) L7 [\[2112.04510\]](#).
- [203] E. Abdalla et al., *Cosmology intertwined: A review of the particle physics, astrophysics, and cosmology associated with the cosmological tensions and anomalies*, *JHEAp* **34** (2022) 49 [\[2203.06142\]](#).



- [204] KILO-DEGREE SURVEY, DARK ENERGY SURVEY collaboration, *DES Y3 + KiDS-1000: Consistent cosmology combining cosmic shear surveys*, *Open J. Astrophys.* **6** (2023) 2305.17173 [2305.17173].
- [205] A. Albrecht et al., *Report of the Dark Energy Task Force*, [astro-ph/0609591](#).
- [206] M. Bartelmann, *Gravitational Lensing*, *Class. Quant. Grav.* **27** (2010) 233001 [1010.3829].
- [207] LSST DARK ENERGY SCIENCE collaboration, *Large Synoptic Survey Telescope: Dark Energy Science Collaboration*, [1211.0310](#).
- [208] D. Spergel et al., *Wide-Field InfrarRed Survey Telescope-Astrophysics Focused Telescope Assets WFIRST-AFTA 2015 Report*, [1503.03757](#).
- [209] C. Heymans et al., *KiDS-1000 Cosmology: Multi-probe weak gravitational lensing and spectroscopic galaxy clustering constraints*, *Astron. Astrophys.* **646** (2021) A140 [2007.15632].
- [210] DES collaboration, *Dark energy survey year 3 results: cosmological constraints from the analysis of cosmic shear in harmonic space*, *Mon. Not. Roy. Astron. Soc.* **515** (2022) 1942 [2203.07128].
- [211] T. Hamana et al., *Cosmological constraints from cosmic shear two-point correlation functions with HSC survey first-year data*, *Publ. Astron. Soc. Jap.* **72** (2020) 16 [1906.06041].
- [212] N. Kaiser, *Weak gravitational lensing of distant galaxies*, *Astrophys. J.* **388** (1992) 272.
- [213] P. Schneider, L. van Waerbeke, M. Kilbinger and Y. Mellier, *Analysis of two-point statistics of cosmic shear: I. estimators and covariances*, *Astron. Astrophys.* **396** (2002) 1 [astro-ph/0206182].
- [214] KiDS collaboration, *KiDS-1000 Cosmology: Cosmic shear constraints and comparison between two point statistics*, *Astron. Astrophys.* **645** (2021) A104 [2007.15633].
- [215] W. Hu and M. J. White, *Power spectra estimation for weak lensing*, *Astrophys. J.* **554** (2001) 67 [astro-ph/0010352].
- [216] M. L. Brown, P. G. Castro and A. N. Taylor, *CMB temperature and polarisation pseudo- $C(l)$  estimators and covariances*, *Mon. Not. Roy. Astron. Soc.* **360** (2005) 1262 [astro-ph/0410394].
- [217] C. Hikage, M. Takada, T. Hamana and D. Spergel, *Shear Power Spectrum Reconstruction using Pseudo-Spectrum Method*, *Mon. Not. Roy. Astron. Soc.* **412** (2011) 65 [1004.3542].
- [218] E. Hivon, K. M. Gorski, C. B. Netterfield, B. P. Crill, S. Prunet and F. Hansen, *Master of the cosmic microwave background anisotropy power spectrum: a fast method for statistical analysis of large and complex cosmic microwave background data sets*, *Astrophys. J.* **567** (2002) 2 [astro-ph/0105302].
- [219] M. Tegmark, *How to measure CMB power spectra without losing information*, *Phys. Rev. D* **55** (1997) 5895 [astro-ph/9611174].

- [220] M. Tegmark and A. de Oliveira-Costa, *How to measure CMB polarization power spectra without losing information*, *Phys. Rev. D* **64** (2001) 063001 [[astro-ph/0012120](#)].
- [221] I. Szapudi, S. Prunet, D. Pogosyan, A. S. Szalay and J. R. Bond, *Fast CMB analyses via correlation functions*, *Astrophys. J.* **548** (2000) L115 [[astro-ph/0010256](#)].
- [222] G. Chon, A. Challinor, S. Prunet, E. Hivon and I. Szapudi, *Fast estimation of polarization power spectra using correlation functions*, *Mon. Not. Roy. Astron. Soc.* **350** (2004) 914 [[astro-ph/0303414](#)].
- [223] HSC collaboration, *Cosmology from cosmic shear power spectra with Subaru Hyper Suprime-Cam first-year data*, *Publ. Astron. Soc. Jap.* **71** (2019) 43 [[1809.09148](#)].
- [224] A. Nicola, C. García-García, D. Alonso, J. Dunkley, P. G. Ferreira, A. Slosar et al., *Cosmic shear power spectra in practice*, *JCAP* **03** (2021) 067 [[2010.09717](#)].
- [225] C. García-García, D. Alonso and E. Bellini, *Disconnected pseudo- $C_\ell$  covariances for projected large-scale structure data*, *JCAP* **11** (2019) 043 [[1906.11765](#)].
- [226] KiDS, EUCLID collaboration, *KiDS and Euclid: Cosmological implications of a pseudo angular power spectrum analysis of KiDS-1000 cosmic shear tomography*, *Astron. Astrophys.* **665** (2022) A56 [[2110.06947](#)].
- [227] G. Efstathiou, *Myths and truths concerning estimation of power spectra*, *Mon. Not. Roy. Astron. Soc.* **349** (2004) 603 [[astro-ph/0307515](#)].
- [228] P. Schneider, L. Van Waerbeke and Y. Mellier, *B-modes in cosmic shear from source redshift clustering*, *Astron. Astrophys.* **389** (2002) 729 [[astro-ph/0112441](#)].
- [229] A. Heavens, A. Refregier and C. Heymans, *Intrinsic correlation of galaxy shapes: Implications for weak lensing measurements*, *Mon. Not. Roy. Astron. Soc.* **319** (2000) 649 [[astro-ph/0005269](#)].
- [230] D. B. Thomas, L. Whittaker, S. Camera and M. L. Brown, *Estimating the weak-lensing rotation signal in radio cosmic shear surveys*, *Mon. Not. Roy. Astron. Soc.* **470** (2017) 3131 [[1612.01533](#)].
- [231] F. Köhlinger, M. Viola, W. Valkenburg, B. Joachimi, H. Hoekstra and K. Kuijken, *A direct measurement of tomographic lensing power spectra from CFHTLenS*, *Mon. Not. Roy. Astron. Soc.* **456** (2016) 1508 [[1509.04071](#)].
- [232] F. Köhlinger et al., *KiDS-450: The tomographic weak lensing power spectrum and constraints on cosmological parameters*, *Mon. Not. Roy. Astron. Soc.* **471** (2017) 4412 [[1706.02892](#)].
- [233] E. van Uitert et al., *KiDS+GAMA: cosmology constraints from a joint analysis of cosmic shear, galaxy-galaxy lensing, and angular clustering*, *Mon. Not. Roy. Astron. Soc.* **476** (2018) 4662 [[1706.05004](#)].
- [234] SDSS collaboration, *The SDSS Coadd: Cosmic Shear Measurement*, *Astrophys. J.* **761** (2012) 15 [[1111.6622](#)].
- [235] G. Efstathiou, *Hybrid estimation of cmb polarization power spectra*, *Mon. Not. Roy. Astron. Soc.* **370** (2006) 343 [[astro-ph/0601107](#)].

- [236] B. Horowitz, U. Seljak and G. Aslanyan, *Efficient Optimal Reconstruction of Linear Fields and Band-powers from Cosmological Data*, *JCAP* **10** (2019) 035 [[1810.00503](#)].
- [237] U. Seljak, G. Aslanyan, Y. Feng and C. Modi, *Towards optimal extraction of cosmological information from nonlinear data*, *JCAP* **12** (2017) 009 [[1706.06645](#)].
- [238] S. P. Oh, D. N. Spergel and G. Hinshaw, *An Efficient technique to determine the power spectrum from cosmic microwave background sky maps*, *Astrophys. J.* **510** (1999) 551 [[astro-ph/9805339](#)].
- [239] F. Elsner and B. D. Wandelt, *Efficient Wiener filtering without preconditioning*, *Astron. Astrophys.* **549** (2013) A111 [[1210.4931](#)].
- [240] E. F. Bunn and B. Wandelt, *Pure E and B polarization maps via Wiener filtering*, *Phys. Rev. D* **96** (2017) 043523 [[1610.03345](#)].
- [241] D. K. Ramanah, G. Lavaux and B. D. Wandelt, *Optimal and fast  $\mathcal{E}/\mathcal{B}$  separation with a dual messenger field*, *Mon. Not. Roy. Astron. Soc.* **476** (2018) 2825 [[1801.05358](#)].
- [242] N. Estrada, B. R. Granett and L. Guzzo, *Cosmology behind the mask: constraining the parameters of  $\Lambda$ CDM with the unmasked galaxy density field from VIPERS*, *Mon. Not. Roy. Astron. Soc.* **512** (2022) 2817 [[2108.01926](#)].
- [243] O. H. E. Philcox, *Cosmology without window functions: Quadratic estimators for the galaxy power spectrum*, *Phys. Rev. D* **103** (2021) 103504 [[2012.09389](#)].
- [244] J. D. Bilbao-Ahedo, R. B. Barreiro, D. Herranz, P. Vielva and E. Martínez-González, *On the regularity of the covariance matrix of a discretized scalar field on the sphere*, *JCAP* **02** (2017) 022 [[1701.06617](#)].
- [245] J. R. Bond, A. H. Jaffe and L. Knox, *Estimating the power spectrum of the cosmic microwave background*, *Phys. Rev. D* **57** (1998) 2117 [[astro-ph/9708203](#)].
- [246] J. D. Bilbao-Ahedo, R. B. Barreiro, P. Vielva, E. Martínez-González and D. Herranz, *ECLIPSE: a fast Quadratic Maximum Likelihood estimator for CMB intensity and polarization power spectra*, *JCAP* **07** (2021) 034 [[2104.08528](#)].
- [247] U. Seljak, *Weak lensing reconstruction and power spectrum estimation: minimum variance methods*, *Astrophys. J.* **506** (1998) 64 [[astro-ph/9711124](#)].
- [248] U.-L. Pen, *Fast power spectrum estimation*, *Mon. Not. Roy. Astron. Soc.* **346** (2003) 619 [[astro-ph/0304513](#)].
- [249] P. McDonald, *Renormalization group computation of likelihood functions for cosmological data sets*, *Phys. Rev. D* **99** (2019) 043538 [[1810.08454](#)].
- [250] P. McDonald, *Improved renormalization group computation of likelihood functions for cosmological data sets*, *Phys. Rev. D* **100** (2019) 043511 [[1906.09127](#)].
- [251] B. Leistedt, H. V. Peiris, D. J. Mortlock, A. Benoit-Lévy and A. Pontzen, *Estimating the large-scale angular power spectrum in the presence of systematics: a case study of Sloan Digital Sky Survey quasars*, *Mon. Not. Roy. Astron. Soc.* **435** (2013) 1857 [[1306.0005](#)].

- [252] D. J. Mortlock, A. D. Challinor and M. P. Hobson, *Analysis of cosmic microwave background data on an incomplete sky*, *Mon. Not. Roy. Astron. Soc.* **330** (2002) 405 [[astro-ph/0008083](#)].
- [253] W. Hu, *Weak lensing of the CMB: A harmonic approach*, *Phys. Rev. D* **62** (2000) 043007 [[astro-ph/0001303](#)].
- [254] N. Martinet, J. Harnois-Déraps, E. Jullo and P. Schneider, *Probing dark energy with tomographic weak-lensing aperture mass statistics*, *Astron. Astrophys.* **646** (2021) A62 [[2010.07376](#)].
- [255] EUCLID collaboration, *Euclid preparation: I. The Euclid Wide Survey*, *Astron. Astrophys.* **662** (2022) A112 [[2108.01201](#)].
- [256] G. Szegő, *Orthogonal Polynomials*, American Math. Soc: Colloquium publ. American Mathematical Society, 1975.
- [257] S. Vanneste, S. Henrot-Versillé, T. Louis and M. Tristram, *Quadratic estimator for CMB cross-correlation*, *Phys. Rev. D* **98** (2018) 103526 [[1807.02484](#)].
- [258] A. Lewis, A. Challinor and N. Turok, *Analysis of CMB polarization on an incomplete sky*, *Phys. Rev. D* **65** (2002) 023505 [[astro-ph/0106536](#)].
- [259] K. M. Smith, *Pseudo- $C_\ell$  estimators which do not mix E and B modes*, *Phys. Rev. D* **74** (2006) 083002 [[astro-ph/0511629](#)].
- [260] J. Grain, M. Tristram and R. Stompor, *Polarized CMB spectrum estimation using the pure pseudo cross-spectrum approach*, *Phys. Rev. D* **79** (2009) 123515 [[0903.2350](#)].
- [261] A. Hall and A. Taylor, *Non-Gaussian likelihood of weak lensing power spectra*, *Phys. Rev. D* **105** (2022) 123527 [[2202.04095](#)].
- [262] A. Taruya, M. Takada, T. Hamana, I. Kayo and T. Futamase, *Lognormal property of weak-lensing fields*, *Astrophys. J.* **571** (2002) 638 [[astro-ph/0202090](#)].
- [263] S. Hilbert, J. Hartlap and P. Schneider, *Cosmic-shear covariance: The log-normal approximation*, *Astron. Astrophys.* **536** (2011) A85 [[1105.3980](#)].
- [264] B. Horowitz and U. Seljak, *Cosmological constraints from thermal Sunyaev–Zeldovich power spectrum revisited*, *Mon. Not. Roy. Astron. Soc.* **469** (2017) 394 [[1609.01850](#)].
- [265] B. Bolliet, B. Comis, E. Komatsu and J. F. Macías-Pérez, *Dark energy constraints from the thermal Sunyaev–Zeldovich power spectrum*, *Mon. Not. Roy. Astron. Soc.* **477** (2018) 4957 [[1712.00788](#)].
- [266] S.-S. Li et al., *KiDS-1000: Cosmology with improved cosmic shear measurements*, *Astron. Astrophys.* **679** (2023) A133 [[2306.11124](#)].
- [267] DES collaboration, *Dark Energy Survey Year 3 results: Cosmological constraints from galaxy clustering and weak lensing*, *Phys. Rev. D* **105** (2022) 023520 [[2105.13549](#)].
- [268] DES collaboration, *Dark Energy Survey Year 3 results: Cosmology from cosmic shear and robustness to data calibration*, *Phys. Rev. D* **105** (2022) 023514 [[2105.13543](#)].

- [269] DES collaboration, *Dark Energy Survey Year 3 results: Cosmology from cosmic shear and robustness to modeling uncertainty*, *Phys. Rev. D* **105** (2022) 023515 [[2105.13544](#)].
- [270] X. Li et al., *Hyper Suprime-Cam Year 3 results: Cosmology from cosmic shear two-point correlation functions*, *Phys. Rev. D* **108** (2023) 123518 [[2304.00702](#)].
- [271] A. Schneider and R. Teyssier, *A new method to quantify the effects of baryons on the matter power spectrum*, *JCAP* **12** (2015) 049 [[1510.06034](#)].
- [272] S. K. Giri and A. Schneider, *Emulation of baryonic effects on the matter power spectrum and constraints from galaxy cluster data*, *JCAP* **12** (2021) 046 [[2108.08863](#)].
- [273] G. Aricò, R. E. Angulo, S. Contreras, L. Ondaro-Mallea, M. Pellejero-Ibañez and M. Zennaro, *The BACCO simulation project: a baryonification emulator with neural networks*, *Mon. Not. Roy. Astron. Soc.* **506** (2021) 4070 [[2011.15018](#)].
- [274] H.-J. Huang, T. Eifler, R. Mandelbaum and S. Dodelson, *Modelling baryonic physics in future weak lensing surveys*, *Mon. Not. Roy. Astron. Soc.* **488** (2019) 1652 [[1809.01146](#)].
- [275] J. Salcido, I. G. McCarthy, J. Kwan, A. Upadhye and A. S. Font,  *$SP(k)$  – a hydrodynamical simulation-based model for the impact of baryon physics on the non-linear matter power spectrum*, *Mon. Not. Roy. Astron. Soc.* **523** (2023) 2247 [[2305.09710](#)].
- [276] DES collaboration, *Dark Energy Survey Year 3 Results: Multi-Probe Modeling Strategy and Validation*, [2105.13548](#).
- [277] T. Baldauf, M. Mirbabayi, M. Simonović and M. Zaldarriaga, *LSS constraints with controlled theoretical uncertainties*, [1602.00674](#).
- [278] T. Sprenger, M. Archidiacono, T. Brinckmann, S. Clesse and J. Lesgourgues, *Cosmology in the era of Euclid and the Square Kilometre Array*, *JCAP* **02** (2019) 047 [[1801.08331](#)].
- [279] M. G. Moreira, F. Andrade-Oliveira, X. Fang, H.-J. Huang, E. Krause, V. Miranda et al., *Mitigating baryonic effects with a theoretical error covariance*, *Mon. Not. Roy. Astron. Soc.* **507** (2021) 5592 [[2104.01397](#)].
- [280] M. Pellejero-Ibanez, R. E. Angulo, M. Zennaro, J. Stuecker, S. Contreras, G. Arico et al., *The bacco simulation project: bacco hybrid Lagrangian bias expansion model in redshift space*, *Mon. Not. Roy. Astron. Soc.* **520** (2023) 3725 [[2207.06437](#)].
- [281] T. D. Kitching and A. N. Taylor, *On Mitigation of the Uncertainty in Nonlinear Matter Clustering for Cosmic Shear Tomography*, *Mon. Not. Roy. Astron. Soc.* **416** (2011) 1717 [[1012.3479](#)].
- [282] I. G. McCarthy, J. Schaye, S. Bird and A. M. C. Le Brun, *The BAHAMAS project: Calibrated hydrodynamical simulations for large-scale structure cosmology*, *Mon. Not. Roy. Astron. Soc.* **465** (2017) 2936 [[1603.02702](#)].
- [283] A. Schneider, R. Teyssier, D. Potter, J. Stadel, J. Onions, D. S. Reed et al., *Matter power spectrum and the challenge of percent accuracy*, *JCAP* **04** (2016) 047 [[1503.05920](#)].



- [284] U. Seljak, *Analytic model for galaxy and dark matter clustering*, *Mon. Not. Roy. Astron. Soc.* **318** (2000) 203 [[astro-ph/0001493](#)].
- [285] J. A. Peacock and R. E. Smith, *Halo occupation numbers and galaxy bias*, *Mon. Not. Roy. Astron. Soc.* **318** (2000) 1144 [[astro-ph/0005010](#)].
- [286] A. Cooray and R. K. Sheth, *Halo Models of Large Scale Structure*, *Phys. Rept.* **372** (2002) 1 [[astro-ph/0206508](#)].
- [287] LSST DARK ENERGY SCIENCE collaboration, *Machine Learning LSST 3x2pt analyses – forecasting the impact of systematics on cosmological constraints using neural networks*, [2403.11797](#).
- [288] M. Vogelsberger, F. Marinacci, P. Torrey and E. Puchwein, *Cosmological Simulations of Galaxy Formation*, *Nature Rev. Phys.* **2** (2020) 42 [[1909.07976](#)].
- [289] R. A. Crain and F. van de Voort, *Hydrodynamical simulations of the galaxy population: enduring successes and outstanding challenges*, *Ann. Rev. Astron. Astrophys.* **61** (2023) 473 [[2309.17075](#)].
- [290] J. Schaye et al., *The FLAMINGO project: cosmological hydrodynamical simulations for large-scale structure and galaxy cluster surveys*, *Mon. Not. Roy. Astron. Soc.* **526** (2023) 4978 [[2306.04024](#)].
- [291] C. Hernández-Aguayo et al., *The MillenniumTNG Project: high-precision predictions for matter clustering and halo statistics*, *Mon. Not. Roy. Astron. Soc.* **524** (2023) 2556 [[2210.10059](#)].
- [292] R. Davé, D. Anglés-Alcázar, D. Narayanan, Q. Li, M. H. Rafieferantsoa and S. Appleby, *Simba: Cosmological Simulations with Black Hole Growth and Feedback*, *Mon. Not. Roy. Astron. Soc.* **486** (2019) 2827 [[1901.10203](#)].
- [293] D. Nelson et al., *The Illustris Simulation: Public Data Release*, *Astron. Comput.* **13** (2015) 12 [[1504.00362](#)].
- [294] V. Springel et al., *First results from the IllustrisTNG simulations: matter and galaxy clustering*, *Mon. Not. Roy. Astron. Soc.* **475** (2018) 676 [[1707.03397](#)].
- [295] N. E. Chisari, M. L. A. Richardson, J. Devriendt, Y. Dubois, A. Schneider, A. L. Brun, M. C. et al., *The impact of baryons on the matter power spectrum from the Horizon-AGN cosmological hydrodynamical simulation*, *Mon. Not. Roy. Astron. Soc.* **480** (2018) 3962 [[1801.08559](#)].
- [296] J. Schaye et al., *The EAGLE project: Simulating the evolution and assembly of galaxies and their environments*, *Mon. Not. Roy. Astron. Soc.* **446** (2015) 521 [[1407.7040](#)].
- [297] A. M. C. L. Brun, I. G. McCarthy, J. Schaye and T. J. Ponman, *Towards a realistic population of simulated galaxy groups and clusters*, *Mon. Not. Roy. Astron. Soc.* **441** (2014) 1270 [[1312.5462](#)].
- [298] J. Salcido and I. G. McCarthy, *Implications of feedback solutions to the  $S_8$  tension for the baryon fractions of galaxy groups and clusters*, [2409.05716](#).
- [299] M. P. van Daalen, I. G. McCarthy and J. Schaye, *Exploring the effects of galaxy formation on matter clustering through a library of simulation power spectra*, *Mon. Not. Roy. Astron. Soc.* **491** (2020) 2424 [[1906.00968](#)].

- [300] W. Elbers et al., *The FLAMINGO project: the coupling between baryonic feedback and cosmology in light of the  $S_8$  tension*, *Mon. Not. Roy. Astron. Soc.* **537** (2025) 2160 [2403.12967].
- [301] N. E. Chisari et al., *Modelling baryonic feedback for survey cosmology*, *Open J. Astrophys.* **2** (2019) 4 [1905.06082].
- [302] N. Fanidakis, C. M. Baugh, A. J. Benson, R. G. Bower, S. Cole, C. Done et al., *The evolution of active galactic nuclei across cosmic time: what is downsizing?*, *Mon. Not. Roy. Astron. Soc.* **419** (2011) 2797 [1011.5222].
- [303] A. Schneider, R. Teyssier, J. Stadel, N. E. Chisari, A. M. C. Le Brun, A. Amara et al., *Quantifying baryon effects on the matter power spectrum and the weak lensing shear correlation*, *JCAP* **03** (2019) 020 [1810.08629].
- [304] E. Semboloni, H. Hoekstra, J. Schaye, M. P. van Daalen and I. J. McCarthy, *Quantifying the effect of baryon physics on weak lensing tomography*, *Mon. Not. Roy. Astron. Soc.* **417** (2011) 2020 [1105.1075].
- [305] D. Copeland, A. Taylor and A. Hall, *The impact of baryons on the sensitivity of dark energy measurements*, *Mon. Not. Roy. Astron. Soc.* **480** (2018) 2247 [1712.07112].
- [306] A. Chudaykin and M. M. Ivanov, *Measuring neutrino masses with large-scale structure: Euclid forecast with controlled theoretical error*, *JCAP* **11** (2019) 034 [1907.06666].
- [307] CAMELS collaboration, *The CAMELS Project: Expanding the Galaxy Formation Model Space with New ASTRID and 28-parameter TNG and SIMBA Suites*, *Astrophys. J.* **959** (2023) 136 [2304.02096].
- [308] ACT, DESI collaboration, *Evidence for large baryonic feedback at low and intermediate redshifts from kinematic Sunyaev-Zel'dovich observations with ACT and DESI photometric galaxies*, 2407.07152.
- [309] L. Bigwood, M. A. Bourne, V. Irsic, A. Amon and D. Sijacki, *The case for large-scale AGN feedback in galaxy formation simulations: insights from XFABLE*, 2501.16983.
- [310] J. M. Z. Matilla, Z. Haiman, A. Petri and T. Namikawa, *Geometry and growth contributions to cosmic shear observables*, *Phys. Rev. D* **96** (2017) 023513 [1706.05133].
- [311] DES collaboration, *DES Y1 results: Splitting growth and geometry to test  $\Lambda$ CDM*, *Phys. Rev. D* **103** (2021) 023528 [2010.05924].
- [312] K. Zhong, E. Saraivanov, V. Miranda, J. Xu, T. Eifler and E. Krause, *Growth and geometry split in light of the DES-Y3 survey*, *Phys. Rev. D* **107** (2023) 123529 [2301.03694].
- [313] J. Ruiz-Zapatero et al., *Geometry versus growth - Internal consistency of the flat  $\Lambda$ CDM model with KiDS-1000*, *Astron. Astrophys.* **655** (2021) A11 [2105.09545].
- [314] DES collaboration, *Consistency of cosmic shear analyses in harmonic and real space*, *Mon. Not. Roy. Astron. Soc.* **503** (2021) 3796 [2011.06469].



- [315] T. Tröster et al., *Joint constraints on cosmology and the impact of baryon feedback: Combining KiDS-1000 lensing with the thermal Sunyaev–Zeldovich effect from Planck and ACT*, *Astron. Astrophys.* **660** (2022) A27 [[2109.04458](#)].
- [316] T. Ferreira, D. Alonso, C. Garcia-Garcia and N. E. Chisari, *X-Ray–Cosmic-Shear Cross-Correlations: First Detection and Constraints on Baryonic Effects*, *Phys. Rev. Lett.* **133** (2024) 051001 [[2309.11129](#)].
- [317] A. Aires, N. Kokron, R. Rosenfeld, F. Andrade-Oliveira and V. Miranda, *Mitigation of nonlinear galaxy bias with a theoretical-error likelihood*, [2410.08930](#).
- [318] F. Bernardeau, T. Nishimichi and A. Taruya, *Cosmic shear full nulling: sorting out dynamics, geometry and systematics*, *Mon. Not. Roy. Astron. Soc.* **445** (2014) 1526 [[1312.0430](#)].
- [319] H. Miyatake et al., *Hyper Suprime-Cam Year 3 results: Cosmology from galaxy clustering and weak lensing with HSC and SDSS using the emulator based halo model*, *Phys. Rev. D* **108** (2023) 123517 [[2304.00704](#)].
- [320] KILO-DEGREE SURVEY, DES collaboration, *DES Y3 + KiDS-1000: Consistent cosmology combining cosmic shear surveys*, *Open J. Astrophys.* **6** (2023) 2305.17173 [[2305.17173](#)].
- [321] C. García-García, M. Zennaro, G. Aricò, D. Alonso and R. E. Angulo, *Cosmic shear with small scales: DES-Y3, KiDS-1000 and HSC-DR1*, *JCAP* **08** (2024) 024 [[2403.13794](#)].
- [322] R. E. Angulo, M. Zennaro, S. Contreras, G. Aricò, M. Pellejero-Ibañez and J. Stücker, *The BACCO simulation project: exploiting the full power of large-scale structure for cosmology*, *Mon. Not. Roy. Astron. Soc.* **507** (2021) 5869 [[2004.06245](#)].
- [323] G. Aricò, R. E. Angulo and M. Zennaro, *Accelerating Large-Scale-Structure data analyses by emulating Boltzmann solvers and Lagrangian Perturbation Theory*, [2104.14568](#).
- [324] M. Zennaro, R. E. Angulo, M. Pellejero-Ibañez, J. Stücker, S. Contreras and G. Aricò, *The BACCO simulation project: biased tracers in real space*, *Mon. Not. Roy. Astron. Soc.* **524** (2023) 2407 [[2101.12187](#)].
- [325] PLANCK collaboration, *Planck 2018 results. VI. Cosmological parameters*, *Astron. Astrophys.* **641** (2020) A6 [[1807.06209](#)].
- [326] J. Schaye, C. Dalla Vecchia, C. M. Booth, R. P. C. Wiersma, T. Theuns, M. R. Haas et al., *The physics driving the cosmic star formation history*, *Mon. Not. Roy. Astron. Soc.* **402** (2010) 1536 [[0909.5196](#)].
- [327] W. Press, S. Teukolsky, W. Vetterling and B. Flannery, *Numerical Recipes in FORTRAN: The Art of Scientific Computing*. Cambridge University Press, 3rd ed., 2007.
- [328] EUCLID collaboration, *Euclid preparation: LIX. Angular power spectra from discrete observations*, *Astron. Astrophys.* **694** (2025) A141 [[2408.16903](#)].
- [329] EUCLID collaboration, *Euclid preparation. XII. Optimizing the photometric sample of the Euclid survey for galaxy clustering and galaxy-galaxy lensing analyses*, *Astron. Astrophys.* **655** (2021) A44 [[2104.05698](#)].

- [330] M. Davis, G. Efstathiou, C. S. Frenk and S. D. M. White, *The evolution of large-scale structure in a universe dominated by cold dark matter*, *Astrophys. J.* **292** (1985) 371.
- [331] A. Arbey and F. Mahmoudi, *Dark matter and the early Universe: a review*, *Prog. Part. Nucl. Phys.* **119** (2021) 103865 [[2104.11488](#)].
- [332] D. Spergel et al., *Wide-Field Infrared Survey Telescope-Astrophysics Focused Telescope Assets WFIRST-AFTA 2015 Report*, [1503.03757](#).
- [333] DESI collaboration, *The DESI Experiment Part I: Science, Targeting, and Survey Design*, [1611.00036](#).
- [334] BICEP2 collaboration, *Detection of B-Mode Polarization at Degree Angular Scales by BICEP2*, *Phys. Rev. Lett.* **112** (2014) 241101 [[1403.3985](#)].
- [335] PLANCK collaboration, *Planck intermediate results. XXX. The angular power spectrum of polarized dust emission at intermediate and high Galactic latitudes*, *Astron. Astrophys.* **586** (2016) A133 [[1409.5738](#)].
- [336] CAMELS collaboration, *The CAMELS project: Cosmology and Astrophysics with MachinE Learning Simulations*, *Astrophys. J.* **915** (2021) 71 [[2010.00619](#)].
- [337] C. C. Lovell, A. P. Vijayan, P. A. Thomas, S. M. Wilkins, D. J. Barnes, D. Irodotou et al., *First Light And Reionization Epoch Simulations (FLARES) - I. Environmental dependence of high-redshift galaxy evolution*, *Mon. Not. Roy. Astron. Soc.* **500** (2021) 2127 [[2004.07283](#)].
- [338] J. P. Gardner et al., *The James Webb Space Telescope*, *Space Sci. Rev.* **123** (2006) 485 [[astro-ph/0606175](#)].
- [339] X. Barcons et al., *Athena (Advanced Telescope for High ENergy Astrophysics) Assessment Study Report for ESA Cosmic Vision 2015-2025*, [1207.2745](#).
- [340] LISA collaboration, *Laser Interferometer Space Antenna*, [1702.00786](#).
- [341] A. Schneider, S. K. Giri, S. Amodeo and A. Refregier, *Constraining baryonic feedback and cosmology with weak-lensing, X-ray, and kinematic Sunyaev-Zeldovich observations*, *Mon. Not. Roy. Astron. Soc.* **514** (2022) 3802 [[2110.02228](#)].
- [342] UK National Energy System Operator, *Historic GB Generation Mix*. 2024.
- [343] I. Kwan and D. Rutherford, *Transatlantic Airline Fuel Efficiency Ranking, 2014*. The International Council on Clean Transportation, 2014.
- [344] S. Portegies Zwart, *The Ecological Impact of High-performance Computing in Astrophysics*, *Nature Astron.* **4** (2020) 819 [[2009.11295](#)].
- [345] M. J. Geller and J. P. Huchra, *Mapping the Universe*, *Science* **246** (1989) 897.
- [346] SDSS collaboration, *The Sloan Digital Sky Survey: Technical Summary*, *Astron. J.* **120** (2000) 1579 [[astro-ph/0006396](#)].
- [347] C. J. Conselice, A. Wilkinson, K. Duncan and A. Mortlock, *The Evolution of Galaxy Number Density at  $z < 8$  and Its Implications*, *Astrophys. J.* **830** (2016) 83 [[1607.03909](#)].

- [348] J. Rhodes, E. Huff, D. Masters and A. Nierenberg, *The End of Galaxy Surveys*, *Astron. J.* **160** (2020) 261 [[2010.06064](#)].
- [349] OpenAI et al., *GPT-4 Technical Report*, [2303.08774](#).
- [350] M. L. [Boas](#)<sup>1</sup>, *Mathematical Methods in the Physical Sciences*. Wiley, Hoboken, USA, 3rd ed., 2006.
- [351] M. Chevallier and D. Polarski, *Accelerating universes with scaling dark matter*, *Int. J. Mod. Phys. D* **10** (2001) 213 [[gr-qc/0009008](#)].
- [352] R. Tsutsui, T. Nakamura, D. Yonetoku, T. Murakami, S. Tanabe, Y. Kodama et al., *Constraints on  $w_0$  and  $w_a$  of Dark Energy from High Redshift Gamma Ray Bursts*, *Mon. Not. Roy. Astron. Soc.* **394** (2009) L31 [[0807.2911](#)].
- [353] E. Amaldi, *From the discovery of the neutron to the discovery of nuclear fission*, *Physics Reports* **111** (1984) 1.
- [354] S. Mele, *The Measurement of the Number of Light Neutrino Species at LEP*, *Adv. Ser. Direct. High Energy Phys.* **23** (2015) 89.
- [355] J. J. Bennett, G. Buldgen, P. F. De Salas, M. Drewes, S. Gariazzo, S. Pastor et al., *Towards a precision calculation of  $N_{\text{eff}}$  in the Standard Model II: Neutrino decoupling in the presence of flavour oscillations and finite-temperature QED*, *JCAP* **04** (2021) 073 [[2012.02726](#)].
- [356] J. Lesgourgues, G. Mangano, G. Miele and S. Pastor, *Neutrino Cosmology*. Cambridge University Press, Cambridge, 2013, [DOI](#).
- [357] EUCLID collaboration, *Euclid preparation - LIV. Sensitivity to neutrino parameters*, *Astron. Astrophys.* **693** (2025) A58 [[2405.06047](#)].

---

<sup>1</sup>*How did you get a B in a red box?* — Peter Thomas

---

*I always rip out the last page of a book. Then it doesn't have to end. I hate endings!*

—The Doctor

---